3D Bioprinting of an in vitro Osteochondral Model for Osteoarthritis Disease Modelling

Patricia Santos Beato

Department of Biochemical Engineering and Division of Surgery & Interventional Science,

University College London (UCL)

EngD Biochemical Engineering & Bioprocess Leadership

2023

I, Patricia Santos Beato, confirm that the work presented in this thesis is my own. Where information has been derived from other sources, I confirm that this has been indicated in the thesis.

Signed: Patricia Santos Beato

Abstract

Osteoarthritis is the most prevalent joint disease globally. There is no cure or a reliable human disease model to understand it further and test new treatments. Developing reliable disease models is key to improving our understanding of these pathologies. This thesis has three main research focuses: 1) investigate the use of self-assembling peptides, Peptigels®, for 3D-bioprinting cartilage *in vitro* models; 2) use a hydroxyapatite (HA) ink, to 3D-print bone-like *in vitro* models, 3) combine the developed cartilage and bone-like *in vitro* models to make osteochondral tissue constructs. Firstly, Peptigels® Alpha 1, 2, and 4 were screened, assessing their rheological, pH, diffusion, and printability properties. Alpha 1 and 4 were chosen to test their chondrogenic potential by 3D-bioprinting. Circular disc structures were 3D-bioprinted with human primary chondrocytes. They were compared to a cell pellet cartilage "gold standard" model. Alpha 1 demonstrated better chondrogenic potential than Alpha 4, inducing chondrogenic marker expression significantly faster than the "gold standard" ($p < 0.05$). Secondly, an HA ink was used to 3D-print grid structures seeded with Saos-2 cells or human primary osteoblasts (HOBs). These structures promoted osteogenic marker expression in Saos-2 faster than their 2D control ($p < 0.05$). Finally, these HA structures were combined with Alpha 1. Acellular-HA, Saos-2-seeded HA, and HOBs-seeded HA were tested. Osteogenic and chondrogenic marker expression demonstrated that the HA construct did not compromise the chondrogenic behaviour of Alpha 1. The osteogenic potential of the HA construct was compromised due to the change in the cell culture medium. These osteochondral models demonstrated the expected tissue marker expression, confirming that non-animal-derived human osteochondral tissue models can be developed. Further culture medium composition optimisation and comparison to native osteochondral tissues should be performed. Additional work should focus on inducing osteoarthritis on these constructs and compare them to *in vivo* samples to have a reliable disease model.

Impact statement

The current disease modelling and drug testing techniques predominantly utilise animal models, yet these models need to mirror the pathophysiology exhibited in human diseases. This deficiency is likely the cause of over 90% of drug failures in human clinical trials. Therefore, exploring *in vitro* human disease models as an alternative is essential, as they could foster disease-specific research and more efficient initial drug screening and pre-clinical testing.

This work uses 3D-bioprinting as the biofabrication strategy to create more reliable and reproducible osteochondral tissue models for drug development and disease research *in vitro*. Primary human cells are also used, offering a more physiologically relevant model than animal models or cell lines. Additionally, using non-animal-derived materials can reduce the ethical concerns and potential variability associated with animal-derived materials. This work has the potential to contribute to further understanding of osteochondral diseases and injuries and develop new therapeutic approaches to treat them.

Here, different self-assembling peptide hydrogels, Peptigels®, were characterised and optimised for the 3D-bioprinting process, experimentally and *in silico*. This has enabled a thorough screening of the potential bioinks, an optimisation of the 3D-bioprinting parameters, and a further understanding of the shear stresses and pressure forces that arise in the printing process through CFD (Computational Fluid Dynamics) modelling. Complete characterisation of the 3D-bioprinted cartilage tissue models was also performed based on the previous optimisation steps. A hydroxyapatite (HA)-based bone tissue model was validated using primary human osteoblasts and Saos-2 cells. Finally, a novel osteochondral tissue model was developed, combining the cartilage and validated HA-based bone models. The production of these tissues would allow disease models to be closer to human pathophysiology and be more sustainable and controllable. These models could be included in clinical research to study different stages of diseases such as osteoarthritis. Additionally, they can be used as initial drug testing platforms to assess drug efficacies and toxicities without animal-based models.

Overall, these models have been proven to be manufactured at a scaled-up level through the automation of 3D-bioprinting technologies, which could be further improved for industrial use. The manufactured models have a reduced component of animal-derived materials, making them sustainable and tunable. They perform better than current gold standards, such as 3D pellet models for cartilage tissue modelling. By creating these tissue models that closely resemble native tissues using human primary cells, we can enable more accurate testing of potential drugs and therapies, leading to more efficient drug development. These models can also be used to study diseases' underlying mechanisms and facilitate personalised medicine development.

UCL Research Paper Declaration Form 1

referencing the doctoral candidate's own published work(s)

1. **For a research manuscript that has already been published** (if not yet published, please skip to section 2)

   a) **What is the title of the manuscript?**

   Biofabrication of the osteochondral unit and its applications: Current and future directions for 3D bioprinting

   b) **Please include a link to or doi for the work**

   10.1177/20417314221133480

   c) **Where was the work published?**

   Journal of Tissue Engineering

   d) **Who published the work?** (e.g. OUP)

   SAGE

   e) **When was the work published?**

   06/11/2022

   f) **List the manuscript's authors in the order they appear on the publication**

   Patricia Santos-Beato, Swati Midha, Andrew A. Pitsillides, Aline Miller, Ryo Torii, Deepak M. Kalaskar

   g) **Was the work peer reviewed?**

Yes

h) **Have you retained the copyright?**

Yes

i) **Was an earlier form of the manuscript uploaded to a preprint server?** (e.g. medRxiv). If 'Yes', please give a link or doi)

<u>No</u>

If 'No', please seek permission from the relevant publisher and check the box next to the below statement:

☒

*I acknowledge permission of the publisher named under **1d** to include in this thesis portions of the publication named as included in **1c**.*

2. **For a research manuscript prepared for publication but that has not yet been published** (if already published, please skip to section 3)

   a) **What is the current title of the manuscript?**
   b) **Has the manuscript been uploaded to a preprint server?** (e.g. medRxiv; if 'Yes', please give a link or doi)
   c) **Where is the work intended to be published?** (e.g. journal names)
   d) **List the manuscript's authors in the intended authorship order**
   e) **Stage of publication** (e.g. in submission)

3. **For multi-authored work, please give a statement of contribution covering all authors** (if single-author, please skip to section 4)

   Patricia Santos Beato – investigation, visualization, writing – original draft, writing – review & editing.

   Swati Midha – writing – review & editing.

Andrew A. Pitsillides – supervision, writing – review & editing.

Aline Miller – supervision, writing – review & editing.

Ryo Torii – supervision

Deepak M. Kalaskar – funding acquisition, supervision, writing – review & editing.

4. **In which Chapter(s) of your thesis can this material be found?**

   Chapter 1

5. **e-Signatures confirming that the information above is accurate** (this form should be co-signed by the supervisor/ senior author unless this is not appropriate, e.g. if the paper was a single-author work)

Candidate

Patricia Santos Beato

Date:

06/09/2023

Supervisor/ Senior Author (where appropriate)

Deepak kalaskar

Date

30/09/2023

UCL Research Paper Declaration Form 2

referencing the doctoral candidate's own published work(s)

1. **For a research manuscript that has already been published** (if not yet published, please skip to section 2)

   j) **What is the title of the manuscript?**

   Evaluation of a synthetic peptide-based bioink (PeptiInk Alpha 1) for *in vitro* 3D bioprinting of cartilage tissue models

   k) **Please include a link to or doi for the work**

   https://doi.org/10.36922/ijb.0899

   l) **Where was the work published?**

   International Journal of Bioprinting

   m) **Who published the work?** (e.g. OUP)

   AccScience Publishing

   n) **When was the work published?**

   06/09/2023

   o) **List the manuscript's authors in the order they appear on the publication**

   Patricia Santos-Beato, Andrew A. Pitsillides, Alberto Saiani, Aline Miller, Ryo Torii, Deepak M. Kalaskar

   p) **Was the work peer reviewed?**

Yes

q) **Have you retained the copyright?**

Yes

r) **Was an earlier form of the manuscript uploaded to a preprint server?** (e.g. medRxiv). If 'Yes', please give a link or doi)

No

If 'No', please seek permission from the relevant publisher and check the box next to the below statement:

☒

*I acknowledge permission of the publisher named under **1d** to include in this thesis portions of the publication named as included in **1c**.*

2. **For a research manuscript prepared for publication but that has not yet been published** (if already published, please skip to section 3)

   f) **What is the current title of the manuscript?**
   g) **Has the manuscript been uploaded to a preprint server?** (e.g. medRxiv; if 'Yes', please give a link or doi)
   h) **Where is the work intended to be published?** (e.g. journal names)
   i) **List the manuscript's authors in the intended authorship order**
   j) **Stage of publication** (e.g. in submission)

3. **For multi-authored work, please give a statement of contribution covering all authors** (if single-author, please skip to section 4)

   Patricia Santos Beato – conceptualization, formal analysis, investigation, visualization, writing – original draft.

Andrew A. Pitsillides – conceptualization, supervision, writing – review & editing.

Alberto Saiani – supervision, writing – review & editing.

Aline Miller – supervision, writing – review & editing.

Ryo Torii – supervision

Deepak M. Kalaskar – funding acquisition, supervision, writing – review & editing.

4. **In which Chapter(s) of your thesis can this material be found?**

   Chapter 2 and Chapter 3

5. **e-Signatures confirming that the information above is accurate** (this form should be co-signed by the supervisor/ senior author unless this is not appropriate, e.g. if the paper was a single-author work)

Candidate

Patricia Santos Beato

Date:

06/09/2023

Supervisor/ Senior Author (where appropriate)

Deepak kalaskar

Date

30/09/2023

Acknowledgements

I want to thank my supervisors, Prof. Deepak Kalaskar, Prof. Ryo Torii and Prof. Gary Lye, for the opportunity and their supervision in this EngD. I would also like to thank UKRI and the EPSRC for the funding provided.

I would also like to thank the industrial partner Manchester Biogel Ltd for facilitating the Peptigels® used in this research and the excellent team which provided guidance with the laboratory assays and troubleshooting. I especially thank Aline Miller and Alberto Saiani for their guidance and support throughout this journey.

This work would not have been possible without the help and collaboration of multiple external researchers.

Firstly, I would like to thank Dr Swati Midha deeply. Swati, you have been my true guide from the beginning until the end of this EngD. I will be forever grateful for your immense patience and loving support when I first started in the lab and your predisposition to advise me. Thank you for teaching me to plan, work hard, and take coffee breaks.

Secondly, I thank Rosanne Roys for being a wonderful Masters student. You made working with ceramic printing and our trips to Stanmore fun and rewarding. I have learnt so much from you. A big section of this thesis would not have been possible without you; thank you.

Thirdly, I would like to thank Andrew Pitsillides. Thank you for your support, your guidance, and your time. In every meeting we had, I felt heard and valued. Thank you so much for all the time invested in getting the cartilage paper out and for showing me how to be more concise in my writing. I hope we can collaborate in the future!

Finally, I would like to thank our collaborators from IIT Indore. I want to thank Apurba Das for the support given while I visited IIT Indore at the start of the EngD. Additionally, I would like to thank Ankan and Tapas for their support in the lab and for being extremely welcoming during my visit.

Outline of the thesis

This thesis work is composed of 6 Chapters. **Figure 0.1** shows a schematic diagram with an overview of the thesis structure and the content included.

Chapter 1 provides a comprehensive introduction to the osteochondral tissue, the components necessary to recreate this tissue *in vitro*, the current manufacturing tissue engineering technologies, and a thorough review of the current approaches to 3D bioprinting osteochondral tissue models. It delves into the materials used, the cell choice, and the current applications and limitations of these 3D bioprinted tissue models.

Chapter 2 is the first experimental chapter. It focuses on screening and characterising three Peptigel® candidates (Alpha 1, Alpha 2, Alpha 4) based on their rheological properties, pH, diffusion properties and printability for subsequent use as PeptiInks®. From the three Peptigels®, two are selected for further 3D bioprinting optimisation (Alpha 1 and Alpha 4). A computational fluid dynamics model is presented to model the 3D bioprinting process and understand shear stress levels and pressure forces that arise when printing these two PeptiInks®. Finally, 3D bioprinting optimisation tests different printing pressures and speeds in the two selected PeptiInks®.

Chapter 3 investigates using the two selected PeptiInks® as candidates to manufacture 3D bioprinted human cartilage tissue models *in vitro*. Both PeptiInks® are bioprinted, and cell viability, cell proliferation, histological information, and immunofluorescence labelling assessments are performed to compare both candidates. Results are compared to the current cartilage *in vitro* tissue model "gold standard". Alpha 1 is chosen, presenting the best chondrogenic properties, and further assessment of mRNA expression is performed to characterise the 3D bioprinted cartilage model fully.

Chapter 4 focuses on developing a 3D-printed human bone-like tissue model *in vitro* based on previously optimised hydroxyapatite ink. Material characterisation is performed, focusing on the material's rheological properties, assessment of size changes of the 3D printed scaffolds, and compressive modulus of the scaffolds. These

scaffolds' cell cytocompatibility and osteogenic potential are assessed and characterised using Saos-2 cells. A proof-of-concept 3D-printed bone-like model using human primary osteoblasts is also investigated.

Chapter 5 targets the combination of Chapter 3 and Chapter 4, bringing together the cartilage and bone-like tissue models to manufacture a 3D bioprinted human osteochondral tissue model. Firstly, an initial characterisation of acellular hydroxyapatite scaffolds' effect on the Alpha 1-based cartilage section is performed. Secondly, a thorough assessment of an osteochondral tissue model with Saos-2 cells populating the hydroxyapatite scaffold is done. Finally, a proof-of-concept using primary human cells is investigated using human osteoblasts on the hydroxyapatite scaffold is preliminarily investigated.

Chapter 6 is a conclusion chapter where all objectives and hypotheses presented across previous chapters are summarised, and the key findings are highlighted.

Finally, **Appendix 1** shows the additional section required for the completion of the EngD, targeting the impact of this technology in the industry. Additional and supporting data is also presented in the subsequent appendix sections.
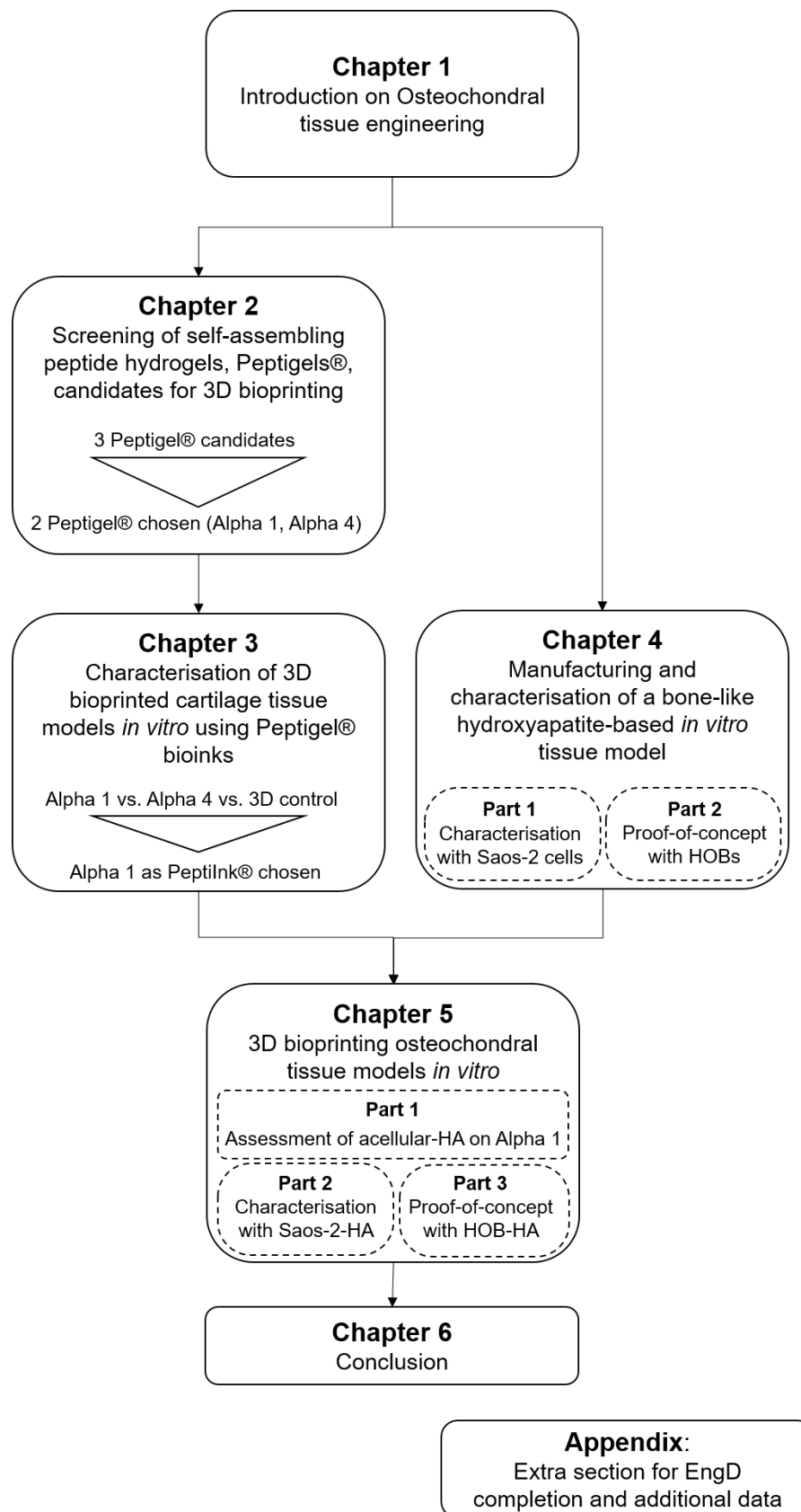
Chapter 1
Introduction on Osteochondral tissue engineering

Chapter 2
Screening of self-assembling peptide hydrogels, Peptigels®, candidates for 3D bioprinting

3 Peptigel® candidates

2 Peptigel® chosen (Alpha 1, Alpha 4)

Chapter 3
Characterisation of 3D bioprinted cartilage tissue models *in vitro* using Peptigel® bioinks

Alpha 1 vs. Alpha 4 vs. 3D control

Alpha 1 as PeptiInk® chosen

Chapter 4
Manufacturing and characterisation of a bone-like hydroxyapatite-based *in vitro* tissue model

Part 1
Characterisation with Saos-2 cells

Part 2
Proof-of-concept with HOBs

Chapter 5
3D bioprinting osteochondral tissue models *in vitro*

Part 1
Assessment of acellular-HA on Alpha 1

Part 2
Characterisation with Saos-2-HA

Part 3
Proof-of-concept with HOB-HA

Chapter 6
Conclusion

Appendix:
Extra section for EngD completion and additional data

Figure 0.1. Thesis structure diagram

Table of Contents

List of Figures

26

28

30

31

List of Tables

List of Equations

List of Abbreviations

1. 2D - Two Dimensional
2. 3D - Three Dimensional
3. ADSCs - Adipose Derived Stem Cells
4. Aggrecan - Aggregating Proteoglycan
5. AGC - Aggrecan
6. ALP - Alkaline Phosphatase
7. ANOVA – Analysis of Variance
8. αMEM - Minimum Essential Medium Eagle-α
9. BMP-2 - Bone Morphogenetic Protein-2
10. BMSCs – Bone marrow-derived Mesenchymal Stem Cells
11. BSA – Bovine Serum Albumin
12. C - Concentration
13. CAD – Computer Aided Design
14. CB6-HA - Curcubit[6]uril 1,6-diaminohexane conjugated hyaluronic acid
15. CFD – Computational Fluid Dynamics
16. CGC – Critical Gelation Concentration
17. Col-I – Collagen type-I
18. Col-II – Collagen type-II
19. Col-X – Collagen type-X
20. CPC – Calcium Phosphate Cement
21. CS-AEMA - Chondroitin sulphate amino ethyl methacrylate
22. CT – Cycle Threshold
23. DAPI - 4′,6-diamidino-2-phenylindole
24. dECM - Decellularised Extracellular Matrix
25. EngD – Doctorate in Engineering
26. FACS - Fluorescent Activated Cell Sorting
27. FBS – Foetal Bovine Serum
28. FDM - Fused Deposition Modelling
29. FE – Finite Element
30. FGF - Fibroblast Growth Factor

31. G - Gauge

32. g – Gravitational force

33. GAG - Glycosaminoglycan

34. GAPDH - Glyceraldehyde-3-phosphate dehydrogenase

35. GDF-5 - Growth Differentiation Factor-5

36. gelMA – Gelatine Methacryloyl

37. GF – Growth Factor

38. HA - Hydroxyapatite

39. HAMA - Methacrylated hyaluronic acid

40. hBMSCs – Human Bone marrow-derived Mesenchymal Stem Cells

41. HCHs – Primary Human Chondrocytes

42. HOBs – Primary Human Osteoblasts

43. HPMC - Hydroxypropyl methylcellulose

44. HUVECs - Human Umbilical Vein Endothelial Cells

45. H&E - Haematoxylin and Eosin

46. IGF-1 - Insulin-like Growth Factor-1

47. IL-1β – Interleukin-1β

48. iPSCs – Induced Pluripotent Stem Cells

49. MBG – Manchester Biogel Ltd

50. MMPs – Matrix Metalloproteinases

51. MSCs – Mesenchymal Stem Cells

52. NICE – National Institute of Health and Clinical Excellence

53. OCT – Optimal Cutting Temperature

54. OA – Osteoarthritis

55. PBS - Phosphate-buffered Saline

56. PCL – Poly-ϵ-caprolactone

57. PDGF - Platelet-derived Growth Factor

58. PEG - Polyethelene glycol

59. PEGDMA - Poly(ethylene glycol) dimethacrylate

60. PHB - Poly(3-hydreoxyputyrate)

61. PLA – Poly(lactic) acid

62. PVP - Polyvinylpyrrolidone

63. qPCR - Quantitative Polymerase Chain Reaction

64. RUNX2 - Runt-related Transcription Factor-2

65. SCs – Stem Cells

66. SEM - Scanning Electron Microscopy

67. TCP – Tricalcium phosphate

68. TGF-β - Transforming Growth Factor-β

69. TNF-α - Tumour Necrosis Factor-α

70. VEGF – Vascular Endothelial Growth Factor

71. VOF – Volume of Fluid

Chapter 1: Introduction to Osteochondral tissue engineering

1.1 Introduction to the Osteochondral Unit

The osteochondral tissue is a composite tissue with a complex architecture formed by the intersection of bone and hyaline cartilage [1], as shown in Figure 1.1 [2]. The cartilage section has three distinct zones, which are characterised by cell shape and distribution as well as extracellular matrix protein composition and organisation [1]. These cartilage areas are divided into superficial, middle and deep zones. The deep cartilage zone is in contact with the tidemark zone, where uncalcified and calcified cartilage meet. The subchondral bone section is connected to the calcified cartilage section through the cement line [2].
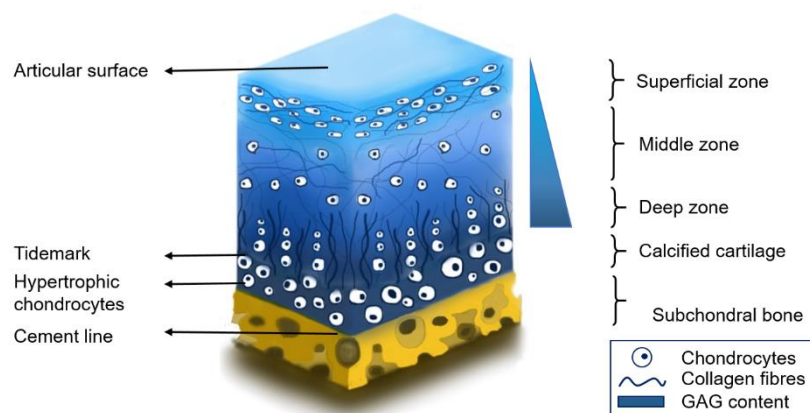
Figure 1.1. Osteochondral unit. The distribution of chondrocytes and collagen fibre alignment changes gradually from the superficial zone, parallel to the articular surface, to a distribution perpendicular to the tidemark in the deep zone. Across these zones, there is also an increase in GAG content from the superficial zone toward the deep zone. GAG: Glycosaminoglycan. From Santos-Beato et al. [2]

1.1.1 Cartilage section

Articular cartilage presents an extracellular matrix of 65% to 85% water [3], and only 2% of the total volume are chondrocytes [4], a hypocellular tissue. Major extracellular matrix components include collagen type-II (10-20% of the wet weight) and aggregating proteoglycans (aggrecans) (5-10% of the wet weight) [5]. The cartilage zones can be distinguished by cell and protein characteristics. The superficial zone is characterised by a dense layer of collagen fibres parallel to the surface and populated with elongated chondrocytes. Higher levels of proteoglycans, such as lubricin [6] and synovial fluid constituents [7], alongside the collagen fibres, make this section smooth and have reduced friction. The middle zone presents anisotropic collagen fibres [8,9] and the highest levels of glycosaminoglycan (GAG) chondroitin sulphate [10]. Here, the chondrocytes present their characteristic circular shape and are randomly distributed [3]. Finally, the deep or radial zone presents collagen fibres perpendicular to the tidemark [11], with high levels of GAG keratan sulphate [10]. Here, the chondrocytes are organised in columns perpendicular to the tidemark. Cartilage is a tissue with an elastic modulus ranging from 1.9 MPa to 15 MPa [12]. These mechanical properties vary gradually as the tissue gets closer to the calcified cartilage section, which limits it from the subchondral bone section.

1.1.2 Calcified cartilage section

The tidemark connects uncalcified and calcified cartilage. Calcified cartilage is a thin interlayer of hard tissue which connects the hyaline articular cartilage and the subchondral bone [13]. It is a transition zone where the mechanical stresses and stimuli which affect the hyaline cartilage section are transmitted to the subchondral bone [14]. Its composition is characterised by an approximate 65% dry weight of hydroxyapatite (HA) [14], and the dry weight of collagen type-II is 20% less than hyaline cartilage [14]. This composition further changes close to the cement line, which forms the connection with the subchondral bone tissue.

1.1.3 Subchondral bone section

Subchondral bone is the bony layer which is connected to calcified cartilage through the cement line. It can be divided into the subchondral bone plate and the subchondral bone trabecula [15]. The subchondral bone plate presents a compact structure with pores, blood vessels and nerve fibres [15]. The subchondral bone trabeculae undergo continuous bone remodelling and are cancellous structures subjacent to the subchondral bone plate. These regions vary in thickness depending on joint geometry, age, weight or exercise levels [11]. Overall, it presents an approximate compressive modulus of 4 GPa [16] and provides mechanical and nutritional support for the cartilage section [15]. It mainly comprises extracellular bone matrix and three major cell types: osteoblasts, osteoclasts and osteocytes (Section 1.2.1). The organic component of the calcified bone matrix is collagen fibres, 90% being collagen type-I and the rest being proteoglycans such as osteonectin, osteopontin and osteocalcin [17]. Bone also presents an inorganic component; 50% of the dry weight of the matrix is HA. These two components are arranged in complex hierarchical structures, which give bone its mechanical properties.

1.2 Osteochondral Tissue Engineering

The osteochondral tissue is a complex tissue with a particular hierarchical structure. Tissue engineering attempts to achieve exemplary architecture and mechanical properties are yet to succeed. Multiple parameters such as cell choice, materials, growth factors (GFs) or external cues need to be optimised to develop this composite tissue. A summary of these parameters can be seen in Figure 1.2.
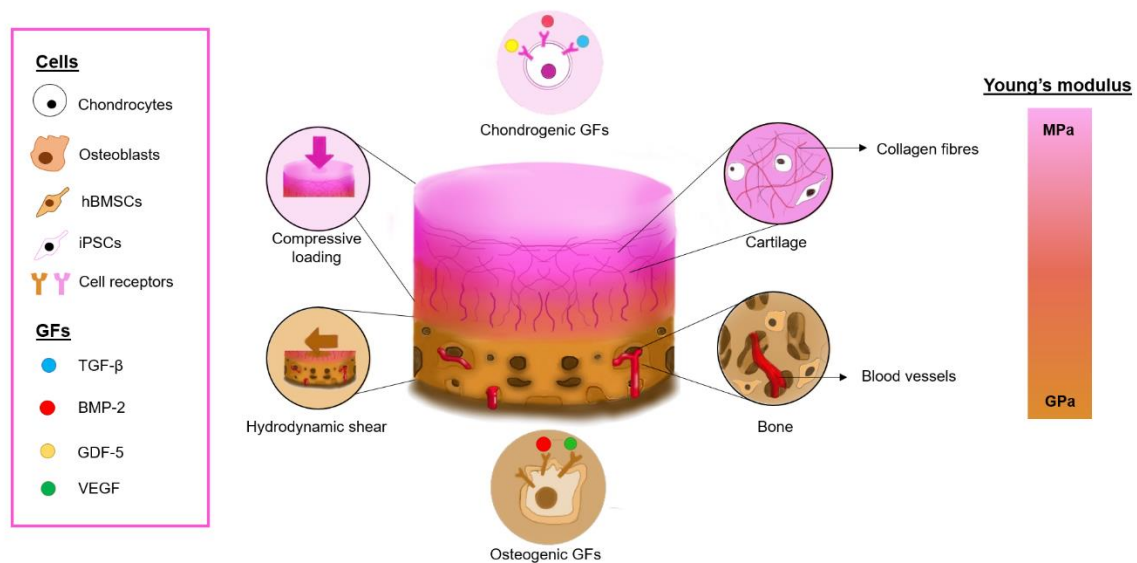
Figure 1.2. Key parameters in osteochondral unit development. hBMSCs: human Bone Marrow-derived Mesenchymal Stem Cells; BMP-2: Bone Morphogenetic Protein 2; GDF-5: Growth Differentiation Factor 5; GFs: growth factors; iPSCs: induced pluripotent stem cells; TGF-β: Transforming growth factor-beta; VEGF: Vascular Endothelial Growth Factor. From Santos-Beato et al. [2]

1.2.1 Cells

Various cell types, including chondrocytes, osteoblasts, osteoclasts and osteocytes, form the osteochondral tissue. The cartilage section presents chondrocytes, which differ in shape and distribution across the depth of the tissue (Figure 1.1). These cells must be distributed in a specific way to mimic the hyaline cartilage section of the osteochondral tissue and change shape and phenotypic expression. As previously explained, chondrocytes change from an elongated shape parallel to the cartilage surface in the superficial zone to a characteristic round shape in the middle and radial zones. Additionally, closer to the osteochondral interface, chondrocytes become hypertrophic, increasing in size and having a 10 to 20-fold enlargement [18]. These cells are considered transient chondrocytes, where they can either enter a terminal state in the growth plate by becoming apoptotic [19] or directly become osteoblasts [20–

[24]. These hypertrophic chondrocytes differ from chondrocytes in expressing proteins such as collagen type-X and vascular endothelial GF alpha (VEGFα) [25].

The bone section presents three different cell types: osteoblasts, osteoclasts and osteocytes. Osteoblasts are bone cells which synthesize and secrete the bone matrix, promoting bone formation, remodelling and healing [26]. Once these osteoblasts have laid down bone-matrix (osteoid) they transform into osteocytes [27]. These osteocytes are responsible for the bony matrix maintenance, controlling osteoblast and osteoclast activity [28]. Osteoclasts are the bone cells that degrade bone, initiating normal bone remodelling processes and regulating procedures such as the differentiation of osteoblast precursors, immune responses and cytokine secretion [29].

All these bone and cartilage cells form a complex system into which cartilage tissue must be maintained, and the bone formation, maintenance and remodelling must be in equilibrium. Diseases such as osteoarthritis (OA) can develop if this specific metabolic network is disturbed. Therefore, to create a representative osteochondral tissue model that can subsequently be used to model diseases, all these cells must be present and form their metabolic pathways to find tissue equilibrium. However, these cells, especially primary cells, present limitations when expanded and used in *in vitro* models. They present finite lifespans, limited expansion capacities, and potential phenotypic changes when expanded in two dimensions (2D) [2]. Alternatives to these primary cells could be cell lines [30,31] or the use of stem cells (SCs), which could be differentiated post-expansion into bone or cartilage lineages using GFs or additional mechanical cues. Regardless of the strategy, these cell types should be present to develop a representative tissue, and the interplay between them must be mimicked as closely as possible.

1.2.2 Physico-chemical parameters

The osteochondral unit presents a gradual change in mechanical properties, such as compressive moduli, which increase from the cartilage surface towards the subchondral bone region. Cartilage presents a compressive modulus which varies

from 0.24 to 1 MPa [32]. Changes in the extracellular matrix composition and architecture determine the changes in this mechanical characteristic. Human cortical bone presents a Young's modulus, varying from 1 MPa to 18.6 GPa [33,34]. These changes depend on bone location, which determines the mechanical stresses to which bone is subjected.

Achieving the osteochondral tissue mechanical properties seen *in vivo* has proven to be a challenging task when recreating this tissue *in vitro* [2]. Most materials used have compressive moduli multiple orders of magnitude lower than what *in vivo* measurements have shown [35–37]. However, when neo-cartilage and initial bone healing tissues develop, the mechanical properties observed highly differ from the final characteristics as well. For example, human talar cartilage anlagen was found to increase in stiffness by a factor of 2.5 over 16 weeks of gestation [38]. Furthermore, neo-cartilage constructs *in vitro* showed an increase in tensile Young's moduli of 4.4 times over 84 days of culture [39]. Bone callus mechanical properties were also assessed in New Zealand white rabbits, showing Young's moduli ranging between 0.1 to 1000 MPa, being linearly correlated to the bone mineral density [40]. This suggests, that for cells to regenerate these particular tissues, softer than *in vivo* environments might be beneficial to trigger the regeneration response. Moreover, softer environments in combination with external cues such as compression or shear have shown to mimic the conditions required for tissue regeneration closely, achieving neo-cartilage formation [41] or bone mineralisation [42].

When developing an osteochondral tissue model *in vitro,* adequate extracellular matrix deposition must be achieved to mimic the tissue characteristics. Extracellular matrix deposition is highly dependent on the application of mechanical cues such as compressive and shear stress [42–44]. These cues not only guide extracellular matrix deposition but also facilitate cell differentiation. In human embryonic development, the movement of joints ensures the formation of the osteochondral interface and the transition of chondrocytes into hypertrophic chondrocytes close to the subchondral region [45,46]. *In vitro* culture of chondrocytes in three-dimensional (3D) configurations has demonstrated a closer to *in vivo* behaviour when subjected to dynamic loading [47]. Forces ranging from 10% strain [47] to 1-5% strain [44,48] have been tested at a similar

frequency of 1 Hz across investigations. These have shown that proteoglycan and collagen content was highly increased compared to static conditions. Regarding bone maturation, hydrodynamic shear has also been shown to induce rapid bone maturation [42]. However, studies here lack standardisation and optimisation *in vitro* as the shear stresses range from millipascals [49,50] to pascals [51,52].

Although mechanical cues have improved and accelerated bone and cartilage tissue maturation *in vitro,* static conditions may also be suitable environments to develop these tissues. As further discussed below, adding chemical cues such as GFs is essential for *in vivo* and *in vitro* osteochondral tissue development.

1.2.3 Growth factors (GFs)

GFs are biologically active secreted molecules that can affect the growth of cells, promote or inhibit mitosis and affect cellular differentiation [53]. These GFs can carry out osteogenesis and chondrogenesis, promoting the formation of the osteochondral tissue. GFs such as insulin-like GF-1 (IGF-1), transforming GF β-1 (TGFβ-1), TGFβ-2 and TGFβ-3 are some GFs which induce chondrocyte proliferation and collagen formation and deposition [54]. Other GFs, such as bone morphogenetic protein-2 (BMP-2), are essential when differentiating mesenchymal SCs (MSCs) into osteoblastic lineages and promote osteoblast proliferation [55]. This is key when developing bone tissues, which also require vascularisation. Other GFs, such as VEGF, platelet-derived GF (PDGF), and fibroblast GF (FGF), can be used to promote angiogenesis [56–59].

When developing osteochondral tissues *in vitro*, GFs such as TGF-β and BMP-2 have been used to differentiate SCs. Cartilage *in vitro* cultures of primary chondrocytes [60–62] or human MSCs [63–65] have used a standardised dose of 10 ng/mL of TGF-β to promote chondrocyte differentiation and cartilage formation. However, the use of BMP-2 enormously varies when used to differentiate human SCs into their osteogenic lineage, going from 0.5 ng/mL [63] to 50 ng/mL [66]. Although complete standardisation of dose and exposure time to these GFs is still to be performed for developing osteochondral tissues *in vitro*, their use has been proven key when developing them.

1.3 Traditional fabrication methods

Osteochondral tissue development *in vitro* has been attempted using multiple conventional tissue engineering approaches such as self-assembly, gas foaming, phase separation, freeze-drying or electrospinning. These techniques and their applications in osteochondral tissue engineering are discussed below.

1.3.1 Self-assembly or scaffold-free approaches

The self-assembly technique has recently been used for drug screening and understanding organ development or tissue regeneration [67]. It is a tissue engineering technique which relies on the cell's ability to produce a natural extracellular matrix without the influence of external energy [68]. Within this approach, there are different ways by which high cell density populations have been recreated for cartilage tissue manufacturing *in vitro*. These include using non-adherent materials, such as agarose substrates, encouraging cell-cell interactions and facilitating chondrogenic phenotype expression [69]. Alternatively, scaffold-free approaches such as pellet culture, aggregate culture or cell-sheet engineering have also been used [70]. Pellet culture relies on the centrifugation of cells into a pellet where, when cultured in a tissue-specific medium, extracellular matrix deposition is achieved. Cartilage [71,72] and bone [73] tissues have been developed using this approach.

Scaffold-free techniques promote native tissue integration, facilitate matrix deposition and do not have harmful by-products which could arise from a scaffold-based approach. However, they present disadvantages, such as failing to meet clinical translation criteria [70], requiring high cell-seeding densities, and needing more specific construct architecture control. Therefore, this approach presents substantial limitations when recreating osteochondral tissue models *in vitro*.

1.3.2 Gas foaming

Gas foaming is mixing polymers with a gas phase to form a foam [74]. The result is a polymer matrix with interconnected pores into which cells can be seeded using this porous structure as a scaffold. It is a simple and inexpensive method which can be used in scaffolds whose shape and density can be controlled [75].

Articular cartilage tissue models *in vitro* for subsequent implantation *in vivo* have been developed using this method [76]. Chen *et al.* designed a 3D hyaluronic acid poly(L-lactide-co-ε-caprolactone)/silk fibroin gas foamed scaffold for cartilage regeneration. These scaffolds presented large pore areas and high mechanical stability, which sustained chondrocytes and enabled their proliferation [76]. Bone tissue models have also been developed using this technique [77]. Giannitelli *et al.* developed a polyurethane-based gas-foamed scaffold where MSCs attached and proliferated [77] - the porosity of the scaffolds allowed for osteogenesis.

Although this technique has been used to develop the two tissues of interest that form the osteochondral unit, it presents disadvantages such as lack of porosity at the dense surface of the scaffold [78] or the lack of control over the pore size, pore interconnectivity and scaffold architecture.

1.3.3 Thermally-induced phase separation

Thermally-induced phase separation is a method by which a polymer membrane can be manufactured by mixing a polymer with a substance that acts as a solvent at high temperatures, casting the solution into a film [79]. It has been used to develop 3D porous polymeric scaffolds to develop cartilage [80], bone [81–84], and osteochondral tissues [85–87]. It is a conventional technique to fabricate highly porous matrices with interconnected pore networks [88]. It is a low-cost, versatile technology which enables the production of different pore sizes and controls the degree of interconnectivity [89]. However, the polymers that can be used with this technique are limited; therefore, there is a primary limitation in the material use.

1.3.4 Freeze-drying

Freeze-drying is a technique for scaffold fabrication which enables the production of a complex scaffold geometry with uniform pore morphology [90]. It relies on converting solutions into solids through four steps: pre-treatment, freezing, primary drying, and secondary drying [91]. It is a technique that has been used to develop bone [92] models *in vitro* as well as cartilage [91] and osteochondral models [93].

This technique enables the production of a wide range of pore-size scaffolds [94], has demonstrated the potential to manufacture multi-layer scaffolds, and can be used with natural and synthetic polymers. However, it requires significant energy and time to manufacture the scaffolds. Additionally, the pore sizes, although homogeneous, tend to be in the smaller range, compromising the penetration and differentiation of specific cell types [95].

1.3.5 Electrospinning

Electrospinning is an electrohydrodynamic technique based on the extrusion of a polymer solution, emulsion or melt through a spinneret under the application of a strong electric field [96]. This results in the fibre production and deposition on a collector [96]. This technique enables the production of complex geometries, the deposition of multiple materials, and the deposition of randomly or aligned fibres [96]. It has previously been used in the production of bone [97] tissue models *in vitro*. Naderi *et al.* developed an electrospun poly(3-hydroxybutyrate) (PHB) and keratin-based scaffold, which was seeded with MG-63 cells [97]. These cells showed a significant increase in their alkaline phosphatase (ALP) activity when the scaffolds included keratin instead of PHB alone. Cartilage has also been manufactured using electrospinning techniques. Garrigues *et al.* developed an electrospun matrix which enhanced the chondrogenesis of adipose-derived SCs (ADSCs) [98].

This technique enables the manufacturing of constructs with multicomponent fibre compositions, manufacturing versatility of the fibre orientation and control over the fibre variables, such as diameter [96]. However, it still needs to be improved, such as the scaling up the manufacturing process. Therefore, there are more investigations

where this technique has been used in combination with others, such as freeze-drying [99] or even 3D printing as well as freeze-drying [100], which enables a better scalability process.

1.4 3D bioprinting of the osteochondral tissue

1.4.1 Introduction to 3D bioprinting

As previously discussed, osteochondral tissue models have been developed using multiple tissue engineering techniques. However, these presented common disadvantages, such as the need for more control over the architectural design, porosity and scalability limitations. 3D bioprinting is a technique that enables layer-by-layer manufacturing of bespoke 3D CAD (Computer Aided Design) designs and is capable of circumventing limitations observed in tissue engineering-based manufacturing techniques. It allows for multi-structural and controlled manufacturing and homogeneous deposition of encapsulated cells within the bioprinted structures. Multiple 3D bioprinting techniques have been used in osteochondral 3D bioprinting: photopolymerisation-based, extrusion-based and jetting-based.

Photopolymerisation-based bioprinting uses photo-curable liquid bio-resins, radiated at their specific curing wavelengths to harden them, Figure 1.3(a). This hardening process happens through the linking of molecules [101]. These specific bioprinters usually have a light source and sets of mirrors suspended above or below a resin bath. The mirrors focus the light beams in the regions of interest to polymerise them and build the 3D structure layer-by-layer. Although this technique has good manufacturing resolution and does not require support materials, it is an expensive technique that only allows for photopolymers to be utilised. These materials can be toxic even after polymerisation, making it a less viable technique to develop cell-laden structures.

Extrusion-based is a fluid dispensing system, which can rely on mechanical or pneumatic forces controlled by an automated robotic system, Figure 1.3(b). This technique deposits filaments of bioink in consecutive planes, building up the 3D

structure. These filaments' thickness varies according to different printing variables such as extrusion pressure, printing speed, nozzle size and material characteristics. This specific bioprinting technique is affordable, widely used and available, and can be used with multiple printing materials, from hydrogels to ceramic-based inks. However, its resolution is limited, having been reported to go as low as 200 μm [102]. It has been the most commonly used 3D bioprinting technique for developing osteochondral tissues [2], as it enables manufacturing cell-laden and acellular materials.

Jetting-based bioprinting performs the manufacturing process by ejection of material droplets that can be mixed with cells or be fully acellular, Figure 1.3(c). This technique has high agility, high throughput and enables for single-cell printing [103]. The resolution of this technique can go as low as 10 μm, enabling the manufacturing of complex structures with highly detailed designs. However, it has drawbacks, such as a limited range of materials that can be used, and materials that can experience high shear that will affect cell viability [103].
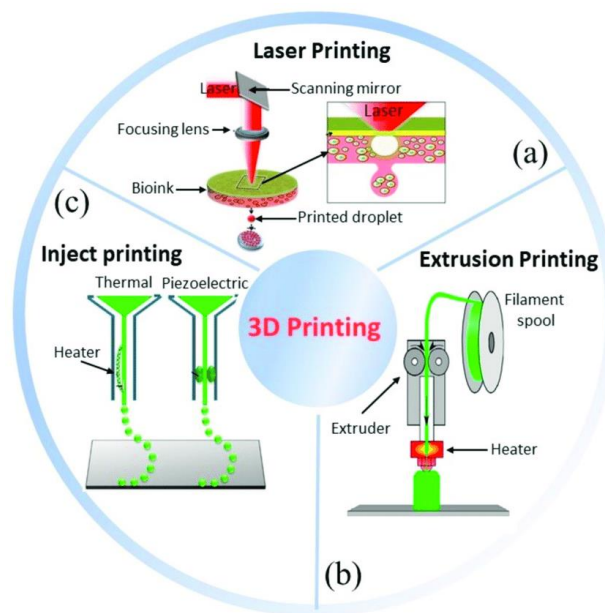
Figure 1.3. Three leading bioprinting technologies: (a) laser or photopolymerisation-based [104]**, (b) extrusion-based** [105]**, and (c) inject or jetting-based printing** [106]**. From Morouço et al.** [107]**. Parts of the figure are reprinted from** [104–106] **open access under Creative Commons CC BY 4.0 license.**

53

Although all these techniques have been used to develop osteochondral tissues *in vitro,* 89% of the published work used extrusion-based bioprinting as the manufacturing technique [2]. Extrusion-bioprinting presents a short manufacturing time [108] and a wide range of materials to be used combined with high cell densities, which enable the manufacturing of constructs which can closely resemble *in vivo* osteochondral tissues [30,35,109]. This technique has been used to develop osteochondral tissues using various materials and cell types, further discussed below.

1.4.2 Materials used in osteochondral tissue 3D bioprinting

The materials used in 3D bioprinting, which are combined with cells, are defined as bioinks. These materials give a physical microenvironment where cells can survive, move and differentiate [110]. The chosen bioinks must have mechanical integrity and be structurally stable to manufacture tissue constructs. Additionally, they should be shear thinning and have rapid solidification and formability [2] to be printed at high resolutions.

Extrusion-based bioprinting of osteochondral tissue models *in vitro* has used various materials [2], Figure 1.4. These materials vary depending on the section of the osteochondral model that is manufactured. Cartilage, bone and calcified sections require different materials as they present various tissue mechanical properties. Cartilage sections are mainly manufactured with alginate (26%) and PCL (poly-ε-caprolactone) (15%) [2]. Alginate presents instant gelation when in contact with calcium ions. It is easy to use and can be mixed with various materials. However, it presents low mechanical properties (3-5 kPa) [36,37] and does not promote cell attachment. Other polymeric components, such as PCL or PLA (poly(lactic) acid), are used to enhance the mechanical properties of these constructs and increase their compressive modulus. PCL has been reported to increase the mechanical properties of alginate constructs by more than 10^3, achieving up to 2-3 MPa compressive moduli [35]. Additionally, most reported investigations mix this material with animal-derived hydrogels, which provide better cell attachment properties, such as gelatine, gelMA (gelatine methacryloyl), hyaluronic acid or collagen. Although these materials provide

the constructs with better properties than those achieved with alginate, they have disadvantages such as batch-to-batch variations, sustainability issues and ethical concerns.

Bone sections also rely on alginate (19%) and PCL (17%) when 3D bioprinted [2]. However, they present additional materials such as HA, tricalcium phosphate (TCP), or a mixture of both, which are also added to these sections to account for the mineral component of bone [2]. The inclusion of these materials also increases the mechanical properties of these sections. They are increasingly used in the calcified cartilage section, which presents similar properties to those observed in subchondral bone. This specific region of the osteochondral models, when specifically manufactured, uses alginate (19%) and methylcellulose (19%) alongside mineral phases (HA, TCP) to gradually transition from the cartilage tissue model to the bone section [2].

Overall, the general tendency observed in manufacturing these osteochondral tissues, in terms of the material choice, is to combine cellular and acellular printing to develop hard-soft hybrid structures [64]. A clear example is the PCL-based scaffold produced by Daly and Kelly [64], which presented a porous bone region and a grid structure in the cartilage section. GelMA (20 wt%) with MSCs embedded into the scaffold was produced using extrusion and jetting-based bioprinting. They differentiated the cells using specific GFs for 28 days of culture. Although the hard-soft hybrid structure approach is commonly used, the cell choice varies in reported investigations, further discussed below.
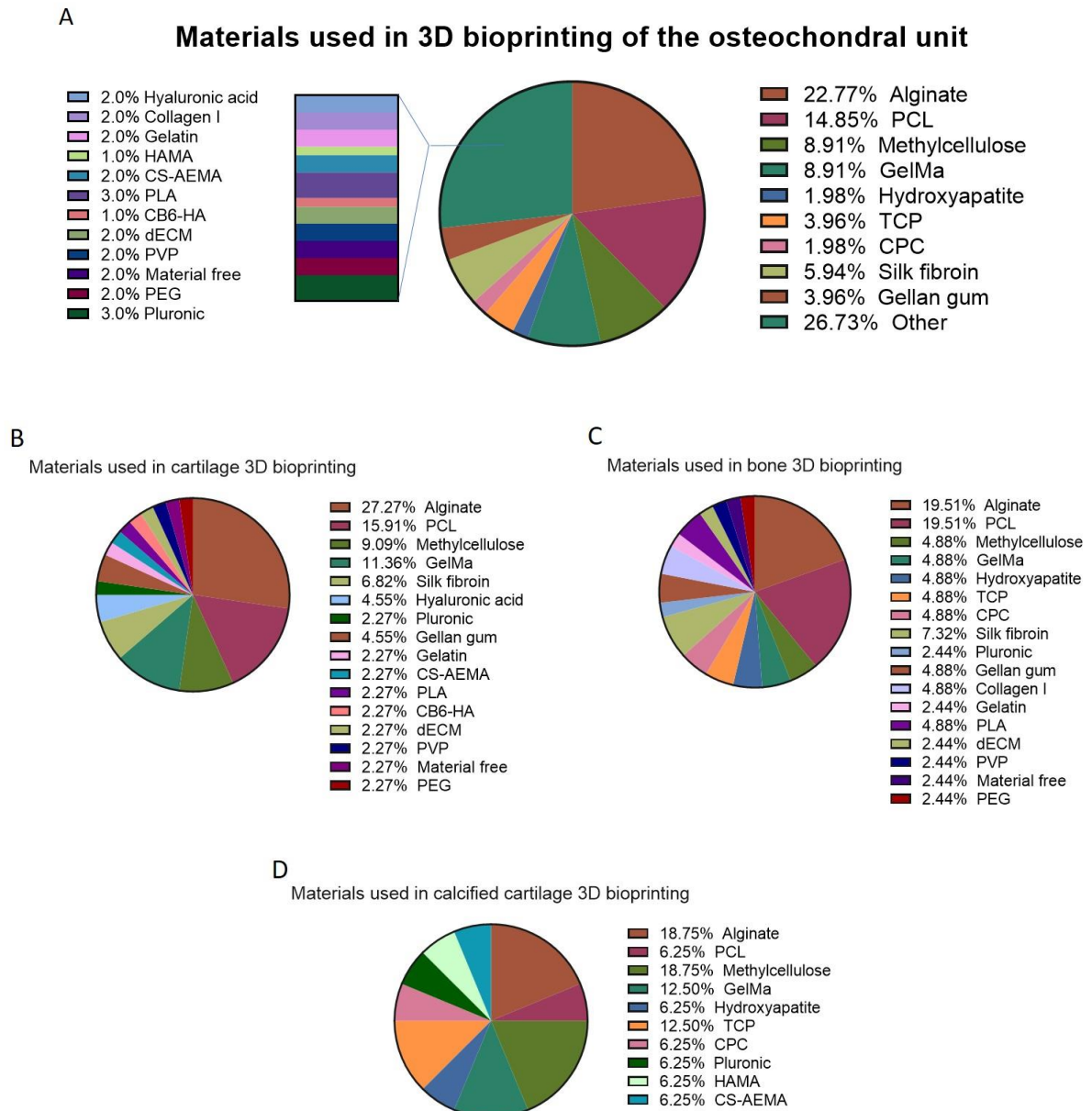
Figure 1.4. A) Pie chart diagram showing some bioinks for osteochondral unit (bone + cartilage) bioprinting. Data is based on 24 papers published between 2012 and 2022. CB6-HA (CB[6] (cucurbit[6]uril + DAH-HA (1,6-diaminohexane (DAH)-conjugated hyaluronic acid (HA)); CPC (calcium phosphate cement); CS-AEMA (chondroitin sulphate amino ethyl methacrylate); dECM (decellularised extracellular matrix); GelMA (gelatine methacryloyl); HAMA (methacrylated hyaluronic acid); PCL (poly-ε-caprolactone); PEGDMA (Poly(ethylene glycol) dimethacrylate; PLA (poly(lactic) acid); PVP (polyvinylpyrrolidone); TCP (tricalcium phosphate). B) Bioinks used in the cartilage section of the osteochondral unit in the reviewed papers. C) Bioinks used in the bone section of the osteochondral unit in the reviewed papers. D) Bioinks used in the calcified cartilage section of the osteochondral unit in the reviewed papers. From Santos-Beato et al. [2]

56

1.4.3 Cell types used in osteochondral tissue 3D bioprinting

Osteochondral tissues present a variety of cell types *in vivo.* Cartilage presents chondrocytes, which turn into hypertrophic chondrocytes in the calcified cartilage section. The subchondral bone presents osteoblasts, osteoclasts and osteocytes. As previously explained, this cell variety should be represented in an *in vitro* osteochondral tissue model. Both primary cells and cell lines have been explored in osteochondral tissue 3D bioprinting to develop representative osteochondral tissue models.

The cartilage section has been primarily manufactured using primary chondrocytes due to their inherent tendency to form cartilage in 3D cultures. However, these cells, which are commonly expanded in 2D culture conditions, tend to dedifferentiate and express both hypertrophic and mineralisation markers [111]. Alternatively, bone marrow-derived MSCs (BMSCs) or induced pluripotent SCs (iPSCs) have been used and differentiated using GFs [63,112,113] either alone or in co-culture with primary chondrocytes [114]. The bone section has been previously manufactured using BMSCs or human osteoblast cell lines such as MG-63 cells [115,116]. The BMSCs were also used as bone progenitor cells, which differentiated into osteoblasts following the addition of GFs [117–119]. Cell lines are chosen to develop osteochondral models where general cell tissue behaviour is sought. Primary cells are selected when performing patient-specific disease modelling.

Human cells are used in over 70% of the osteochondral bioprinted samples [2] as they present tissue mimicry and are more relevant when representing human physiology. Within these human cells, 88% are primary cells, and only 12% are cell lines [2]. Chondrocytes and BMSCs are the preferred cell types, accounting for 29% and 43% of primary cells used, respectively [2]. Following these trends, primary cells are the most promising options for developing osteochondral tissue models. However, there are issues with human primary cells, such as availability, low proliferation rate and patient-dependent variations. Therefore, using cell lines can overcome some of these issues and help develop the initial osteochondral models.

Overall, the cell choice will depend on the subsequent use of the 3D bioprinted osteochondral tissues. 3D bioprinted osteochondral tissues, which are developed for implantation or personalised drug testing, require the use of primary human cells. These will closely resemble the patient's disease profile and will not be rejected by the host when implanted. However, if these 3D bioprinted constructs are used for a generalised disease model or drug testing, cell lines which closely represent primary cell behaviour could also be used.

1.5 Applications of 3D bioprinted osteochondral tissues

1.5.1 3D bioprinted osteochondral tissues for regenerative therapy

The use of 3D bioprinted osteochondral tissues for implantation remains at the laboratory investigation or pre-clinical stages. The main current limitation in regenerative medicine of osteochondral tissue defects is the need to recapitulate the structure and function of the entire osteochondral tissue [2]. 3D bioprinting strategies have used hydrogels and polymers in combination with ceramic phases and autologous/allogenic cells to develop these osteochondral tissues [120,121].

Only a few 3D bioprinted osteochondral tissues have been tested *in vivo*. A biphasic construct was developed using human MSCs and articular chondrocytes alongside a photo-crosslinkable hydrogel to develop a cartilage model by Idaszek *et al.* [122]. This combination and TCP microparticles were used to develop an adjacent calcified cartilage section. These 3D bioprinted constructs were implanted in rodent osteochondral defects, which showed in 12 weeks repaired articular cartilage [122].

More complicated osteochondral designs have been 3D bioprinted, recreating gradient-structure scaffolds that mimic the different articular cartilage zones. Sun *et al.* developed a scaffold with different porosities using PCL and rabbit BMSCs. When these osteochondral tissues were implanted in rabbits, a cartilage structural distribution similar to native cartilage tissue was accomplished [123].

More significant defects have also been attempted to be regenerated using 3D bioprinted osteochondral constructs. However, these investigations show different outcomes. Reinforced MSC-laden alginate gels were 3D bioprinted by Critchley *et al.* to develop biphasic osteochondral constructs [124]. These were implanted in a caprine model for six months and demonstrated hyaline-like cartilage formation. However, significant variations in the neo-tissue formation were observed; therefore, further standardization of these 3D bioprinted constructs is needed. Other studies, such as those performed by Mancini *et al.*, also demonstrated the osteochondral healing potential of a 3D bioprinted biphasic structure. They developed a biphasic structure implanted in an equine model for six months using articular cartilage progenitor cells with human MSCs alongside hyaluronic acid and PCL. This resulted in limited cartilage tissue formation and raised concerns about implant viability and hydrogel resorption *in vivo.* Issues with these more significant defects being regenerated with 3D bioprinted constructs can be due to structural and material issues and fixation/integration of the implants at the injury site [125].

1.5.2 3D bioprinted osteochondral tissues for disease modelling and drug screening

Osteochondral tissue models *in vitro* have been used to recreate osteochondral-related diseases such as OA. Multiple investigations have focused on recreating OA *in vitro* by the addition of inflammatory cytokines, pro-catabolic mediators [126], co-culture settings [127], and external flow-induced stress or mechanical strain [47,128]. However, these models are not manufactured through 3D bioprinting but with conventional tissue engineering techniques.

A recent example of a 3D bioprinted OA disease model was developed to recreate and reverse early OA symptoms by introducing therapeutic agents. Singh *et al.* developed a 3D bioprinted osteochondral-based *in vitro* disease model for early OA [129]. Silk fibroin-based bioinks alone and combined with nano-HA were used to 3D bioprint cartilage and bone sections. Human ADSCs were pre-conditioned into the chondrogenic and osteogenic lineages and bioprinted. Constructs were cultured in a

pro-inflammatory medium for seven days, which presented cytokines IL-1β (interleukin 1β) and TNF-α (tumour necrosis factor-alpha). Initial OA symptoms were observed and partially reversed by adding anti-inflammatory agents (Celecoxib or Rhein) for seven days. However, the recreation of OA through the addition of cytokines will not fully recreate all the symptoms of OA. Therefore, further investigations to recreate the later stages of OA are necessary. The progressive stages of OA and its characteristic symptoms are further discussed below.

1.6 Osteoarthritis (OA) disease modelling as a final application for 3D bioprinted osteochondral tissue models *in vitro*

1.6.1 Introduction to OA

OA is the most prevalent joint disease globally, affecting one in ten adults in the UK [130] and 54.4 million adults in the US [131]. According to the National Institute of Health and Clinical Excellence (NICE) [132], the prevalence of OA increases with ageing, affecting around 50% of the population above the age of 75. With a growing ageing population globally, this progressive disease represents a severe socio-economic challenge [133]. Currently, the available treatments focus on providing symptomatic relief instead of reversing the damage or curing the disease. The approximate cost of the provided OA treatments ranges between $3.4-13.2 billion annually in the US [134] and £10.2 billion in the UK [135].

1.6.1.1 Progressive stages of OA

OA is a disease that affects the totality of the joint [136]. It can be induced through mechanical loading, and genetic and acquired elements contribute to its development [137]. It is a progressive disease which has been divided into three stages: stage I, cartilage matrix in the osteochondral unit presents proteolytic breakdown; stage II, cartilage surface presents fibrillation and erosion, releasing the breakdown products

into the synovial fluid; stage III, synovial cells phagocyte the breakdown products, and there is inflammation observed in the synovium due to the production of inflammatory cytokines and proteases [138]. These different stages are shown in Figure 1.5.
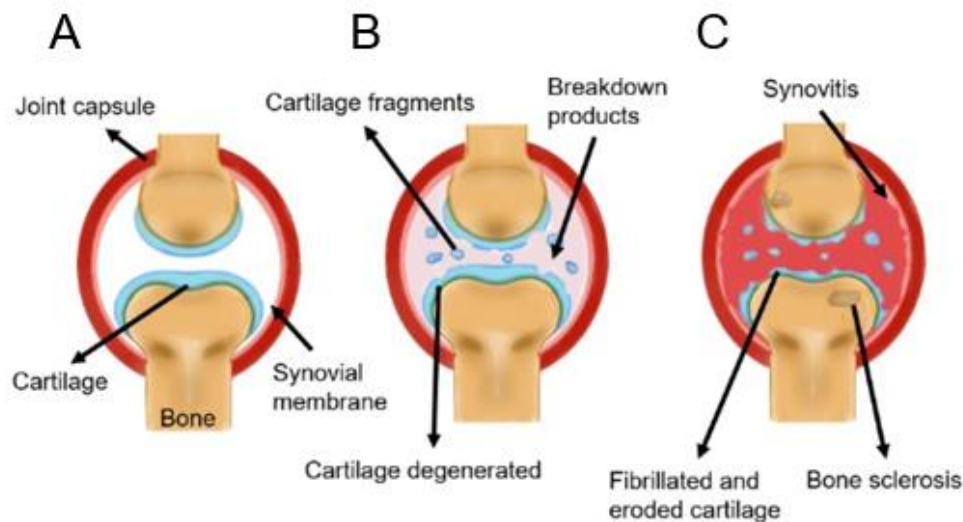
Figure 1.5. Schematic diagram of OA progression. A) Normal healthy joint; B) Early OA, showing cartilage degeneration and appearance of breakdown products in the synovial fluid; C) Late OA, showing cartilage loss, bone sclerosis formation, and synovitis. The amount of breakdown products in the synovial fluid increases dramatically. OA: Osteoarthritis. From Santos-Beato et al. [2]

As OA progresses, multiple joint tissues, such as cartilage, synovium, bone, and bone marrow, as well as menisci, ligaments, muscles, and neural tissues, are involved. All these different tissues maintain joint stability, balance, and proprioception, ensuring organ, tissue and molecular homeostasis [139]. Initial OA at the cellular level is observed through the proliferation and augmented matrix remodelling in cartilage and bone tissues [136]. Cartilage matrix destruction is intensified by producing pro-inflammatory cytokines such as IL-1 and tissue-destructive enzymes like matrix metalloproteinases (MMPs) by articular chondrocytes. As the extracellular cartilage matrix is lost, articular chondrocytes vary their phenotype and become hypertrophic. Matrix calcification starts appearing around these chondrocytes, which leads to a thinning of the cartilage surface and an upward shift of the tidemark [136]. Simultaneously, tissue sclerosis

61

thickens the cortical plate at the bone level, generating a high bone turnover with the formation of osteophytes at the outer joint edges [140].

At the biomechanical level, there is a formation of bone which promotes the thickening of subchondral bone. This increased bone formation is accompanied by slower mineralisation [136], which leads to a thicker new bone but with greater compliance and less resistance than the original thinner subchondral bone [136]. Furthermore, bone attritions are associated with bone cartilage loss [141] and bone marrow lesions occurrence [142]. Overall, these physical changes in bone and cartilage lead to stiffening of the osteoarthritic joints. Additionally, there is increased crosstalk between cartilage and bone at the molecular level as OA progresses. Microchannels appear from the subchondral bone into the calcified and uncalcified cartilage. These channels become more abundant with OA progression, presenting higher endothelial cell proliferation and a high vascular density [143].

1.6.2 Potential use of osteochondral tissue models *in vitro* for OA disease modelling – current limitations and future directions

In the last ten years, immense progress has been achieved in 3D bioprinting cartilage, bone and osteochondral models [2]. However, using the 3D bioprinted osteochondral tissues for disease modelling remains largely unexplored. Although OA is a disease that affects the whole joint, the central tissue of interest when modelling and exploring potential drugs is the osteochondral tissue. Due to numerous challenges and limitations when recreating a functional and lasting osteochondral tissue construct, 3D bioprinted osteochondral tissues have yet to be primarily used for OA disease modelling. Three general challenges stand out when translating these models into the disease modelling space: using materials with mechanical properties closer to physiological values, establishing vascularisation in the bone compartment, and including multiple tissue types to further recreate the osteochondral tissue disease model.

1.6.2.1 Material choice: Combining acellular and cell-laden 3D bioprinting

Bone and cartilage display very different mechanical moduli, as previously discussed. Current bioinks do not mimic these mechanical properties. Therefore, new material combinations must be explored to optimise the mechanical properties [2].

Obtaining the diversity of properties that the osteochondral tissue presents *in vivo* requires softer materials in the cartilage section and more robust materials in the bone compartment that present a gradient between them and ensure the cohesion of both sections. The high mechanical modulus of bone is the most challenging issue, as high viscosity bioinks, which would increase the Young's modulus of the bioprinted construct, would generate high extrusion pressures. If these are combined with cells, high extrusion pressures could lead to high shear stresses in the extrusion process, compromising cell viability [2]. Combining acellular and cellular printing is the most efficient way to achieve constructs with higher compressive moduli. A combination of materials, such as PCL and alginate [115], or the inclusion of nano-HA [144] in bioprintable materials, have been successfully used to enhance the mechanical properties of the 3D bioprinted osteochondral constructs.

1.6.2.2 Tissue maturation: Using external cues to improve tissue development *in vitro* and model OA biomechanically

Introducing compressive stress in cartilage tissue development *in vitro* and shear stress in bone tissue development *in vitro* have been shown to improve and accelerate tissue maturation when compared to static culture conditions [145,146]. Including these mechanical cues could ease the development of healthy osteochondral tissue constructs which could then be introduced into bioreactors to induce OA.

Cartilage-based models have already been used to recreate mechanically induced OA through compressive loading [147] and adding inflammatory cytokines [148]. Using static and cyclic loading, Young *et al.* aimed to produce a cell-based OA model [147]. Porcine chondrocytes encapsulated in a hydrogel were placed in a compression device. A static load of more than 40 psi for 24 hours was found to generate a decreased

63

extracellular matrix anabolism, with higher matrix degradation and increased oxidative stress. Additionally, 60 psi of static loading was concluded to be enough to induce OA into chondrocytes. Although OA can be induced mechanically, it has also been proven to be generated chemically by adding inflammatory cytokines. Houtman *et al.* used healthy osteochondral explants and applied loading or added inflammatory (IL-1β) or hypertrophy (triiodothyronine) precursors [148]. They performed compression for four days and cultured other explants in different inflammatory or hypertrophic precursors for six days. The three treatments showed OA-related changes in the explants, proving that specific symptoms can be recreated *in vitro.* The pro-inflammatory treatment showed the most severe cartilage breakdown, and the mechanical strain triggered extracellular matrix changes, such as abnormal elastic properties.

Overall, including bioreactors to accelerate tissue development and introduce OA-specific symptoms would decrease the time frame of OA modelling investigations and enable the recreation of specific OA symptoms.

1.6.2.3 Long-term tissue viability: Improving vascularisation of the bone compartment and communication between cartilage and bone

OA is a slowly progressive disease. Therefore, osteochondral tissues which can be kept viable for prolonged culture periods are required to model it. This is necessary to study different stages of the disease and assess the long-term effects of OA drugs and treatment strategies. Maintaining the correct culture conditions for cartilage and bone requires a culture set-up that enables the division of culture media. A divided insert was used by Kleuskens *et al.* to demonstrate that human osteochondral explants could be maintained viable and functional for up to 4 weeks [149]. However, this device relies on diffusion as a mechanism to feed the inner sections of these constructs. Therefore, larger tissue models would require an alternative approach, such as adding vascularisation to keep the whole tissue viable.

Different techniques such as 3D micro moulding [150], perfusion of 3D bioprinted channels [151] or adding vascular cells such as HUVECs (human umbilical vein

endothelial cells) to produce capillary-like structures have been used to vascularise bone constructs [144]. Chiesa *et al.* recreated bone *in vitro* with robust vascularisation using endothelial cells and 3D bioprinting [144]. Adding these ensures that the osteochondral tissue stays viable for longer and that there is communication between the bone and the cartilage components. This communication becomes essential when OA stages are recreated, characterised by enhancing communication between these tissues [143].

1.6.2.4 Incorporating additional tissues for OA disease modelling

OA is a disease that affects the whole joint. Although the tissue of primary interest is the osteochondral tissue composite structure, further complexity is required to be added to develop disease models of this disease fully. Components such as the synovial fluid and the synovial membrane add to the complexity of the interplay between the joint tissues. A key aspect is to incorporate immune cells, which have previously been used to recreate OA symptoms. For example, Samavedi *et al.* developed a 3D chondrocyte-macrophage co-culture system which evaluated the interaction between activated murine macrophages and osteoarthritic human chondrocytes. The co-culture system showed closer to *in vivo* observed scenarios than the corresponding monocultures [127]. Another example is the investigation by Stellavatto *et al.,* which developed an OA model based on the co-culture of human chondrocytes and synoviocytes, which showed cellular responses that closely resembled *in vivo* OA symptoms [152].

Overall, the existing investigations show a need to expand further the materials used for 3D bioprinting osteochondral models, achieving cohesion between the bone and cartilage sections and better mechanical properties. Additionally, further exploration regarding introducing vascularisation systems, additional joint tissues, and bioreactors for tissue maturation and disease inducement should be performed to use these 3D bioprinted constructs as disease models of OA.

This thesis investigates new materials as bioinks, to develop 3D bioprinted cartilage tissue models (Chapters 2 and 3). Additionally, further investigations are shown using HA as a bioink to develop bone-like tissue models (Chapter 4). Finally, these two sections are combined, and strategies to ensure cohesion between them and characterising their interactions are investigated (Chapter 5).

Chapter 2: Hybrid computational and experimental approach for screening fully synthetic self-assembling bioinks for 3D bioprinting

2.1 Introduction

Hydrogels are three-dimensional (3D) crosslinked polymer networks, which can absorb and retain large amounts of water [153], approximately 90% [154]. They are a common biomaterial choice when modelling different tissues *in vitro* due to properties such as tuneable elasticity and stiffness, high water content, biocompatibility, and biodegradability [155]. Multiple tissue engineering-based biofabrication techniques have been used to develop tissue scaffolds using naturally derived hydrogels, such as alginate, gelatine, hyaluronic acid, or chitosan (further information found in Chapter 1). Within these, techniques such as foam processing, solvent casting, and freeze-drying have been used (Chapter 1), presenting limited control over the porosity, cell distribution within the material, and architecture of the manufactured construct [155]. More advanced manufacturing techniques, such as 3D bioprinting, have shown the potential to overcome these limitations and, therefore, have been tested to manufacture hydrogel-based structures.

3D bioprinting has been defined generally as a technology that enables the printing of structures using viable cells, biomaterials and biological molecules [156,157]. However, more specific definitions describe it as a technology that enables the fabrication of living constructs, tissues or organs. Starly *et al.* define it as a technology which enables "the digital fabrication of living constructs encapsulating cells, biomolecules, and biological moieties in spatially patterned structures" [158], whilst Goel *et al.* describe it as "an upcoming technique to fabricate tissues and organs through periodic arrangement of various biological materials, including biochemicals, and biocells, in a precisely controlled manner" [159]. Multiple 3D bioprinting techniques have been used to manufacture tissue models *in vitro.* These include jetting-based,

photopolymerisation-based, and extrusion-based bioprinting. Within these techniques, extrusion-based 3D bioprinting technology enables the broadest range of materials to be used, higher cell density deposition, and rapid print time [160]. However, the cell viability ranges are set to be between 40 and 95% and have a resolution of approximately 100 μm [160]. Despite these minor disadvantages, 3D extrusion-based bioprinting is the most used technique in 3D bioprinting [161].

Multiple studies have focused on 3D bioprinting tissue models *in vitro*, such as cartilage, using extrusion-based technologies [63,112,114,162,163]. Apart from alginate, most of the existing 3D bioprinted models rely on animal-derived materials or bioinks such as gelatine methacryloyl (gelMA) [112], hyaluronic acid [63,112,162,163] or chondroitin sulphate [112,163].

Animal-derived hydrogels present multiple advantages, such as their biomimetic properties like cytocompatibility and similarities with the native viscoelastic environment to resident cells [164]. However, they present several limitations, such as generally low mechanical stiffness, limited long-term stability in culture, and batch-to-batch variation [164]. Additionally, ethical issues and sustainability problems are associated with animal-derived materials, acknowledged increasingly as critical in determining research methodologies. Animal-derived materials, such as gelatine, are obtained from bovine and porcine sources, as well as fish and poultry [165]. Although these materials come from the animal industry as by-products, the issues regarding sustainability and ethical concerns around the animal industry apply, such as animal welfare, greenhouse gas emissions, and land use [166]. Alternative materials are now needed more than ever to make research more sustainable and to move away from animal-based models.

Synthetic hydrogels are 3D swelling networks of covalently or ionically cross-linked hydrophilic homopolymer or copolymer hydrogels [167]. These non-animal-derived materials are a more sustainable and ethical alternative for manufacturing different tissue models *in vitro.* There are multiple synthetic hydrogels, such as synthetic polymer-based or peptide-based hydrogels. Synthetic polymers, such as polyethylene glycol (PEG), poly-ε-caprolactone (PCL) or poly(L-lactic) acid (PLA), are widely used in 3D bioprinting. They can be easily tuned in terms of their mechanical properties and

degradation. However, they present limitations such as high melting points, which would compromise cell viability, and difficulties in encapsulating cells [168]. Synthetic peptide-based hydrogels have tuneable properties that can be engineered to mimic the advantages of naturally derived polymers [164]. Peptide hydrogels are custom peptide sequences that have user-defined properties [169]. These are promising materials to be explored in cell culture and 3D bioprinting due to their potential to exhibit the advantages of naturally derived polymers as well as the potential to control multiple characteristics such as degradability, cell interaction, or internal structure assembly.

Self-assembling peptide hydrogels are a subset of these synthetic peptide-based hydrogels, which use the peptide secondary structure motifs provided by proteins to design how small peptides will self-assemble [169]. Within the commercially available self-assembling peptides, Manchester Biogel Ltd (MBG) (Alderley Edge, Manchester, UK) offers a wide range of peptide hydrogels named Peptigels® which can be used for cell culture and are investigated in this chapter. These Peptigels® self-assemble through two distinct processes. Firstly, the peptides themselves self-assemble to form fibrillary structures [170]. Secondly, these fibrils are entangled and associated into a 3D percolated network when the concentration is above the critical gelation concentration (CGC) [170]. These two processes are shown in Figure 2.1. These self-assembling peptides are β-sheet peptides, which are interesting as they can form very stable hydrogels with tailorable properties [171].
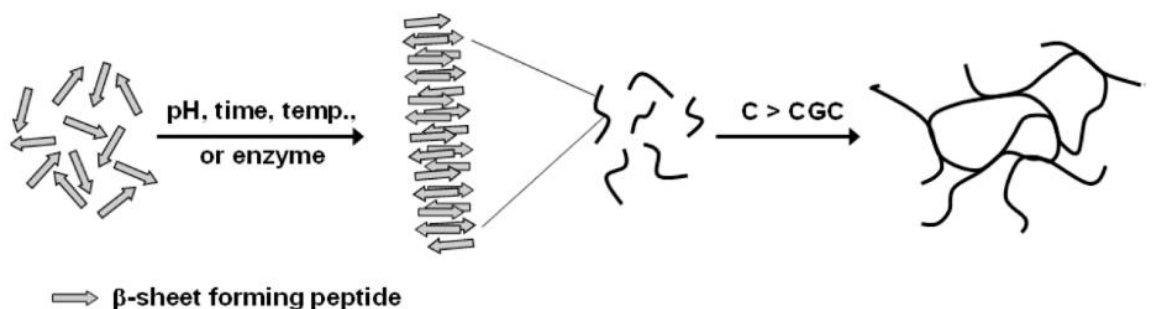
Figure 2.1. Schematic representation of the self-assembling and gelation processes of β-sheet forming peptides. CGC - critical gelation concentration; C – concentration. Figure reproduced from [171].

These Peptigels® present multiple advantages, such as being animal-free, having no batch-to-batch variation, being biocompatible, and being ready to use. They are also printable due to their shear-thinning properties. Based on these characteristics, three Peptigels® were selected to be screened as potential bioinks for 3D bioprinting and manufacturing cartilage tissue models *in vitro*.

2.1.1 Synthetic self-assembling peptide candidates for 3D bioprinting

Synthetic polymers have previously been used in 3D bioprinting [172]. Some examples include PEG [35,173,174], PEG methacrylated (PEGMA) [175–177], or PCL [178–180]. However, these synthetic polymers are usually mixed with natural materials to overcome limitations such as lack of cell attachment and difficulty embedding cells before 3D bioprinting.

Synthetic self-assembling peptide hydrogels present the advantages of synthetic polymers, such as tuneable properties and low batch-to-batch variations. These self-assembling peptide hydrogels assemble themselves in β-sheet protein configurations and stay stable without further crosslinking or additional manufacturing steps [181,182]. Peptigels® Alpha 1, Alpha 2, and Alpha 4 were selected as candidates to assess their potential as bioinks and subsequent use in cartilage *in vitro* 3D bioprinting. Their properties, such as charge and compressive modulus, as well as the various cells that have been cultured embedded in these Peptigels®, are shown in Table 2.1.

Table 2.1. Properties of the Peptigels® used, including charge, compressive modulus and the cell types cultured embedded in the selected Peptigels®.

Peptigel®	Charge	Compressive modulus [183]	Cells used in culture
Alpha 1	Neutral	3 – 5 kPa	Chondrocytes, nucleus pulposus [184–186]
Alpha 2	Positive	6 – 8 kPa	Neuronal cells [187]
Alpha 4	Positive	0.35 – 0.7 kPa	Stem cells [183,188,189]

As shown in Table 2.1, the selected Peptigels® have been used with various cell types, demonstrating their potential for cell culture and tissue manufacturing applications. Within these, the culture of chondrocytes and nucleus pulposus cells was extensively studied using Alpha 1 [184–186], primarily as a potential injectable cell delivery system for intervertebral disc injuries. Additionally, neuronal cell-based studies have been performed using Alpha 1 and Alpha 2 [187], whilst Alpha 4 has been used with a variety of cells such as induced pluripotent stem cell (iPSC)-derived cardiomyocytes [189] , and kidney organoids derived from human iPSCs [188].

Within these studies, Raphael *et al.* focused on the use of Alpha 1 as a bioink for 3D bioprinting epithelial cells [190]. This preliminary study demonstrated high cell viability post-bioprinting of Alpha 1, independent of its compressive modulus. Although this study showed the possibility of 3D bioprinting Alpha 1, no data presented 3D bioprinting optimisation or further material characterisation, as well as the investigation of other Peptigels® as bioinks.

2.1.2 3D bioprinting process steps and challenges

Extrusion-based 3D bioprinting is one of the techniques used in 3D bioprinting (Chapter 1). In short, it is a layer-by-layer manufacturing method which is characterised by the extrusion of bioinks using a force through a printing nozzle. The materials are usually used as bioinks as shear-thinning (they reduce their viscosity as a force is applied).

The extrusion-based 3D bioprinting process is characterised by three steps: flow initiation, filament deposition, and post-printing recovery [191]. The flow initiation starts

the bioprinting process, where the material starts to flow. The force required to initiate material flow is the yield stress. This yield stress will determine the required force or pressure to start the 3D bioprinting process. Below this yield stress, these materials behave like solids and, above it, flow [192]. Higher yield stresses require higher extrusion forces, which could negatively impact cell viability in cell-laden bioinks [193]. Therefore, bioinks with lower yield stress are preferred.

The bioink flow and filament deposition are characterised by the viscosity of the bioink. Shear-thinning materials are usually used in extrusion-based 3D bioprinting. As their viscosity changes with force application, the flow and material deposition depend on this force. However, other parameters, such as gelation temperature, can influence the viscosity behaviour [194]. Pressure and printing speed parameters must be optimised to ensure that the material deposition is the required one. Further information regarding the optimisation of these parameters experimentally is shown in Section 2.1.4.2.

Finally, the bioink flow stops when the shear stress falls below the yield stress [195]. The post-printing recovery material behaviour will determine the recovery of the printed shape and filaments. The ability to restore the original structure is known as self-healing, and the time taken to reach the equilibrium state is the self-healing time [196–198]. Materials with a slow self-healing or post-printing recovery will tend to expand and lose their initial configuration. In order to maintain the initial shape and ensure a good resolution, a fast shape post-printing recovery is needed.

2.1.3 Optimisation of the 3D bioprinting process

Experimental bioprinting optimisation must be performed to assess multiple parameters' effect on the filament quality. Multiple investigations focus on assessing parameters such as the printing pressure, printing speed, syringe and collector bed temperatures, nozzle size and geometry, printing distance and layer height or z-step [191,194,199]. These parameters are assessed to see changes in material fibre formation from the nozzle [191], assess shape fidelity using zigzag patterns [199], and layer stacking to assess 3D shape fidelity [191,194]. Additionally, *in silico* investigations on 3D

bioprinting have attempted to further optimise this extrusion process calculating the shear stresses and forces that arise within the printing nozzle.

2.1.3.1 In silico modelling of the 3D bioprinting process

Based on the rheological characterisation of the bioinks, *in silico* modelling of the bioprinting process can be performed by fitting the viscometry results to a Power Law model. Multiple investigations have focused on this mathematical model to mimic the behaviour of shear-thinning materials [191,200]. The modelling of the extrusion process can help visualise and predict the magnitude of the shear stresses experienced by the cells in the bioink during the 3D bioprinting process. This is performed especially before the actual physical printing such that the bioink formulation and printing conditions could be optimised without wasting bioink, with the potential benefit of a shorter timeframe.

CFD (Computational Fluid Dynamics) has been used in multiple industries to optimise diverse industrial processes and could be used to perform an *in silico* modelling of the 3D bioprinting process. It is a valuable and efficient tool that enables quick testing and modification of dimensions or design features of pieces of equipment. The experimental optimisation process of 3D bioprinting different bioinks is time-consuming and costly due to the high quantities of material used. It is also a process that cannot estimate the shear stresses generated in the extrusion process. Therefore, the potential damage generated to cells during this extrusion process cannot be predicted. There is a clear need to find a different method characterising bioink printability and quantifying shear stresses generated in the extrusion process. This would allow us to assess both bioink suitability and potential cell damage.

Previous research has attempted to characterise biomaterials and their printability according to the obtained rheological values and consistency [199] or their mechanical characteristics [201]. A more promising method was developed by Paxton *et al.* by which, in a two-step method, bioinks printability was assessed. They first screened the bioink formulation to investigate fibre formation, and then a rheological evaluation would show the yield point, shear-thinning and recovery behaviour. A mathematical model was developed. It provided a theoretical understanding of the pressure-driven,

shear-thinning extrusion through bioprinter needles of the bioinks with cells modelled as microparticles [191]. This was the first method to assess the forces that could be generated on the cells and the bioink printability. However, the model relied on assumptions such as friction-free laminar flow and non-slip boundary conditions. These contributed to the overestimation of the extrusion velocity and shear. More accurate bioprinting process predictions could be obtained by further improving these theoretical models. This would save time and printing material use, and obtain a relative measure of cell viability based on resulting shear stress.

2.2 Objectives and Hypotheses

This chapter aims to characterise the rheological, pH, and diffusion properties of three Peptigels® to optimise their 3D bioprinting process experimentally and computationally (*in silico*).

Objectives:

1. Perform physico-chemical characterisation of Peptigel® candidates provided by MBG.
2. Select Peptigels® based on rheological characteristics, pH and diffusion properties.
3. Optimise the 3D bioprinting process for the selected Peptigels®.
4. Use *in silico* CFD modelling to understand the shear stresses and pressure in the bioprinting process.

Hypotheses:

1. Parameters such as viscosity, diffusion, and pH can enable the screening of Alpha 1, Alpha 2, and Alpha 4 as potential bioinks.
2. Optimisation of the 3D bioprinting of the Alpha 1, Alpha 2, and Alpha 4, can be achieved through the assessment of extrusion pressure and printing speed effects on filament deposition width.
3. *In silico* modelling can be used to understand the shear forces arising from the 3D bioprinting process.

2.3 Methods

2.3.1 Material characterisation

2.3.1.1 Rheological measurements

Peptigels® Alpha 1, Alpha 2, and Alpha 4 were obtained from MBG (Alderley Edge, UK). Rheological tests were performed using a Kinexus pro+ rheometer (Netzsh, Germany) with parallel sandblast plate geometry (40 mm, 0.5 mm gap size), equilibrated to room temperature (25°C) and a solvent trap to prevent the Peptigel® from drying. Peptigels® alone and mixed with cell culture medium in a 1:10 (1 mL of Peptigel® and 100 µL of medium) or a 1:5 (1 mL of Peptigel® and 200 µL of medium) ratio were tested in triplicate to ensure reproducibility. These ratios were suggested by the manufacturer (MBG) based on previous investigations of cell culture using these Peptigels® [184–189]. For all mixtures, rotational shear-viscosity measurements were performed in triplicate. Flow sweeps at 1% strain with a shear rate ranging from 150 s^{-1} to 1 s^{-1} were performed to assess the viscosity behaviour under shear stress (up to the maximum allowed by the rheometer). Rheological measurements with and without medium were undertaken to assess the effect of different medium-to-gel ratios on their viscosity and material properties.

2.3.1.2 pH measurements

Peptigels® pH was measured across 72 hours in PBS (Phosphate-buffered saline). 500 µL of Peptigel® were pipetted in 6 well plates and submerged in 7 mL of PBS. Samples were kept at 37°C and 5% CO_2 to simulate cell culture conditions. pH measurements were taken using the HANNA Edge pH probe. This pH meter was placed submerged in the PBS at time points: 30 minutes, 1 hour, 2 hours, 3 hours, 4 hours, 6 hours, 24 hours, 48 hours, and 72 hours. The pH measurements were compared to PBS alone. The pH measurements of Alpha 1 differed from the rest in that the whole PBS volume was changed three times within the first hour, following the manufacturer's advice. This was due to the acidic nature of the Peptigel®, which was

75

expected to be neutralised further with PBS change. All other Peptigels® did not have any PBS changes across the 72 hours of measurements.

2.3.1.3 Diffusion of the medium throughout the Peptigel®

Peptigel® diffusion properties were assessed throughout 24 hours. 1.5 mL of the Peptigels® were pipetted into 5 mL glass vials. 1 mL of cell culture medium with phenol red was added on top of the hydrogel. These vials were kept at room temperature inside a cell culture cabinet where images were taken at intervals: 0 minutes, 30 minutes, 1 hour, 2 hours, 3 hours, 6 hours, 20 hours, and 24 hours. The diffusion of the medium was assessed visually through the Peptigel® changing colour as the phenol red diffused through.

2.3.2 Initial experimental bioprinting optimisation and filament width quantification

Paxton *et al.* propose a 3D bioprinting screening and optimisation method for new bioinks using multiple assessment points. They recommend determining a printing pressure window where filament continuity is assessed. The lower limit of the printing window would be determined by those pressures requiring printing speeds that were not reasonable [191]. The upper limit is determined by pressures requiring printing speeds that are too high to ensure shape fidelity [191]. These guidelines are followed here.

Initial 3D bioprinting optimisation of the Peptigels® was performed visually using a 25 gauge (25G) nozzle. Nozzles were chosen over needles due to the reduced shear stress the material experiences when extruded in the printing. A 25G nozzle was chosen over a 22G nozzle due to the expected higher resolution, as the outlet of 25G is smaller than 22G. A printing speed of 10 mm/s was chosen as the constant variable to assess the printing pressure window. Three printing pressures (8, 10, and 12 kPa) were chosen to print a zigzag pattern, as reported in other 3D bioprinting optimisation

assessments [202,203]. A printing pressure window, or range, was chosen through visual assessment. Printing pressures that generated discontinuous filament deposition or excessive material deposition that led to adjacent filaments merging were excluded.

Once the printing pressure window was determined, further optimisation was performed by changing the printing speed. Four different printing speeds (4, 6, 8, and 10 mm/s) were used to print the same zigzag pattern with the previously selected printing pressures using a 25G nozzle. Three structures were printed for each printing speed-pressure combination. These structures were further analysed to quantify the filament resolution corresponding to each printing speed. The printed structures were photographed using a bright field microscope, and the filament width was measured using Fiji ImageJ (1.53t software version). Filament width was measured in triplicate at six different locations within the filament. The average width and corresponding standard deviation were plotted and compared to the theoretical width (printing nozzle diameter).

2.3.3 Printing optimisation *in silico*

2.3.3.1 CFD extrusion modelling

The CFD modelling was performed using the streamlined computational modelling suite ANSYS Workbench (ANSYS, Inc. Cannonsburg PA, USA). More specifically, the geometrical design process was carried out in DesignModeler, whose output was fed to ANSYS Meshing for computational mesh generation, and the simulation was performed using Fluent. The steps followed were designing the scenario, dividing it into rectangular cells (meshing), solving the simulation, and visualising the results.

2.3.3.1.1 Geometrical Design

One type of geometry was considered to model the extrusion process of Alpha 1 and Alpha 4 mixed with culture medium in a medium-to-gel ratio of 1:10 and 1:5,

respectively. The 25G nozzle was chosen as it presented a compromise between the expected shear stresses appearing in the printing process and the theoretical filament resolution. As it is known, needles generate higher cell damage when used in 3D bioprinting [200], and the smaller the nozzle/needle outlet, the higher the shear stresses that arise, the higher the potential cell damage. Therefore, the 25G conical nozzle was chosen among the other potential candidates, shown in Figure 2.2. The dimensions [204,205] of the nozzle design are summarised in Table 2.2.

Figure 2.2. Different potential nozzles and needles from CELLINK that could be used for 3D bioprinting.

The geometrical model was made axisymmetric around the horizontal axis in Figure 2.3, as the extrusion flow was expected to be laminar and, therefore, axisymmetric in such an axisymmetric geometry. It was divided into two sections, a nozzle section and an adjacent air section, into which the gel would be extruded. The air section was further divided into two areas: one where the extruded filament was expected to develop, and a surrounding area that would enable any filament distortion to be generated if needed. Figure 2.3 shows the different parts into which the nozzle design was divided represented in a reduced model of a 25G nozzle. The schematic of the nozzle design is shown in Figure 2.4.
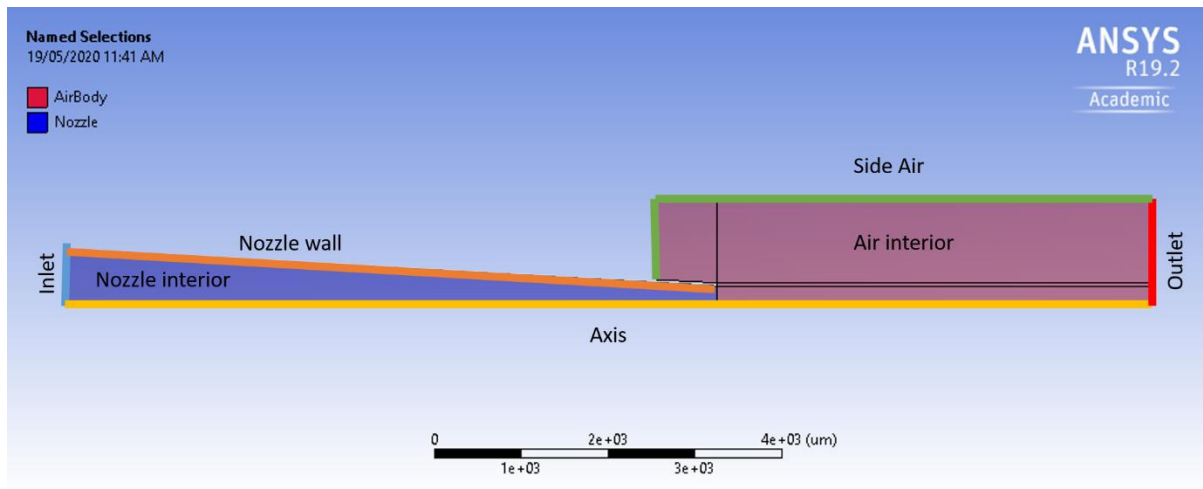
Figure 2.3. Reduced 25G nozzle design with named areas.

Table 2.2. Original dimensions for nozzle 2D axisymmetric model.

Design		Inlet radius	Nozzle/ Needle Length	Air body length	Air body width	N value
Nozzle	25 G	1.97 mm	32 mm	50 mm	10 mm	0.125 mm
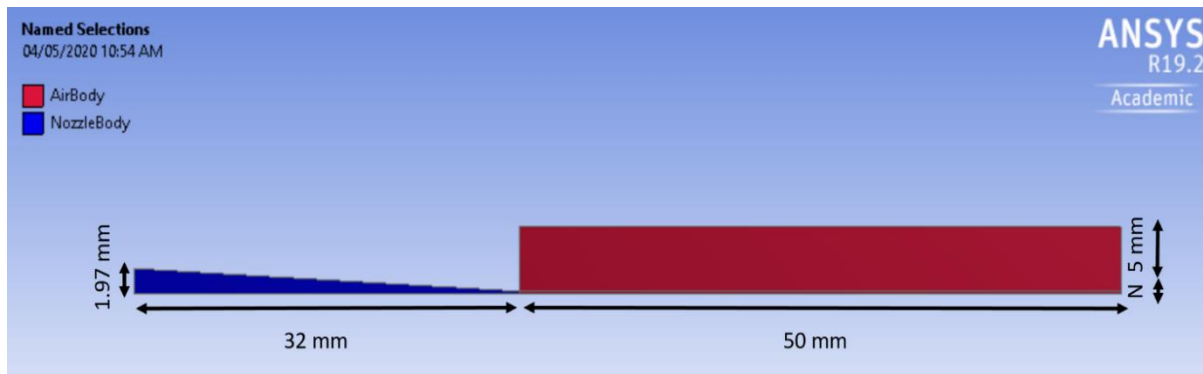
Figure 2.4 Dimensions of the 25G conical nozzle design.

2.3.3.1.2 Mesh design and convergence

The completed design was divided into a set of rectangular cells through meshing. The meshing of the final design was performed by meshing the nozzle and air surfaces using quadrangular bodies, shown in Figure 2.5. This mesh shape was chosen as it is more cost-effective and provides better accuracy of results for the same number of nodes as other common shapes [206]. The resulting mesh was altered by specifying the edge number of divisions, generating a larger number of mesh components closer to the tip of the nozzle and at the interface between the bodies. Here is where the more prominent pressure, velocity, and strain rate changes were expected to happen.
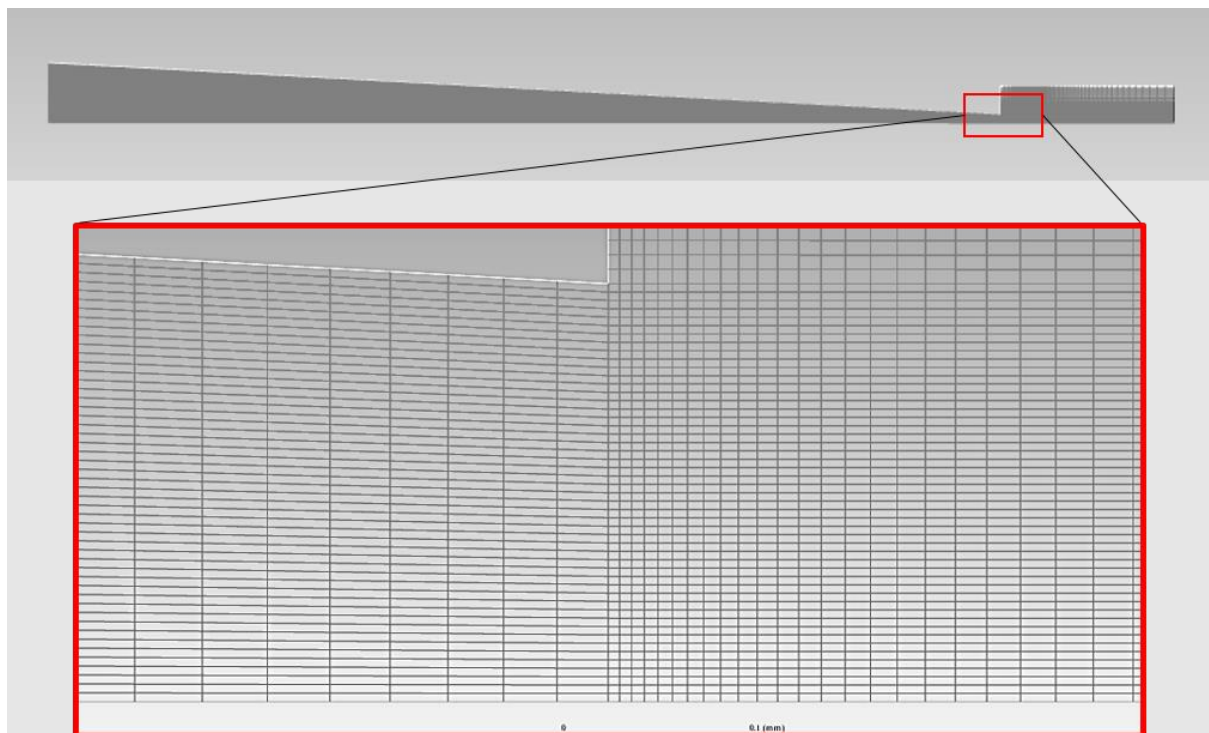
Figure 2.5. Top: Meshed entire 25G nozzle design. Bottom: Zoomed-in contact region between nozzle outlet and air body showing rectangular cells.

Multiple mesh designs and mesh element numbers were tried to ensure the simulation results obtained were independent of the number of these divisions. When this is achieved, the model mesh is defined as converged. The observed value to assess convergence was the maximum strain rate. These values were extrapolated from the Fluent solver into the CFD Post ANSYS results viewer. When the obtained values differed less than 5% between meshes of different resolutions, the mesh with the least number of elements was considered to converge. The convergence graph can be found in Appendix A2.1.

2.3.3.1.3 Solution conditions

a) Modelling specifications

Fluent was used to develop the simulation of the filament extrusion. The solver selected 2D axisymmetric conditions, and the gravitational force (g = 9.81 m/s^2) was included in the simulation and applied in the horizontal axis direction.

Axisymmetric condition

The solver was set to axisymmetric, as the flow was expected to be laminar and symmetric about the horizontal axis. Therefore, the lower limit on the air body and the nozzle was defined as the "axis". Using this boundary condition reduces the extent of the computational model, reducing computational data and time. ANSYS Fluent assumes zero normal velocity and zero normal gradients of all variables at the symmetry plane [207].

Multiphase model – continuity and momentum equations

A volume of fluid (VOF) multiphase model was selected to model two immiscible fluids, the Peptigel® of interest and the air it is being extruded into.

ANSYS Fluent uses this model to solve a single set of momentum equations and tracks the volume fraction of the fluids. Briefly, this method allows capturing the presence of the two fluids in any local region using the volume fraction of each fluid (ϕ_L and ϕ_A for liquid and air, respectively) that ranges from 0 to 1. When any local region is filled with the liquid (bioink), $\phi_L = 1$ and $\phi_A = 0$, and if filled with the air, $\phi_L = 0$ and $\phi_A = 1$. Further information on how this VOF model works can be found in the ANSYS Fluent Theory Guide [208].

Pressure-velocity coupling

Due to the multiphase flow nature of the simulation, the SIMPLE pressure-velocity coupling algorithm was selected to derive an additional pressure condition that reformats the continuity equation. The SIMPLE algorithm is the default algorithm in Fluent, and it is generally used for simple problems such as laminar flows [209] like the extrusion process modelled. This algorithm enforces mass conservation to obtain a pressure field using a relationship between velocity and pressure corrections [210]. Further information on the underlying equations can be found in section 18.4.3 of the ANSYS Fluent Theory Guide.

Viscosity behaviour of materials

The materials tested were Alpha 1 and Alpha 4 mixed with cell culture medium that showed the best rheological behaviour and was also recommended by MBG to be used. These were the 1:10 medium-to-gel ratio for Alpha 1 and the 1:5 medial-to-gel ratio for Alpha 4. The obtained rheological viscometry measurements were fitted into the Power Law model for subsequent CFD simulation.

In the tested Peptigels®, which are shear-thinning materials, the viscosity was used as a characteristic input. The Power Law model represented the viscosity of these materials. This model describes the material viscosity as a function of the shear rate. It is a model characterised by three parameters: power law index *n,* shear rate $\dot{\gamma}$*,* and

the shear stress σ. The relationship is shown in Equation 1. Table 2.3 shows the parameters obtained for the specific mixtures of the Peptigels® modelled.

Equation 1. Power Law model: shear stress (σ), viscosity (η), shear rate ($\dot{\gamma}$), and power law index *n*.

$$\sigma = \eta\dot{\gamma}^n \ (1)$$

Table 2.3. Power law parameters for the Peptigels® used.

Material	η	n
Alpha 1 with 100 µL of medium (1:5)	9.496	-0.789
Alpha 4 with 200 µL of medium (1:10)	26.18	-0.901

Boundary conditions

The boundary conditions selected included the non-slip condition applied on the nozzle wall. The inlet condition was set to be a pressure input. The pressure values were chosen according to the experimental values found when assessing the material printing window, Section 2.3.2.

The simulations were all set to be pressure-solved. To initialise the model, the nozzle was filled with the gel of interest. This implied that the data does not account for the stresses and pressures generated in filling up the nozzle. A final simulation of flow times ranging from 1 and 0.5 s was computed using different time step lengths according to the extrusion stage to ensure convergence and filament formation. The simulation times differed according to the filament time formation; once the filament was obtained the simulation was stopped.

2.3.3.1.4 CFD-Post result post-processing

The results obtained from ANSYS Fluent were processed using the ANSYS post-processer software for fluid dynamic simulations, CFD-Post. In this platform, the shear stresses during the extrusion process were computed by multiplying the molecular viscosity and strain rate obtained values. Maximum and average values of shear stress (т) in the nozzle were calculated by multiplying the dynamic viscosity (μ) of the material and the strain rate ($\dot{\gamma}$), as shown in Equation 2.

Equation 2. Shear stress (т), dynamic viscosity (μ), and strain rate ($\dot{\gamma}$).

$$\tau = \mu\,\dot{\gamma} \quad (2)$$

2.3.4 Statistical analysis

GraphPad Prism 9 was used for the graphical representation of data and statistical analysis. All graphs show error bars representing the standard deviation.

2.4 Results

2.4.1 Rheological characterisation of Peptigels® and the effect of culture medium

Flow sweeps of Alpha 1, Alpha 2, and Alpha 4 with different ratios of medium (1:10 or 1 mL of Peptigel® with 100 µL of medium; 1:5 or 1 mL of Peptigel® with 200 µL of medium) were performed. The results are shown in Figure 2.6. This specific rheological measurement showed the viscosity changes with respect to strain rate. This information was critical to understanding how the material would flow during bioprinting. This test was done in all samples, confirming that the Peptigels® were shear-thinning, non-Newtonian fluids. Figure 2.6A shows the viscosity difference in Alpha 1 for different medium-to-gel ratios. As expected, the larger the medium volume added, the less viscous the material. This was particularly visible at higher shear strain rates, 10 s^{-1} and above. Unexpectedly, in the lower medium-to-gel ratio, Alpha 1 showed a slight increase in viscosity compared to its pure form. Figure 2.6B shows the viscosity difference for Alpha 2 and the mixture of this material with different medium ratios. As observed, there were minimal differences between the pure Peptigel® form and the different mixtures. Figure 2.6C shows the changes in viscosity for Alpha 4 and the mixture of this bioink with different medium ratios. As expected, the higher the volume of medium added, the lower the viscosity of the Peptigel®, confirming that the highest medium-to-gel ratio mixture would be printed easily.
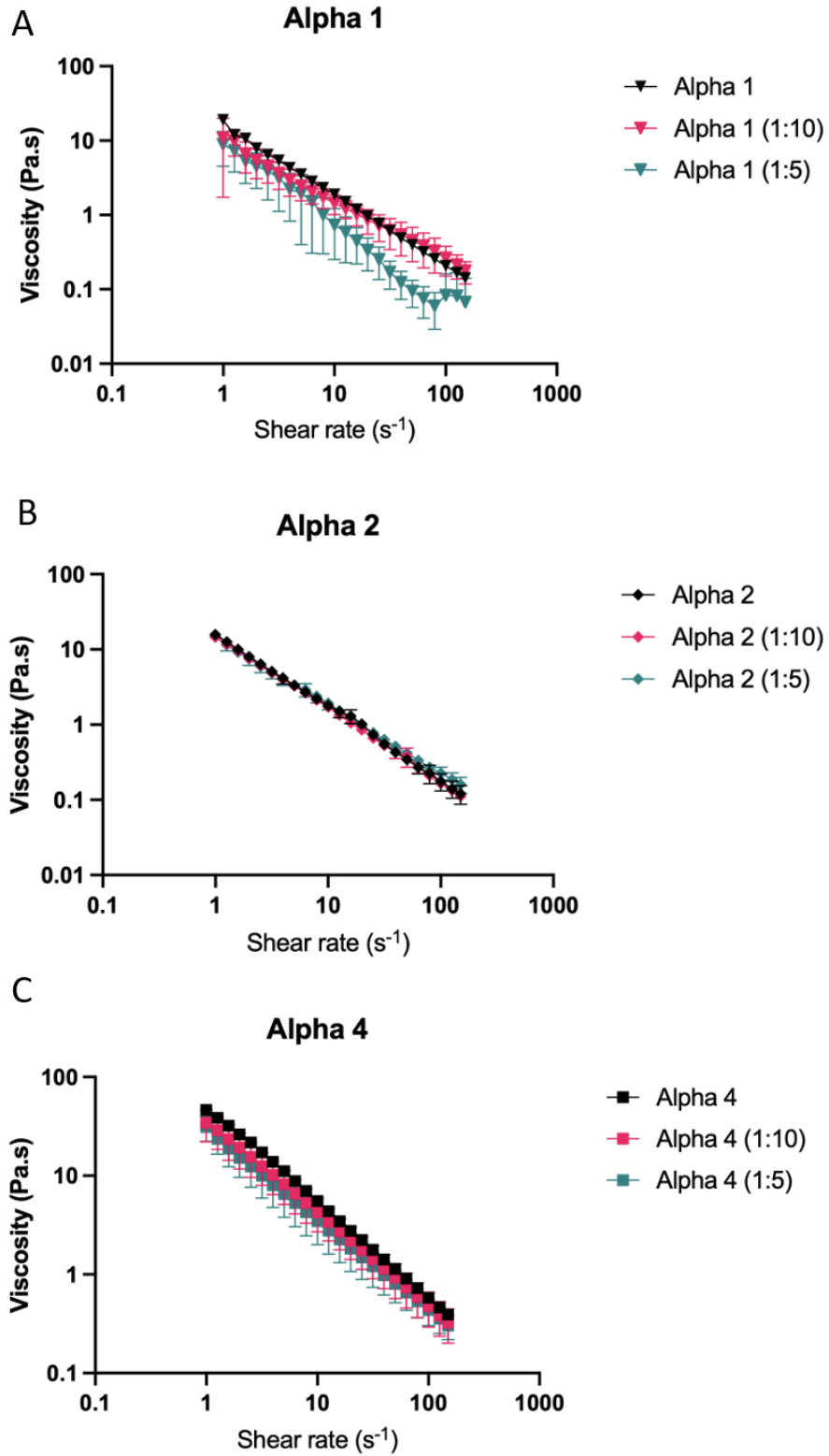
Figure 2.6. Viscosity measurements of A) Alpha 1, B) Alpha 2, and C) Alpha 4 mixed with different ratios of cell culture medium-to-gel volume. N = 3, and error bars show standard deviations.

2.4.2 Characterisation of Peptigel® pH changes for potential cell culture use

Peptigels® require, as per the manufacturer's advice, to have multiple culture medium changes to be pH equilibrated. Sudden changes in the pH of the cell culture medium could impact cell survival. Thus, it was important to characterise pH changes in the tested Peptigels®. pH measurements of the Peptigels® were performed while incubating them in PBS. Figure 2.7A shows the pH measurements taken across 72 hours. PBS alone was the control. Figure 2.7B shows the set-up used to measure the pH, with pipetted Peptigel® domes at the centre of 6 well-plate wells submerged in PBS. To ensure future cell viability within the Peptigel®, the pH is expected to be between 6.5 and 7.5. As shown in Figure 2.7A, when compared to PBS, both Alpha 1 and Alpha 4 presented pH levels within the 6.5-7.0 range, following a similar trend and final value as the control PBS over 72 hours. However, Alpha 2 appeared more acidic, showing a quick decrease in pH within the first 2 hours and a final pH lower than 6.5 at 72 hours. Based on these results, Alpha 1 and Alpha 4 appeared to be the best candidates for potential subsequent cell viability.
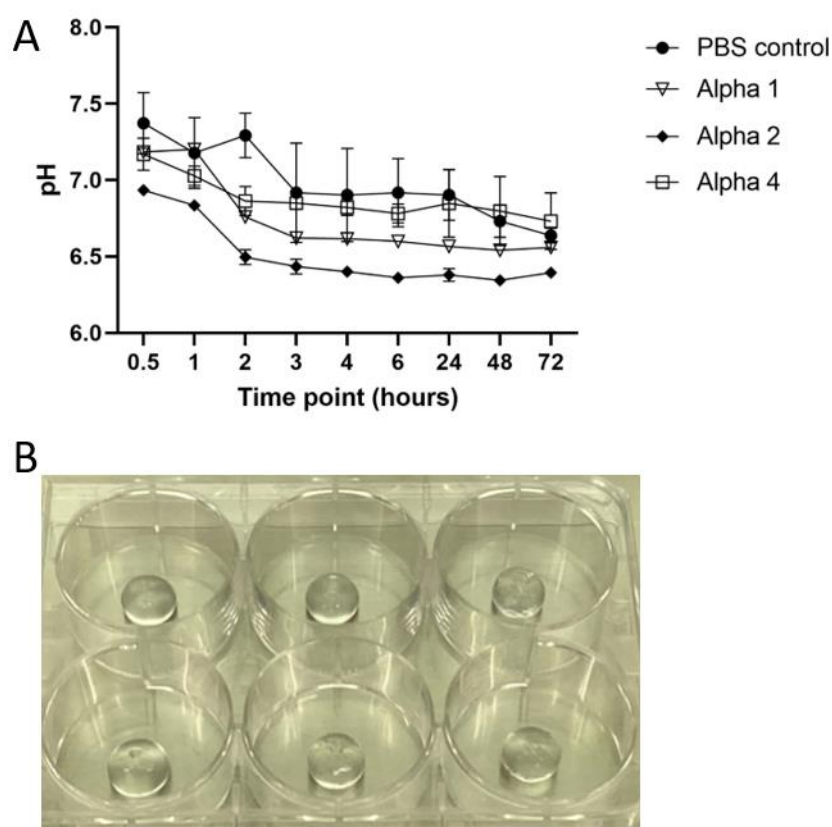
Figure 2.7. A) pH measurements taken across 72 hours of the different Peptigels; n = 3. Error bars show standard deviations. B) Set-up to measure the pH of the Peptigel domes submerged in PBS.

2.4.3 Diffusion properties of Peptigels®

The assessment of diffusion properties of the Peptigels® was performed using 1 mL of culture medium with phenol red, added on top of 1.5 mL of Peptigel®, to visually monitor the spread of the medium through the Peptigel®. Figure 2.8 shows different images of the Peptigel®-medium system taken at different time points. The tested Peptigels® presented different diffusion properties. Alpha 1 showed the fastest diffusion rate, showing the culture medium being diffused through 75% of the Peptigel® after only 3 hours. The culture medium changed from pink to yellow through diffusion in the Peptigel®. The acidic nature of Alpha 1 was clear here, showing the importance of performing cell culture medium changes across the first hour of cell

culture to ensure the neutralisation of the Peptigel®. Alpha 4 presented a slower diffusion rate, showing a diffusion of around 75% of the Peptigel® after 6 hours. Finally, Alpha 2 presented the slowest diffusion rate, showing minimal phenol red uptake after 24 hours. Due to the low diffusion properties of Alpha 2, this Peptigel® was not further characterised *in silico* or optimised for 3D bioprinting.
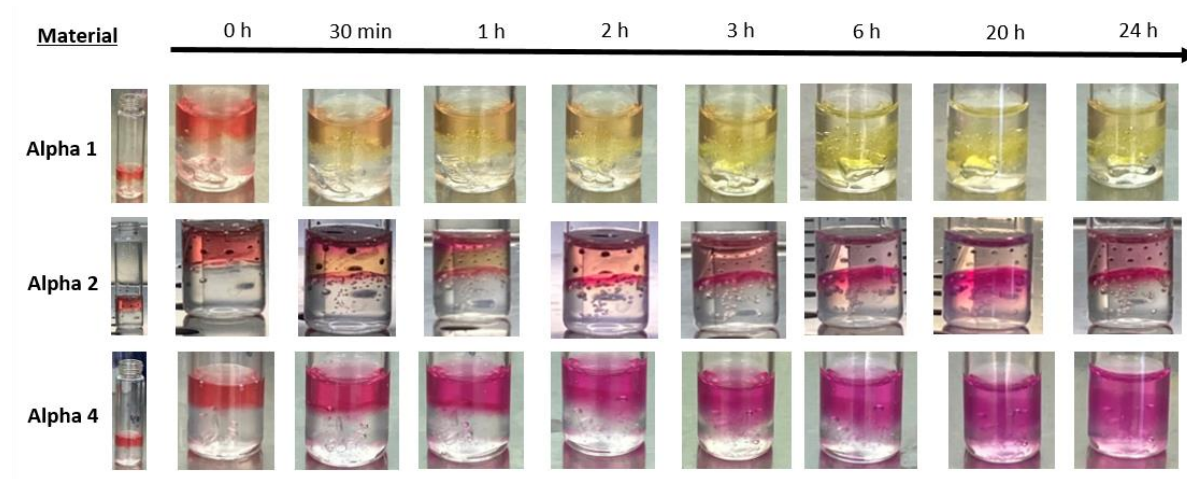
Figure 2.8. Diffusion experiment through visual assessment of medium diffusion through Alpha 1, Alpha 2, and Alpha 4. N=1.

2.4.4 Printing pressure and printing speed optimisation of Peptigels®

A printability assessment was first performed to determine the printing pressures suitable for 3D bioprinting the selected Peptigels®. Different combinations of printing pressures and printing speeds were tested to achieve the highest printing resolution and continuous filament deposition. As shown in Figure 2.9, the higher the printing pressure, the more material is deposited, giving a thicker deposited filament. Figure 2.9 shows the resulting printed zigzag patterns of Alpha 1 with a medium-to-gel ratio of 1:10 and Alpha 4 with a medium-to-gel ratio of 1:5. These ratios have the best rheological properties in terms of viscosity (Section 2.4.1). The Peptigels®, which were printed with a 25G nozzle, presented similar filament characteristics in printing pressure window between 8 and 10 kPa, where the filament was continuous in low

printing speeds (4 and 6 mm/s), and no merging was observed between adjacent filaments. Higher printing pressures (> 12 kPa) in both materials showed filament deposition merging in all printing speeds tested.
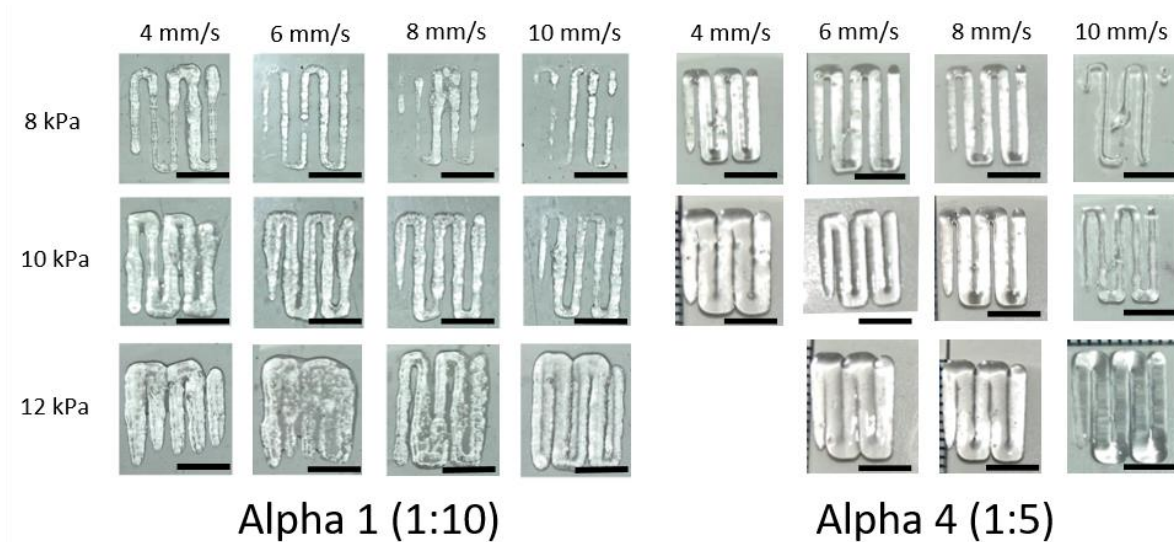
Figure 2.9. Visual assessment of filament deposition of the Peptigels® using a 25G conical nozzle, different pressures (8, 10, and 12 kPa) and different printing speeds (4, 6, 8, and 10 mm/s). Scale bar is 5 mm.

Based on these printing pressure parameters, further optimisation was performed based on the printing speed's effect on the printed structure. Microscope images were taken of the deposited filaments, and their width was quantified using Fiji ImageJ software (version 1.53t). Figure 2.10 shows the computed filament thickness that the printed structures presented. As expected, the higher the printing speed, the lower the filament thickness. Additionally, the lower the printing pressure, the lower the filament thickness. When comparing both materials, overall, Alpha 1 presented a better resolution when printed using the same printing pressures as Alpha 4. This can be due to the differences in medium-to-gel ratio, which differ between materials based on manufacturer advice. The theoretical filament thickness value is based on the diameter of the 25G nozzle (250 µm). Both Alpha 4 and Alpha 1, when printed at 10 mm/s and 8 kPa, approached this theoretical value the most. However, 10 mm/s speed

presented limitations such as lack of quick control over the change of printing parameters for the printer user. Therefore, the optimised manufacturing process used a final printing speed of 5 mm/s and a printing range of 8 to 12 kPa when printing the structures with both materials.
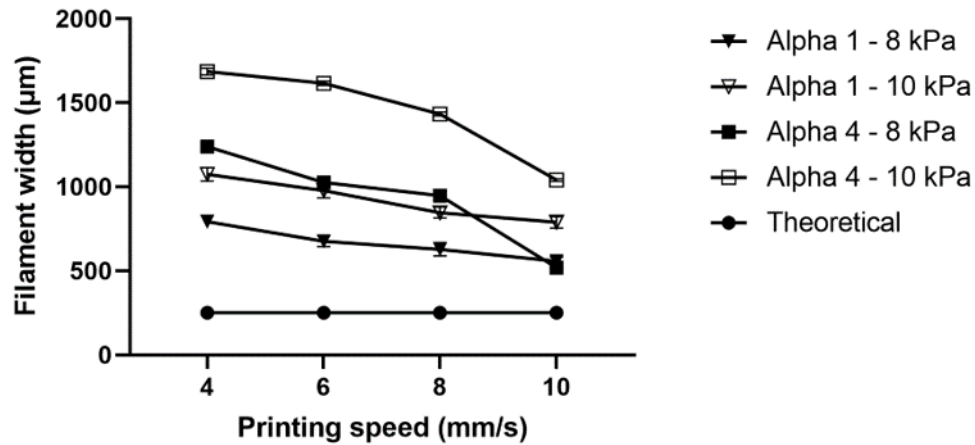
Figure 2.10. Filament width quantification of Alpha 1 with a medium-to-gel ratio of 1:10 and Alpha 4 with a medium-to-gel ratio of 1:5. N=3, and error bars show the standard deviation.

2.4.5 CFD modelling of the extrusion process of Alpha 1 and Alpha 4

The CFD model was used to quantify and visualise the shear stresses and pressures arising from the extrusion process of Alpha 1 and Alpha 4 using the optimal printing pressures found in section 2.4.4. These quantities were assessed under two different input pressures for different bioinks. The comparison between conical and needle-based nozzles was not investigated in this research. It is well established that needle-based nozzles compromise cell viability more than the conical nozzles as they need higher extrusion pressures [200,211]. Additionally, different sizes of the conical nozzle were also not modelled as the goal was to understand the shear stresses arising in the already chosen conical nozzle. As previously mentioned, a 25G nozzle was chosen over the 22G nozzle due to the theoretically higher filament resolution and

over the 27G nozzle due to the expected lower shear stresses that the bioprinting process would generate. The current investigation focuses only on the 25G nozzle; however, further investigations with 27G and 22G could be performed (more information is found in Section 2.5).

This model was used to investigate the effect the printing window pressures have on the shear stresses created in the nozzle. Only 8 and 10 kPa inlet pressures, found to be optimal for 3D printing these materials (Section 2.4.4), were tested here, and the shear stresses were compared between the two materials, Alpha 1 (1:10) and Alpha 4 (1:5).

The contour maps of both the shear stresses and pressures when Alpha 1 (1:10), Figure 2.11, and Alpha 4 (1:5), Figure 2.12, are printed using the 25G nozzle at pressures 8 or 10 kPa, presenting very similar patterns. The contour maps enable the visual understanding of where the higher shear stresses arise and how far these shear stresses cover the nozzle area. Figures 2.11 and 2.12 show the shear stresses capped at 120 Pa. This shear stress was found to be detrimental to cell viability for adherent cells, smooth muscle cell line Crl-1444, leading to cell damage and loss [212]. Although the levels of shear stress that cause cell damage are cell-dependent, this value can indicate how much damage could be caused to our cells. As seen in Figures 2.11 and 2.12, the area that presents high shear stresses (> 120 Pa) arises at the tip of the nozzle and extends from the walls. This area is only located at the tip of the nozzle, confirming that cells do not experience high levels of shear when printed with these Peptigels® in most of the nozzle area.
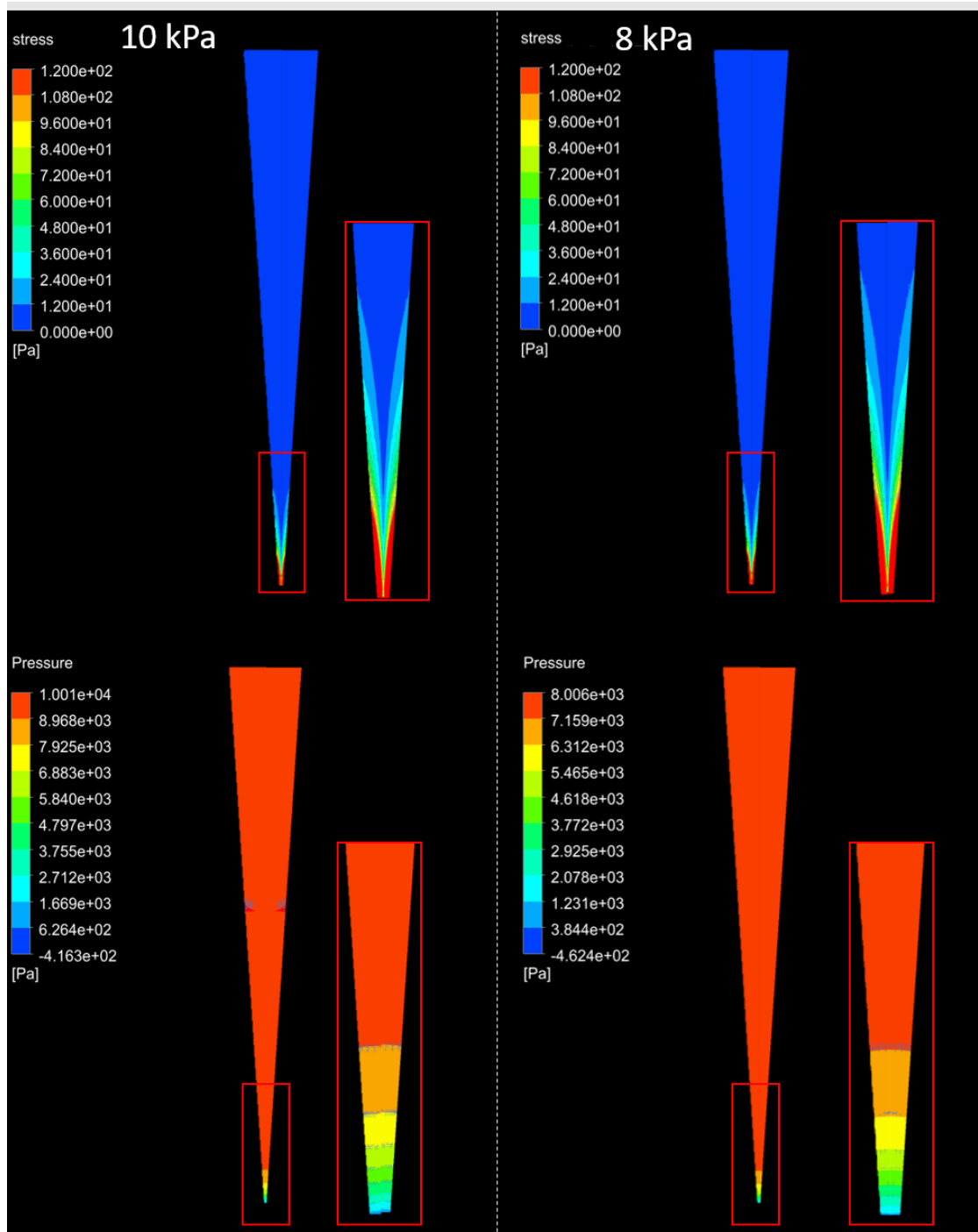
Figure 2.11. Contour maps showing the shear stress across the nozzle (top) and the pressure values (bottom) when printing Alpha 1 mixed with cell culture medium in a 1:10 medium-to-gel ratio using a 25G conical nozzle. The left-hand side shows the forces using an inlet pressure of 10 kPa. The right-hand side uses 8 kPa as inlet pressure. Red boxes depict the section highlighted, represented magnified to the right-hand side of the full nozzle map.

93
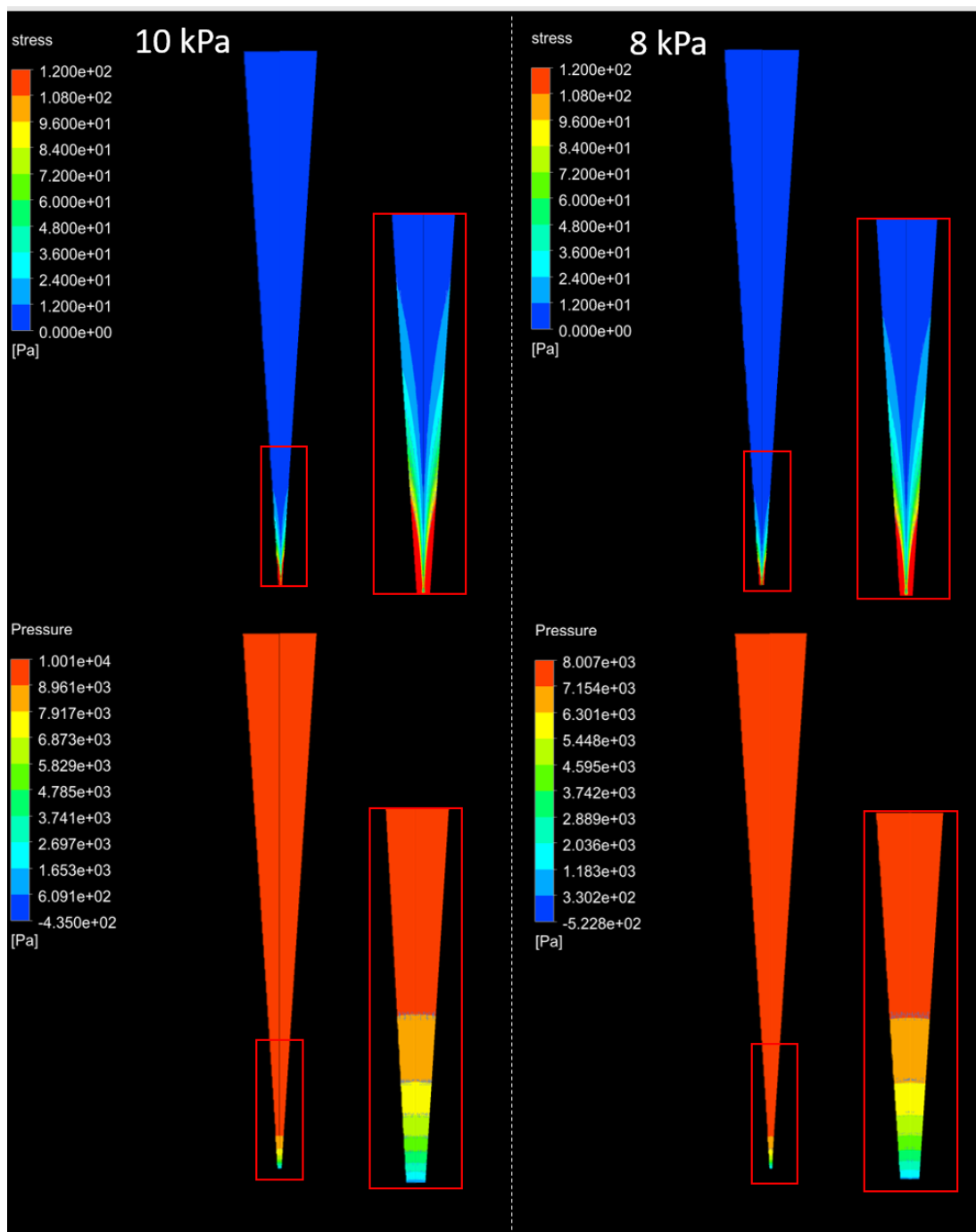
Figure 2.12. Contour maps showing the shear stress across the nozzle (top) and the pressure values (bottom) when printing Alpha 4 mixed with cell culture medium in a 1:5 medium-to-gel ratio using a 25G conical nozzle. The left-hand side shows the forces using an inlet pressure of 10 kPa. The right-hand side uses 8 kPa as inlet pressure. Red boxes depict the section highlighted, represented magnified to the right-hand side of the full nozzle map.

94

The average and maximum stresses were found and plotted to compare materials and printing pressures further, Figure 2.13. As expected, lower printing pressures generated lower shear stresses. When comparing materials, there were minimal differences in the shear stresses generated. Overall, when assessing the average shear stress, low levels of shear stress were observed, ranging from 60 to 70 Pa. Based on these results, both Peptigels® were promising candidates for 3D bioprinting cell-laden tissue models, as the *in silico* modelling showed low levels of shear stress would be experienced by the cells in most of the nozzle.
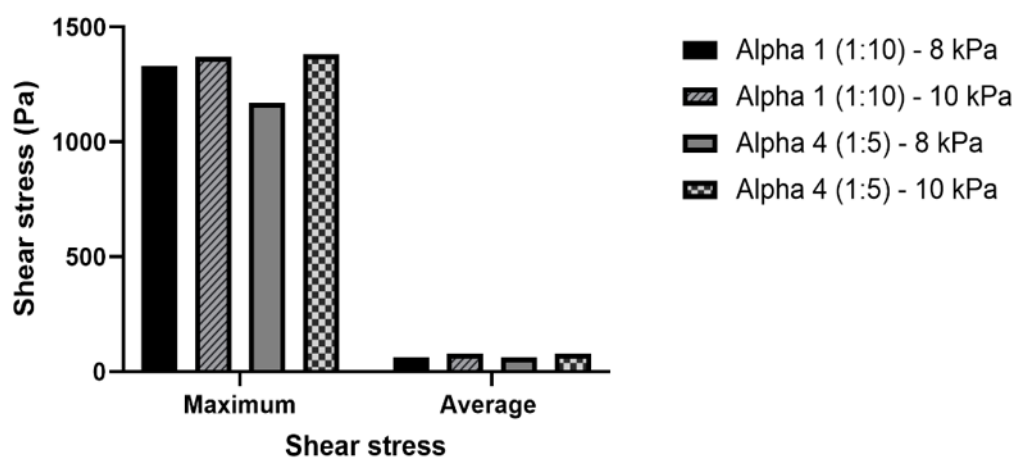
Figure 2.13. Indicative figure. Maximum and average shear stresses experienced in the nozzle when extruding different Peptigels® at different pressures.

2.5 Discussion

Synthetic hydrogels have been widely used in 3D bioprinting [172]; among them, peptide-based self-assembling hydrogels have recently started to be investigated [213]. These synthetic polymers, made of different amino acids, can be self-assembling peptides. These present the advantages of synthetic polymers, such as low batch-to-batch variations and tuneable properties, as well as benefits from the structural self-assembling properties. These peptide-based self-assembling hydrogels assemble themselves in β-sheet protein configurations and stay stable without further crosslinking or additional manufacturing steps [181,182]. Extensive research exists on the 3D printing of self-assembling peptide hydrogels, which are cell-seeded subsequently [214–216], as opposed to cell-laden 3D bioprinted. However, further investigations of cell-laden self-assembling peptide hydrogels, making them bioinks, are yet to be performed. Commercial self-assembling peptides, such as Peptigels®, are promising candidates as bioinks for future use when manufacturing *in vitro* tissue models. Three different Peptigels® have been physically and chemically characterised to screen the best candidates for 3D bioprinting in this chapter.

Firstly, Alpha 1, Alpha 2, and Alpha 4 were rheologically characterised to investigate their viscosity properties. Rheological characterisation of the used hydrogels is required to understand the potential use of these materials as bioinks. According to Paxton *et al.*, supplementary rheological evaluations should be performed to understand the behaviour that the material experiences in the flow initiation, the filament formation, and the post-printing recovery [191], explained in Section 2.1.2. These rheological measurements include assessing yield stress, shear-thinning characterisation, and recovery behaviour. The characterisation of these Peptigels® focused on understanding their shear-thinning properties, and other parameters such as yield stress and recovery behaviour were not quantified rheologically. Additional data showing the quantification of storage and loss moduli values, used to determine the yield stress, is shown in Appendix A2.2. Post-printing recovery was not assessed rheologically, but investigated indirectly through filament deposition resolution (Section 2.4.4).

As seen in Figure 2.6, all Peptigels® were shear-thinning, decreasing their viscosity with increasing shear strain. These Peptigels® were mixed with cell culture medium in different medium-to-gel ratios, and the viscosity properties were compared to those of pure Peptigels®. Cell culture medium was added to the Peptigels® to assess their behaviour when used in the future as cell-laden bioinks, which would require cells in the cell culture medium to be mixed with the Peptigel® prior to bioprinting. Alpha 1 and Alpha 4 decreased viscosity with increased cell culture medium added. This was expected as the addition of cell culture medium further diluted the Peptigels®, making them less viscous. However, Alpha 1 showed a slight increase in the viscosity when mixed in a 1:10 medium-to-gel ratio in high shear stress values ($> 10 \text{ s}^{-1}$). This is hypothesized to be due to the effect of cell culture medium salts on the Peptigel® structure, increasing its self-assembly, which could increase its viscosity over time [217]. However, further time-dependent measurements should be performed to confirm this theory. Alpha 2 did not show differences between the tested Peptigel® mixtures. It maintained the expected shear-thinning behaviour, but adding the cell culture medium did not decrease its viscosity. When comparing viscosities across Peptigels®, it could be observed that Alpha 4 was the most viscous material, and therefore, it was expected to require the highest printing pressure in the 3D bioprinting process. Additionally, Alpha 1 and its mixtures were the least viscous out of the three Peptigel® candidates, making it the best candidate for 3D bioprinting when trying to minimise the extrusion pressure needed.

Secondly, the Peptigels® pH and diffusion properties were characterised. pH characterisation of the used bioinks is essential to further assess how these materials will interact with embedded cells. Cell culture medium should be maintained at pH 6.5 to 7.5 [218]. Therefore, the hydrogel environment should maintain this range to ensure optimal cell proliferation and viability. These Peptigels® are recommended to be pre-conditioned with cell culture medium changes within the first hour of cell culture to ensure pH equilibrium. This investigation focused on further understanding this pre-conditioning's effect on the surrounding cell culture medium. It was hypothesized that the Peptigels® were leaching out ions that would affect the pH of the surrounding medium. PBS was used as a control, and the Peptigels® were left in PBS solution for 72 hours. Measurements were taken to assess changes in pH in the PBS solution.

97

Figure 2.7A shows that Alpha 4 was the Peptigel® that followed the pH of PBS the closest, followed by Alpha 1. Alpha 4 and Alpha 1 presented pH values within the 6.5-7.5 range, confirming their potential use in cell-laden 3D bioprinting. Alpha 2 presented an acidic nature, with a pH below 6.5 at some time points. These low pH values would present a limitation when using this Peptigel® for cell culture.

Peptigel® diffusion properties were also assessed by adding 1 mL of culture medium with phenol red on Peptigel® samples (1.5 mL) and evaluating the penetration of phenol red across the material. Figure 2.8 shows that Alpha 1 and Alpha 4 had complete diffusion of phenol red from 6 hours onwards. The tested Peptigel® volume was 1.5 mL, whilst the 3D bioprinted samples are planned to be approximately 200 μL (Chapter 3). Therefore, it was expected that in 200 μL of Peptigel®, the cell culture medium would reach the centre of the printed samples in approximately 30 minutes. This further confirmed that the diffusion of nutrients from the cell culture medium would reach the cells encapsulated in the centre of the Peptigels® within 2 hours of culture medium submersion. Alpha 2 demonstrated low diffusion properties, showing that after 24 hours, phenol red had not penetrated the Peptigel® fully. Oxygen and nutrient diffusion are critical properties of a hydrogel to ensure the cell viability of encapsulated cells, especially in thick constructs [219]. Based on these observations, Alpha 2 demonstrated an acidic pH and low diffusion properties, which were expected to compromise cell viability in future experiments. Therefore, only Alpha 1 and Alpha 4, which showed pH values within accepted ranges and a fast rate of medium diffusion, were further used in 3D bioprinting optimisation.

Alpha 1 and Alpha 4 were further investigated, and 3D bioprinting optimisation was performed. Based on the manufacturer's advice, Alpha 1 was combined with cell culture medium at a medium-to-gel ratio of 1:10 and Alpha 4 at a 1:5 ratio. These mixtures were used to assess 3D bioprinting filament deposition using different extrusion pressures and printing speeds, Figure 2.9. A zigzag pattern was chosen to assess filament deposition continuity and fusion of adjacent filaments. Figure 2.9 shows that 12 kPa of extrusion pressure led to a filament deposition, which presented fused adjacent filaments in both materials at all printing speeds tested. Therefore, only

8 and 10 kPa extrusion pressures were pursued for further filament width quantification and comparison to theoretical levels.

Filament deposition resolution has been assessed similarly in reported literature. For example, He *et al.* assessed the optimal distance between the nozzle and the print bed by measuring the filament extrusion length (before deposition) using different pressure values and temperatures [199]. This printing distance was linearly correlated with the deposited filament line width. They assessed their printing shape fidelity by printing zigzag patterns and looking at the corners. Sharp corners, linked with lower printing distances, were accepted. Curve corners found in higher printing distances were rejected [199]. Finally, they also addressed printing shape fidelity by looking at the pore area of printed lattices. The closer the area was to the used CAD (Computer Aided Design) model pore area, the better the resolution of the bioprinting process. This measure is similar to filament width, assessed by other investigations such as those conducted by O'Connell *et al.* [194].

Figure 2.10 shows the expected correlation between increasing printing speeds and deposited filament widths. The theoretical value, which corresponds to the diameter of the 25G nozzle, was approximated at 10 mm/s printing speed and an extrusion pressure of 8 kPa. Although this parameter combination would give the best resolution, it presented a main disadvantage: the printing speed. When these experiments were performed, the printed structures were not printed sequentially. Issues in the printing process, such as delayed flow and clogging, were avoided. A slower printing speed was chosen to ensure no filament discontinuity when printing multiple structures sequentially. A lower printing speed of 5 mm/s enables the user to change the printing pressure parameters on time to avoid sections of the printed constructs not being printed.

A 25G conical nozzle was used to assess the filament width change across the two printing pressures and printing speeds. No other nozzle sizes were investigated, as 25G was expected to give the best compromise between filament resolution and resulting shear stress in the printing process. The correlation between the size of printing nozzles and the shear stress generated has been well documented [220–222].

Therefore, smaller nozzles, such as 27G, were not investigated regardless of the better printing resolution to avoid cell death.

Finally, a CFD-based investigation was conducted to estimate the shear stress and pressure that the Peptigels® were encountering through the bioprinting process. The extrusion of both Alpha 1 and Alpha 4 was modelled and shear stresses and pressure values were investigated, Figures 2.11 and 2.12. The visualisation of the shear stresses was performed through contour maps capped at 120 Pa, which has been reported to be damaging shear stress for adherent cells [212]. As seen in these figures, neither Alpha 1 nor Alpha 4 presented shear stresses above 120 Pa, apart from the walls in the tip of the nozzle. This confirmed that the maximum shear stress, Figure 2.13, was concentrated in a single area and that its effect on the embedded cells would be short and not maintained across the nozzle. The average shear stress across the nozzle was below the 120 Pa threshold, in the 60-78 Pa range for all scenarios, Figure 2.13. The pressure maps of these extrusion scenarios depicted that the maximum pressure across the nozzle would be the same value as the extrusion pressure chosen.

These preliminary models suggested that the experienced shear stress and pressure levels during the extrusion of Alpha 1 and Alpha 4 would not damage embedded cells, affecting their survival during the printing process. Although extensive work has been done to model and quantify the shear stresses in the 3D bioprinting extrusion process [200,223], minimal investigations have been done regarding these Peptigels®; comparison with existing documentation was not feasible. The only research regarding the *in silico* modelling of Peptigels® was performed by Chiesa *et al.* [213]. In this investigation, they modelled a different Peptigel®, F9, extrusion through a cylindrical nozzle. This material was mixed with water and NaOH instead of a cell culture medium, and other concentrations and pH levels were compared. The FE model was built following the same conditions as the presented model: 2D axial symmetry, no-slip boundary conditions and no pressure outlet condition. However, in their model, multiple issues are present, such as the assumed density of the Peptigel® being that of water and presenting a constant velocity inlet rather than a pressure one. Although the viscosity levels of F9 and Alpha 1 mixed with cell culture medium at a 1:10 ratio

were similar, the *in silico* modelling results cannot be compared due to fundamental differences such as the geometry of the nozzle chosen and the inlet variables being expressed in velocity rather than extrusion pressure. They found a maximum shear stress of less than 60 Pa, whilst in our investigations the average shear stress found was higher than 60 Pa, in a range of 60-78 Pa. Further work regarding mathematical validation of the used model and experimental validation regarding fluid flow must be performed so this model can be used quantitatively. However, as it stands, the model has been a valuable tool for estimating and predicting low cell death based on the tested printing parameters in subsequent experiments, as shown in Chapter 3.

2.6 Limitations and Future Work

The presented chapter focuses on experimentally and computationally screening three Peptigels® as candidates for 3D bioprinting. Throughout the proposed investigations, multiple limitations were encountered.

Firstly, rheological evaluations were performed to understand the viscosity changes the Peptigels® would experience during the 3D bioprinting process. The viscosity measurements were performed on the Peptigels® alone and mixed with two different medium-to-gel ratios. The combination with the culture medium was meant to mimic the behaviour of these bioinks after being mixed with cells in the culture medium for 3D bioprinting. However, two limitations were encountered here. Firstly, the Peptigels® experienced changes in mechanical properties after contact with the salts in the cell culture medium, as previously reported [217]. Therefore, the longer the Peptigel® was in touch with the cell culture medium, the more the mechanical properties would change. Time-dependent viscosity measurements should be performed to fully understand the effect that culture medium contact has on the rheological properties of the Peptigels® and, subsequently, the 3D bioprinting. Secondly, the effect the embedded cells would have on the rheological properties of the Peptigels® was not investigated. Previous work has modelled the embedded cells as microparticles [191]. Further tests following these reported studies or using cells should be performed to understand the material behaviour changes better.

Secondly, Peptigel® chemical characteristics such as pH and diffusion were assessed. First, pH measurements were set with a pH probe submerged in PBS, where the Peptigels® were incubated. These measurements give an understanding of the pH changes that would take place in the surrounding culture medium of culture Peptigels®. However, further investigations should focus on measuring the pH levels inside the Peptigel®. Smaller pH probes could be used to measure pH changes at the core of the Peptigels® and further understand the pH levels the embedded cells will experience. Second, diffusion properties were estimated by visually assessing the diffusion of phenol red through the Peptigels®. This experimental set-up can enable the visualisation of the nutrient diffusion. However, other important variables, such as

oxygen diffusion, were not assessed. Further investigations should focus on measuring the changes in oxygen levels inside the Peptigels®, such as using an optical fibre oxygen sensor [219].

Thirdly, only a 25G nozzle was tested, and 3D bioprinting parameters were optimised for this size. Previous literature has reported increased shear stress and cell death when using small nozzles [200,221,222]. However, no specific investigations have been performed regarding the shear stresses and pressures when 3D bioprinting these Peptigels® using a 27G nozzle. Investigations using 27G nozzle should be performed to assess the forces that arise in the 3D bioprinting process. If the forces were found to not compromise cell viability, this would enable the optimisation of a 3D bioprinting process with a better resolution.

Finally, the investigations regarding the shear stresses that arise in the 3D bioprinting process, used 120 Pa as the threshold level for cell damage. This value was obtained from previous literature on anchorage-dependent cell damage under shear stress [212]. However, the used cells do not coincide with the cells planned to be used in the subsequent investigations (found in Chapter 3). These cells, primary human chondrocytes (HCHs), have not been used to investigate the specific levels of shear stress that would compromise their viability. Therefore, to make the use of this CFD model more complete, further investigations of the effect that different shear stress levels have on HCHs viability should be performed.

2.7 Summary

Three different Peptigels® were assessed for their properties to support 3D bioprinting manufacturing. All three presented shear thinning properties, measured through rheological viscometry. pH measurements showed that Alpha 1 and Alpha 4 maintained a range within the 6.5-7.5 pH that would support cell survival. Additionally, Alpha 1 and Alpha 4 presented adequate diffusion properties to ensure cell viability at the centre of the manufactured constructs. Alpha 2 showed an acidic pH nature and low diffusion properties, which led to the rejection of this Peptigel® as a potential bioink. Based on these initial assessments, Alpha 1 and Alpha 4 were chosen as the potential Peptigels® to use in the 3D bioprinting process.

Further 3D bioprinting optimisation was performed on the bioinks (Peptigels® mixed at the optimal medium-to-gel ratio) by assessing the printing pressure window and the printing speeds' effect on the deposited filament resolution. A final optimisation parameter combination of 8-10 kPa of pressure and 5 mm/s printing speed was chosen to avoid filament discontinuity and ensure good printing resolution.

Finally, *in silico* modelling was further performed to assess the different shear stresses that arose when printing these materials through the 25G nozzle. Optimal mixtures of Alpha 1 (1:10) and Alpha 4 (1:5) were modelled with the printing pressure window values. Minimal differences across materials and pressures were observed. High shear stresses (>120 Pa) were only observed at the tip of the nozzle, confirming that for most of the nozzle volume, the cells would not experience damaging shear stress when printed with these parameters.

In Chapter 3, the 3D bioprinting optimised parameters shown here are used to assess the potential of these materials as bioinks to develop human cartilage tissue models *in vitro.*

Chapter 3: Characterisation of 3D bioprinted cartilage tissue models *in vitro* using self-assembling peptide-based bioinks

3.1 Introduction

Cartilage presents an extraordinarily complex structure of four distinct articular cartilage zones [224], making it extremely complicated to replicate *in vitro.* These four zones are commonly known as the superficial, middle, deep, and calcified cartilage zones (Figure 1.1). The superficial zone comprises collagen fibres parallel to the surface, combined with elongated-shaped chondrocytes. Immediately under the superficial zone, the middle zone has collagen fibres, which have a randomised orientation in combination with rounded-shaped chondrocytes. The deep zone, further down, exhibits perpendicular collagen fibres to the tide mark. Chondrocytes in this area remain rounded and are positioned in files perpendicular to the time mark. Finally, the innermost calcified cartilage zone is in contact with bone and presents hypertrophic chondrocytes [224] .

Cartilage tissues present no vasculature; nutrients are distributed through diffusion [225], making tissue healing a slow and challenging process. These difficulties in tissue regeneration have made cartilage a critical tissue to study *in vitro* to develop replacement tissues [226,227] and new tissue regeneration strategies [228,229].

Different manufacturing techniques have been used to develop cartilage *in vitro* tissue models, such as freeze-drying [230,231], gel-pressing [232] or selective laser sintering [233]. Although widely used, these techniques present disadvantages such as the lack of control over the architecture, needing elevated temperatures or using toxic solvents [234]. As an alternative, 3D bioprinting presents different advantages, such as the high precision of the technology, the low cost, and the control over the construct architecture [234].

Different 3D bioprinting techniques, such as jetting-based, photopolymerisation-based and extrusion-based, have been used to develop cartilage tissue models, extrusion-based being the most popular [161]. Most extrusion-based cartilage tissue models have been developed with animal-derived materials such as gelatine methacrylate (gelMA) [112,235–242], hyaluronic acid-based [163,236,241] and chondroitin sulphate-based materials [112,163]. Alginate is the most used material due to its ease of printability and low cost. However, its poor cell attachment properties require it to be mixed with other materials, such as previously mentioned. To avoid using animal-derived materials for developing 3D bioprinted cartilage tissue models, we assess two different self-assembling Peptigels® as potential candidates, previously screened and characterised in Chapter 2.

Differences in hydrogel performances (synthetic or natural) make it extremely complex to define a hydrogel-based "gold standard" system for cartilage manufacturing *in vitro*. Therefore, to assess the performance of any new hydrogel for tissue manufacturing, comparing it to the native tissue is the preferred strategy. Alternatively, the chondrocyte 3D pellet model [72,243] can be used when native tissue explants are unavailable. However, the 3D pellets present multiple disadvantages regarding the cell viability in the centre of the pellet, which leads to limitations when trying to scale up this tissue, and the need for more control over the architecture.

Synthetic self-assembling peptides are assessed to further develop the research field of cartilage *in vitro* 3D bioprinting and transform it into a more ethical and sustainable tissue modelling approach. Manchester Biogel Ltd (MBG) has previously reported the chondrogenic potential that Alpha 1 has for bovine chondrocytes and the manufacturing of cartilage-like structures such as the nucleus pulposus [184,186]. Further building on this previous knowledge, Alpha 1 and Alpha 4 are investigated as potential candidates for 3D bioprinting human cartilage *in vitro* tissue models. Their behaviour is compared to the current cartilage gold standard 3D pellet chondrocyte culture.

This chapter assesses Alpha 1 and Alpha 4 as potential Peptigels® for *in vitro* cartilage tissue model development. These Peptigels®, when mixed with cell culture medium, are considered PeptiInks® and are used here. Cell viability post-bioprinting and histological assessment were performed to assess cell proliferation and cartilage-

specific characteristics, such as extracellular matrix production, in both PeptiInks®. Based on these results, further analysis of the genetic expression of embedded chondrocytes in Alpha 1 was performed through comparative qPCR to confirm further its potential use as a cartilage tissue model PeptiInk®. It must be noted that methods and data regarding the 3D pellet control and Alpha 1 cultures were previously published by Santos-Beato *et al.* [244]. In this chapter, this data is shown and compared to Alpha 4.

3.2 Objectives and Hypothesis

This chapter aims to optimise and characterise the 3D bioprinting process of cartilage tissue models *in vitro* using Alpha 1 and Alpha 4 Peptigels®.

Objectives:

1. Develop and optimise a 3D bioprinting protocol to develop cartilage tissue models *in vitro*.
2. Characterise human primary chondrocytes (HCHs) cell viability in Alpha 1 and Alpha 4 post-bioprinting.
3. Histologically characterise cartilage tissue *in vitro* models 3D bioprinted with Alpha 1 and Alpha 4.
4. Explore the genetic expression of PeptiInk® embedded HCHs in the best PeptiInk® candidate.

Hypothesis:

1. Alpha 1 and Alpha 4 support 3D bioprinting of a human cartilage tissue model *in vitro*.

3.3 Methods

3.3.1 Cell culture

Human primary chondrocytes (HCHs; Cell Applications, San Diego, CA) were purchased and consistently used between passages 5 and 7. HCHs were cultured in a chondrogenic growth medium (Cell Applications, San Diego, CA) and incubated at 37°C in a humidified atmosphere with 5% pCO_2. The purchased cells were expanded, and a cell bank was created. When in culture, the medium was changed every two to three days.

3.3.2 PeptiInk® cell encapsulation

HCHs were manually mixed into Alpha 1 or Alpha 4 (Manchester Biogel Ltd, Alderley Edge, UK) at a concentration of $1x10^6$ cells/mL using a ratio of 1 mL of PeptiInk® to 100 µL of cell culture medium (1:10) for Alpha 1, and a ratio of 1 mL of PeptiInk® to 200 µL of cell culture medium (1:5) for Alpha 4 (optimisation shown in Chapter 2). Cell-laden PeptiInks® were loaded into 3 mL printing cartridges (Nordson, USA) using a positive displacement pipette (Gilson Scientific, Dunstable, UK). Loaded cartridges were centrifuged to remove air micro-bubbles for 2 minutes at 3,500 rpm and immediately printed into 12-well culture plates.

3.3.3 3D bioprinting of HCH cell-laden Alpha 1 and Alpha 4

The 3D bioprinting process was performed using the BIOX6 (CELLINK, Sweden). Circular disc structures with an outer diameter of 5 mm and a thickness of 1 mm with 60% infill density were 3D bioprinted using a 25G conical nozzle. The extrusion pressure that ranged between 8 kPa and 10 kPa, and a printing speed of 5 mm/s. The optimisation of this bioprinting process is further explained in Chapter 2, Section 2.4.4. 50 µL of culture medium was added to the printed structures and left for one minute so initial PeptiInk® surface hardening happened. This pre-step reduced the initial

PeptiInk® degradation. Subsequently, the printed structures were fully submerged in chondrogenic medium. In the case of Alpha 1, half of the medium was changed three times during the first hour to ensure pH equilibrium. The culture medium was changed for both PeptiInks® twice a week over the culture period. Cell constructs were cultured for up to 14 days at 37°C in a humidified atmosphere with 5% pCO_2.

3.3.4 Cell pellet formation and culture

3D control cell pellet cultures were formed following a protocol from Yeung *et al.*[245]. In summary, $4x10^5$ cells were centrifuged in 500 µL of culture medium at 1,750 rpm for 5 minutes in 15 mL tubes. After 72 hours, the pellets were gently aspirated into ultra-low adhesion 24-well plates (ScienceCell, 0383), with one pellet per well cultured in 1 mL of chondrogenic culture medium. The culture medium was changed every two to three days. The cell pellets were cultured for up to 14 days at 37°C in a humidified atmosphere with 5% pCO_2.

3.3.5 2D HCH culture

2D HCH control cultures were set up by seeding 15,000 cells in 24-well plates and culturing them with chondrogenic growth medium. They were incubated for up to 14 days at 37°C in a humidified atmosphere with 5% pCO_2, and their medium was changed every 2 to 3 days.

3.3.6 Cell viability and percentage cell survival semi-quantification

Cell viability was assessed using a live/dead assay. 3D bioprinted constructs were assessed 2 hours post-bioprinting (day 0), on day 7, and on day 14. Samples were cut in half to visualise cell viability in the centre of the constructs. 3D pellet and 2D samples did not require sectioning. Samples were washed twice with PBS (Phosphate-buffered

saline) (Gibco, 20012-019) and then incubated at 37°C for 30 minutes in live/dead cytotoxicity assay (Invitrogen, L3224) using a concentration of 5 µL of calcein-AM and 20 µL of ethidium homodimer per 10 mL of PBS. After incubation, samples were rinsed twice again using PBS and imaged using an Olympus DP80 microscope. Multiple z-stacks were taken at x10 and x20 magnifications using FITC (488 nm) and TRITC (532 nm) filters. Cell viability and semi-quantification were assessed using Fiji ImageJ software (1.53t version).

In summary, red and green image channels were separated, and three random regions of interest were selected to perform manual cell counting. Average cell survival percentages for each time point were calculated and compared to 3D and 2D controls. This semi-quantification depicted the percentage of dead and alive cells at a specific time point. 3D pellet and 2D HCH control samples were stained, imaged and semi-quantified following the same protocol.

3.3.7 DNA quantification

DNA quantification was assessed using a Quant-iT PicoGreen dsDNA Assay Kit (Thermo Fisher, P7589). 3D bioprinted constructs and 3D cell pellets were mixed with pre-warmed (37°C) protease solution (10 mg/mL) (Sigma Aldrich, P5147-1G) and pipetted up and down until the PeptiInk® or cell-matrix was dissolved. This mixture was then incubated at 37°C for 5 minutes. Sequentially, these samples were mixed with 500 µL of 2X TE Buffer from the Quant-iT PicoGreen dsDNA Assay Kit (Thermo Fisher, P7589) and 1% Triton X in UltraPure™ DNase/RNase-Free Distilled Water (Thermo Fisher, 10977-035). Mixtures were then incubated at 37°C for 30 minutes and placed at -20°C. Samples were subjected to three freeze-thaw cycles before the assay was performed. PicoGreen dye was diluted in a concentration of 1:200 in the 2X TE Buffer. 100 µL from each sample were pipetted in a black/opaque 96 well-plate. An additional 100 µL of the PicoGreen dye solution was added and left for 5 minutes under constant mixing at room temperature. Fluorescence was immediately measured using a plate reader at excitation and emission wavelengths of 480 and 520 nm, respectively. DNA concentration was obtained from these measurements. DNA

percentage change was calculated using the day 0 values as the comparison points. DNA levels on day 0 were set as 100%, and day 7 and day 14 values were computed as percentage changes with respect to day 0.

3.3.8 Histological processing and cryosectioning

3D bioprinted constructs and 3D pellets were washed with PBS for 5 minutes at different time points (day 0, 7, 14) and then fixed overnight at 4°C in 10% formalin solution in neutral buffer (Sigma Aldrich, HT501128). After fixation, samples were washed for 5 minutes in PBS and then left for 3 hours in 30% sucrose (Sigma Life Sciences, S9378) solution in PBS to dehydrate them. They were then submerged in a 50:50 ratio mixture of 30% sucrose solution and OCT (Optimal Cutting Temperature) mounting medium (VWR chemicals, 361603E) overnight at 4°C. Samples were then placed in cryomolds filled with OCT mounting medium and snap-frozen using liquid nitrogen. The samples were cryosectioned, using a ThermoScientific cryotome FSE, in 8 µm thick slices for further immunohistochemistry processing.

3.3.9 H&E staining

Routine haematoxylin and eosin (H&E) staining of 3D bioprinted constructs and 3D cell pellets sections were conducted at time points day 0, 7, and 14 on the cryosections. The first protocol attempts did not show the blueing of the cell nuclei. Therefore, the protocol had to be further optimised.

Excess OCT mounting media was removed by submerging the slides in 70% ethanol. Haematoxylin staining was performed for 10 minutes, and Scott's water was subsequently used to ensure nuclei blueing for 1 minute. Eosin staining was done for 15 seconds, followed by a 30 second distilled water wash and 3 washes in 70% ethanol.

3.3.10 Alcian blue staining

Alcian blue staining was conducted on 3D bioprinted constructs and 3D cell pellet cryosections on days 7 and 14. Cryosections were left to defrost at room temperature for 10 minutes and subsequently immersed in 70% ethanol once to wash the excess OCT mounting medium off. They were then immersed in Alcian blue solution (Sigma Aldrich, B8438-500ML) for 15 minutes. The excess dye was washed off for 5 minutes under tap water. Cell nuclei were stained for 1 minute using nuclear red (Sigma Aldrich, 861251-25G), made with 1 gr of nuclear red in 100 mL of distilled water and 0.1 mL of acetic acid (Fisher Scientific, 11307558). Final washing was performed by dipping sections 3 times in 70% ethanol.

3.3.11 Immunofluorescence labelling

Cryopreserved sample sections were rehydrated for 10 minutes with PBTD (PBS + 1.1% DMSO + 0.1% Tween 20) and subsequently fixed for 10 minutes using 10% formalin solution in neutral buffer. Sections were then blocked for 1 hour at room temperature using 5% bovine serum albumin (BSA) (Sigma Aldrich, A2153) in PBTD.

Primary antibody incubation was performed overnight at 4°C, keeping slides in a humidity chamber. Collagen type-II primary antibody (Invitrogen, PA1-36059) was diluted at a ratio of 1:50; aggrecan primary antibody (Abcam, ab3778) was diluted at a ratio of 1:100; SOX-9 primary antibody (Abcam, ab185966) was diluted at a ratio of 1:100 in the PBTD and 5% BSA solution. All sections were washed in PBS for 5 minutes after primary antibody staining was performed.

Secondary antibody incubation was performed at room temperature. For collagen type-II labelling, the secondary antibody AlexaFluor-488 goat anti-rabbit (Invitrogen, A11008) was incubated for 1 hour at a ratio of 1:200 in PBS. Aggrecan labelling was performed with the AlexaFluor 594 goat anti-mouse secondary antibody (Abcam, ab150116) diluted at 1:200 for 3 hours in PBS. SOX-9 labelling was performed with

AlexaFluor 555 goat anti-rabbit (Invitrogen, A21428) incubated for 1 hour at a ratio of 1:200 in PBS.

For F-actin labelling, phalloidin (Invitrogen, A12381) at a ratio of 1:200 in PBTD with 5% BSA was used and incubated for 2 hours at room temperature.

All sections were then washed for 5 minutes in PBS, and nuclei staining was performed by incubating the sections for 3 minutes at room temperature with DAPI (4′,6-diamidino-2-phenylindole) (Thermo Fisher, 62248) diluted at a ratio of 1:200 in PBS. Further section rinsing was done for 5 minutes in PBS before section mounting with fluoroshield (Sigma Aldrich, F6182). Samples were imaged using an Olympus DP80 microscope.

3.3.12 RNA extraction and Comparative qPCR

RNA extraction of the 3D bioprinted constructs was performed by washing the constructs three times with PBS and digesting the PeptiInks® for 5 minutes at 37°C using a protease solution (10 mg/mL) (Sigma Aldrich, P5147-1G). To initiate RNA extraction, the digested mixture was mixed with the RNeasy lysis buffer from the QIAGEN RNeasy Mini kit (74104, QIAGEN) by centrifugation at 10,000 rpm for 3 minutes. The following steps were performed as specified by the RNA extraction kit manufacturer. RNA extraction of the 3D cell pellets was performed as the RNA extraction kit manufacturer QIAGEN specified. mRNA levels were quantified using a Nanodrop spectrophotometer. cDNA was obtained using the High-Capacity RNA-to-cDNA Kit (ThermoFisher, 4387406) as specified by the manufacturer.

Gene expression levels of collagen type-II (Col-II), aggrecan (AGC), and SOX-9 (SOX-9) were analysed by comparative qPCR using GAPDH (glyceraldehyde-3-phosphate dehydrogenase) as a housekeeping gene. Additional non-chondrogenic markers were also assessed to discard non-chondrogenic behaviour (collagen type-I (Col-I), RUNX2 (runt-related transcription factor 2), ALP (alkaline phosphatase), collagen type-X (Col-X). Primer sequences are reported in Table 3.1. Gene expression fold of change was

calculated by the comparative cycle threshold (CT) method, using the expression levels of the 3D cell pellet as the reference for the $2^{-\Delta\Delta Ct}$ calculation.

Table 3.4. Gene sequences used in the performed comparative qPCR.

Primer name	Forward sequence	Reverse sequence
AGC	5'- GCAGCTGGGCGTTGTCA-3'	5'-TGAGTACAGGAGGCTTGAGGACT-3'
ALP	5'-GGGCTCCAGAAGCTCAACAC-3'	5'-GTGGAGCTGACCCTTGAGCAT-3'
Col-I	5'-TGTGCCACTCTGACTGGAAGA-3'	5'-AGACTTTGATGGCATCCAGGTT-3'
Col-II	5'-GGATGGCTGCACGAAACATACCGG-3'	5'-CAAGAAGCAGACCGGCCCTATG-3'
Col-X	5'-ATGATGAATACAC CAAAGGCTACCT-3'	5'-ACGCACACCTGGTCATTTTCTG-3'
GAPDH	5'- GGAGCGAGATCCCTCCAAAAT-3'	5'-GGCTGTTGTCATACTTCTCATGG-3'
RUNX2	5'-TGATGACACTGCCACCTCTGA-3'	5'-GCACCTGCCTGGCTCTTCT-3'
SOX-9	5'-GGCGGAGGAAGTCGGTGAAGAA-3'	5'-GCTCATGCCGGAGGAGGAGTGT-3'

3.3.13 Statistical analysis.

GraphPad Prism 9 was used for the graphical representation of data and statistical analysis. All graphs show error bars representing the standard deviation. For cell viability semi-quantification and DNA quantification, a two-way ANOVA (analysis of variance) was performed. For comparative qPCR analysis, multiple unpaired t-tests with Kolmogorov-Smirnov test were performed. Statistical significance was calculated with a confidence interval of $p < 0.05$

3.4 Results

3.4.1 HCHs survival and growth post-bioprinting in Alpha1 and Alpha 4

Cell viability in the PeptiInks® post-bioprinting was assessed to ensure embedded HCHs had high survival levels throughout the culture period. After assessing the cell viability short term with non-printed materials (Appendix A3.1), a cell viability study post-bioprinting was undertaken, Figure 3.1A. 2D and 3D pellet controls were observed over 14 days to assess expected cell survival without any PeptiInk®. The 2D culture exhibited the expected cell viability, showing that the cells thrived in 2D culture conditions and proliferated. 3D pellet controls showed high initial viability, which then decreased over the first 7 days with elevated levels of cell death in the cell pellet core. This cell death decreased on day 14, potentially due to the previously observed dead cells degrading and leaving only alive cells.

Cell viability in both Alpha 1 and Alpha 4 post-bioprinting was high. Low levels of cell death were seen on days 7 and 14. However, these qualitative observations were further corroborated through semi-quantification. Cell viability semi-quantification based on the obtained images was performed and confirmed what was observed in the images. Figure 3.1B shows that the cell viability in the 2D control was maintained high (60-100%) with no observable cell death across the 14 days of culture and a significant (* - $p < 0.05$) increase in cell viability from day 0 to day 7. The 3D pellet control showed a significant (*** - $p < 0.001$) decrease in cell viability (~46%) in the first 7 days of culture which then increased non-significantly (~54%). Alpha 1 cell viability was highly affected by the bioprinting process, showing an initial 33% viability, which then increased to 46% on day 7 and increased significantly (* - $p < 0.05$) to ~60% on day 14. Alpha 4 cell viability was less affected post-bioprinting, showing ~87% cell viability, which then decreased to 35% in the first 7 days of culture and escalated to 56% on day 14.
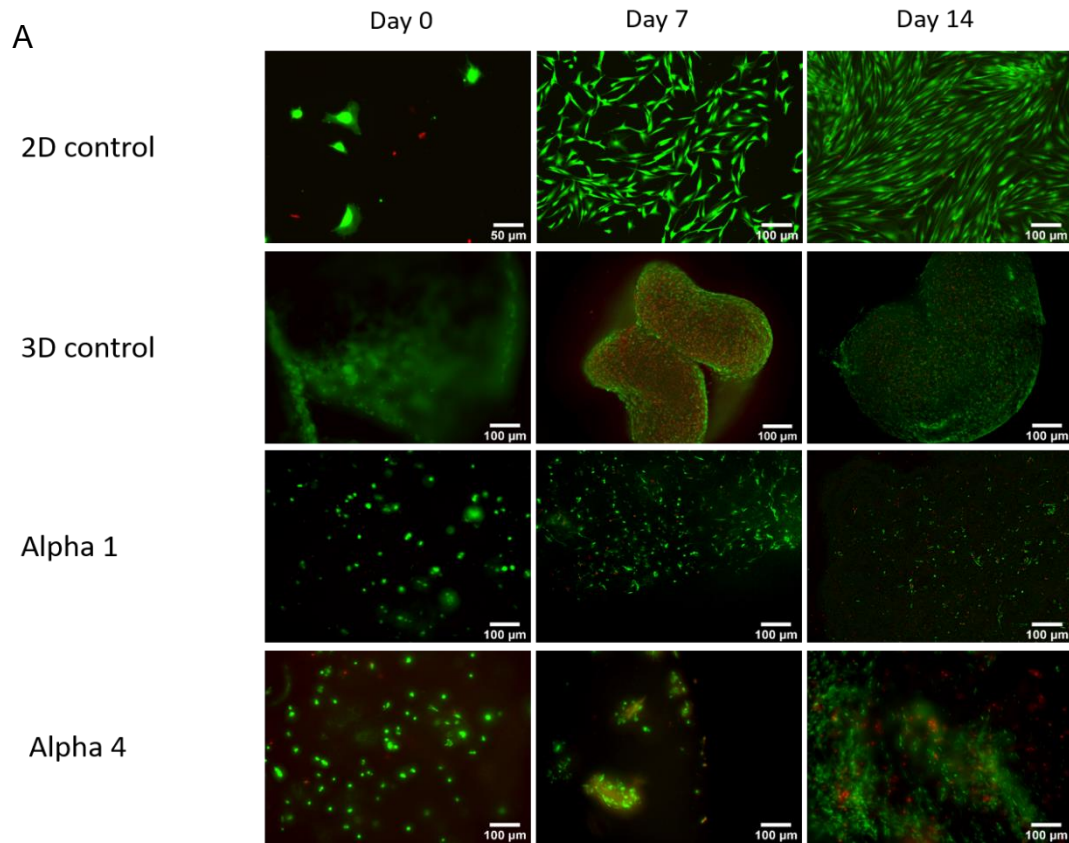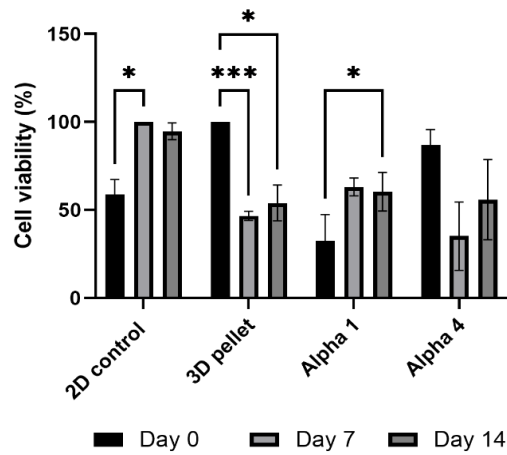
Figure 3.1. A) Live/dead staining of HCHs across 14 days of culture in 2D, 3D pellet control, and 3D bioprinted Alpha 1 and Alpha 4 Peptilnks®. Green shows alive cells, red shows dead cells. B) Cell viability percentage semi-quantification values obtained from the images above. Error bars show standard deviation. Two-way ANOVA was used to compute statistical differences - * - p < 0.05; *** - p < 0.001. N =3. 3D control and Alpha 1 data were previously published by Santos-Beato *et al.* [244].

3.4.2 DNA quantification for cell proliferation assessment

DNA quantification protocols from MBG for the PeptiInks® presented interference issues with the PicoGreen dye and incomplete DNA release from the embedded cells. High standard deviations were observed for individual samples when performing only one freeze-thaw cycle. Further optimisation was performed, and an additional two freeze-thaw cycles were incorporated. Three cycles showed a reduction of the standard deviation and higher levels of DNA. No issues were found when calculating DNA concentrations in Alpha 1, 2D, and 3D pellet control. However, Alpha 4 showed low levels of DNA, as shown in the standard curve, Figure 3.2A. Due to the positive charge of the Alpha 4 PeptiInk®, the DNA may bind to the remaining peptide chains and not the PicoGreen dye, interfering in the measurement.

The DNA quantification results showed an expected increase in DNA levels on the 2D control, Figure 3.2B. 3D pellets showed a significant (**** - $p < 0.0001$) decrease in DNA levels across the 14 days of culture, confirming the cell death observed through live/dead previously. PeptiInk® cultures showed a decrease in DNA in the first 7 days of culture. Alpha 1 showed a significant (* - $p < 0.05$) decrease from day 0 to day 14 but no significant changes from day 7 to day 14. Alpha 4 showed a significant (* - $p < 0.05$) increase in DNA levels from day 7 to day 14. The phenomenon observed in the first 7 days was potentially due to the cells adapting to the PeptiInk® environments, where cells which did not adapt to this unfamiliar environment died. Maintenance of DNA levels after day 7 in Alpha 1 suggested that there was no cell proliferation. However, this PeptiInk® experiences fast degradation when embedded with cells, as shown in Section 3.4.3. This degradation impeded quantifying the DNA changes, as there was no constant volume of PeptiInk® to compare along the culture time. Alpha 4 did not visibly degrade in the first 14 days of culture; therefore, the DNA increase accurately represented the cell proliferation in this PeptiInk® over the second week of culture. Figure 3.2C shows the percentage change in DNA concentration, showing that the 2D culture experienced an increase in cell numbers, triplicating in 14 days of culture. Alpha 4 also showed an increase in cell numbers across the 14 days, with a 200% percentage change on day 14 with respect to day 0. Only Alpha 1 and the 3D pellet showed a reduction in cell numbers. Alpha 1 showed a total reduction of 51%

change on day 14 with respect to day 0. The 3D pellet experienced the highest degree of cell death over the 14 days of culture, with a DNA percentage decrease of 75% on day 14 with respect to day 0.
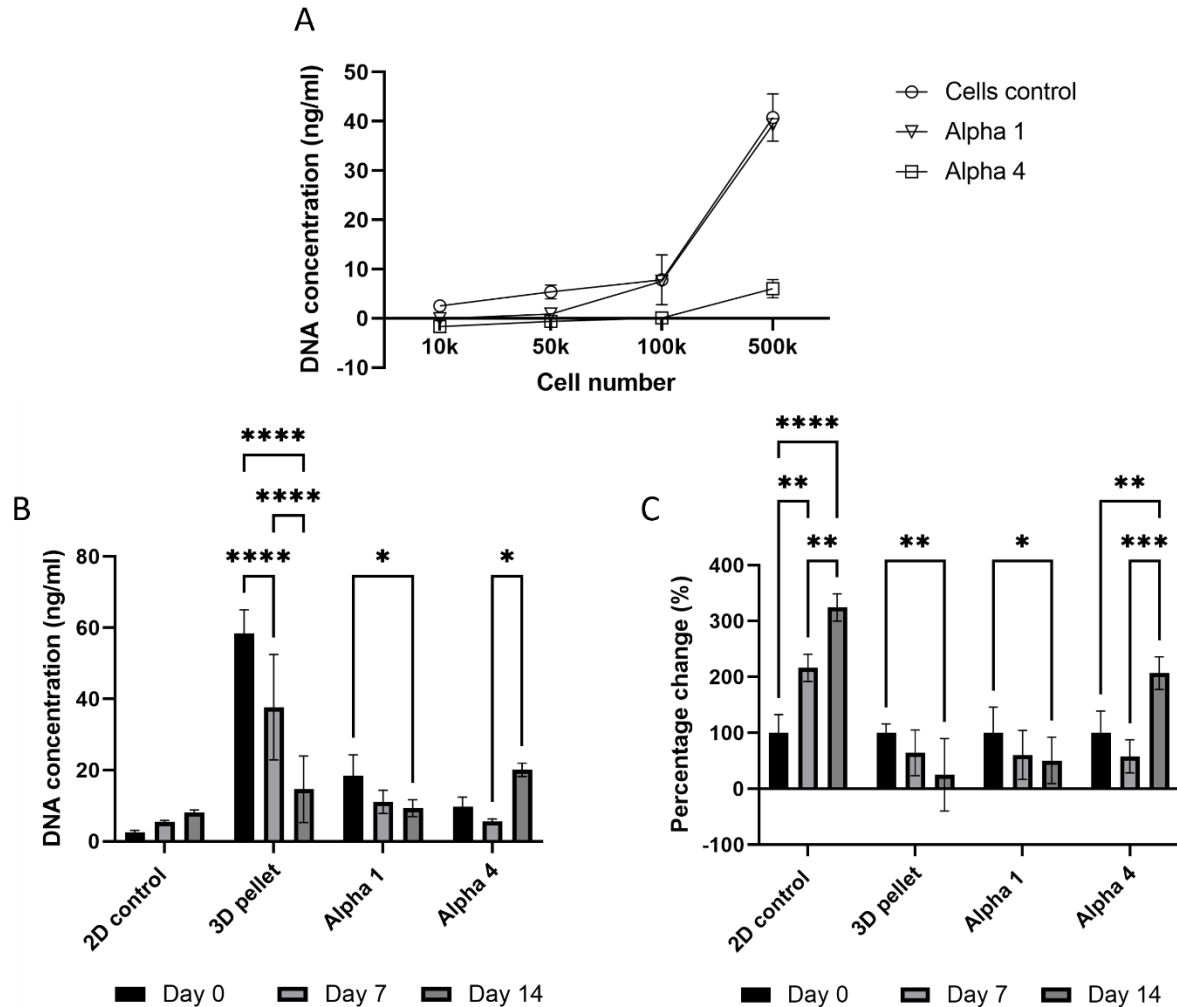
Figure 3.2. A) PicoGreen standard curve of cells control, Alpha 1 and Alpha 4 embedded cells. N = 3. B) DNA quantification obtained with PicoGreen of the 3D pellet control, Alpha 1 and Alpha 4 over the 14 days of culture. N = 3 for the 2D control and Alpha 4; N = 6 for the 3D pellet; N = 9 for Alpha 1. C) Percentage change in DNA quantification over the 14 days of culture. Day 0 is 100% for all samples; values of day 7 and day 14 were computed with respect to day 0. N = 3 for the 2D control and Alpha 4; N = 6 for the 3D pellet; N = 9 for Alpha 1. Two-way ANOVA was performed to assess statistical significance: **** - $p < 0.0001$; *** - $p < 0.001$; ** - $p < 0.01$; * - $p < 0.05$. DNA 3D control and Alpha 1 data were previously published by Santos-Beato et al. [244].

3.4.3 Histological processing optimisation and cryosectioning for histological characterisation of PeptiInks®

Structural information of the embedded cells within the PeptiInks® was assessed through histological stains of PeptiInks® and 3D pellet control sections. An initial wax embedding and sectioning protocol was used. The necessary dehydration steps led to a loss of structural information within the PeptiInks® as they shrunk. The proposed wax embedding method also led to a prevalent delamination of the sample sections from the embedding wax.

An alternative method to ensure cellular structural information was preserved within the PeptiInk® was explored. An OCT-based embedding protocol and subsequent cryosectioning were optimised to ensure minimal PeptiInk® size change and delamination post-processing. Dehydration of the sample using 30% sucrose was performed to facilitate subsequent OCT mounting medium penetration. Both slow-freezing of the samples using dry ice and fast-freezing doing submersion of samples in liquid nitrogen avoided sample delamination and facilitated cryosectioning. Different cutting thicknesses were tested (5-15 μm), and a final thickness of 8 μm showed adequate staining and subsequent visualisation.

3.4.3.1 H&E staining for cell morphology and extracellular matrix deposition assessment

Routine H&E staining was attempted in PeptiInk® samples. Blueing of the nuclei was not observed following this protocol. Therefore, an additional submersion step using Scott's water was introduced. Submersion times were optimised performed to guarantee adequate staining and visualisation of differences between ECM cellular deposition and PeptiInk® material.

H&E staining images, Figure 3.3, showed the expected rounded cell shape in the 3D pellet controls. Cells here appeared compact from day 7, showing a fewer nuclei in the pellet core, further confirming the observed cell death through live/dead staining.

Additionally, from day 7 to day 14, the pellet size growth showed an apparent increase in cell numbers. Images of the 3D pellet on day 0 were not obtained as the 3D cell pellet fully formed after 72 hours in non-adherent culture.

Alpha 1 and Alpha 4 cultures showed a homogeneous distribution of the HCHs on day 0, confirming the expected uniform cell deposition through 3D bioprinting. Cells embedded in Alpha 1 reorganised in cell clusters across the PeptiInk® surface from day 7, larger and more numerous on day 14. The cells in these clusters presented a different cell morphology, being more spread out. Those which remained in the core of the PeptiInk® maintained their chondrogenic round cell shape. Cells present in Alpha 4 had a completely different morphology, being spread out and forming a cell layer in the PeptiInk® surface from day 7. Most cells in Alpha 4 cultures appeared to shift from the centre to the surface of the PeptiInk®. Therefore, only a few cells remained in the core.

Overall, Alpha 1 and Alpha 4 showed extremely different cell behaviours. Alpha 4 had a positively charged nature, which was hypothesised to drive the spread and change in cell morphology, which differed from the observed round shape in the 3D pellet control.
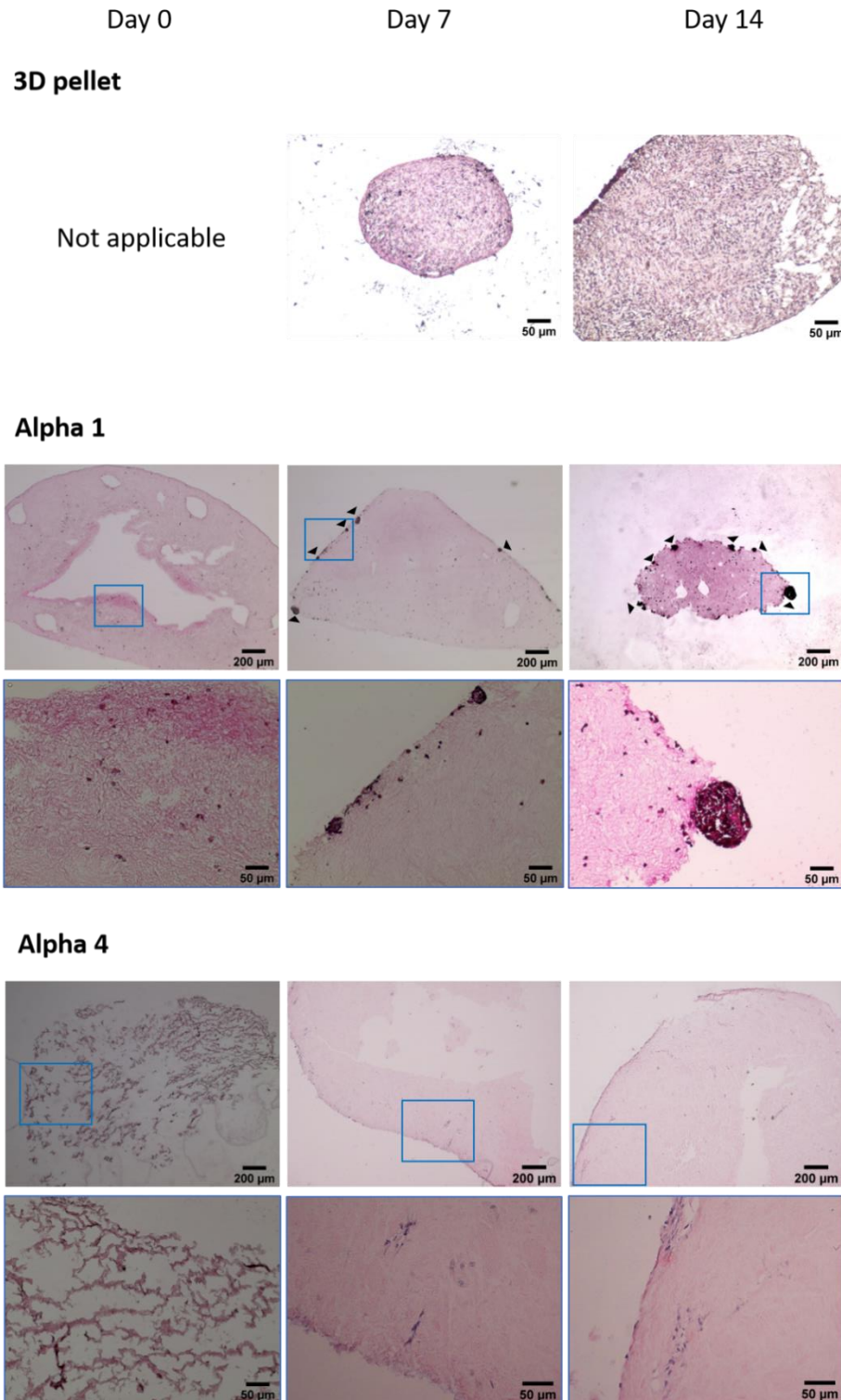
Figure 3.3. H&E staining images of the 3D pellet control, Alpha 1 and Alpha 4 over the 14 days of culture. The top row in each sample shows images at a lower magnification, and the bottom row has higher magnification images corresponding to the highlighted squares in the images above. Black triangles point to the observed surface cell cluster formations in Alpha 1. 3D control and Alpha 1 data were previously published by Santos-Beato *et al.* [244].

3.4.3.2 Alcian blue staining to assess the production of GAGs as a marker of cartilage tissue

Alcian blue staining was performed on sections of the 3D pellet and both Alpha 1 and Alpha 4 PeptiInks® on day 7 and day 14 of culture to assess the production of glycosaminoglycans (GAGs) across the culture period, Figure 3.4. The 3D pellet showed the expected production of extracellular GAGs from day 7 until day 14. Alpha 1 presented no GAGs production on day 7 and initial production inside the cell clusters that appeared on the PeptiInk® surface on day 14. Alpha 4 showed the production of GAGs on the surface, where the cell layer was formed from day 7, becoming more visible on day 14.

Total staining of the PeptiInks® and the 3D pellets was attempted (Appendix A3.2). However, PeptiInk® background staining made it challenging to discern the spatial location of the GAGs production. An Alcian blue retrieval protocol for subsequent quantification through optical density measurement was also attempted. However, all cell-embedded PeptiInks® gave a lower signal than the acellular controls, making it impossible to quantify GAGs production accurately.
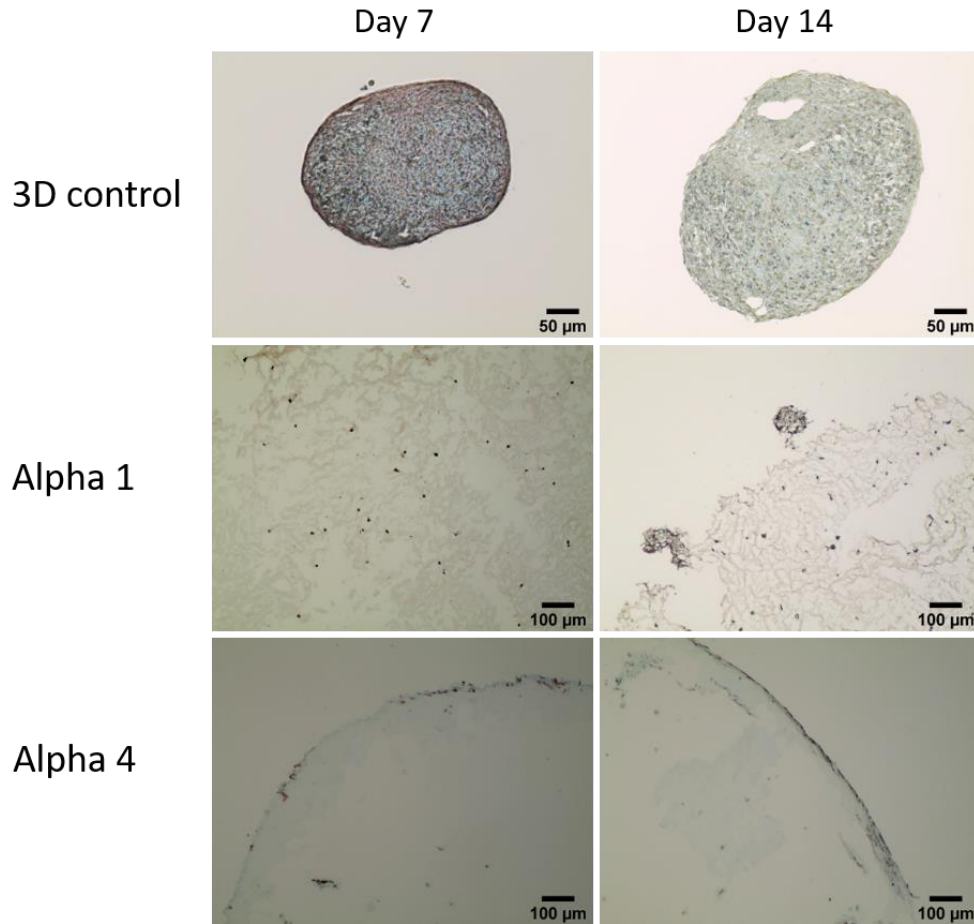
Figure 3.4. Alcian blue staining images of cryosections of the 3D cell pellet, Alpha 1 and Alpha 4 on days 7 and 14 of culture. Blue areas illustrate zones where there is GAGs production. Red dots show the cell nuclei, stained with nuclear red.

3.4.3.3 Histological assessment through immunofluorescence labelling of cartilage-specific and cell morphology markers

3.4.3.3.1 F-actin labelling for cell morphological assessment

F-actin was labelled to visualise further the cellular structure attained across the PeptiInk® culture systems and the 2D and 3D controls. As seen in Figure 3.5, the 2D HCH control labelling depicted how the cultured cells proliferated across the 14 days of culture and presented a spread-out morphology characteristic of cells such as fibroblasts, differing from the chondrogenic expected round cell shape. This further

illustrated how these cells, when cultured in 2D, tend to dedifferentiate and revert to a fibroblastic stage [246–248]; however, to confirm that further tests such as DNA sequencing and FACs (Fluorescent Activated Cell sorting) would be required.

3D pellet F-actin labelling once more confirmed the features observed through H&E staining. A compact arrangement of cells kept their expected circular shape, increased cell numbers over the 14-day culture period, and cell death was observed at the pellet's core.

Alpha 1 and Alpha 4 F-actin labelling also showed the previously observed cell distribution in H&E. Day 0 showed a uniform distribution of cells across the PeptiInks® as well as the expected chondrogenic circular cell shape. Subsequent time points in the Alpha 1 culture showed cell cluster formations, and increased size in the PeptiInk® surface. Alpha 4 subsequent time points depicted the formation of cell sheets in the PeptiInk® surface. These sheets were made of spread-out chondrocytes, which have a fibroblastic morphology. Underneath these densely populated surface cell sheets were HCHs which also presented a fibroblastic morphology and a random distribution.

	Day 1	Day 7	Day 14
2D control			
3D control	Not applicable		
Alpha 1			
Alpha 4			
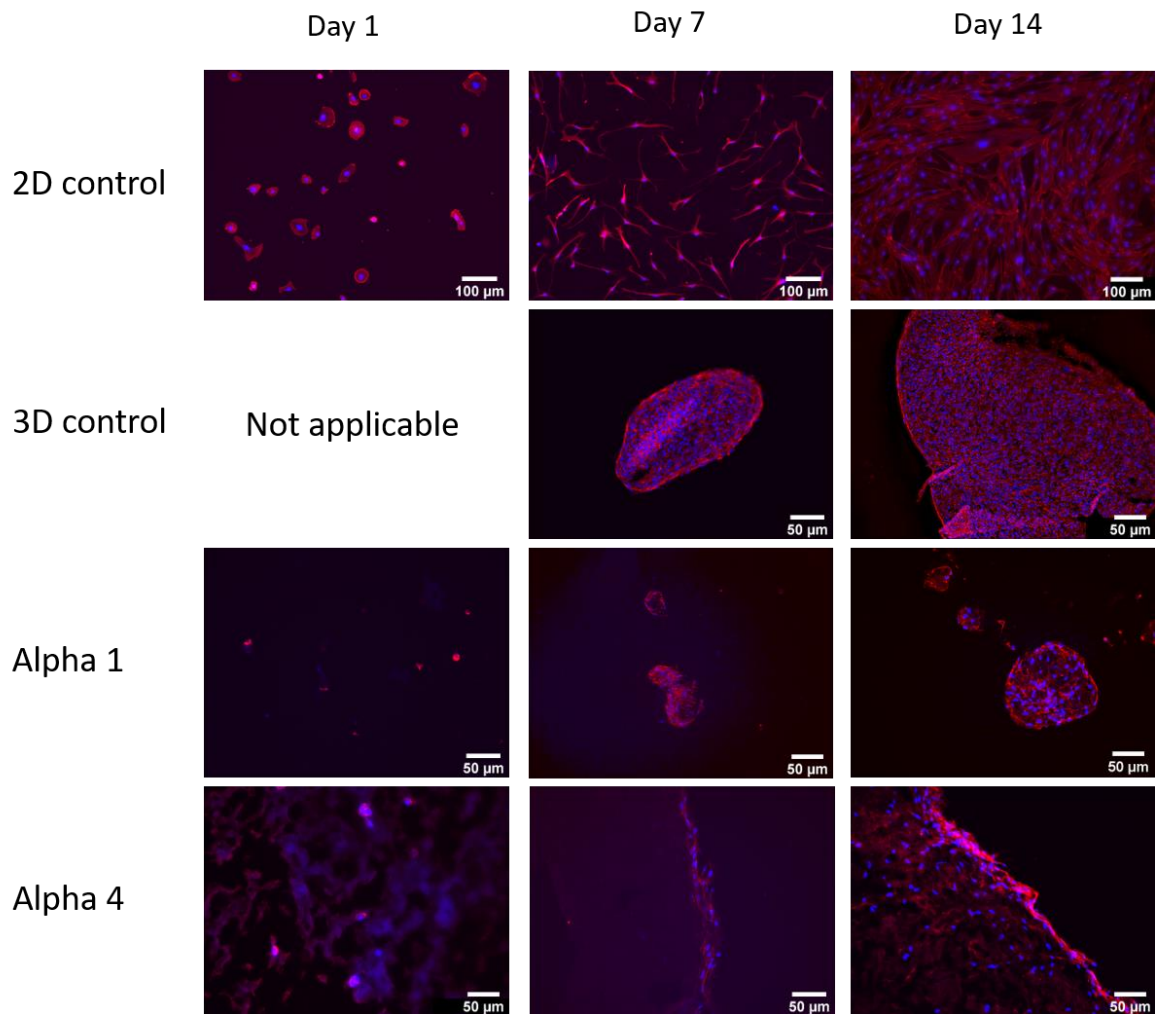
Figure 3.5. F-actin labelling (red) and nuclei (blue) of HCHs in 2D and 3D controls and Alpha 1 and Alpha 4 3D bioprinted structures across 14 days of culture. Day 1 is 24 hours post-bioprinting and cell seeding. 3D pellet control day 1 has no image as there is no pellet formation at this time point.

3.4.3.3.2 SOX-9 labelling to assess the chondrogenic potential of PeptiInks®

SOX-9 was chosen as an early chondrogenic marker, illustrating the initial chondrogenic potential of the PeptiInk® cultures. SOX-9 is an extensively studied pivotal transcription factor for the development of adult cartilage [249]. It has shown *in vitro* and *in vivo* to ensure not only the differentiation of cells into the chondrogenic lineage but also the avoidance of chondrogenic cells to differentiate into different cell types, such as into the osteoblastic lineage [250].

2D control cultures showed no SOX-9 expression, shown in Figure 3.6, indicating that the cells expanded in this culture had a low chondrogenic potential. This explained why their cell morphology appeared fibroblastic. 3D pellet control systems showed SOX-9 expression on day 7 and day 14 of culture. This intracellular and intranuclear expression made it difficult to visualise when labelling cell nuclei with DAPI. The SOX-9 expression decreased from day 7 to day 14. However, further quantification through comparative qPCR was required to confirm this observation.

PeptiInk® cultures presented low levels of SOX-9 expression on day 1 post-bioprinting. SOX-9 expression increased drastically in Alpha 1 from day 7 to day 14, Figure 3.6. Alpha 4 did not present SOX-9 expression, implying a low chondrogenic potential. Based on these initial observations, Alpha 1 showed better potential regarding chondrogenesis, and it was chosen as the material to develop the cartilage *in vitro* model.
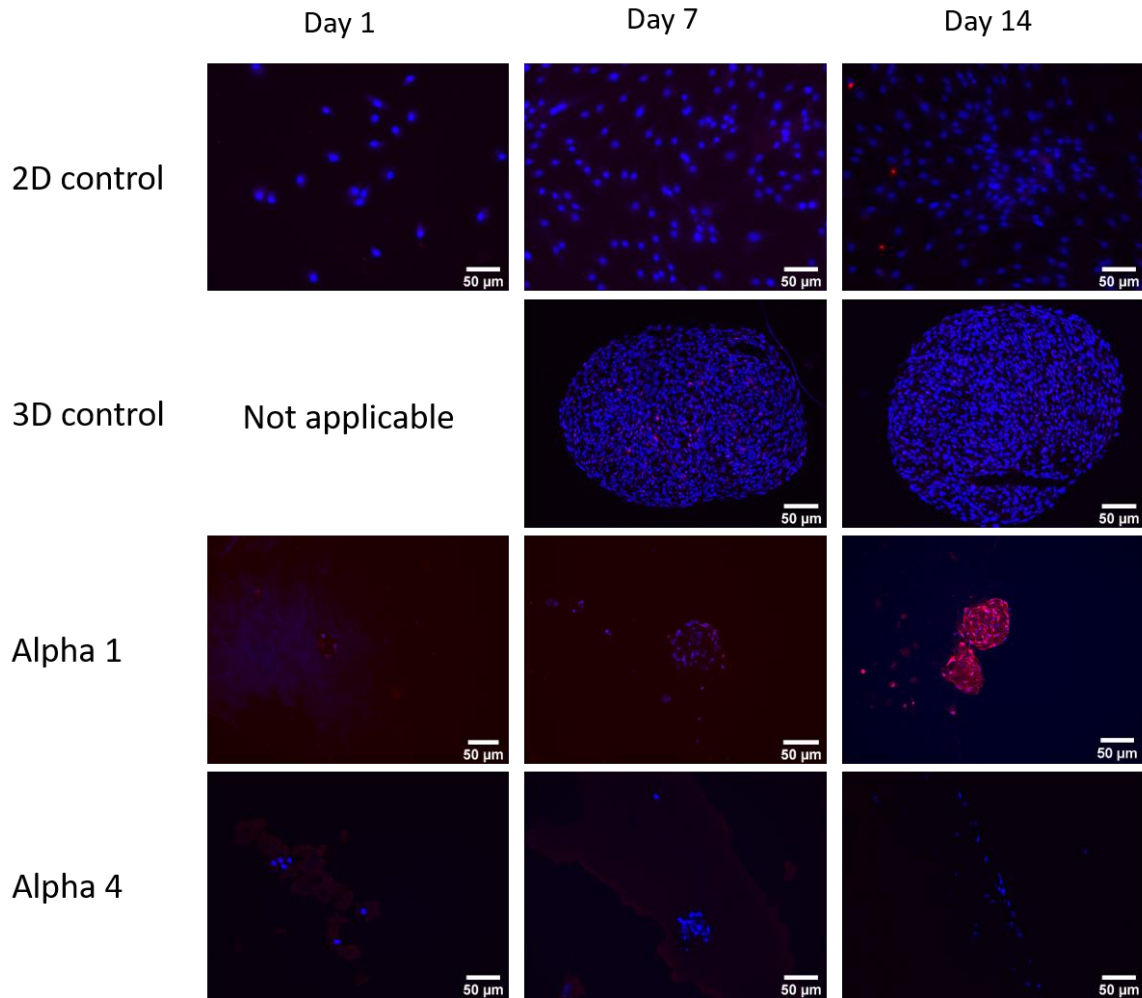
Figure 3.6. SOX-9 labelling (red) and nuclei (blue) of HCHs in 2D and 3D controls and Alpha 1 and Alpha 4 3D bioprinted structures across 14 days of culture. Day 1 is 24 hours post-bioprinting and cell seeding. 3D pellet control day 1 has no image as there is no pellet formation at this time point. 3D control and Alpha 1 day 7 and day 14 data were previously published by Santos-Beato *et al.* [244].

3.4.3.3.3 Collagen type-II and aggrecan labelling to assess primary extracellular matrix cartilage protein production in PeptiInks®

Collagen type-II and aggrecan labelling were performed to assess the expression of later chondrogenic markers. 2D controls showed low levels of collagen type-II both on day 7 and day 14, Figure 3.7. The expression was intracellular and low compared to the 3D pellet. Aggrecan expression was visible from day 1 and increased over the 14 days, Figure 3.8.

The 3D pellet control presented collagen type-II expression on the surface at day 7. The expression increased and spread across the 3D pellet matrix until day 14. These observations contradicted previous research, which stated collagen type-II was initially expressed at the core of the cell pellet and then spread across [251,252]. Aggrecan expression appeared across the 3D pellet from day 7 and was maintained on day 14, which did comply with previous observations [251,252].

PeptiInk® cultures showed different collagen type-II expression patterns. Alpha 1 presented visible expression levels from day 1, which increased across the 14 days of culture, being more prominent in the cell clusters formed on the PeptiInk® surface. Alpha 4 showed no visible collagen type-II and prominent levels of autofluorescence from the PeptiInk® itself. Aggrecan expression had maintained intracellular levels in the Alpha 1 system, whereas Alpha 4 aggrecan expression was observed from day 7 and maintained up to day 14.

These fluorescent antibody labelling protocols enabled quick assessment of the presence of the chosen chondrogenic proteins. However, the nature of some of the antibodies used, such as the polyclonal collagen type-II antibody, could lead to false positives. Additionally, these observations were merely qualitative. To quantify the expression of these proteins, comparative qPCR measurements were done to assess the mRNA expression.
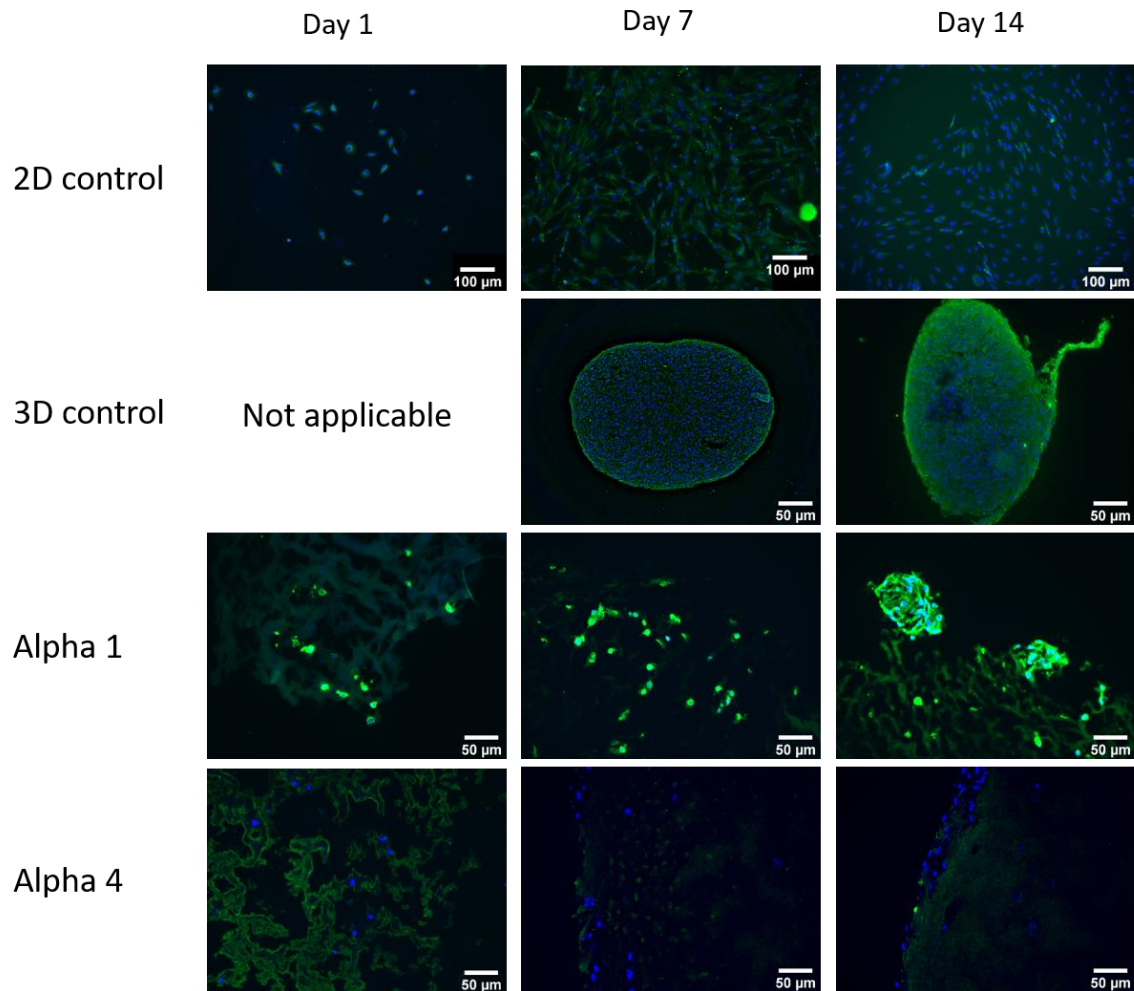
Figure 3.7. Collagen type-II labelling (green) and nuclei (blue) of HCHs in 2D and 3D controls and Alpha 1 and Alpha 4 3D bioprinted structures across 14 days of culture. Day 1 is 24 hours post-bioprinting and cell seeding. 3D pellet control day 1 has no image as there is no pellet formation at this time point. 3D control and Alpha 1 day 7 and day 14 data were previously published by Santos-Beato *et al.* [244].
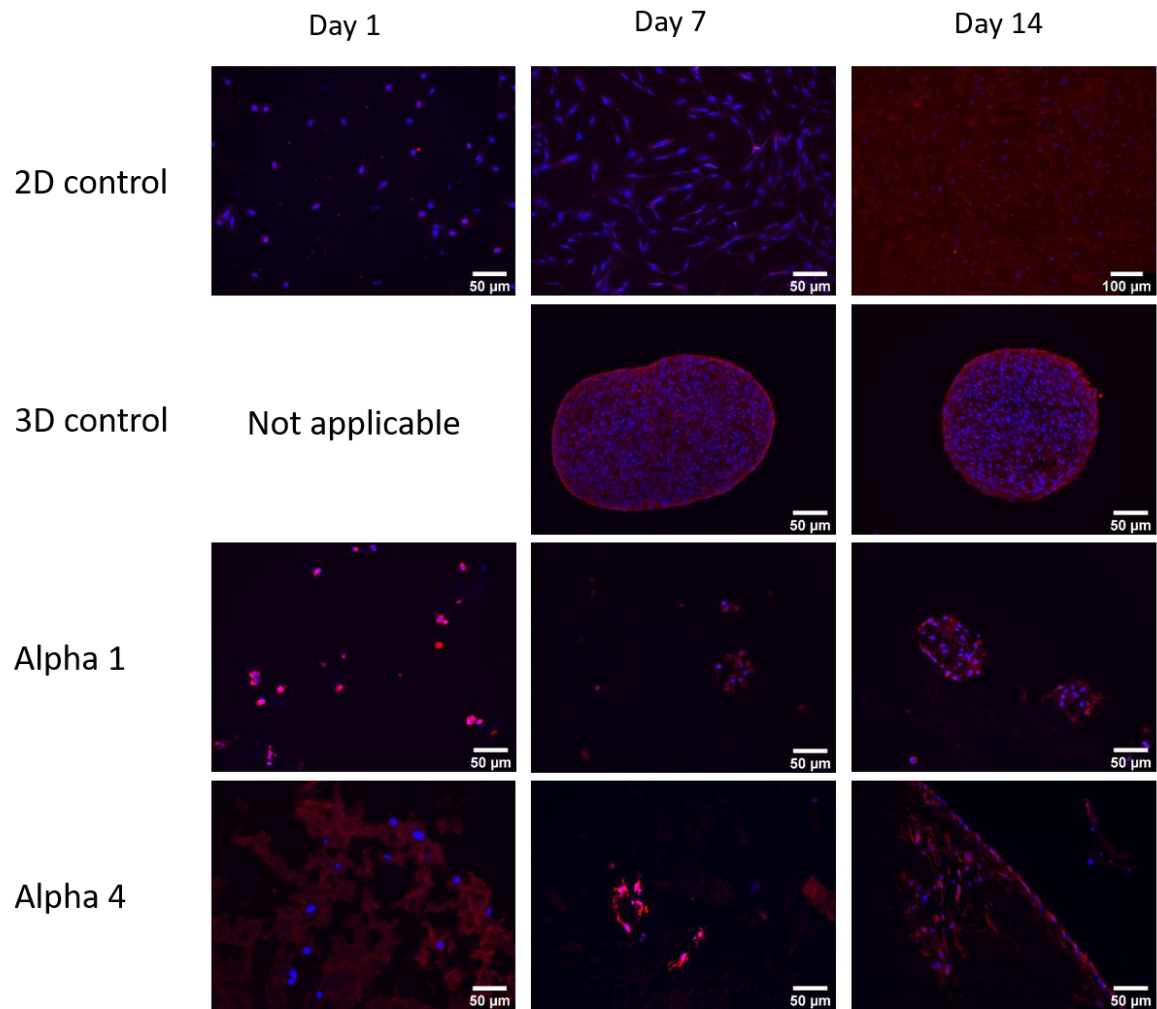
Figure 3.8. Aggrecan labelling (red) and nuclei (blue) of HCHs in 2D and 3D controls and Alpha 1 and Alpha 4 3D bioprinted structures across 14 days of culture. Day 1 is 24 hours post-bioprinting and cell seeding. 3D pellet control day 1 has no image as there is no pellet formation at this time point. 3D control and Alpha 1 day 7 and day 14 data were previously published by Santos-Beato *et al.* [244].

3.4.4 Comparative qPCR analysis to assess chondrogenic mRNA expression of HCHs embedded in PeptiInks®

Comparative qPCR was performed with the GAPDH gene as a housekeeping gene. The analysis was performed by taking the 3D pellet mRNA expression on day 7 or day 14 as the control sample. Markers assessed previously through immunofluorescence labelling (collagen type-II, aggrecan, SOX-9) were assessed to quantify the chondrogenic behaviour of Alpha 1 against the 3D pellet control. Alpha 4 analysis was not performed, as the chondrogenic markers did not show visible expression when assessed through immunofluorescence labelling. Additional osteogenic markers (collagen type-I, RUNX 2 and ALP) and hypertrophic markers (collagen type-X) were also investigated to discard any changes in chondrogenic behaviour.

Firstly, the mRNA expression profile was compared across the "gold standard" time points, using the 3D pellet day 7 profile as a control to assess day 14 mRNA expression. Figure 3.9A shows no significant differences between the two time points in any chondrogenic, osteogenic or hypertrophic markers. There was an upregulation of collagen type-II, aggrecan and SOX-9 expression from day 7 to day 14. However, significance was not observed due to the large standard deviation across samples and the low sample numbers (n =3). These non-significant changes in the 3D pellet control across the 14 days of culture suggested that a potential increase in chondrogenic mRNA expression was expected. However, a larger sample population was required to confirm this behaviour.

Secondly, the mRNA expression profile of Alpha 1 was compared to the 3D pellet control in the first 7 days of culture, Figure 3.9B. Significant (* - $p < 0.05$) upregulation on collagen type-II, aggrecan and SOX-9 mRNA expression was observed in Alpha 1. No significant changes were observed in the osteogenic and hypertrophic mRNA marker expression levels, further confirming the chondrogenic profile of the PeptiInk® embedded cells.

Finally, the expression profile of Alpha 1 on day 14 was assessed by comparing it to the 3D pellet control on day 14, Figure 3.9C. The expression observed in chondrogenic mRNA markers in Alpha 1 showed non-significant changes with respect to the 3D

pellet control. Collagen type-II, aggrecan and SOX-9 mRNA expressions were upregulated with respect to the 3D pellet control. However, the high variability across the Alpha 1 samples on day 14 affected the statistical significance of these observed differences. No significant differences were also observed in the additional osteogenic and hypertrophic markers. This suggested that the embedded chondrocytes maintained their chondrogenic profile and were not reversing into an osteoblastic profile.
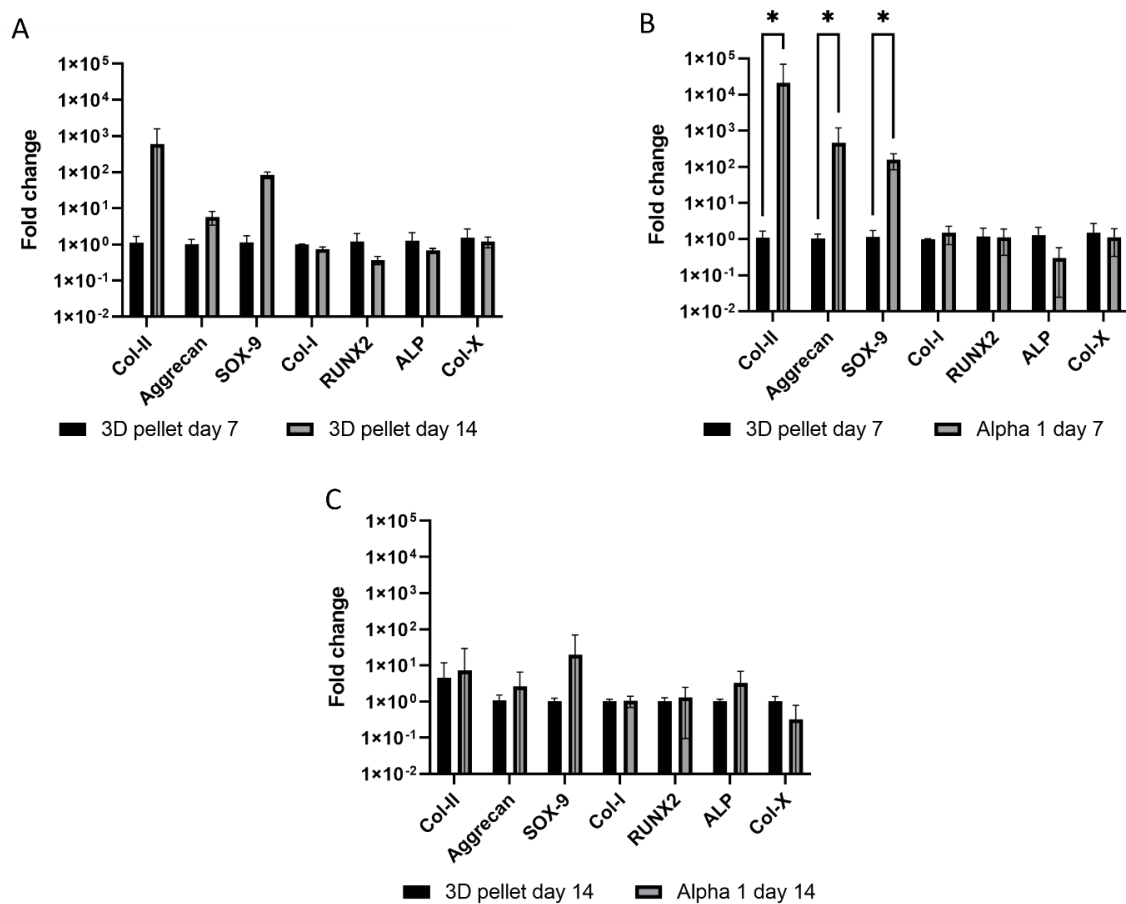
Figure 3.9. A) Comparative qPCR showing fold change in all tested genes across culture time in the 3D pellet control. B) Comparative qPCR showing fold change in all tested genes on day 7. Alpha 1 mRNA expression on day 7 is compared to mRNA expression of the 3D pellet on day 7. Significant differences (* - p < 0.05) are seen in collagen type-II, aggrecan and SOX-9 expression. C) Comparative qPCR showing fold change in all tested genes on day 14. Alpha 1 mRNA expression on day 14 is compared to mRNA expression of the 3D pellet on day 14. N = 3 for the 3D pellet control; N = 9 for Alpha 1. Multiple t-tests with the Kolmogorov-Smirnov test were performed. 3D control and Alpha 1 chondrogenic genes data were previously published by Santos-Beato *et al.* [244].

3.5 Discussion

Developing a human *in vitro* cartilage model is crucial to understand this tissue further and combine it with other tissue models, such as bone, to develop osteochondral tissue models. Moving away from animal-derived materials previously used, such as gelMA [112,235–242] and hyaluronic acid [163,236,241], is vital to address the ethical and sustainability issues that the current models present. Animal-derived materials have advantages such as cell attachment properties and functionalisation. However, they present disadvantages such as batch-to-batch variations and lack of control over the chemical composition. Synthetic materials are a more promising alternative that can be fully tuneable without these issues. PeptiInks® are self-assembling peptide hydrogels which are synthetic, non-animal derived and have no batch-to-batch variations. Two different PeptiInks®, Alpha 1 and Alpha 4, were tested here to investigate their potential use as 3D bioprintable materials for cartilage tissue modelling *in vitro.*

Initial viability tests post-bioprinting of both PeptiInks® showed higher than 50% cell viability after 14 days of culture, Figure 3.1. Initial loss of cell viability in Alpha 1 post-bioprinting suggested that the rheological properties of this material compromised the initial cell survival. However, the loss of early cell viability was overcome in the first 7 days of culture, where viability increased from 33% to 46% and then to 60% on day 14. Alpha 4 on the other hand presented a high post-bioprinting viability (87%) but a lower cell viability maintenance. It showed a cell viability loss in the first 7 days, down to 35%, which then increased again on day 14 to 56%. Cells appeared to adapt and survive or die within the first 7 days, unlike in Alpha 1, where cells seemed to recover in the first 7 days.

Further DNA quantification confirmed the behaviour observed in the live/dead image semi-quantification. A PicoGreen DNA quantification standard curve was developed to assess whether the DNA extraction protocol of the PeptiInk® embedded cells was successfully extracting the DNA material. Additionally, the standard curve enabled the visualisation of any interferences that could arise from the PeptiInks® with the PicoGreen dye. As seen in Figure 3.2A, the DNA material from Alpha 1 embedded

cells was successfully extracted, and the DNA measurements were similar to those of cell suspension controls. This suggested that the neutral charge of Alpha 1 did not interfere with this quantification protocol. Alpha 4 measurements showed that the DNA quantification using PicoGreen was not the best protocol to quantify DNA amounts accurately. It was expected that the positively charged nature of Alpha 4 interfered with the DNA material, which is negatively charged, and competed with the PicoGreen dye, generating a lower signal.

The PicoGreen data showed a steady decline in DNA material in the 3D pellet, confirming the observed cell death from the necrotic pellet core. Alpha 1 and Alpha 4 measurements showed a similar trend: cell death post-bioprinting and then cell recovery over the subsequent 14 days of culture. Alpha 1 measurements accurately represented what was observed in the semi-quantification of the live/dead images. However, Alpha 4 measurements showed discrepancies, especially in the early post-bioprinting results. These differences were observed in the standard curve, where Alpha 4 interfered with the PicoGreen dye. Although exact values cannot be trusted, the overall trend in DNA values corresponded to the semi-quantification values, further confirming the general cell viability changes over the 14 days.

Once cell viability was assessed, histological information of both PeptiInks® and the 3D pellet control was obtained through H&E and Alcian blue staining, Figure 3.3 and Figure 3.4, respectively. H&E stains of the 3D pellet control illustrated the circular shape that HCHs had, the increase in cell pellet size over time, and the production of the extracellular matrix that occurred. Overall, the 3D pellet control images showed that the manufactured control was performing as expected. H&E images also confirmed on day 0 the homogenous distribution of HCHs across the 3D bioprinted PeptiInk® structures. On day 7 these images showed the critical differences observed in both Alpha 1 and Alpha 4. Alpha 1 showed the initial formation of cell clusters on the surface of the PeptiInk®, which increased in size and numbers on day 14. These clusters resembled the structure of the 3D pellet control, suggesting that Alpha 1 promoted and facilitated the cell migration and self-assembling of HCHs into cartilage-like structures. Alpha 4 showed a completely different behaviour where HCHs appeared on the PeptiInk® surface with a spread-out morphology. Over the 14 days,

a cell sheet was formed over the surface of Alpha 4, presenting a cell morphology different from the expected circular chondrocyte cell shape. The migration of these cells towards the surface was potentially due to the higher availability of nutrients and oxygen on the PeptiInk® surface, which was in direct contact with the cell culture medium. Changes in the cell shape were also expected to be due to the charge difference of Alpha 4, which did not promote a chondrogenic fate for the embedded HCHs.

Alcian blue staining showed the expected GAGs production of the 3D pellet control over the 14 days. PeptiInk® Alcian blue images showed complementary information previously seen on the H&E staining. Alpha 1 sections on day 14 showed the presence of surface 3D cell clusters, which had GAGs production within the clusters. No production of GAGs was observed within the PeptiInk®, suggesting that the production of this extracellular matrix component was dependent on the cell configuration and density. Alpha 4 images showed the concentration of the HCHs along the PeptiInk® surface and minimal GAGs production was observed both on day 7 and day 14. This suggested once more that the chondrogenic potential of Alpha 4 was limited and lower than that of Alpha 1.

Further histological information was gathered through immunofluorescence labelling of cellular components such as F-actin filaments and cartilage key markers such as collagen type-II, aggrecan and SOX-9. F-actin labelling, seen in Figure 3.5, confirmed the spread-out morphology characteristic of HCHs expanded in 2D cultures. This morphology was reversed entirely on the 3D pellet control systems, where the HCHs regained the expected circular shape, as seen in Figure 3.5. PeptiInk® images depicted once more the cell homogenous distribution across the PeptiInks® on day 1, and the changes in cell self-assembling between the two PeptiInks® over the 14 days of culture. Alpha 1 showed the 3D cell clusters on day 7 on the PeptiInk® surface, which enlarged on day 14. Alpha 4 showed the spread-out morphology of the HCHs on the PeptiInk® surface and the random distribution of cells below this cell sheet, especially visible on day 14.

SOX-9 is a transcription factor that determines the chondrogenic fate of HCHs, ensuring they maintain their chondrogenic phenotype and do not reverse into

osteogenic lineages [250]. The immunofluorescence labelling of this transcription factor, shown in Figure 3.6, showed that cells in the 2D culture were not expressing SOX-9. Minimal expression was also seen across the different time points of the Alpha 4 embedded HCHs. This low expression profile confirmed that the HCHs in 2D cultures tended to dedifferentiate [246–248]. A similar cell behaviour was expected to occur in Alpha 4 cultures, as the SOX-9 expression was not visible. Low intra-nuclear expression of SOX-9 was observed in the 3D pellet control, especially on day 7. Only the Alpha 1 PeptiInk® culture showed visible levels of SOX-9 expression on the cell surface clusters on day 14, confirming the chondrogenic potential that this PeptiInk® presented.

Although SOX-9 expression is a good indicator of the chondrogenic potential that the different culture systems have, further analysis of late chondrogenic markers is also necessary. Collagen type-II and aggrecan are the main components of the cartilage extracellular matrix [253]. Following a similar pattern as the SOX-9 labelling, 2D cultures and HCHs embedded in Alpha 4 showed a low expression of collagen type-II, Figure 3.7. Aggrecan expression was also low in the 2D culture but was visible in the Alpha 4 culture system, Figure 3.8.

The 3D pellet control showed collagen type-II and aggrecan expression from day 7. Aggrecan expression was constant across the 14 days of culture, being prevalent on the 3D pellet surface and across the matrix. Collagen type-II expression was more prevalent on the 3D pellet surface on day 7 and spread across the matrix on day 14. These observations differed from the previously reported work [251,252]. However, the end product, where the specific matrix proteins were produced across the days of culture, was the expected one. This behaviour was also observed in the cell clusters that appeared in Alpha 1. Collagen type-II was present on the HCHs across the PeptiInk® and primarily expressed in the surface clusters. Aggrecan expression was visible on day 14 of the cell clusters on Alpha 1. Although visible on day 7, the expression highly increased over the second week of culture, following the pattern on the 3D pellet control.

These immunofluorescence images, although informative, give qualitative information. Further quantification was required through alternative measurement techniques such

as comparative qPCR. Alpha 4 had already shown low levels of all chondrogenic markers. Therefore, mRNA extraction and comparative qPCR analysis were not performed in this PeptiInk®. Alpha 1 was chosen as the candidate for cartilage *in vitro* tissue modelling based on the immunofluorescence results. Further characterisation of the chondrogenic potential of Alpha 1 against the 3D pellet control was performed through comparative qPCR.

Comparative qPCR results confirmed the chondrogenic behaviour observed in Alpha 1 and discarded any potential changes towards the osteogenic or hypertrophic lineage. The 3D pellet control results showed the expected chondrogenic behaviour of the 3D pellet across the 14 days of culture. Although the changes were not significant due to the low sample numbers (n = 3), there was a general upregulation of all chondrogenic markers (COL2, ACG, SOX9), suggesting that the chondrogenic potential was increased across the culture time as the cell numbers and 3D pellet size increased. The osteogenic and hypertrophic gene expressions had no significant changes, suggesting no change in the HCHs' genetic expression across the 3D pellet culture time.

Fold changes observed in the Alpha 1 culture against the corresponding 3D pellet time points suggested a faster inducement of chondrogenesis in the Alpha 1 culture with respect to the 3D pellet control, Figure 3.9. In the first 7 days of culture, there was a significant increase (* - $p < 0.05$) in the chondrogenic marker expressions, which became not significantly different on day 14. This suggested that HCHs responded faster to the Alpha 1 culture and reached a phenotypic expression, which was maintained and matched with the "gold standard" expression levels on day 14. No significant changes in osteogenic or hypertrophic markers in either day 7 or day 14 suggested that HCHs maintained the expected phenotypic expression. These results suggested that short-term cultures (7 days) were enough to obtain a chondrogenic behaviour of the embedded HCHs in Alpha 1 cultures.

Although these results were highly encouraging and further confirmed the previously reported capacity of Alpha 1 to promote chondrogenic behaviour [184,185], Alpha 1 presented multiple limitations. The most impactful one is the lack of long-term stability of the PeptiInk® when mixed with cells. Preliminary studies in Appendix A3.4

demonstrated how the PeptiInk® was stable for up to 32 days in acellular conditions but fully degraded by day 21 when mixed with cells. Multiple techniques to slow down the degradation rate of this PeptiInk® were tested without conclusive results. One involved mixing Alpha 1 with different ratios of Alpha 4, which showed excellent stability over long-term cultures. However, the difference in PeptiInk® charges generated a mix of cellular responses, and this approach was discarded. PeptiInk® degradation was hypothesised to be due to an MMP (matrix metalloproteinases)-mediated degradation mechanism. An additional preliminary experiment was set up with ilomastat, a general MMP inhibitor, to address whether suppressing MMPs would slow down the PeptiInk® degradation and affect the chondrogenic behaviour. The overall conclusion from this short-term investigation was that the PeptiInk® degraded at a comparable rate when MMPs were inhibited and that this inhibition compromised the chondrogenic potential of Alpha 1. The lack of changes in PeptiInk® degradation further confirmed a previously tested hypothesis, where PeptiInk® degradation was proved to be cell endocytosis-mediated [254]. HCHs embedded in the ilomastat-treated Alpha 1 cultures also showed no self-assembly and lower chondrogenic expression, suggesting that this treatment is not a recommendable approach to avoid Alpha 1 degradation. Full results can be found in Appendix A3.5.

Despite the observed instability of Alpha 1 when embedded with HCHs, this material showed high cell viability and better chondrogenic potential than Alpha 4. Additionally, comparative qPCR results showed that the mRNA expression of chondrogenic markers was significantly higher after 7 days of culture than the current "gold standard". These observations fully supported the choice of Alpha 1 as the most promising material choice for 3D bioprinting cartilage *in vitro* models.

3.6 Limitations and Future Work

This chapter focuses on developing a 3D bioprinted cartilage tissue model *in vitro* using Peptigels® Alpha 1 and Alpha 4. The presented investigations had multiple limitations, further discussed here.

Firstly, the cells used to develop these cartilage tissue models were primary HCHs. Although these cells were representative of human physiology, they were from one donor. Previous work has highlighted the donor-dependent differences that arise when using primary HCHs [60,255–257]. Therefore, the presented investigations should be repeated with multiple cell sources to perform a more representative investigation. Additionally, the cell viability observed post-bioprinting for Alpha 1 could be improved. These changes in cell viability could be once again donor-dependent or process-dependent. Therefore, in addition to testing multiple cell sources, 3D bioprinting parameters could be further investigated to maximise cell viability. This specific future investigation was also mentioned in Chapter 2, where cell-specific shear stress damage was suggested to improve the computational 3D bioprinting process optimisation.

Secondly, limitations arising from the use of Alpha 1 were prevalent. In the first place, Alpha 1 was found to degrade, when mixed with HCHs, after 14 days of culture. This limited the experimental time frame. An initial investigation to mitigate this degradation using ilomastat, shown in Appendix A3.5, was unsuccessful. However, further investigations should be conducted to slow down this degradation process to enable longer culture times. These extended periods would enable a more mature extracellular cartilage matrix to be secreted by the HCHs and have a better cartilage tissue model.

Thirdly, limitations in the characterisation assays should be assessed and mitigated to understand the manufactured tissue model better. In the first place, DNA quantification using PicoGreen demonstrated interferences when measuring DNA levels in Alpha 4. This was hypothesised to be due to the positive charge of Alpha 4, which would bind to the negatively charged DNA, inhibiting its binding to the PicoGreen dye. Other DNA quantification methods, such as electrophoresis or UV absorbance, should be tested

to find a more accurate and reliable method. In the second place, GAG quantification should be performed to corroborate the information obtained from the Alcian blue staining. Protein extraction protocols should be optimised to quantify the production of these GAGs and other proteins, such as collagen type-II. Although protein extraction was attempted using company protocols, no proteins could be quantified. Therefore, no preliminary data is shown in Chapter 3 or in the Appendix.

Finally, limitations of the RNA extraction protocol were seen in the qPCR results. High standard deviations were observed across some Alpha 1 chondrogenic gene measurements (Figure 3.9). These could be due to differences across samples or limitations arising from the RNA extraction protocol, which would compromise the final qPCR results. Adding a 2D HCH control would enable the comparison between RNA levels. Therefore, the RNA extraction method could be assessed in terms of effectivity. Additionally, native tissue controls would allow for the experimental controls and the tissue models to be compared to *in vivo* samples. This comparison would highlight the key variables that have to be optimised to ensure the manufactured tissue model is improved.

3.7 Summary

Two PeptiInks®, Alpha 1 and Alpha 4, were used to develop *in vitro* cartilage tissue models and compared to a 3D pellet control (current "gold standard") in terms of cell viability, histological features, chondrogenic protein production through immunofluorescence and mRNA expression. Based on these results, Alpha 1 was chosen as the most promising PeptiInk® to manufacture cartilage tissue models *in vitro*.

Alpha 1 and Alpha 4 showed high cell viability for HCHs cultured for up to 14 days. Histological assessments showed that cells formed a cell sheet around the Alpha 4 culture system and had low production of chondrogenic proteins. Immunofluorescence images of Alpha 4 showed its low chondrogenic potential and led to Alpha 1 being chosen as the preferred material for cartilage *in vitro* tissue modelling. Histological assessment of Alpha 1 showed that cells self-assembled into cell clusters similar to the 3D pellet control. Chondrogenic protein production was assessed through immunofluorescence and mRNA expression. Significant upregulation of chondrogenic mRNA levels was observed in Alpha 1 cultures with respect to the 3D pellet.

Alpha 1 was chosen as the preferred material for 3D bioprinting cartilage tissue models *in vitro* and subsequent manufacturing of osteochondral tissue models. Although it presents issues such as long-term stability and fast degradation rate, short-term cultures (7 days) have proven to be enough to obtain chondrogenic behaviour of the embedded HCHs. The development of this cartilage tissue model, alongside the bone-like tissue model results shown in Chapter 4, form the basis of the osteochondral model manufacturing shown in Chapter 5.

Chapter 4: Manufacturing and characterisation of a hydroxyapatite-based scaffold and their evaluation for developing an *in vitro* bone tissue model

4.1 Introduction

Bone tissue is formed of organic and inorganic compounds. Hydroxyapatite (HA) is the main inorganic component, accounting for 65% to 70% of the dry weight of bone [258]. Collagen type-I and water comprise the organic phase of bone [259,260]. The amounts of each phase and additional extracellular matrix proteins vary with factors such as age [261], gender [262] and bone location [263].

Bone is a tissue that can be affected by various diseases such as osteoporosis, osteomalacia, bone tumours or bone cancer. Osteoporosis develops in older populations when the bone mass and mineral density decrease and when the structure and strength of bone change with age [264]. It is highly prevalent, affecting approximately 10 million men and women in the USA [265]. It is often not diagnosed until a bone fracture happens [264], and current treatments focus on slowing down or stopping the loss of bone density but not reversing it [266]. Other diseases affect younger populations, such as osteomalacia, which is characterised by vitamin D and calcium level imbalances due to lack of sunlight exposure and incorrect diet [267], leading to soft and weak bones [268].

Additionally, bone cancer is a rare type [269], which has different survival rates depending on the type of cancer. Chondrosarcoma presents the highest survival, with almost 70% surviving their cancer for 5 years or more after diagnosis. Osteosarcoma, Ewing sarcoma and chordoma have a survival rate which varies between 40 and 55% after 5 years or more of diagnoses [270]. Most importantly, bone is a frequent site of metastasis due to breast or prostate cancers [271].

Overall, bone is subjected to various diseases, requiring further research to find potential cures or understand their onset mechanisms. However, sources of variation in bone characteristics make the choice of a generalised *in vivo* bone model extremely difficult. Alternative approaches have focused on developing *in vitro* bone tissue models to study healthy bone tissue, diseased bone tissue and bone remodelling processes.

Bone *in vitro* tissue models are usually formed of scaffolds, cells and cytokines [272]. Scaffolds provide a 3D temporary structure into which bone cells can form an extracellular matrix and facilitate oxygen and nutrient delivery or waste removal [272]. Multiple techniques such as freeze drying [273–277], solvent casting [275,278] and particulate-leaching [279,280] have been used to manufacture porous structures to develop bone tissue models. However, these approaches lack control over the pores' size, distribution and interconnectivity [272]. 3D printing is considered a promising technique to overcome these limitations, as it enables control over the structure and porosity of the scaffolds during manufacturing.

Current 3D printed bone tissue models have used organic materials such as alginate [31,281–289], collagen [104,281,285], chitosan [282,290] or gelatine [285,287–291]. Some of these have been mixed with HA to account for the predominant inorganic bone compound and increase the compressive moduli and structural integrity of the 3D printed structures [31,104,281,282]. However, the use of these natural materials presents limitations such as poor mechanical properties [282,292–294], high degradation rates [292,293], and limited long-term stability [288,295–302]. Therefore, HA alone has been further investigated to circumvent these limitations whilst developing *in vitro* bone tissue models.

HA has been previously used to 3D print bone models *in vitro.* Investigations regarding HA as the only or main material to 3D print bone models *in vitro* are summarised in Appendix A4.1 Table A4.1. Overall, 3D printing of these HA-based inks enables rapid and consistent manufacturing of bespoke scaffolds. However, it requires long processing times, including sintering, and it must be mixed with sacrificial materials such as polymers to produce controlled architectures. The existing research has demonstrated the capacity of 3D printing HA inks with different techniques, such as

robocasting or extrusion-based 3D printing [303–308] and stereolithography or photopolymerisation-based 3D printing [309–311]. The reported 3D-printed HA scaffolds have porous structures to ensure cell infiltration. Additionally, a cuboidal or square infill pattern has increased the compressive strength [309]. The reported compressive strength of the 3D-printed scaffolds varies drastically from 22.5 MPa [309] to 750 MPa [308]. These are dependent on the sintering temperature and the porosity. Higher sintering temperatures and lower porosities increase compressive strength [308,312].

Finally, HA is exceptionally stable, releasing low levels of calcium ions [304] and increasing its compressive strength after submersion in simulated body fluid [307]. Additionally, this material supports bone-like cell proliferation and osteogenic behaviour in short-term studies (7 days) [305,309–311]. Nonetheless, these investigations have focused on short-term cell cultures with non-human primary cells. Therefore, further studies should focus on the effect of long-term human-based primary cell cultures using these HA scaffolds.

Roopavath *et al.* [303] focused on developing an HA-based ink and optimising the printing parameters to develop bone scaffolds using extrusion-based 3D printing. Multiple infill patterns and densities were assessed [303], and the effect of sintering temperatures on the final scaffold compressive modulus. However, no *in vitro* cell viability or osteogenic potential-focused investigations were performed on these scaffolds. Additionally, there is no reported standardised HA ink preparation protocol. Therefore, a protocol is proposed and used in this chapter for preparing the HA ink. Using this optimised HA composition, this chapter focuses on characterising the rheological properties of this material, the shrinking effect that sintering has on the HA 3D printed scaffolds, and characterising their compressive mechanical properties.

Additionally, this chapter focuses on assessing the HA scaffolds' effect on bone-like cells to develop a simplified bone-like tissue model *in vitro.* A long-term study was performed using different bone-like cells to further develop these previously optimised 3D-printed scaffolds. Saos-2 cells were chosen as a starting point to test and characterise their long-term viability and osteogenic behaviour when seeded on these HA 3D-printed scaffolds. This well-established cell line is used for *in vitro* investigation with various materials [313–316]. It is the least cancerous cell line and has the most

mature osteoblastic behaviour out of other cell lines, such as MG-63 [313]. However, it differs from human osteoblasts in cell size and overexpression of osteogenic genes, such as ALP [313]. Further investigations using primary human osteoblasts (HOBs) were also performed to confirm that these HA scaffolds could be used to develop human bone tissue models *in vitro.*

4.2 Objectives and Hypotheses

This chapter aims to characterise the HA ink for 3D printing scaffolds and investigate the use of these scaffolds to model bone tissue *in vitro.*

Objectives:

1. Characterise the used HA ink for extrusion-based 3D printing through rheological assessment.
2. Physically characterise the HA scaffolds based on their size and compressive modulus.
3. Perform a long-term biological characterisation of the HA scaffolds using 2 cell types: Saos-2 cell line and HOBs.

Hypothesis:

1. An HA-based ink can be used to manufacture scaffolds with mechanical properties similar to bone tissue.
2. HA scaffolds will support cell viability and osteogenic behaviour in the long-term culture of Saos-2 cells and HOBs.

4.3 Methods

4.3.1 HA-based Ink Printability

4.3.1.1 Ink materials and composition

The composition of the HA-based ink was adopted from previously published work [303,312]. Briefly, The HA powder was provided by Ceramysis (Sheffield, UK). Hydroxypropyl methylcellulose (HPMC) (Sigma Aldrich, H7509) was used in a concentration of 1.5% w/vol in deionized water. [312]. The inks were prepared by mixing 1.5% w/vol HPMC with the HA powder at a ratio of 1:2 (HPMC:HA) and mixing manually using a spatula for 10 minutes. Inks were loaded into 3 mL printing cartridges and subsequently used for 3D printing. This HA ink preparation process was developed and standardised as there were no records of ink preparation in previous research [303,312].

4.3.1.2 Rheological characterisation

Rheological analysis of three different batches of HA ink was performed to assess the viscosity of the material and confirm the expected shear thinning behaviour. Oscillatory shear rheometry was performed using a Kinexus pro+ rheometer (Netzsh, Germany). A parallel 40 mm sandblast plate geometry was used with a 0.5 mm gap size. Temperature equilibrium was maintained at 25°C, and a solvent trap was used to prevent the ceramic ink from drying.

4.3.1.3 HA-based scaffold printing process

The HA ceramic ink was used to 3D print scaffolds with a geometry of 10x10x3 mm^3 with a rectilinear infill pattern and infill density of 50%. The printing pressure ranged between 120-200 kPa, and the printing speed between 5-8 mm/s. The printing nozzle used was a 22G needle. The print bed temperature was kept at 60°C to ensure the

deposited filaments dried out and the material spreading was minimised. Scaffolds were printed directly onto a glass Petri dish covered with a silicone mat (Toastbags, silicone baking mat, Sainsbury's). This was the best surface onto which scaffolds could be printed and subsequently detached without scaffold cracking. The width of the deposited HA filaments was quantified following the same method as Section 2.3.2. Four different layer heights were assessed (0.41, 0.25, 0.2, and 0.15 mm), and a final layer height of 0.15 mm was adopted to manufacture all samples.

4.3.2 HA-based scaffold post-printing processing

3D-printed scaffolds were left at 60°C overnight to dry and facilitate their subsequent handling. Scaffolds were then sintered with a Carbolite RHF 1600 furnace. Scaffolds were placed on alumina crucibles (Almath, SUB100100) and sintered at 1320°C. The temperature was ramped up at a speed of 2°C per minute and held at 1320°C for 5 hours. This sintering process had previously been optimised [303], so further optimisation was not required. Before cell seeding, 3D-printed HA scaffolds were autoclaved. The full process is summarised in Figure 4.1.
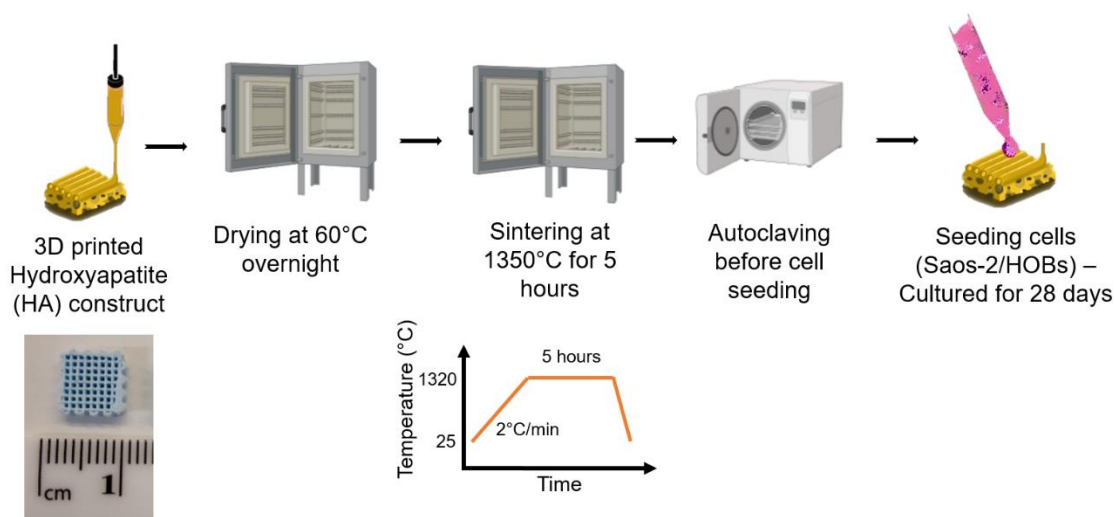
Figure 4.1. Schematic showing the different manufacturing and processing steps for the HA scaffolds. Scaffolds are 3D printed and left overnight at 60°C to dry. Sintering occurs in a furnace with a temperature increase of 2°C/min until 1320°C temperature is held for 5 hours. Scaffolds are then autoclaved, and subsequent cell seeding takes place.

4.3.3 Physical characterisation of HA-based scaffolds

4.3.3.1 Shrinkage post-sintering

3D-printed scaffold images were taken before and after sintering was performed. Fiji ImageJ software (1.53t version) was used to measure the width of the scaffolds in triplicate. A total of 24 scaffolds were measured, and the changes in size were statistically analysed.

4.3.3.2 Mechanical testing

The compressive strength of the sintered scaffolds was investigated using a Zwick Roell Z005 universal testing machine. Compressive tests were performed with a pre-load setting of 1 N and 0.5 mm/min compressive speed. The compression limit was set at 0.5 mm of deformation, 16.6% of the scaffold's height. A total of 7 scaffolds were tested, and their compressive moduli were calculated using the force value at which the first scaffold crack was observed. This first crack was chosen as the "failure" scaffold point.

4.3.4 Biological characterisation *in vitro* of HA-based scaffolds

4.3.4.1 Cell culture and HA-based scaffold cell seeding

Two cell types were used to characterise the 3D-printed scaffolds biologically. Initially, the Saos-2 cell line was used to optimise the characterisation assays and consistently characterise the 3D-printed scaffolds with a bone-like cell line. Subsequently, HOBs were used to prove that these cells could be used to develop a bone model using primary human cells. A summary of the culture conditions is shown in Table 4.1.

Saos-2 cells were used and cultured using αMEM medium (Sigma Aldrich, M6199-500ML) supplemented with 10% FBS (Foetal Bovine Serum) and 1% penicillin-

streptomycin during the expansion process at 37°C and 5% pCO_2. The culture medium was changed every 2-3 days during the cell expansion.

Autoclaved HA scaffolds were pre-conditioned in supplemented αMEM medium overnight and placed in ultra-low adhesion 24-well plates (ScienceCell, 0383). A density of 1×10^5 cells per scaffold was seeded on top of the HA scaffolds in a volume of 50 µL. Scaffolds were left without additional medium for 1 hour to ensure cell attachment. Finally, 1 mL of pro-calcifying medium (αMEM, 10% FBS, 1% penicillin-streptomycin, 50 µg/mL ascorbic acid (Sigma Aldrich, A4544), 2 mM β-glycerophosphate (Sigma Aldrich, G9422), 10 nM dexamethasone (Sigma Aldrich, D4902)) was added per well. Scaffolds were cultured at 37°C and 5% pCO_2. The pro-calcifying medium was changed every 3 days.

HOBs were purchased from PromoCell (PromoCell GmbH, Germany) and cultured using Cell Applications (Cell Applications, San Diego, CA) bone culture media supplemented with 10% FBS and 1% penicillin-streptomycin at 37°C and 5% pCO_2. Supplemented medium was changed every 2-3 days when HOBs were expanded in 2D culture.

HOBs were seeded on pre-conditioned HA scaffolds following the same steps and set-up as with the Saos-2 cells. HOBs were seeded at the same cell density as Saos-2 cells (1×10^5 cells per scaffold). When seeded on top of the HA scaffolds, they were cultured with the medium supplemented with the same previous supplements (50 µg/mL ascorbic acid + 2 mM β-glycerophosphate + 10 nM dexamethasone in supplemented Cell Applications bone culture medium), making the pro-calcifying bone medium, changed every 3 days, at 37°C and 5% pCO_2.

2D control cultures of Saos-2 cells and HOBs were performed in 12-well plates with a seeding density of 1×10^4 cells per well. Cells were cultured at 37°C and 5% pCO_2 with the corresponding pro-calcifying medium and with a medium change every 3 days. All cell culture experiments were performed for 28 days, and the primary time points assessed were day 1, day 14 and day 28.

Table 4.5. Cell culture conditions summary table.

Cell type	Saos-2		HOBs	
Culture set-up	2D	HA scaffold	2D	HA scaffold
Cell seeding density (cells)	1×10^4 per well	1×10^5 per scaffold	1×10^4 per well	1×10^5 per scaffold
Culture time	28 days		28 days	
Expanding cell culture medium	αMEM + 10% FBS + 1% penicillin-streptomycin		Cell Applications bone medium + 10% FBS + 1% penicillin-streptomycin	
Pro-calcifying bone cell culture medium	αMEM + 10% FBS + 1% penicillin-streptomycin + 50 µg/mL ascorbic acid + 2 mM β-glycerophosphate + 10 nM dexamethasone		Cell Applications bone medium + 10% FBS + 1% penicillin-streptomycin + 50 µg/mL ascorbic acid + 2 mM β-glycerophosphate + 10 nM dexamethasone	

4.3.4.2 Cell viability and metabolic activity

Cell viability was assessed through live/dead assay and PrestoBlue measurements at different time points.

Live/dead assay was performed 24 hours post-seeding and on day 14 to assess cell viability over the first 14 days of culture. Samples were washed twice with PBS (phosphate-buffered saline) (Gibco, 20012-019) and then incubated at 37°C for 30 minutes in live/dead cytotoxicity assay (Invitrogen, L3224) using a concentration of 5 µL of calcein-AM and 20 µL of ethidium homodimer per 10 mL of PBS. After incubation, constructs were rinsed twice again using PBS and imaged using an Olympus DP80 microscope.

Cell metabolic activity was measured using the PrestoBlue™ Cell Viability Reagent assay (ThermoFisher, A13261). A 1:10 dilution of this reagent in the pro-calcifying medium was used to incubate 2D and cell-seeded HA scaffolds for 1 hour at 37°C and

5% pCO_2. Acellular HA scaffolds were also incubated and used as blank measurements. Fluorescence was measured at 560 nm excitation and 590 nm emission.

4.3.4.3 Histological Assessment through SEM

Cell-seeded scaffolds at time points day 1, 14 and 28 and acellular scaffolds were fixed overnight at 4°C in 10% formalin solution in neutral buffer (Sigma Aldrich, HT501128). Subsequently, scaffolds were dehydrated with ethanol in increasing concentrations by submerging them for 5 minutes in 6 ethanol concentrations (50%, 70%, 90%, 100%, 100%, and 100%). A gold coater (Polaron Equipment Limited, E5000) was used to gold coat dehydrated scaffolds using 1.25 kV and coating for 90 seconds. Scaffolds were imaged using an SEM (Scanning Electron Microscopy) (Zeiss Gemini) at 3 kV and at two magnifications to assess general cell morphology and cell-specific interaction with the HA particles. Images were processed in Fiji ImageJ software (1.53t version). Cells were highlighted in red using Adobe Photoshop (version 23.2) for ease of differentiation between them and the HA scaffold.

4.3.4.4 Histological assessment through immunofluorescence labelling

Cell-seeded HA scaffolds and 2D cell controls were fixed overnight at 4°C in 10% formalin solution in neutral buffer. Subsequently, collagen type-I and F-actin labelling were performed to assess collagen type-I production and visualize cell morphology.

Samples were rehydrated for 10 minutes with PBTD (PBS + 1.1% DMSO + 0.1% Tween 20) and blocked for 1 hour at room temperature using PBTD and 5% bovine serum albumin (BSA) (Sigma Aldrich, A2153). Primary antibody incubation was performed overnight at 4°C. Collagen type-I primary antibody (Abcam, ab34710) was diluted at a ratio 1:250 in the PBTD and 5% BSA solution. All samples were washed in PBS for 5 minutes after primary antibody staining was performed.

Secondary antibody incubation was performed at room temperature. AlexaFluor-488 goat anti-rabbit (Invitrogen, A11008) was incubated for 2 hours at a ratio of 1:200 in PBS along with F-actin labelling AlexaFluor phalloidin (Invitrogen, A12381) at a ratio of 1:200. All samples were then washed for 5 minutes in PBS and nuclei staining was performed by incubating the samples for 3 minutes at room temperature with DAPI (4′,6-diamidino-2-phenylindole) (Thermo Fisher, 62248) diluted at a ratio of 1:200 in PBS. Further rinsing with PBS was performed for 5 minutes after nuclei staining. Samples were imaged using an Olympus DP80 microscope.

4.3.4.5 RNA Extraction and Comparative qPCR

RNA extraction of the 2D control samples was performed by trypsinising the cells to detach them from the well-plate surfaces. Cell pellets were obtained after centrifugation, and supernatants were discarded. Cell pellets were then processed using the QIAGEN RNeasy Mini kit (74104, QIAGEN).

RNA extraction of the cell-seeded HA scaffolds was performed by washing the scaffolds 3 times with PBS and then mixing the scaffolds with 1.5 mL of TRIzol™ (Thermo Fisher, 15596026) for 10 minutes at room temperature. Scaffolds were slightly crushed with a spatula to ensure the TRIzol was in contact with the cells that had penetrated the micropores of the scaffolds. Submerged scaffolds were vortexed for 10 seconds and the TRIzol was taken and mixed with chloroform in a ratio of 100 µL per 1 mL of TRIzol. The mixture was vortexed for 10 seconds, and then left at room temperature for 1 minute. Subsequent centrifugation at 12,000 g and 4°C was performed for 15 minutes. The aqueous phase was mixed in equal parts with 70% ethanol and processed using the QIAGEN RNeasy Mini Kit.

All extracted RNA was quantified using a Nanodrop spectrophotometer and converted to cDNA using the High-Capacity RNA-to-cDNA Kit (Thermo Fisher, 4387406) for further comparative qPCR analysis. Collagen type-I (Col-I), RUNX2 (runt-related transcription factor 2) and ALP (alkaline phosphatase) gene expression levels were analysed by comparative PCR using GAPDH (glyceraldehyde-3-phosphate

dehydrogenase) as a housekeeping gene. Additional non-osteogenic markers (aggrecan (ACG), collagen type-II (Col-II), collagen type-X (Col-X), and SOX-9) were also assessed to discard phenotypic changes. Primer sequences are reported in Table 3.1 in Chapter 3. Gene expression fold of change was calculated by the comparative cycle threshold (CT) method, using the expression levels of the 2D controls as the reference for the $2^{-\Delta\Delta Ct}$ calculation.

4.3.5 Statistical analysis

GraphPad Prism 9 was used for the graphical representation of data and statistical analysis. All graphs show error bars representing the standard deviation. For metabolic activity measurements through PrestoBlue, a two-way ANOVA (analysis of variance) was performed. For assessing the sintering effect on the sample size, a Welch t-test was performed. For comparative qPCR analysis, multiple unpaired t-tests with Mann-Whitney correction were performed. Statistical significance was calculated with a confidence interval of $p < 0.05$.

4.4 Results

4.4.1 HA ink rheological characterisation and printability assessment

Rheological measurements to characterise the viscosity of the manufactured HA inks were performed for 3 different ink batches. Figure 4.2A shows the viscometry performed with the three different inks. The material behaviour observed was shear-thinning, which explained its ease of printability. The observed low standard deviation depicted that the inks were consistent in terms of their viscosity profile, especially at shear rates higher than 1 s^{-1}.
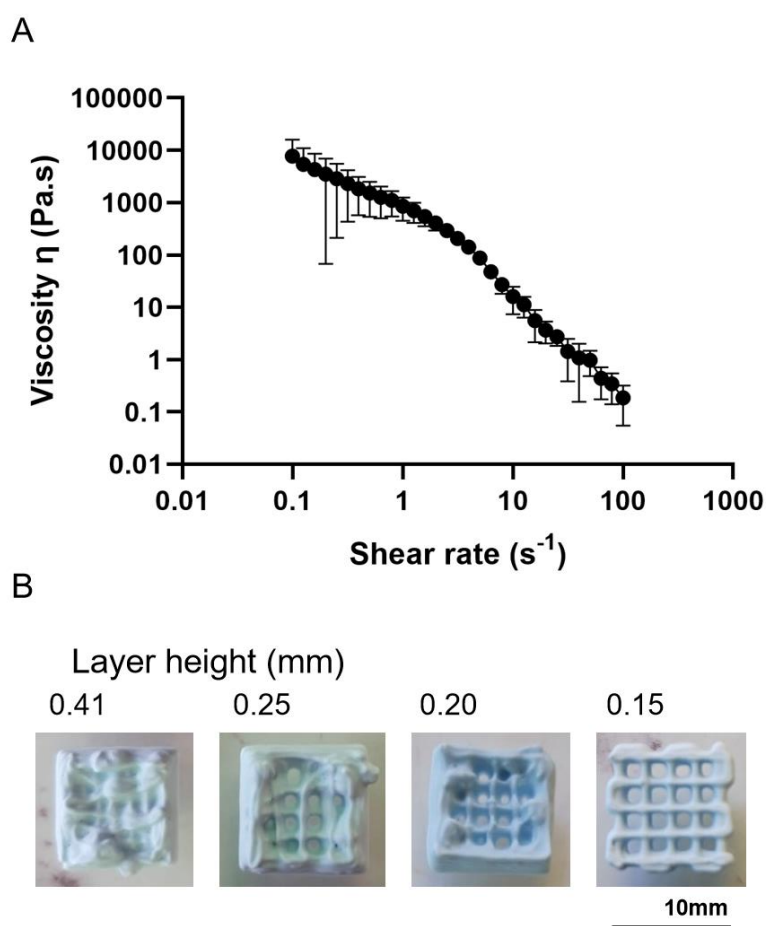
Figure 4.2. A) Viscosity measurements of the HA ink. N =3. Error bars show standard deviation. B) Photographs of 3D printed HA scaffolds with different layer heights (0.41, 0.25, 0.20, 0.15 mm) from Rosanne Roys [317]. The scale bar is 10 mm.

The 3D printing process was optimised firstly in 2D and then in 3D. 2D optimisation focused on optimising the printing speed and the printing pressure. Different printing pressures (120-200 kPa) were tested at two printing speeds (5 and 8 mm/s) to assess the HA filament deposition. The filament width of the HA deposited in 2D was compared to a theoretical filament width value equivalent to the diameter of the printing nozzle. In this case, a 22G needle was used, with a diameter of 410 μm. These filament widths are quantified in Appendix A4.1 Figure A4.1. The 2D quantification showed the expected changes in filament width, where increasing pressure leads to wider filaments and increasing printing speed to thinner filaments. The tested range of pressures and printing speeds was used across the 3D printing of the HA scaffolds. The change of values within these ranges enabled the printer user to ensure filament continuity in case issues such as clogging or excessive material deposition happened. The 3D optimisation was performed by testing different printing layer heights. Figure 4.2B shows images of the scaffolds manufactured at different layer heights. The optimal layer height of 0.15 mm was chosen as it enabled the production of the scaffolds with the expected pores. The infill density of 50% was chosen following previously reported investigations, which described it as the optimal infill density for cell infiltration and higher compressive modulus [303,312,318].

4.4.2 Physical characterisation of HA scaffolds

4.4.2.1 Quantification of the sintering effect on scaffold size

The sintering process, by which these scaffolds were subjected to very high temperatures for long periods, generated the fusion of the ceramic particles. Scaffolds are, therefore, expected to shrink. Here, the width and length of 24 samples were measured before and after sintering to quantify the effect on scaffold size. As seen in Figure 4.3A, there was a significant (**** - $p < 0.0001$) difference between the pre-sintered and the post-sintered scaffolds, with a decrease of 15%. This graph, Figure 4.3A, also illustrates the printing reproducibility across the pre-sintered scaffolds. These scaffolds presented less than 0.1 cm (10%) differences across their length, further confirming the consistency and accuracy of the manufacturing technique.

4.4.2.2 Mechanical characterisation of HA scaffolds through compressive testing

The compressive strength of the scaffolds was assessed through compressive testing. For this investigation, the "failure" point of the scaffolds was determined to be the point at which the first scaffold crack appeared. The force corresponding to this initial failure was used to compute the compressive modulus. As seen in Figure 4.3B, an average of 0.28 MPa was obtained across the 7 analysed samples, which fell close to the lower range limit of trabecular bone compressive strength (0.22 to 10.44 MPa) [319].
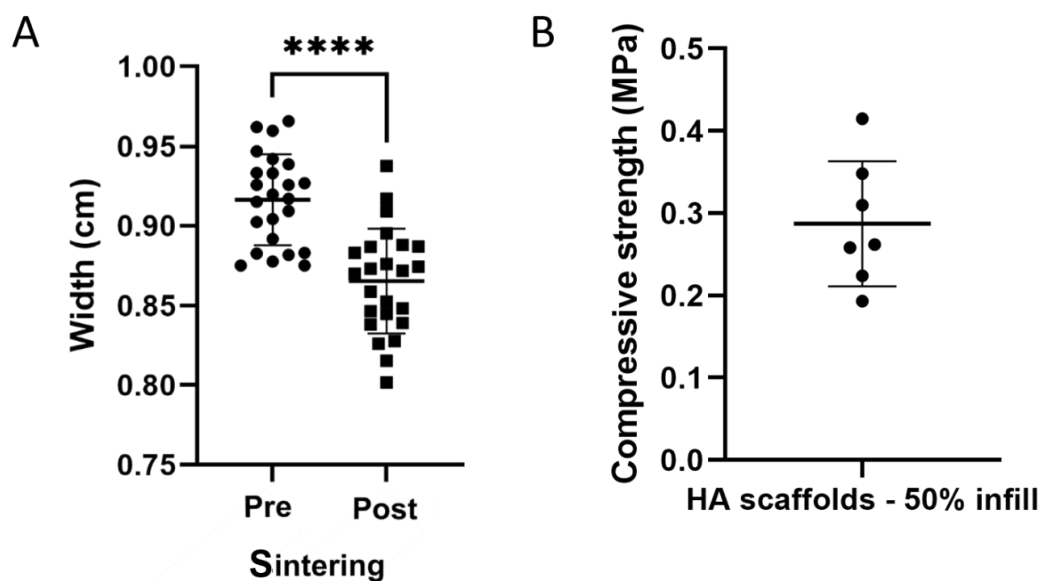
Figure 4.3. A) Scaffold width measurements before (pre) and after (post) sintering process. N = 24. Welch t-test was performed for statistical significance (**** - p < 0.0001). B) Compressive moduli of 50% infill HA scaffolds post-sintering. N=5. Error bars show standard deviation.

4.4.3 Biological characterisation

HA scaffolds were biologically evaluated using 2 different cell types: Saos-2 cell line and HOBs. Saos-2 cells were a starting point to test and characterise their long-term viability and osteogenic behaviour when seeded on the HA 3D printed scaffolds. It is a cell line which presents the least cancerous phenotype out of other bone-like cell lines [313], such as MG-63, and has the most mature osteoblastic behaviour [313]. It differs from bone, with smaller cell sizes and overexpressing osteogenic genes, such as ALP [313]. Fast cell proliferation and high expression levels of osteogenic proteins such as collagen type-I, RUNX2, and ALP were expected to be observed when seeded onto HA scaffolds. HOBs were also used to confirm that these HA scaffolds could be used to develop human bone tissue models *in vitro.* Slower proliferation and lower mineralisation levels were expected when seeding HOBs on HA scaffolds compared to Saos-2 cells.

4.4.3.1 Saos-2 cell viability and metabolic activity assessment

Cell viability of the Saos-2 cells seeded on HA scaffolds was assessed through live/dead staining and metabolic activity measurements. Figure 4.4A shows both the 2D control and the HA scaffold on day 1, 24 hours post-cell seeding and on day 14. These photos showed that Saos-2 cells attached to the HA scaffold from day 1 proliferated and covered the scaffold over the first 14 days, presenting minimal cell death. A similar and expected behaviour was observed on the 2D controls, where cells proliferated and grew on top of one another.

Figure 4.4B depicts the metabolic activity measured across the 28 days of the experiment. A significant increase in metabolic activity from day 1 to day 28 was observed in both HA scaffolds and 2D control samples. The 2D control showed a negative fluorescence value on day 1, potentially due to the minimal time given for the cells to attach and metabolise. This was then significantly (*** - $p < 0.001$) increased on day 14 and even more (**** - $p < 0.0001$) on day 28 with respect to day 1. However,

there was no significant difference between day 14 and day 28, suggesting minimal metabolic changes in the cells of the 2D control during the second week of culture.

The HA Saos-2 cell-seeded scaffolds presented a significant increase in metabolic activity from day 1 to day 14 (** - $p < 0.01$) and to day 28 (*** - $p < 0.001$), being significantly different as well between day 14 and day 28 (* - $p < 0.1$). This increase in metabolic activity, alongside the live/dead images, confirmed an increase in cell numbers on the HA scaffolds across the 28 days of culture and that the cells were metabolically active. The metabolic activity was lower on the HA scaffolds than on the 2D control. Further DNA quantification would be necessary to normalise these metabolic activity levels and understand if these differences are due to cell numbers or substrate-dependent changes in metabolic activity.
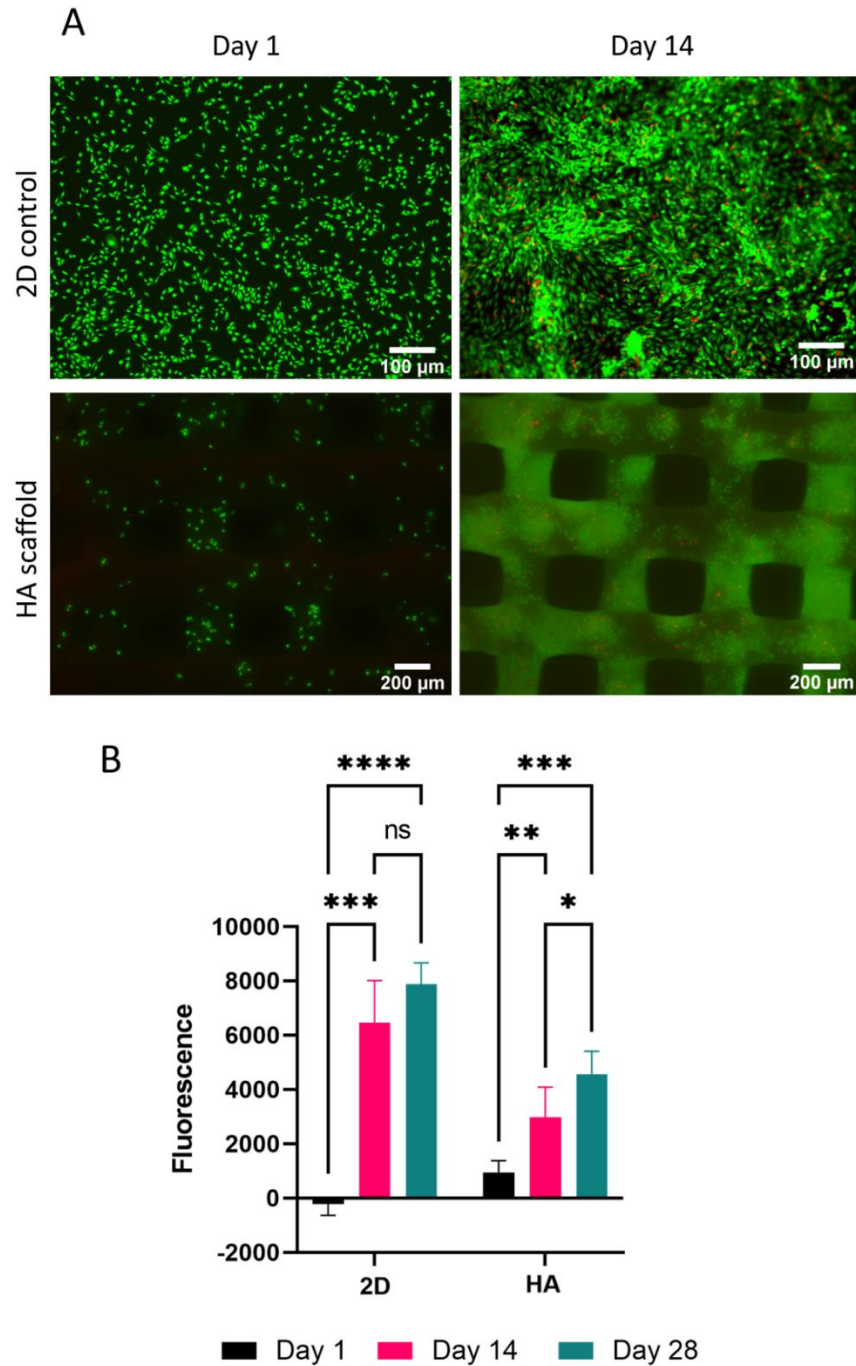
Figure 4.4. A) Live/dead staining of Saos-2 cells on a 2D culture well plate (2D control) and seeded on HA scaffolds; on days 1 and 14. Green shows alive cells; red shows dead cells. B) Metabolic activity measured through PrestoBlue assay of Saos-2 cells seeded on 2D or HA scaffolds measured on days 1, 14, and 28. N = 6. Error bars show standard deviation. Two-way ANOVA was performed; (* - $p < 0.05$; ** - $p < 0.01$; *** - $p < 0.001$; **** - $p < 0.0001$).

4.4.3.2 Saos-2 – HA cell-material interaction assessment through SEM

SEM imaging was used to analyse the morphology of the Saos-2 cells further when seeded on top of HA scaffolds, as well as their scaffold coverage over time and location within the micropores of the HA scaffolds. Overall, it was used to visualise the interaction between the cells and the ceramic particles.

Figure 4.5 shows low and high-magnification images of the HA scaffold surface seeded with Saos-2 cells. On day 1, cells are seen to adapt to the HA particles, maintaining a spread morphology, visible in the higher magnification day 1 image. After day 14, Saos-2 cells formed a monolayer cell sheet across the top surface of the HA scaffold particles. The higher magnification day 14 image depicts tight cell interactions with minimal gaps between cells. This cell monolayer surface coverage increased on day 28, clearly seen in the higher magnification images. However, on the higher magnification image, it is observed that the cells were appearing in between cell particles and growing on top of each other. Assessment of potential mineralisation could not be performed through alizarin red staining, as the scaffold composition interfered with the dye and could not be distinguished from new mineral deposition. This is shown in Appendix A4.2.
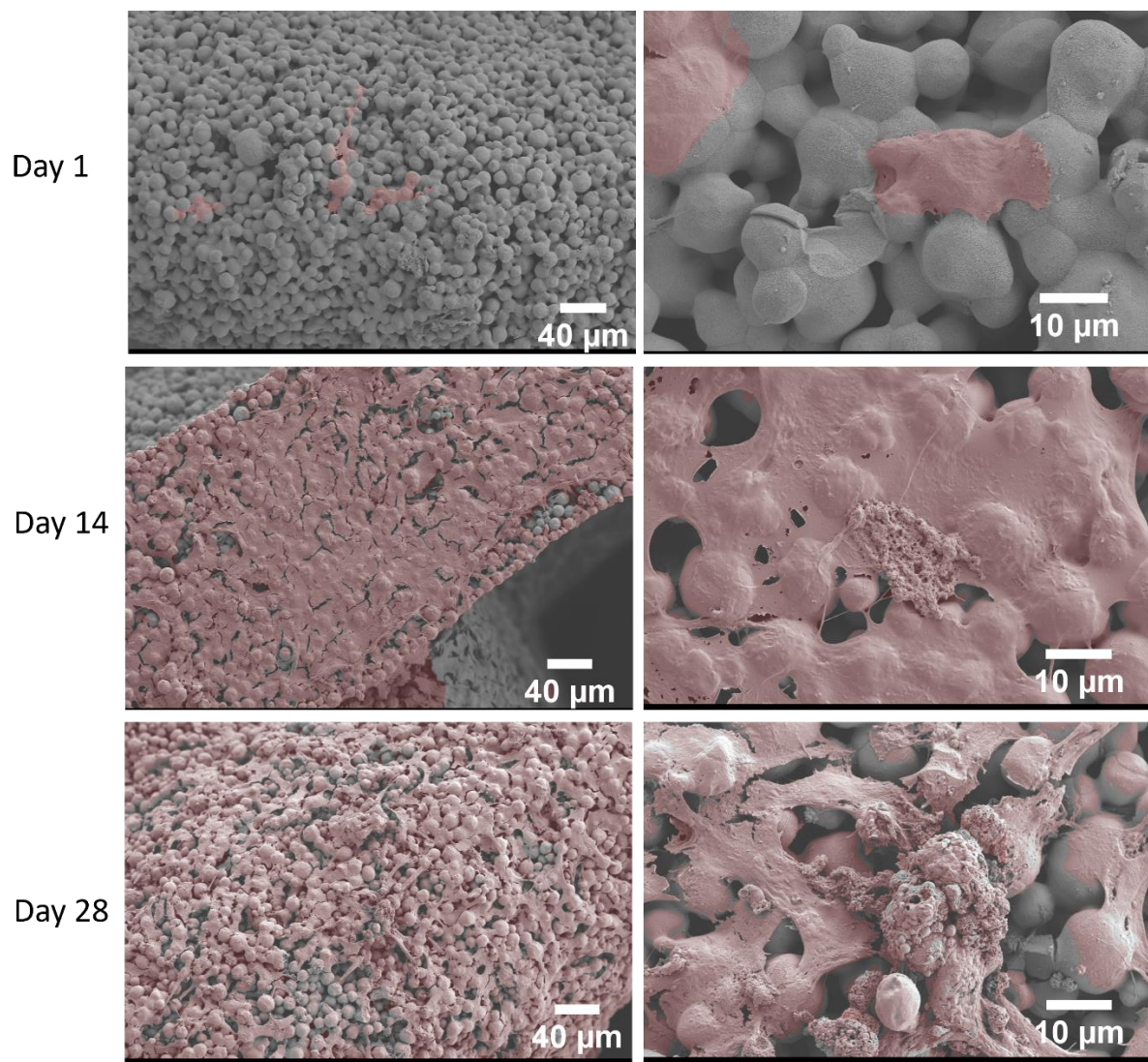
Figure 4.5. SEM images of Saos-2 cells seeded on HA scaffolds on day 1, day 14, and day 28. Left column: images taken at a lower magnification depicting the cell coverage. Right column: images taken at a higher magnification to depict cell-specific response and bone nodule formations. Cell proliferation and scaffold coverage can be seen in the initial 14 days. Additional cell growth on top of existing cells can be observed from day 14 to day 28. Cells were highlighted manually using Adobe Photoshop (version 23.2).

4.4.3.3 Assessment of Saos-2 cells through immunofluorescence labelling

Collagen type-I is a principal bone matrix constituent alongside the HA mineral phase. Collagen type-I immunofluorescence labelling was performed to assess the production of this extracellular matrix protein. As expected, day 1 images show in both 2D control samples and HA scaffolds that this protein had a minimal extracellular expression, Figure 4.6. From day 14 onwards, the levels of collagen type-I, labelled in green, increased. On day 28, the expression of collagen type-I was seen extracellularly. The fluorescence levels were higher on the HA scaffold than on the 2D control, which only appeared on cell clusters. This was expected to be due to the differences in cell density.
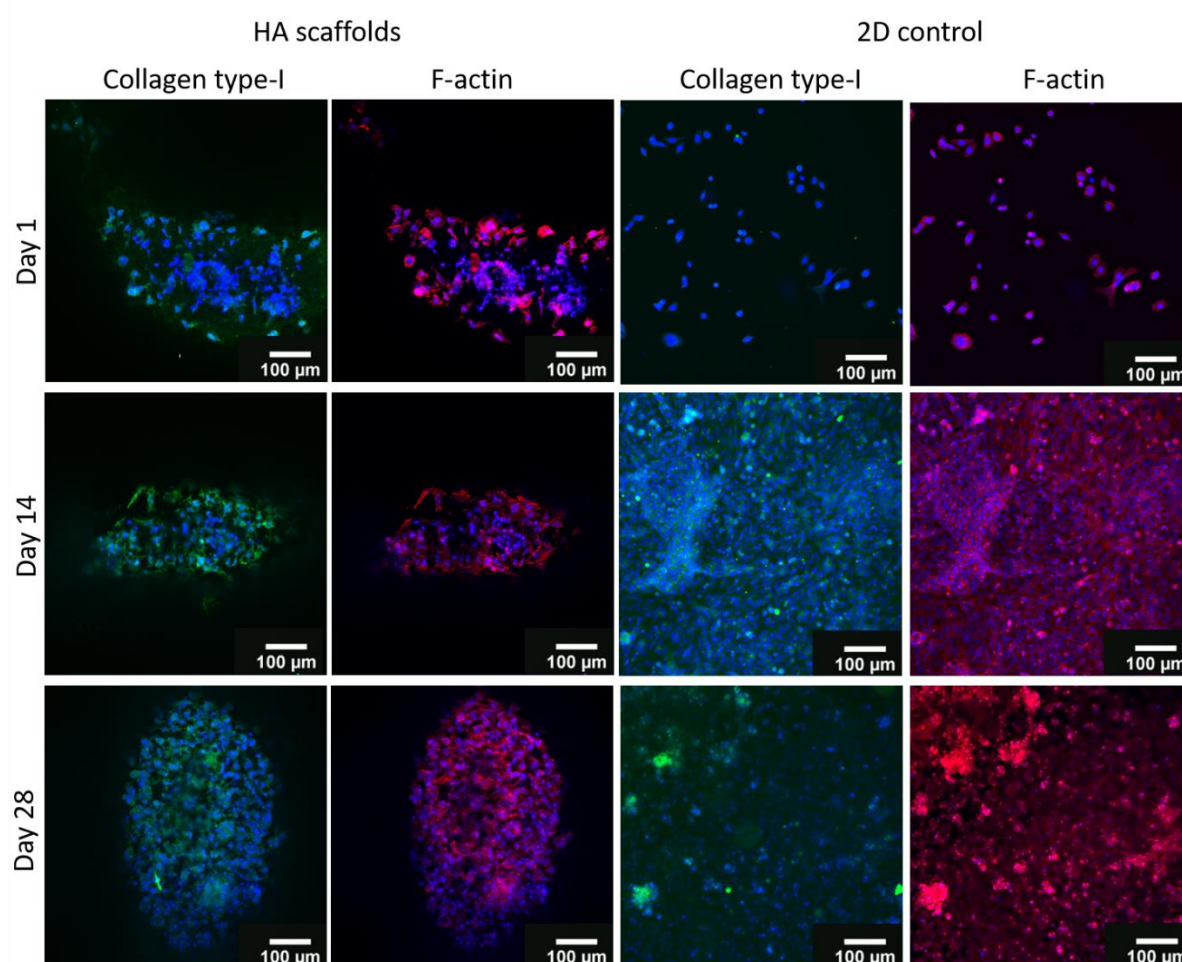
Figure 4.6. Immunofluorescence labelling of collagen type-I (green), F-actin (red) and DAPI (nuclei in blue) of Saos-2 cells seeded on a 2D well-plate or a HA scaffold. Images are taken on day 1, day 14, and day 28. Negative labelling controls are shown in Appendix A4.3.

4.4.3.4 Saos-2 Comparative qPCR analysis to assess osteogenic mRNA expression

Further quantification of osteogenic mRNA expression was performed through comparative qPCR analysis at two different time points, day 14 and day 28. All analysed genes were compared to a housekeeping gene (GAPDH), and the comparative qPCR was performed with respect to the 2D control on the specified time point. In Figure 4.7A, there was a significant (* - $p < 0.1$) difference between the 2D control and the HA constructs for the osteoblastic markers (Col-I, RUNX2 and ALP). These suggested that the HA constructs promoted osteoblastic behaviour further than the 2D control conditions. The observed ALP expression was also highly different, showing a 100-fold increase in the cells seeded onto the HA constructs on day 14. It has been previously reported [313] that these cells overexpress specific markers, including ALP. However, this 100-fold difference showed that the HA construct promoted the expression of ALP mRNA expression and, therefore, the mineralisation potential of these cells when seeded on these scaffolds.

No significant changes were observed across the chondrogenic genes, confirming that these cells were not experiencing phenotypic changes. It was surprising to see that there was a significant downregulation of collagen type-X expression when Saos-2 cells were cultured on HA scaffolds instead of 2D controls on day 14. The downregulation of this mRNA expression suggested that the HA scaffold further promoted the osteoblastic behaviour of Saos-2 cells than the 2D control culture.

Day 28 comparative qPCR results showed no significant differences across any markers, Figure 4.7B. Although the differences in expression were not significant, there was a general upregulation of collagen type-I, and ALP expression of Saos-2 cells seeded on HA scaffolds. These again suggested that the HA scaffold promoted bone maturation, characterised by collagen type-I and ALP expression.
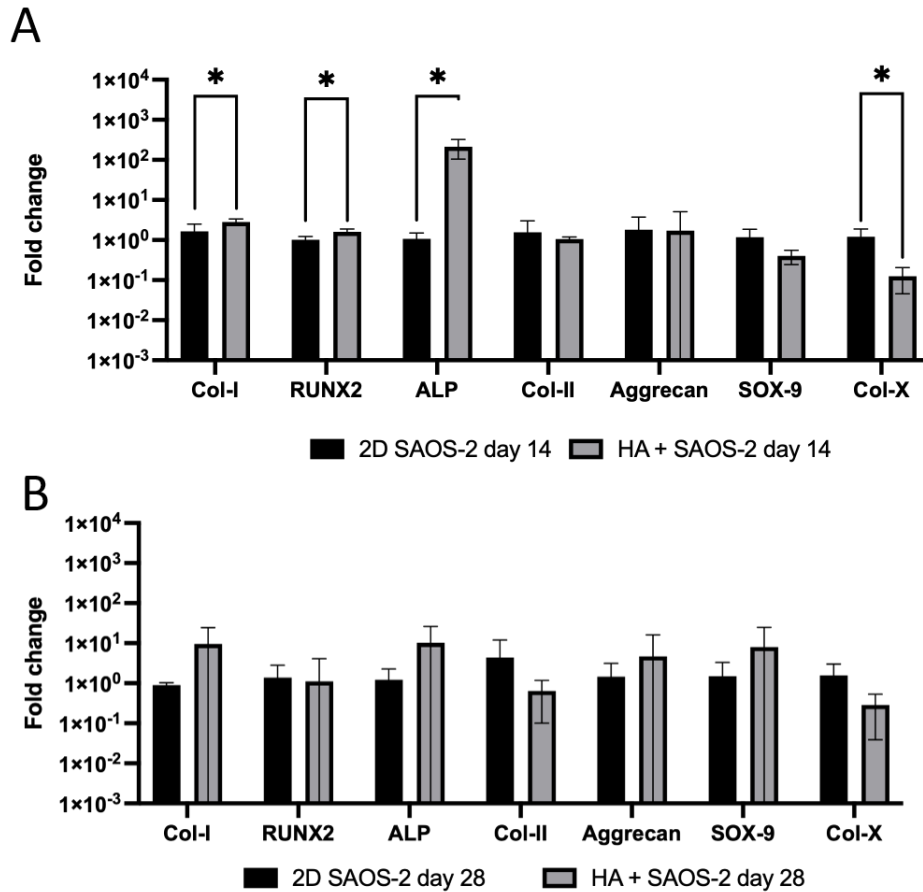
Figure 4.7. A) Comparative qPCR showing fold change in all tested genes on day 14. Saos-2 cells seeded on HA scaffolds mRNA expression on day 14 is compared to the 2D Saos-2 cells control on day 14. Significant differences (* - p < 0.05) are seen in collagen type-I, RUNX2, ALP and Col-X expression. B) Comparative qPCR showing fold change in all tested genes on day 28. Saos-2 cells seeded on HA scaffolds mRNA expression on day 28 is compared to the 2D Saos-2 cells control on day 28. No significant differences are seen across mRNA expression. For both A and B, N = 6. Error bars denote standard deviation. Multiple t-tests with the Mann-Whitney test were performed.

4.4.4 Biological characterisation with HOBs

4.4.4.1 HOBs – HA cell-material interaction assessment through SEM

An initial cell-material interaction assessment was performed through SEM imaging. SEM imaging assessed the cell distribution, shape and proliferation over 28 days of culture. HOBs appeared to form similar cell sheets to the Saos-2 cells. On day 14, Figure 4.8, cells partially covered the scaffold. HOBs presented a spread-out morphology, which enabled them to form these sheets. Day 28 images, Figure 4.8, depicted this phenomenon on the pores and the areas where perpendicular filaments converge. Cell coverage further increased from day 14 to day 28, and cells were seen penetrating the microstructure of the HA scaffold.
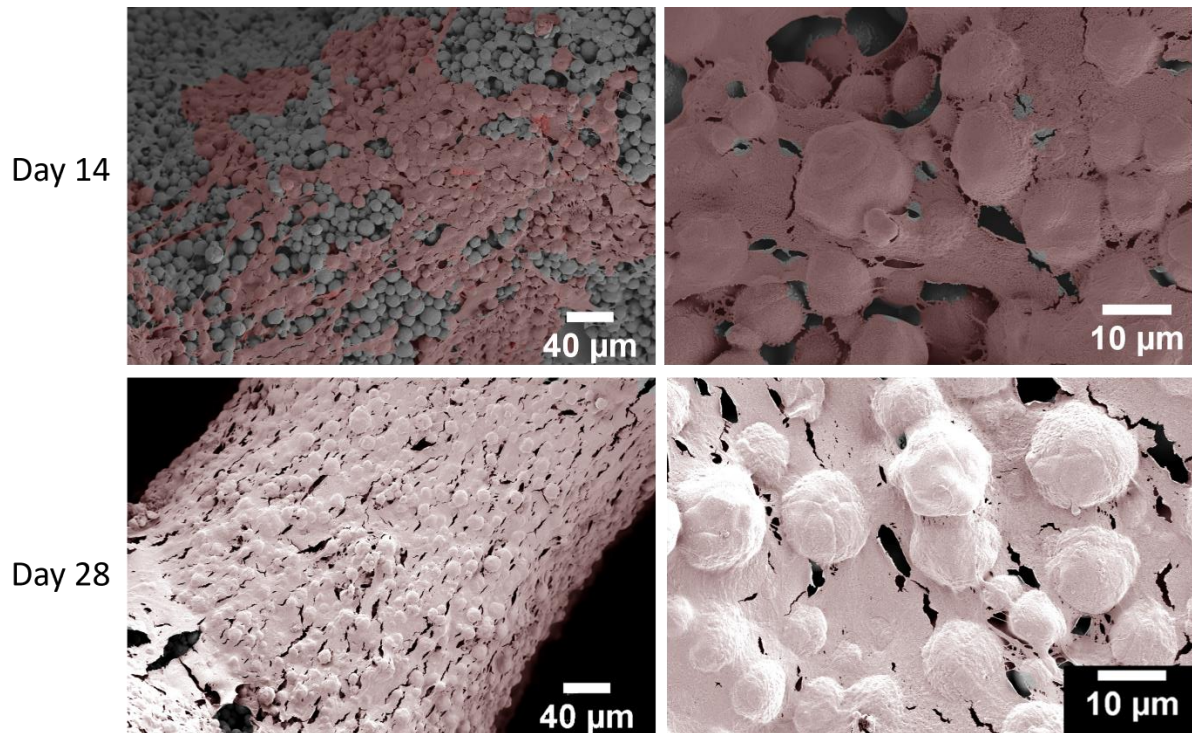
Figure 4.8. SEM images of HOBs seeded on HA scaffolds at day 14 and day 28. Left column: images taken at a lower magnification depicting the cell coverage. Right column: images taken at a higher magnification to depict cell-specific response and bone nodule formations. Cell proliferation and scaffold coverage can be seen in the initial 14 days. Cells were highlighted manually using Adobe Photoshop (version 23.2).

4.4.4.2 Assessment of HOBs through immunofluorescence labelling

Bone-specific protein expression was assessed through immunofluorescence labelling on the HOB-HA seeded scaffolds and compared to the 2D controls. Immunofluorescence labelling of collagen type-I and actin filaments was performed to visualise bone-like matrix deposition and cell morphology, respectively, Figure 4.9. Day 14 and day 28 time points were assessed. The 2D control of HOBs showed the cells producing low levels of collagen type-I deposition, with a few green areas highlighted. Between day 14 and day 28, the 2D control cells changed morphology and went from a more spindle shape to a flattened morphology. Collagen type-I deposition in the 2D control was minimal, potentially due to low cell density. The HA scaffolds showed collagen type-I deposition from day 14 within cell clusters and intracellularly. The levels of this protein increased on day 28, depicted by an increase in the intensity of the green clusters. The presence of this protein appeared mainly in the cell clusters.
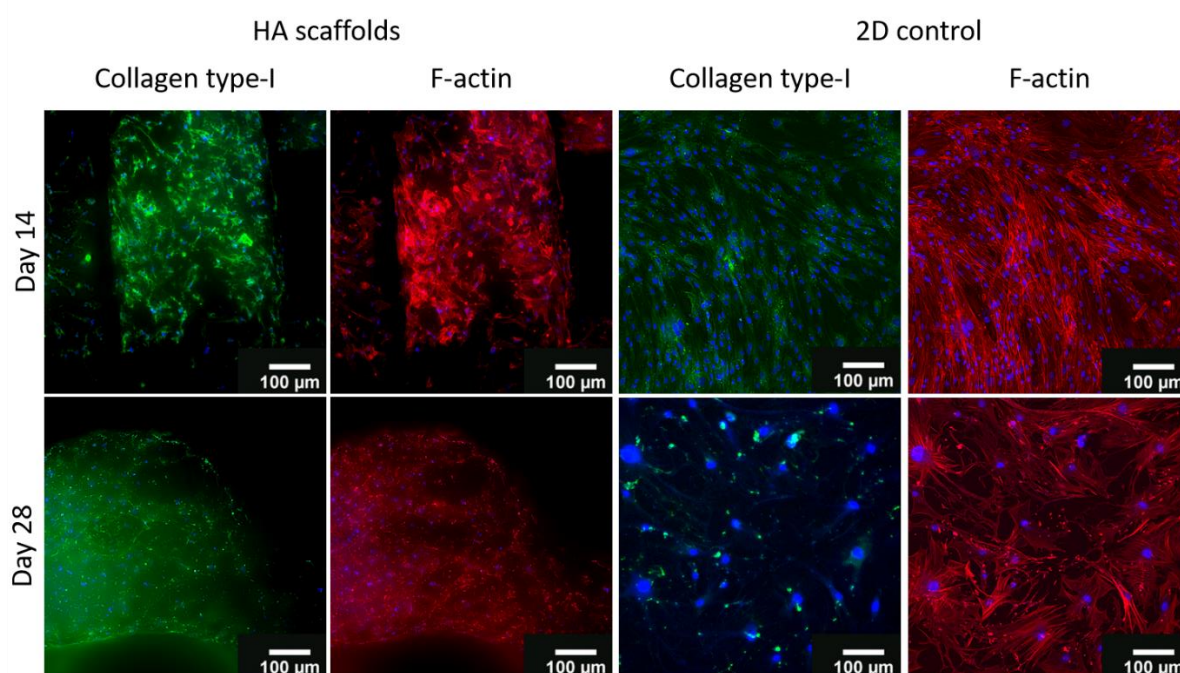
Figure 4.9. Immunofluorescence labelling of collagen type-I (green), F-actin (red) and DAPI (nuclei in blue) of HOBs seeded on a 2D well-plate or on a HA scaffold. Images are taken on day 14 and day 28. Negative controls are shown in Appendix A4.4.

4.4.4.3 HOBs RNA Extraction and Comparative qPCR analysis

Osteogenic genes mRNA expressions were investigated to assess the HA scaffold's effect on the HOBs in terms of osteogenecity. Chondrogenic genes and hypertrophic genes were also measured to ensure cell dedifferentiation was avoided. All mRNA expressions were compared to the expression of GAPDH, the chosen housekeeping gene.

Figure 4.10A depicts the expression changes on day 14. Chondrogenic genes (Col-II, AGC and SOX-9) were downregulated when HOBs were placed on the HA scaffold compared to the 2D HOB control on day 14. A downregulation was also observed in the hypertrophic-associated gene collagen type-X. The osteogenic genes Col-I, RUNX2 and ALP were downregulated as well. Although this downregulation was not significant, it was surprising, as the HA scaffold had been found to improve the expression of these osteogenic genes in Saos-2 cells.

Figure 4.10B shows the mRNA expression observed on day 28 between the 2D control and the HA scaffold. An upregulation of the chondrogenic genes was observed. However, the large standard deviations of some of the measurements, such as in the case of aggrecan, suggested that this experiment should be repeated with more samples. All genes, Col-II, ACG and SOX-9, were upregulated in the HA scaffold with respect to the 2D control. There was also an upregulation of collagen type-X expression, again showing a surprising phenomenon where the HOBs behaved less bone-like than the 2D structures. It is still being determined whether this was because of the differences in cell density or the limitations encountered when extracting the RNA from these cells, which grow in the microstructure of HA. mRNA extraction in 3D scaffolds was less efficient than in the 2D samples. Therefore, a more effective extraction would lead to different results. This would require further optimisation of this extraction method by fully pulverising the HA scaffold.

The expression of the osteogenic genes on day 28 was not significantly different. Only the ALP activity and collagen type-I mRNA expressions were slightly upregulated; however, these differences were not significant. All the measurements of mRNA expression in these HOB-based samples were based on a minimum "n" number of 3.

More sample repetitions are required to fully characterise the behaviour of these cells when seeded on HA scaffolds.
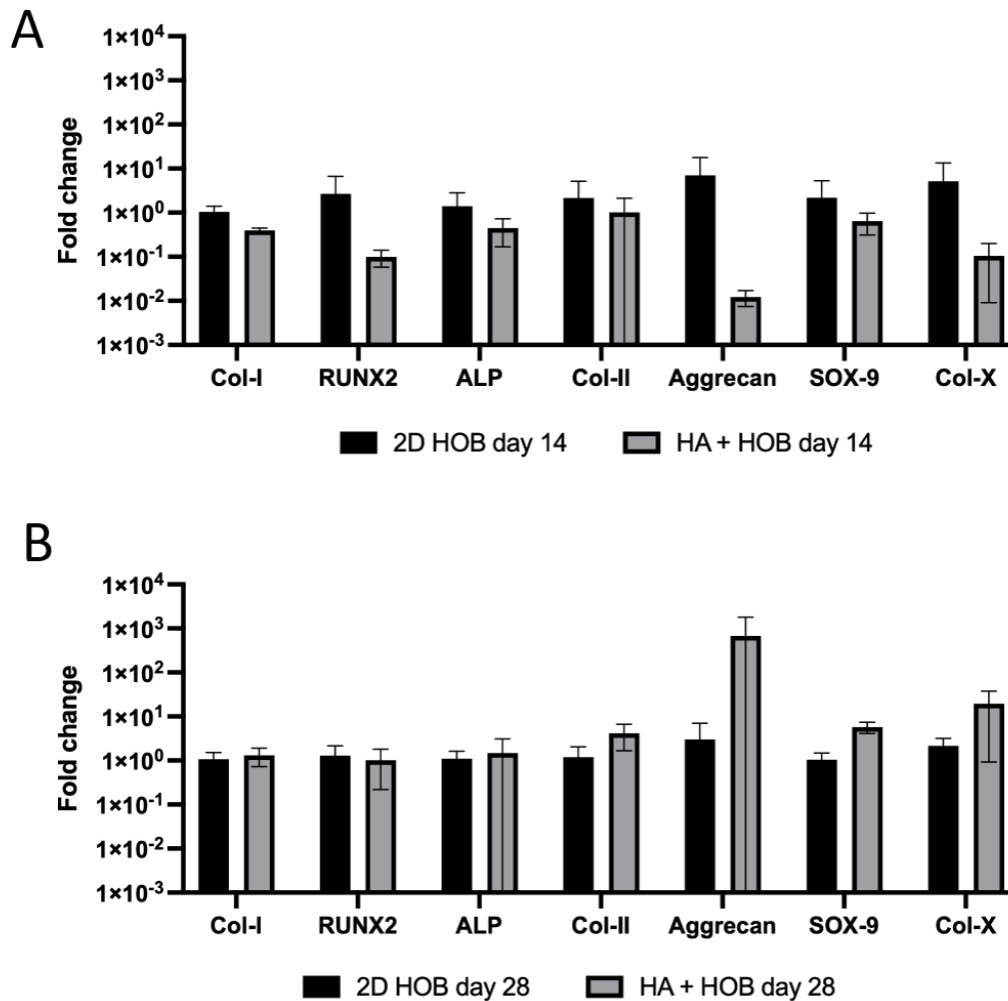
Figure 4.10. A) Comparative qPCR showing fold change in all tested genes on day 14. HOBs seeded on HA scaffolds mRNA expression on day 14 is compared to mRNA expression of the 2D HOBs control on day 14. B) Comparative qPCR showing fold change in all tested genes on day 28. HOBs seeded on HA scaffolds mRNA expression on day 28 is compared to mRNA expression of the 2D HOBs control on day 28. No significant differences are seen across mRNA expression. For both A and B, N = 3. Error bars represent standard deviation. Multiple t-tests with the Mann-Whitney test were performed

4.5 Discussion

Bone has a complex hierarchical structure composed of organic and inorganic materials, with multiple cell types that intricately interact with each other, making it an extremely complicated tissue to mimic *in vitro*. The composition and architectural distribution of this tissue, made of collagen type-I and HA, is complicated to recreate due to the existing interaction between both components and their differences in terms of material characteristics. 3D printing is a manufacturing technique which enables the production of complex structures and control over variables such as porosity and different material deposition. It has been extensively used to develop bone tissue models *in vitro* (Section 4.1 and Appendix A4.1). Collagen type-I is the main organic bone compound that presents complexities when used in manufacturing techniques such as 3D printing and does not reach the required compressive moduli characteristic of bone [320]. To increase the compressive modulus of the manufactured constructs, HA-based inks have been used in combination with sacrificial materials [279,321] and other organic materials, such as alginate [31,281–289], collagen [104,281,285], chitosan [282,290] or gelatine [285,287–291], to mimic the structure of bone. However, the use of these organic materials has been proven to have limitations such as poor mechanical properties [282,292–294], high degradation rates [292,293], and limited long-term stability [288,295–302] of the produced scaffolds. Therefore, the use of HA as the primary and only material to develop these bone scaffolds has been investigated (Appendix A4.1, Table A4.1) to circumvent these issues.

Previous work by Roopavath *et al.* [303] and Sara Malferrari [312] focused on developing and optimising an HA ink to 3D print structures which would be used in the future for *in vivo* implantation [312]. Critical steps in the manufacturing process, such as sintering temperature and time, as well as infill pattern and density, had previously been optimised and investigated. The work described in this chapter focuses on using this optimised ink formulation and investigating its rheological properties, changes in size post-sintering, compressive strength properties, and the effect of the 3D-printed HA scaffolds on bone-like cells (Saos-2 cells and HOBs).

Initial material characterisation was performed by rheologically measuring the viscosity changes of the HA ink with respect to shear rate. Figure 4.2A shows that three batches of HA inks were measured, and the expected shear-thinning behaviour was observed. The overall shear-thinning material behaviour is the predicted one. However, higher viscosity values were observed in lower shear stress levels (< 0.5 s^{-1}) than those reported previously [312]. This higher viscosity could be due to the ink having a higher solid content and lower water percentage due to the ink preparation process, as was manually mixed for 10 minutes to achieve a homogeneous consistency. This amount of mixing time was not previously reported to be standardised. Therefore, a standardised ink manufacturing protocol was developed [317], leading to consistent results across HA ink batches.

Further material characterisation was performed by looking at the changes in size of the printed scaffolds after the sintering process. HA scaffolds underwent a sintering process before autoclaving and cell seeding. In this process, they were subjected to high temperatures (> 1300°C), which led to a fusion of the HA particles, hardening the HA scaffolds. This fusion of particles led to decreased inter-particle space and decreased scaffold size. This decrease percentage must be characterised so an accurate prediction of the scaffold size can be performed and variables, such as cell seeding density, can be accurately calculated. Figure 4.3A shows the significant difference between the 50% infill HA pre-sintered scaffolds and the post-sintered scaffolds, showing a decrease in size. The high temperatures in the sintering process make the HA particles fuse, and the HPMC, used as a polymeric binder, burn off, leaving a pure HA construct. Previous research reported a decrease in scaffold size of nearly 50% for the 50% infill density scaffolds when sintered at 1320 °C for 5 hours [312]. However, here it was found that the size change was closer to 15%, which correlated closer to other reported literature which used similar sintering temperatures ((18-20%) at 1100-1300°C [304,321] or 25% at 1400°C [322]). The decrease in sintering size could be due to the difference in HA ink solid content. The HA particle size was the same as previously reported (~ 25 μm) [303]. However, there is no prior information regarding the HA ink preparation protocol used. Therefore, the changes in HA ink manufacturing, where a 10-minute mixing period was performed, could lead to a loss in solvent content due to evaporation and a higher solid content. This higher

percentage of HA particles would lead to less inter-particle space and decreased shrinkage post-sintering.

Additionally, the compressive moduli of the printed scaffolds were assessed and calculated, taking the point of failure as the point where the first visible crack appears. An average of 0.28 MPa of compressive modulus was obtained for the printed scaffolds. These results differed by more than a factor of 10 from those previously reported with this specific ink composition [312], which ranged close to 5 MPa. These differences could be due to the data analysis and the point at which "failure" of the scaffolds was determined in the previously reported research. Information regarding determining failure points was not found in the previous research; therefore, a new definition was set.

Regardless of the differences in rheological features and mechanical characteristics of the printed scaffolds, the previously optimised ink composition demonstrated ease of printability as well as scaffold reproducibility, observed in the sintering changes which differed less than 0.1 cm (10%) between scaffolds, Figure 4.3A. Additionally, as the intended use of these scaffolds was to develop an *in vitro* bone-like model, changes in size post-sintering were less relevant than if these scaffolds were to be implanted *in vivo* in specific size defects. The compressive moduli differences, although relevant, were not concerning. The measured compressive moduli values fell within the reported compressive characteristics of trabecular bone, 0.22 to 10.44 MPa [319]. However, the reported compressive strength of other HA-based scaffolds varies drastically from 22.5 MPa [309] to 750 MPa [308] (Appendix A4.1, Table A4.1), showing that the presented scaffold compressive strength is far from previously reported values. Additional variables such as infill density, scaffold architecture, and sintering parameters could be further investigated to increase the resulting compressive strength of the manufactured scaffolds.

Initial cell-based investigations were performed using the Saos-2 cell line. This cell line is the least cancerous and displayed the most mature osteoblastic behaviour out of other cell lines, such as MG-63 [313]. It is a well-established cell line used for *in vitro* investigation with various materials [313–316] with a doubling time of 2-3 times greater than HOBs [313]. However, it also differs from bone in aspects such as cell size and

overexpression of specific osteogenic genes such as ALP [313]. Based on the advantages of this cell line, this cell type was used to initially optimise the assays used and fully characterise the HA scaffolds' behaviour on bone-like cells *in vitro.*

Saos-2 cells were cultured in 12-well plates as a 2D control and onto the HA scaffolds at a cell density proportional to previously reported investigations [323]. Cell viability was assessed qualitatively through live/dead staining on day 1 (24 hours post-cell seeding) and day 14, Figure 4.4A. Day 1 images showed that the cell viability on the 2D control was high and that a visible number of cells had attached to the HA scaffold. These cells proliferated and kept the viability high on day 14, showing full coverage of the well plate in the 2D control and nearly complete coverage of the HA scaffold. These images showed initial promising results as the cells proliferated and kept high levels of viability.

Further quantification of these observations was performed by measuring the metabolic activity of the cells using the PrestoBlue[TM] assay. In both the 2D control and the HA scaffolds, a significant increase in metabolic activity from day 1 to day 28 was observed; Figure 4.4B depicts the increase in cell numbers. The metabolic activity of the cells seeded on HA scaffolds was lower than the 2D control. This is hypothesised to be due to differences in cell density and potentially cell-material interactions. However, further investigations are required to understand these differences fully. The overall trend observed also further confirmed the reported increase in cell numbers and cell viability across the 28 days of culture.

Cell-material interaction characterisation was performed visually through SEM imaging of the Saos-2 cells seeded on HA scaffolds at different time points, Figure 4.5. Day 1 showed low cell coverage levels, suggesting cell attachment levels onto the HA scaffold were lower than those observed on the 2D scaffold. This was expected and attempted to be mitigated using low-adhesion well plates, which avoided cells attaching to the well plate, forcing them to attach to the HA scaffold instead. Saos-2 cells had a spread-out morphology and adapted to the shape of the HA particles of the scaffolds. Day 14 images showed the quick cell coverage of the HA scaffold. A flat cell sheet covered most of the HA scaffold, with cells forming cell-cell interactions over

the HA scaffold particles and covering the structure. Day 28 images show further coverage and penetration of the Saos-2 cells into the micropores of the HA structure.

Additionally, higher magnification images show the formation of clusters, which are thought to be calcification nodules. However, further analysis of the composition of these nodules is required. Standard alizarin red staining was not a reliable analysis method here as this staining protocol stains for calcium, which is the major component of HA. Alizarin red staining was performed in both acellular HA scaffolds and day 28 Saos-2 seeded HA scaffolds. However, the differentiation between scaffold mineral and cell-made mineralisation nodules was highly complicated to quantify (Appendix A4.2). A retrieval of this staining was attempted by submerging the stained scaffolds in acetic acid and measuring the neutralised retrieved dye through optical density. However, inconclusive results were obtained (Appendix A4.2). Therefore, further analyses based on mRNA expression or total calcium quantification should be performed.

Alongside the production of calcification nodules, osteogenic behaviour could be observed through the production of collagen type-I protein, the major organic component of bone matrix [259,260]. Initial assessment of this protein production was performed through immunofluorescence labelling of collagen type-I and F-actin filaments to determine the expression of this protein and cell shape, respectively. Both 2D control and HA scaffold Saos-2 cells showed no production of collagen type-I on day 1. Day 14 was the first time point where small amounts of collagen type-I were observed on the HA scaffold, Figure 4.6. Both HA and 2D samples showed a higher cell coverage. However, collagen type-I production was only evident on the HA scaffolds, suggesting that this ceramic substrate promoted the expression of this extracellular protein faster than the 2D culture method.

Furthermore, day 28 images showed higher levels of collagen type-I production on the HA scaffold and initial cell clusters, which presented low levels of this protein in the 2D control. The appearance of cell clusters in the 2D control was due to the high cell density, which forced cells to grow on top of each other. It these nodules, the production of collagen type-I appeared to be more prominent.

Although the immunofluorescence labelling images were a good initial indicator for the production of collagen type-I, further quantification was performed through comparative qPCR in both samples. The 2D control sample was used as the baseline comparison, and the endogenous housekeeping gene was GAPDH. Expression of osteogenic and chondrogenic genes was performed on day 14 and day 28. Day 14 expression profile showed a significant upregulation of all osteogenic genes, Col-I, RUNX2 and ALP activity, Figure 4.7A. A significant downregulation of collagen type-X expression was observed, and no significant changes were seen across the chondrogenic genes. The upregulation of both collagen type-I and RUNX2 showed that the Saos-2 cells were in the proliferative state more than the 2D control. However, the high upregulation of the ALP mRNA levels on the HA cell-seeded scaffold suggested that cells in these scaffolds had exited mitosis and were in the mineralisation stage. Overexpression of ALP on Saos-2 cells has been previously reported [313]. However, here we were comparing two cell culture systems using Saos-2 cells in both, suggesting that the increase of this expression was most likely due to the effect of the HA substrate on the Saos-2 cells.

Comparative qPCR levels analysed on day 28 showed no significant changes across measured mRNA levels, Figure 4.7B. However, both collagen type-I and ALP expression were upregulated on the HA scaffold, suggesting further that the cells had entered an extracellular matrix production state. Chondrogenic genes presented no significant differences in expression. However, there was an upregulation of aggrecan and SOX-9 on the HA scaffolds. SOX-9 is associated with the development of malignant tumours and increased aggressiveness [324]. The upregulation of this gene on day 28 on the HA scaffolds suggested that the scaffold promoted the cancerous behaviour of the cells. However, the upregulation of these chondrogenic genes has already been reported, suggesting that this is normal behaviour on Saos-2 cells cultured in a pro-calcifying medium [324]. Overall, the higher expression of the osteogenic markers on day 14 suggested that the HA scaffold promoted osteogenic behaviour faster than the 2D culture.

Although Saos-2 cells are a well-established cell line used for preliminary testing of bone-related materials or preliminary investigations, it has been proven to not resemble primary cell behaviour fully [313]. Due to these differences, further characterisation using HOBs was performed.

Cell-material interactions between the HOBs and the HA scaffold were investigated using SEM imaging, Figure 4.8. Images on day 14 and day 28 showed that the HOBs, larger than the Saos-2 cells [313], reached a cell coverage comparable to that observed on the Saos-2 cells on day 28. Day 14 images showed that the HOBs also partially formed cell sheets that covered the HA scaffold. These observations show a clear and expected difference in cell proliferation rates using the same cell seeding density. However, similar cell coverage is observed on day 28, suggesting that this culture time is enough for the used HOB cell seeding density to populate the HA scaffold fully. Cell clusters or nodules were also not observed on day 28 when using HOBs. The lack of these formations is potentially due to the differences observed in cell density. Saos-2 cells' high proliferation rate triggered the formation of these mineralisation nodules, where cells grew on top of each other. However, this cell density is not achieved by the HOBs in 28 days of culture. A longer culture time for this specific cell seeding density or a higher cell initial seeding density could lead to a higher cell population and the subsequent formation of mineralisation nodules.

Differences between 2D and HA-seeded HOBs were also observed in collagen type-I production, Figure 4.9. 2D control HOB cultures showed low levels of collagen type-I production despite the high cell density. Cells were seen to change from a more elongated morphology to a spread-out conformation with low levels of collagen type-I expression. HOBs seeded on the HA scaffolds showed expression of collagen type-I from day 14 onwards. Although the cell density on day 14 was insufficient to cover the whole HA construct, high collagen type-I levels were observed. These differences depend not on cell density but on substrate and cell-material interactions. HA scaffolds positively impact collagen type-I production in HOBs compared to the 2D culture controls.

Further quantification of the expression of osteogenic markers in HOBs was performed through comparative qPCR. The control group was the 2D cultured HOBs with the

endogenous housekeeping gene GAPDH. As this was a proof-of-concept model, low numbers of samples (n = 3) were used in this analysis. Expression of osteogenic and chondrogenic markers was assessed on day 14 and day 28. Day 14 expression, Figure 4.10A, showed no significant differences in any of the genes and a general downregulation of all tested genes in the HA scaffolds. Osteogenic markers' (Col-I, ALP and RUNX2) expression was downregulated, suggesting that the cells seeded on HA scaffolds were proliferating less and mineralising less than those in the 2D culture at this specific time point. This was speculated to be due to the differences in cell densities. Day 28 expression levels, Figure 4.10B, also showed no significant differences between the 2D control and the HA scaffolds. However, at this point, Col-I, RUNX2, and ALP levels were similar to the control. This suggested that at this time point, cells behaved similarly in both 2D and HA samples. However, these differences were based on low sample numbers and were not significant. Therefore, further samples should be measured to achieve a definite conclusion. Additionally, the fact that the expression of these proteins in the HA scaffold images of immunofluorescence can be seen but not in the comparative qPCR suggests that the mRNA extraction in the 3D scaffold might not be retrieving all the RNA and, therefore, the values seen in the comparative qPCR are lower.

4.6 Limitations and Further Work

This chapter aimed to characterise the HA ink for 3D printing scaffolds and investigate the use of these scaffolds to model bone tissue *in vitro*. However, multiple limitations were found when undertaking and investigating the set objectives.

Firstly, the HA scaffold characterisation (scaffold shrinkage post-sintering and compressive strength) showed multiple differences with previous work using this specific HA composition [303,312], and other reported investigations, which used HA as the only manufacturing material for 3D printing scaffolds [308,309]. Overall, there needs to be more information regarding the solid and water content of the HA ink used throughout this chapter. Further characterisation of these parameters would enable a better understanding of this effect on scaffold shrinkage post-sintering and mechanical properties. Additionally, the compressive modulus of the presented HA scaffolds (0.28 MPa) falls in the lower range of bone mechanical properties (0.22 to 10.44 MPa [319]). This difference in compressive strength is expected to affect the behaviour of HOBs and Saos-2 cells. Therefore, further investigations to increase this compressive modulus must be performed. Furthermore, HA scaffolds with different compressive moduli could be investigated to corroborate that this variable affects Saos-2 cells and HOBs.

Secondly, regarding the biological characterisation, the experimental set-up was simplified by having the HA scaffolds compared to 2D cell culture on plastic well plates. An additional 2D control with a layer or pellet of HA could be included. This would enable further comparisons to be established and to determine whether the changes seen are material-dependent or configuration-dependent (2D vs. 3D). This control group would help to further understand the differences observed in the metabolic activity of Saos-2 (Section 4.4.3.1). The results show lower metabolic activity in the HA scaffolds, regardless of suspected higher cell numbers. Additional DNA quantification assays should be performed to quantify cell proliferation over time. Additionally, including this control could determine if this metabolic activity difference is due to the material interactions.

Thirdly, two main limitations were encountered in processing the HA scaffolds. In the first place, the availability of microscopes and the thickness of the 3D printed samples limited the imaging resolution when immunofluorescence labelling was performed. Different microscopy set-ups could be investigated to improve the resolution and magnification of the images. In the second place, RNA extraction methods could affect the qPCR results. Due to the bone-like cells penetrating the HA scaffold pores, complete RNA extraction becomes complicated. Fully pulverising the scaffold can compromise the quality of the extracted RNA. However, not breaking the scaffold enough would only extract the RNA of the surface cells. Therefore, multiple extraction methods could be compared to ensure the most efficient extraction.

Finally, two key issues limited the presented investigation regarding the quantification of mineralisation and the use of HOBs. The potential mineralisation of the seeded Saos-2 cells and HOBs was not possible to quantify through standard methods such as alizarin red staining. This specific method stains calcium deposits [325]. Calcium is the main element in HA. Therefore, differentiation between new mineral deposits and the original HA scaffold was challenging. Other analyses, such as calcium quantification, should be investigated to characterise these models further. Furthermore, using HOBs limited the investigation due to these primary cells' low availability and proliferation rate. To fully develop the bone tissue model, HOBs from different donors should be tested, and the sample size should be increased.

4.7 Summary

The 3D-printed HA constructs exhibited mechanical properties consistent with trabecular bone. Moreover, during the initial 14 days of culture, they demonstrated a superior capacity to support the growth and osteogenic behaviour of Saos-2 cells when compared to 2D culture controls. Notably, these seeded scaffolds displayed cell infiltration, propagation throughout the HA structure, and the deposition of collagen type-I.

Furthermore, at day 14, Saos-2 cells cultured on HA scaffolds exhibited significantly elevated expression levels of crucial osteogenic markers, including collagen type-I, RUNX2, and ALP, in contrast to their 2D counterparts. These initial findings, derived from cell line-based experiments, were promising, leading to subsequent characterization with HOBs.

While the assessment involved limited samples, the HOBs showed cell proliferation and collagen type-I production when cultured on HA scaffolds. Notably, no statistically significant differences emerged in the comparative qPCR results, likely attributable to the small sample size. Thus, further research is necessary to draw more robust conclusions. Additionally, exploring variables such as cell seeding density will be crucial to comprehensively understanding the relationship between cell density and the osteogenic potential of HA scaffolds.

These findings show that 3D-printed HA scaffolds can support long-term bone-like cell cultures. Therefore, these bone-like constructs were used to develop an osteochondral tissue model, further explained in Chapter 5.

Chapter 5: 3D Bioprinting proof of concept osteochondral tissue models *in vitro*

5.1 Introduction

Osteochondral tissue units are made by the intersection of hyaline cartilage and bone. They present distinct areas with specific structural differences [1], which makes this complex tissue challenging to mimic *in vitro.* This structure can be divided into four areas, gradually changing from a smooth, surfaced cartilage into a calcified cartilage connecting to the subchondral bone. Cartilage structure, previously described in Chapter 3, changes in the cellular shape and distribution and the extracellular matrix protein composition. As seen in Figure 1.1, chondrocytes go from an elongated shape and distributed parallel to the cartilage surface to a randomised allocation with a characteristic circular shape, which then turns into a columnar placement perpendicular to the tide mark where chondrocytes become hypertrophic. The tidemark zone joins the uncalcified and calcified cartilage and is connected to the subchondral bone plate.

Tissue engineering techniques have been used to recreate osteochondral tissue models *in vitro* (see Chapter 1 for more details). 3D bioprinting has been used within them, as it enables control over the manufactured architecture, different materials, and the homogeneous deposition of cells. A detailed literature review conducted and published as a part of this thesis has confirmed that 3D bioprinting has been used to manufacture osteochondral tissues *in vitro*, mainly using the techniques of extrusion-based and jetting-based bioprinting [2]. These techniques have been used combined with different bioinks, cell types and additional GFs to develop these composite tissues. The most recent investigations have adopted a combination of acellular and cellular 3D bioprinting, enabling the simultaneous use of softer materials, such as gelatine methacryloyl (gelMA) or hyaluronic acid, with more robust materials, such as PLA (poly(lactic) acid) and PCL (poly-ε-caprolactone) [2,115,162,326]. This approach enables the composite structures to achieve better mechanical properties, getting

closer to physiological values. Additionally, these approaches focus on introducing multiple cell types, which achieve better cell proliferation and tissue maturation [124], as well as the formation of the required different tissues.

Although advances have been made in developing these composite tissues, specific characteristics still need to be fully met. These include mechanical properties not matching those of native tissue, the lack of interconnectivity between the cartilage and bone sections, and the inability of these constructs to be kept in culture for long periods of time (further explained in Chapter 1). Attempts to overcome these limitations have been investigated, such as designing complex gradient structures that mimic the connection between the two tissues [60,327], adding extra components to the bone section, such as vasculature [144] or adding mechanical cues to improve the mechanical properties of the samples [42–44].

In an attempt to simplify the current approaches whilst tackling these issues, a 3D bioprinted osteochondral model is presented. Following on the previously optimised 3D bioprinting process of the cartilage section (Chapter 3) and the previously developed bone-like tissue mode *in vitro* (Chapter 4), this chapter focuses on combing the information learnt from Chapters 3 and 4 to assemble a composite structure of osteochondral tissue. Manufacturing these *in vitro* osteochondral models focuses on developing simple structures that tightly interact, avoiding cartilage-bone delamination. Additional objectives were not pursued at this initial stage, such as achieving close-to-native tissue mechanical properties or adding vasculature in the bone section.
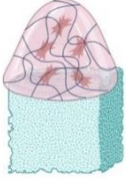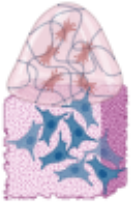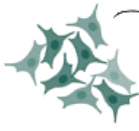
This chapter focuses on developing an osteochondral tissue model *in vitro* using a Peptigel® Alpha 1-based cartilage section and an hydroxyapatite (HA) scaffold-based bone section. Multiple biphasic tissue models are presented and investigated regarding cellular proliferation, protein expression, and mRNA expression. These models include the combination of an Alpha 1-based cartilage section with either an acellular-HA scaffold (Model-1), a Saos-2-seeded HA scaffold (Model-2), or a HOB-seeded HA scaffold (Model-3). These conditions are summarised in Table 5.1

The first experimental set-up, Model-1, consists of an initial characterisation of the effect that the HA scaffold has on the cartilage section. This investigation was performed using an HA scaffold in combination with a 3D bioprinted Alpha 1 section, which had embedded primary human chondrocytes (HCHs). This first set of experiments focused on assessing two manufacturing protocols (upright vs. inverted) and characterising the interaction of Alpha 1 and HA. This was achieved by assessing the chondrogenic protein expression of the Alpha 1 embedded HCHs through immunofluorescence and qPCR when in contact with acellular-HA. These results were compared to HCH-embedded 3D bioprinted Alpha 1 cultured alone as a control (control Model-1), previously characterised in Chapter 3.

The second experimental set-up, Model-2, assessed the behaviour of Saos-2 seeded on HA in combination with the HCH-embedded 3D bioprinted Alpha 1 section, which was cultured for 21 days in an inverted set-up. Immunofluorescence labelling and qPCR focused on assessing the expression of chondrogenic, osteogenic, and hypertrophic markers in the Alpha 1 and HA sections. These results were compared to HCH-embedded 3D bioprinted Alpha 1 cultured with Saos-2 cells in 2D (control Model-2).

The third and final experimental set-up, Model-3, was a proof-of-concept for a fully human primary cell-based osteochondral construct. An HCH-embedded 3D bioprinted Alpha 1 section in combination with an HOB-seeded HA scaffold was manufactured. Immunofluorescence labelling and qPCR focused on assessing the expression of chondrogenic, osteogenic, and hypertrophic markers in the Alpha 1 and HA sections. These results were compared to HCH-embedded 3D bioprinted Alpha 1 cultured with HOBs in 2D (control Model-3).

Table 5.6. Summary of experimental set-ups of various tissue interaction models investigated in Chapter 5. Illustrations created with BioRender.

1ˢᵗ Experimental set-up Model-1		2ⁿᵈ Experimental set-up Model-2		3ʳᵈ Experimental set-up Proof-of-concept Model-3	
Control Model-1	Model-1	Control Model-2	Model-2	Control Model-3	Model-3
3D bioprinted Alpha 1 with HCHs	3D bioprinted Alpha 1 with HCHs + HA	3D bioprinted Alpha 1 with HCHs + 2D Saos-2	3D bioprinted Alpha 1 with HCHs + Saos-2+HA	3D bioprinted Alpha 1 with HCHs + 2D HOBs	3D bioprinted Alpha 1 with HCHs + HOB+HA

5.2 Objectives and Hypotheses

This chapter aims to combine cartilage and bone-like tissue models fabricated from Chapters 3 and 4, respectively, and study various cell and material interactions for optimised osteochondral tissue model fabrication.

<u>Objectives:</u>

1. Optimise the 3D bioprinting process to study the interaction between the cartilage and the bone-like tissue models.
2. Develop three independent tissue models to study the interaction of various materials and cells through immunostaining and short- and long-term protein expressions.

<u>Hypotheses:</u>

1. Incorporating the ceramic scaffold in Model-1 will increase the osteogenic and hypertrophic phenotype of Alpha 1 embedded HCHs.
2. Incorporating bone-like cells in Model-2 and Model-3 will decrease the chondrogenic potential of Alpha 1 and increase the osteogenic phenotype of HCHs.

5.3 Methods

5.3.1 Cell culture

HCHs were used to manufacture the Alpha 1-based cartilage tissue model section. Cell culture conditions remained the same as the ones explained in Section 3.3.1 of Chapter 3.

Saos-2 cells were used in the cell seeding of the HA scaffold for the preliminary characterisation of the osteochondral tissue construct. HOBs were used in the seeding of the HA scaffold for the preliminary proof-of-concept osteochondral tissue system development based on primary human cells. The culture conditions for both Saos-2 cells and HOBs are described in Section 4.3.4.1 in Chapter 4.

5.3.2 Composite structure printing set-up

The initial biphasic construct manufacturing set-up was designed to be a bottom-up process. The HA construct would be placed at the bottom of the wells in the culture well plate, and the Alpha 1 section would be 3D bioprinted on top. This procedure presented complications such as the different positioning of the HA constructs within each well and the movement of these constructs when the Alpha 1 3D bioprinting occurred. Custom-made holders were designed and 3D printed using FDM (Fused Deposition Modelling) PLA printing to circumvent these issues. These were fitted to 12-well plates with a rectangular base where the HA construct would be placed. Figure 5.1 shows the design schematic and photographs of the printed holders.
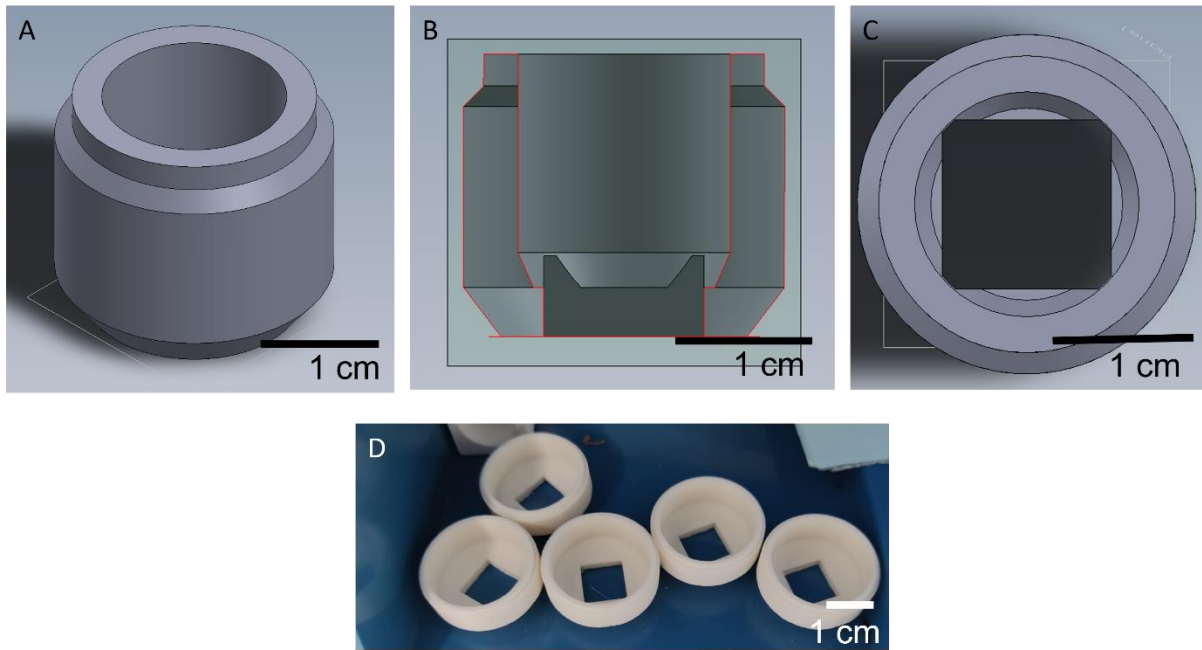
Figure 5.1. 3D printed holder design for upright bioprinting of the osteochondral constructs. A) Shows an isometric view of the holder's CAD (Computer Aided Design). B) Shows side cross-section of the holder CAD design. C) Top view of the CAD holder. D) Photograph of 3D printed holders.

These constructs enabled the 3D bioprinting of the biphasic constructs to be held in place and have a better automated manufacturing process. However, the culture of these constructs for 7 days as a biphasic entity showed multiple issues, such as the constant detachment of the Alpha 1 section from the HA construct and a fast degradation rate of the Alpha 1.

An alternative manufacturing strategy was assessed to overcome the observed issues with an inverted manufacturing procedure. The construct was inverted, presenting the Alpha 1 at the bottom of the well plate and the section HA on top. As previously explained in Section 3.3.3 in Chapter 3, the cartilage structures were printed in 12-well plates. Subsequently, HA scaffolds were manually placed on top of the cartilage sections. This method not only eliminated the issue of delamination between the two sections of the biphasic construct but also prevented Alpha 1 from floating. Gravity pulled the HA construct down, held Alpha 1 in place, and facilitated the penetration of the Alpha 1 cartilage section into the pores of the HA construct. Additionally, due to

the lower surface area of the cartilage section being exposed, the degradation of Alpha 1 was decreased. The upright and inverted manufacturing methods are graphically described in Figure 5.2.
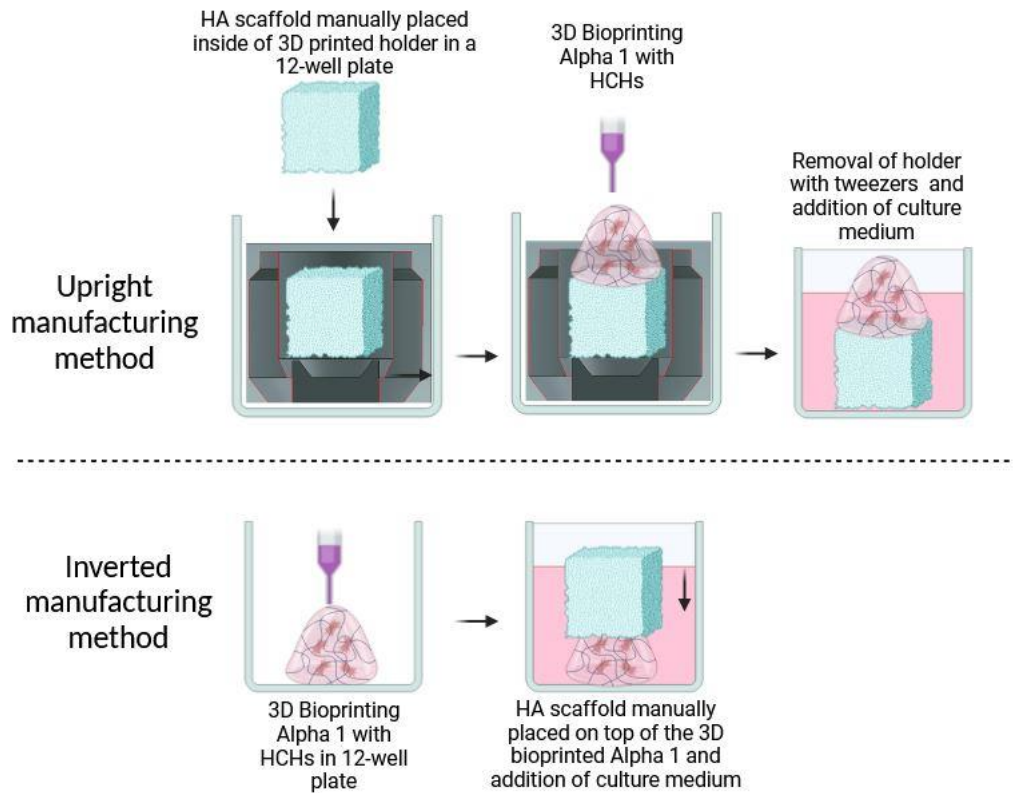
Figure 5.2. Schematic diagram showing the upright and inverted manufacturing methods. The upright method shows acellular HA scaffolds placed inside the 3D printed 12-well plate holders and Alpha 1 with embedded HCHs being 3D bioprinted on top. The inverted method shows Alpha 1 with embedded HCHs being 3D bioprinted in 12 well plates and the acellular HA scaffolds placed over them before cell culture medium immersion. Illustrations were made with BioRender.

5.3.3 3D Bioprinted models cell culture set-up.

Model-1 was manufactured using the inverted manufacturing method. In short, Alpha 1 with embedded HCHs was 3D bioprinted into 12-well plates. HA scaffolds were manually placed over the 3D bioprinted samples. They were cultured for 7 days. Cell

culture conditions remained the same as the ones explained in Section 3.3.1 of Chapter 3.

Model-2 was manufactured using the inverted manufacturing method. Saos-2 cells were seeded on the HA scaffold and cultured for 14 days. The culture conditions for Saos-2 cells are described in section 4.3.4.1 in Chapter 4. On day 14, Alpha 1 with embedded HCHs was 3D bioprinted into 12-well plates. The Saos-2 seeded and pre-cultured HA scaffolds were placed over the 3D bioprinted Alpha 1 samples. They were cultured for another 7 days in chondrogenic medium, as explained in section 3.3.1 of Chapter 3. Control Model-2 was manufactured by seeding 2D Saos-2 cells in 12 well plates, as described in Section 4.3.4.1 in Chapter 4. These cells were cultured for 14 days in pro-calcifying medium. On day 14, Alpha 1 with embedded HCHs was 3D bioprinted over the 2D cell culture. They were cultured for another 7 days in chondrogenic medium, as explained in Section 3.3.1 of Chapter 3. Model-2 and its control were in culture for a total of 21 days.

Model-3 was manufactured using the inverted manufacturing method. HOBs were seeded on the HA scaffold and cultured for 14 days. The culture conditions for HOBs are described in Section 4.3.4.1 in Chapter 4. On day 14, Alpha 1 with embedded HCHs was 3D bioprinted into 12-well plates. The HOBs seeded and pre-cultured HA scaffolds were placed over the 3D bioprinted Alpha 1 samples. They were cultured for another 7 days in chondrogenic medium, as explained in Section 3.3.1 of Chapter 3. Control Model-3 was manufactured by seeding 2D HOBs in 12 well plates, as described in Section 4.3.4.1 in Chapter 4. These cells were cultured for 14 days in pro-calcifying medium. On day 14, Alpha 1 with embedded HCHs was 3D bioprinted over the 2D cell culture. They were cultured for another 7 days in chondrogenic medium, as explained in Section 3.3.1 of Chapter 3. Model-3 and its control were in culture for a total of 21 days.

A summary of the culture set-up is shown in Figure 5.3.
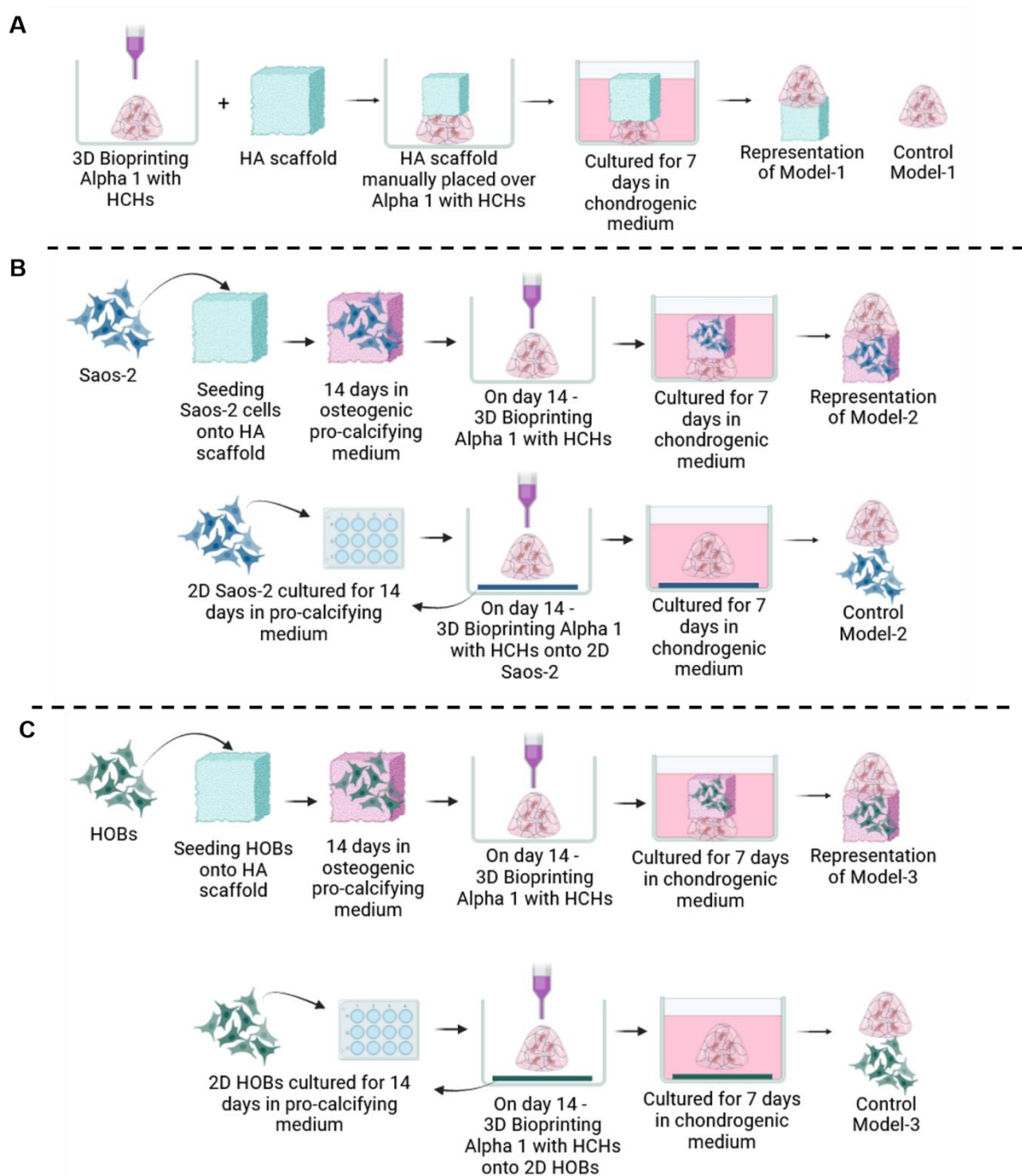
Figure 5.3. A) Manufacturing schematic of Model-1. B) Manufacturing schematic of Model-2. C) Manufacturing schematic of Model-3. Illustrations were made with BioRender.

5.3.4 3D Bioprinted construct biological characterisation

The biological characterisation of the 3D bioprinted constructs was performed to assess cell viability, histological features, protein production, and RNA expression. Physical characterisation of the individual sections (HA scaffold and 3D bioprinted Alpha 1) is not presented as it is expected to be the same as previously reported in Chapters 3 and 4.

5.3.4.1 Cell viability and cell proliferation

DNA quantification was assessed using a Quant-iT PicoGreen dsDNA Assay Kit (Thermo Fisher, P7589). Model-1 constructs were mixed with pre-warmed (37°C) protease solution (10 mg/mL) (Sigma Aldrich, P5147-1G), crushed with a spatula and vortexed until the Alpha 1 and the HA sections were dissolved and broken, respectively. This mixture was then incubated at 37°C for 5 minutes. Sequentially, these samples were mixed with 500 µL of 2X TE Buffer from the Quant-iT PicoGreen dsDNA Assay Kit and 1% Triton X in UltraPure™ DNase/RNase-Free Distilled Water (Thermo Fisher, 10977-035). Mixtures were then incubated at 37°C for 30 minutes and placed at -20°C. Samples were subjected to three freeze-thaw cycles before the assay was performed. DNA extraction of Alpha 1 control Model-1 was performed as stated in Chapter 3, Section 3.3.7.

PicoGreen dye was diluted in a concentration of 1:200 in the 2X TE Buffer. 100 µL from each sample were pipetted in a black/opaque 96 well-plate. An additional 100 µL of the PicoGreen dye solution was added and left for 5 minutes under constant mixing at room temperature. Fluorescence was immediately measured using a plate reader at excitation and emission wavelengths of 480 and 520 nm, respectively. DNA concentration was obtained from these measurements.

5.3.4.2 Histological processing and cryosectioning

3D Bioprinted constructs were fixed overnight at 4°C in 10% formalin solution in neutral buffer (Sigma Aldrich, HT501128). After fixation, samples were washed for 5 minutes in PBS (phosphate-buffered saline) and left for 3 hours in 30% sucrose (Sigma Life Sciences, S9378) solution in PBS (Gibco, 20012-019) to dehydrate them. They were then submerged in a 50:50 ratio mixture of 30% sucrose solution and OCT (Optimal cutting temperature) mounting media (VWR chemicals, 361603E) overnight at 4°C. Samples were then placed in cryomolds filled with OCT mounting media and snap-frozen using liquid nitrogen. The samples were cryosectioned, using a ThermoScientific cryotome FSE, in 8 µm thick slices for further immunohistochemistry processing.

Model-1 constructs were fixed overnight at 4°C in 10% formalin solution in neutral buffer. Instead of being further dehydrated, embedded and cryosectioned, they were directly immunofluorescently labelled as described below.

5.3.4.2.1 H&E staining

Previously optimised H&E (haematoxylin and eosin) staining of 3D bioprinted constructs (Section 3.3.9 in Chapter 3) was performed on the cryosections.

5.3.4.2.2 Immunofluorescence labelling

Model-1 whole fixated samples were physically separated into Alpha 1 and HA parts using a spatula. The labelling process on each part independently was the same as the one described for the cryopreserved sections below.

Cryopreserved sample sections were rehydrated for 10 minutes with PBTD (PBS + 1.1% DMSO + 0.1% Tween 20) and subsequently fixed for 10 minutes using 10% formalin solution in neutral buffer. Sections were then blocked for 1 hour at room temperature using 5% BSA (bovine serum albumin) in PBTD (Sigma Aldrich, A2153).

Primary antibody incubation was performed overnight at 4°C, keeping slides in a humidity chamber. Antibodies were added in pairs onto the cryosections, matching different antibody species. Collagen type-II primary antibody (Invitrogen, PA1-36059) was diluted at a ratio of 1:50; aggrecan primary antibody (Abcam, ab3778) was diluted at a ratio of 1:100 with SOX-9 primary antibody (Abcam, ab185966) diluted at a ratio of 1:100; collagen type-I primary antibody (Abcam, ab34710) was diluted at a ratio of 1:250 with collagen type-X primary antibody (Abcam, ab49945) diluted at a ratio 1:100. All antibodies were diluted into PBTD with 5% BSA. All sections were washed in PBS for 5 minutes after primary antibody staining was performed.

Secondary antibody incubation was performed at room temperature. For collagen type-II, SOX-9 and collagen type-I labelling, secondary antibody AlexaFluor-488 goat anti-rabbit (Invitrogen, A11008) was incubated for 2 hours at a ratio of 1:200 in PBS. For aggrecan and collagen type-X AlexaFluor 594 goat anti-mouse secondary antibody (Abcam, ab150116) diluted at a ratio of 1:200 for 2 hours in PBS. Samples labelled with collagen type-II were incubated with the secondary antibody alongside phalloidin (Invitrogen, A12381) at a ratio of 1:200 in PBS for 2 hours.

All sections were then washed for 5 minutes in PBS, and nuclei staining was performed by incubating the sections for 3 minutes at room temperature with DAPI (4′,6-diamidino-2-phenylindole (Thermo Fisher, 62248) diluted at a ratio of 1:200 in PBS. Samples were then washed with PBS for 5 minutes. Samples were imaged using an Olympus DP80 microscope.

5.3.4.3 RNA Extraction and Comparative qPCR

3D pellet and Alpha 1 controls were processed as previously explained in Section 3.3.12 in Chapter 3. Saos-2 2D culture control was processed as stated in Section 4.3.4.5 in Chapter 4 to extract their mRNA. For Model-1, the RNA extraction was performed as the Peptigel® extraction method (Section 3.3.12 in Chapter 3). In short, the biphasic construct was mixed into pre-warmed (37 °C) protease solution (10 mg/mL) (Sigma Aldrich, P5147-1G) and vortexed for 30 seconds to ensure that the

Alpha 1 section of the biphasic construct was digested. To initiate RNA extraction, 350 μL of the RNeasy lysis buffer with 1% β-mercaptoethanol was mixed with the constructs and vortexed for 1 minute. Subsequently, the QIAGEN RNeasy Mini Kit was used (QIAGEN, 74104), and the suggested instructions were followed.

For Model-2 and Model-3 samples, there was an initial physical separation of both compartments. A spatula was used to peel off the cartilage section from the HA compartment. Both sections were processed separately with different RNA extraction protocols, following the previously optimised methods for each section. The Alpha 1 section was processed as previously stated in Section 3.3.12 of Chapter 3; the HA construct was processed following the RNA extraction method from Section 4.3.4.5 in Chapter 4. mRNA levels were quantified using a Nanodrop spectrophotometer. cDNA was formed using the High-Capacity RNA-to-cDNA Kit (ThermoFisher, 4387406) as specified by the manufacturer.

Gene expression levels of collagen type-II (Col-II), aggrecan (AGC), SOX-9 (SOX-9), collagen type-I (Col-I), RUNX2 (runt-related transcription factor 2), ALP (alkaline phosphatase), and collagen type-X (Col-X) were analysed by comparative qPCR using GAPDH (glyceraldehyde-3-phosphate dehydrogenase) as a housekeeping gene. Primer sequences are reported in Table 3.1, Chapter 3. Gene expression fold of change was calculated by the comparative cycle threshold (CT) method, using the expression levels of the 3D cell pellet or the bone-like 2D cultures for the cartilage and HA sections, respectively, as the reference for the $2^{-\Delta\Delta Ct}$ calculation.

5.3.4 Statistical analysis

GraphPad Prism 9 was used for the graphical representation of data and statistical analysis. All graphs show error bars representing the standard deviation. For DNA quantification, a two-way ANOVA (analysis of variance) was performed. The statistical significance of the qPCR analysis was calculated by doing one-way ANOVA with multiple comparisons for each gene expression and manually plotting the different significant levels in combined graphs. The Kruskal-Wallis one-way ANOVA was

performed for those data sets that did not pass the normality test. Statistical significance was calculated with a confidence interval of $p < 0.05$.

5.4 Results

5.4.1 Optimisation of the 3D bioprinting set-up using Model-1: upright vs. inverted.

Two printing strategies were evaluated to manufacture the osteochondral tissue models: upright, where 3D bioprinted Alpha 1 with HCHs is over the HA scaffold; and inverted, where Alpha 1 with HCHs is 3D bioprinted in 12 well plates and the HA scaffold placed over it; Figure 5.2.

Upright 3D bioprinted samples were manufactured using the 3D-printed custom holders (Figure 5.1). Although this manufacturing strategy showed to be effective by keeping the HA samples in place, it presented other issues, such as the low adhesion between both sections of the biphasic constructs, leading to Alpha 1 delamination, (shown in Appendix A5.1 Figure A5.1). Additionally, even if the samples were kept connected during the culture time, they would rapidly dissolve due to the high Alpha 1 surface area exposed to the culture medium, both above and below, through the pores of the HA construct, as seen in Figure 5.4A.

An alternative inverted manufacturing method was tested to promote adhesion between the two sections of Model-1 and reduce the Alpha 1 surface area directly exposed to the culture medium to avoid degradation. For the inverted approach, the Alpha 1 section was 3D bioprinted at the bottom of the well, and the HA construct was manually placed on top, Figure 5.2. This strategy facilitated the adhesion between both sections due to the force of gravity compressing the HA construct towards Alpha 1. This kept Alpha 1 in place, prevented it from floating and promoted its infiltration in the pores of the ceramic structure. The surface area interaction was reduced by having the bottom of Alpha 1 attached to the well plate and the top in contact with the ceramic section, slowing down the degradation rate, Figure 5.4B. Due to these advantages, the inverted manufacturing method was used to perform further experiments.
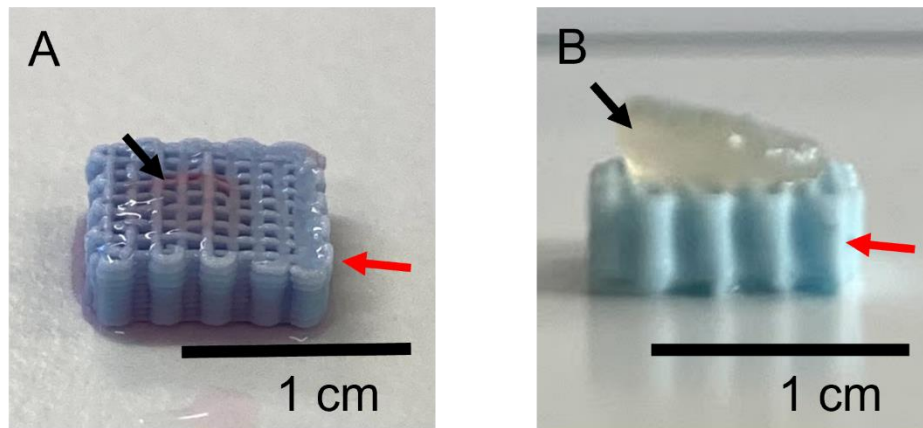
Figure 5.4. Photographs of Model-1 samples manufactured with A) the custom holders using the upright method and B) manufactured using the inverted method. For ease of comparison, the inverted manufactured biphasic construct is imaged with the HA scaffold at the bottom. Black arrows depict the Alpha 1 section after 7 days of culture. Red arrows depict the acellular HA scaffold section.

5.4.2 Characterisation of Model-1 to assess the effect of HA on Alpha 1 embedded HCHs

5.4.2.1 DNA Quantification of Model-1

DNA quantification was used to assess the effect of including an HA construct in direct contact with Alpha 1 on the HCHs viability. Figure 5.5 shows no significant differences between day 0 and day 7 time points when comparing Model-1 and its control. There was a further decrease in the DNA concentration of Model-1; however, this was not significant. These measurements confirmed that the inclusion of this ceramic compartment did not significantly affect the viability of HCHs embedded in Alpha 1 samples.
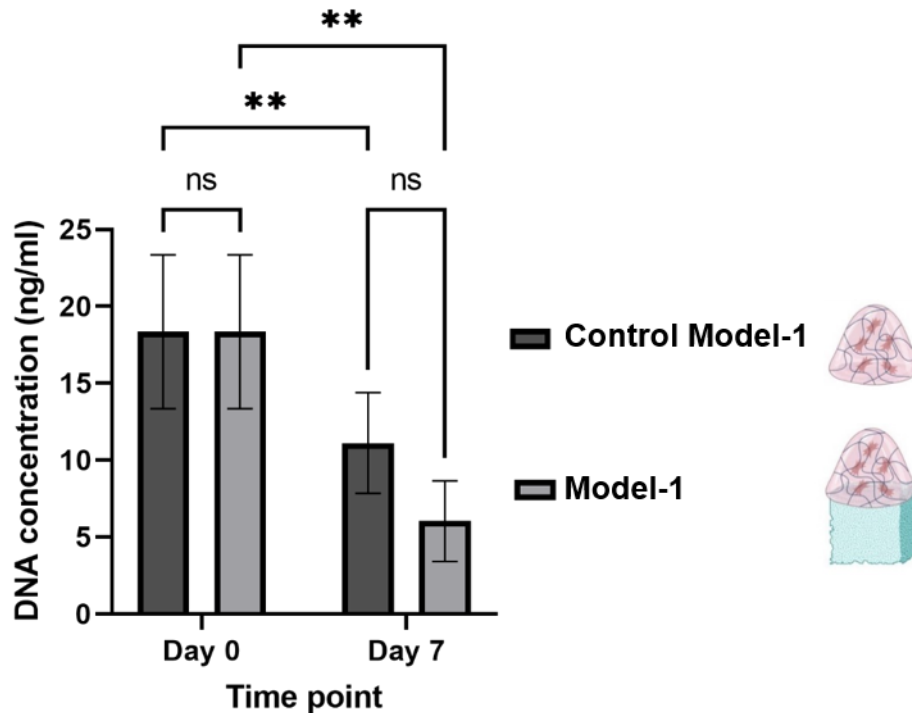
Figure 5.5. DNA quantification was obtained with PicoGreen of the control Model-1 (Alpha 1 with HCHs) and Model-1 (Alpha 1 with HCHs cultured with HA) over 7 days of culture. N = 9 for Alpha 1; N = 3 for Alpha 1 + acellular HA. ** - p < 0.01. Diagrams are added for clarity, made with BioRender.

5.4.2.2 Histological Assessment of Model-1

5.4.2.2.1 H&E staining for cell morphology, extracellular matrix deposition and Alpha 1 penetration assessment in Model-1

Routine H&E was performed on Model-1 and Model-1 without cells as a comparison. This was performed to investigate the cell morphology, matrix deposition on the cartilage section, and Alpha 1 penetration in the HA pores. Figure 5.6 shows the H&E stains performed on cross-sections of samples. The first panel showed the cross-section of a fully acellular Model-1 after being cultured for 7 days in chondrogenic medium. When performing the sectioning and subsequent staining protocol, the HA section dissolved and could not be stained or imaged. This first set of images (Figure 5.6A and B) shows how the acellular Alpha 1, stained in pink, penetrated the ceramic

structure, resulting in a wavy pattern on the bottom surface. Additionally, ceramic particles, imaged as black speckles, were visibly in direct contact with Alpha 1 and penetrating in the contact surface (Figure 5.6). However, whether this was a phenomenon representative of what happens *in vitro* or if it resulted from the staining protocol was unclear.

The second set of images (Figure 5.6C and D) shows Model-1 after 7 days of culture. This set of images also presented signs of Alpha 1 penetration in the HA construct and the infiltration of ceramic particles into Alpha 1. The particle infiltration was higher, making it complicated to discern cell nuclei from ceramic particles due to the similarities in colour post-staining. Regardless, the Alpha 1 section showed a smaller size than its acellular equivalent, further confirming the phenomenon previously observed, where cellularised Alpha 1 degraded faster than acellular ones (Chapter 3).
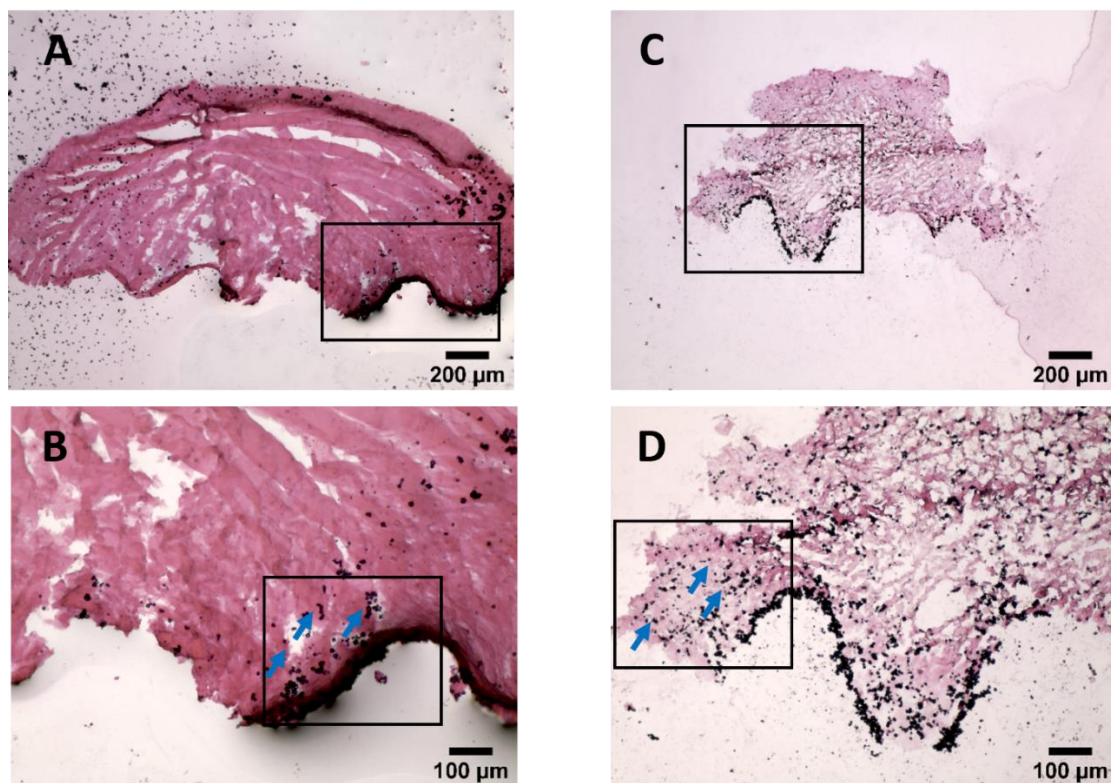
Figure 5.6. A) Low magnification and B) high magnification H&E staining image of acellular Model-1 after 7 days in culture. C) Low magnification and D) high magnification H&E staining image of Model-1 over 7 days of culture. The squares in the bottom images depict the described phenomenon of Alpha 1 penetration in the HA scaffolds and the HA particles (indicated by blue arrows) that dissolved into Alpha 1 during the staining protocol.

5.4.2.2.2 Histological assessment through immunofluorescence labelling in Model-1

Immunofluorescence labelling was performed on Model-1 and compared to its control. The HA section, when sectioned, fully dissolved as labelling protocols were performed. Therefore, the labelling was performed in the samples, whole, to avoid histological information loss. Figure 5.7 shows the immunofluorescence labelling images of both sections of these biphasic constructs.

5.4.2.2.2.1 F-actin labelling for cell morphological assessment in Model-1

F-actin labelling was performed to assess cell morphology. Figure 5.7A shows the Alpha 1 section, depicting the expected circular cell morphology of the embedded HCHs and their self-assembly into cell clusters. Figure 5.7B shows the HA section, which presented HCHs that migrated from the Alpha 1 section. These cells presented a spread-out fibroblastic morphology. This change in morphology was expected, as a stiffer substrate makes HCHs adopt this configuration [328].

5.4.2.2.2.2 SOX-9 labelling to assess changes in chondrogenic potential of Alpha 1 in Model-1

SOX-9 labelling was performed to assess the chondrogenic behaviour of the HCHs. Figure 5.7C shows an extremely low expression of SOX-9 in the cells embedded within the Alpha 1 section. This was unexpected as the expression levels observed in Alpha 1 cultures previously showed high levels of this transcription factor (Chapter 3). However, as these constructs were labelled and imaged as a whole, there was a limitation when performing image acquisition due to refraction from Alpha 1. Further quantification analysis of the expression levels of SOX-9 was later performed to confirm the observed results.

Figure 5.7D shows that the cells that migrated onto the HA section also showed minimal to no expression of SOX-9, as expected. The substrate change can promote

hypertrophic behaviour in chondrocytes [328]; hence, a lower expression of SOX-9 was expected.

5.4.2.2.2.3 Collagen type-II labelling to assess chondrogenic extracellular matrix production in Model-1

Collagen type-II labelling was performed to assess the production of this key chondrogenic extracellular matrix protein. Figure 5.7E shows the expression of collagen type-II appearing mainly inside the cell clusters. This expression was consistent with previous observations in the Alpha 1 culture alone, Section 3.4.3.3.3 of Chapter 3. Elevated levels of collagen type-II expression in the cell clusters were shown, indicating chondrogenic extracellular matrix deposition. Figure 5.7F shows lower levels of collagen type-II expression on the HCH cells which migrated into the HA scaffold.

5.4.2.2.2.4 Aggrecan labelling to assess chondrogenic protein extracellular matrix production in Alpha 1 in Model-1

Aggrecan labelling was performed to assess the production of the chondrogenic extracellular matrix. Figure 5.7G shows elevated levels of aggrecan expression in Alpha 1 with increased red fluorescence, making the surface cell clusters visible and clear. This indicated further chondrogenic extracellular matrix production in these clusters. Low levels of aggrecan expression were also seen in the cells that had migrated onto the HA scaffold, Figure 5.7H. However, these were visibly lower than the expression observed in the cell clusters, confirming that this marker is mostly expressed in those cells which are part of cell cluster formations.

5.4.2.2.2.5 Collagen type-I labelling to assess changes in HCH behaviour towards an osteogenic phenotype in Model-1

Collagen type-I was immunofluorescently labelled to assess the expression of this osteogenic protein in HCHs. Figure 5.7I shows minimal levels of collagen type-I in the Alpha 1 section, represented by a faint glow. This indicated that the HCHs phenotype was healthy and not fibrotic [329]. Figure 5.7J shows elevated levels of collagen type-I expression on the cells that migrated from Alpha 1 onto the HA section, suggesting a phenotype change towards an osteogenic lineage.

5.4.2.2.2.6 Collagen type-X labelling to assess changes in HCH behaviour towards a hypertrophic phenotype in Model-1

Collagen type-X labelling was performed to assess the transition of the HCHs into a hypertrophic state. Figure 5.7K shows no collagen type-X in the Alpha 1 section, suggesting this protein was not expressed. This indicated that chondrocytes were not becoming hypertrophic close to the interface or when in contact with the HA section. Figure 5.7L shows a minimal expression of collagen type-X on the cells that migrated onto the HA section, depicting no HCH hypertrophy in the HCHs attached to HA.

Alpha 1 section   HA section

F-actin

SOX-9
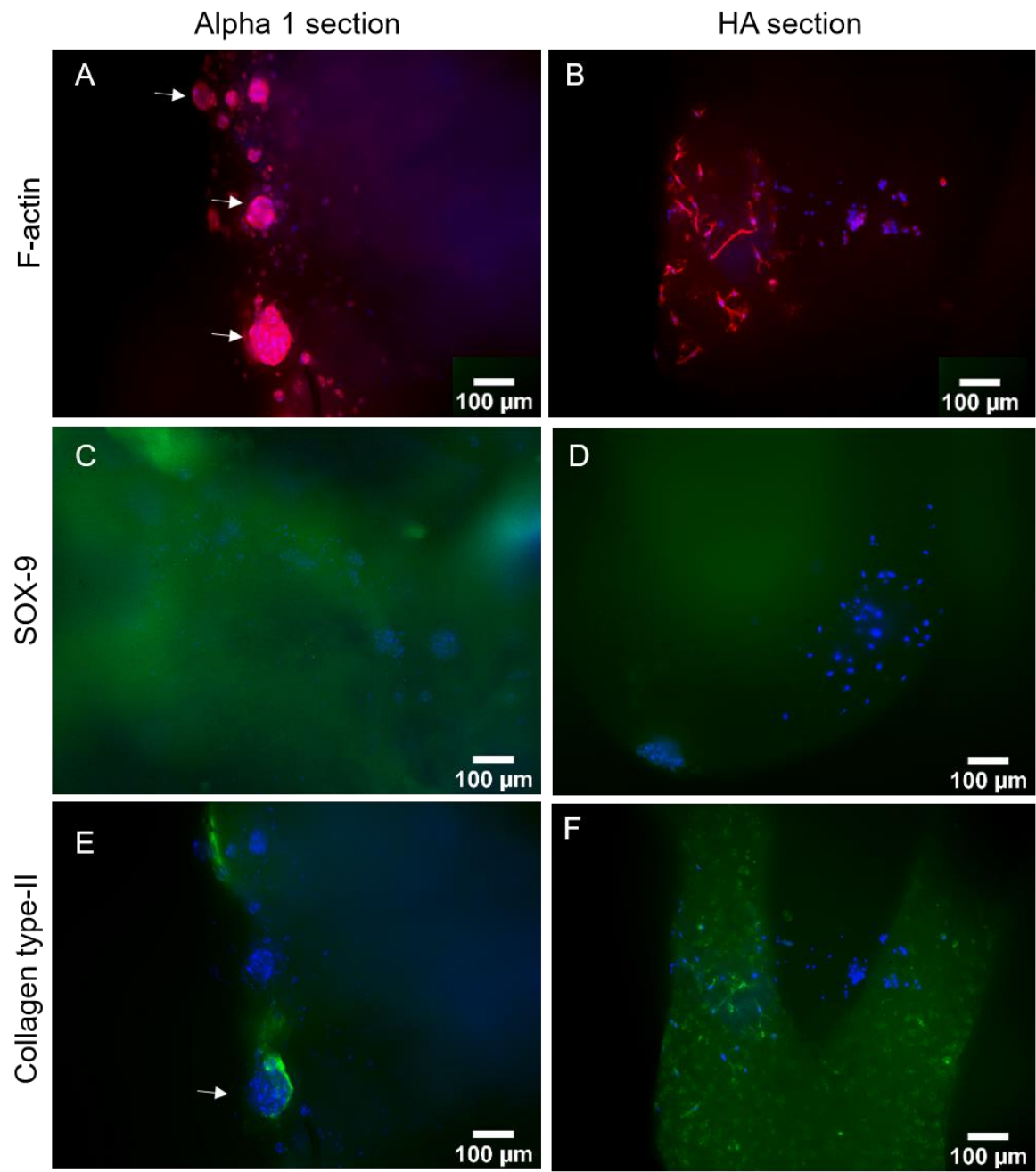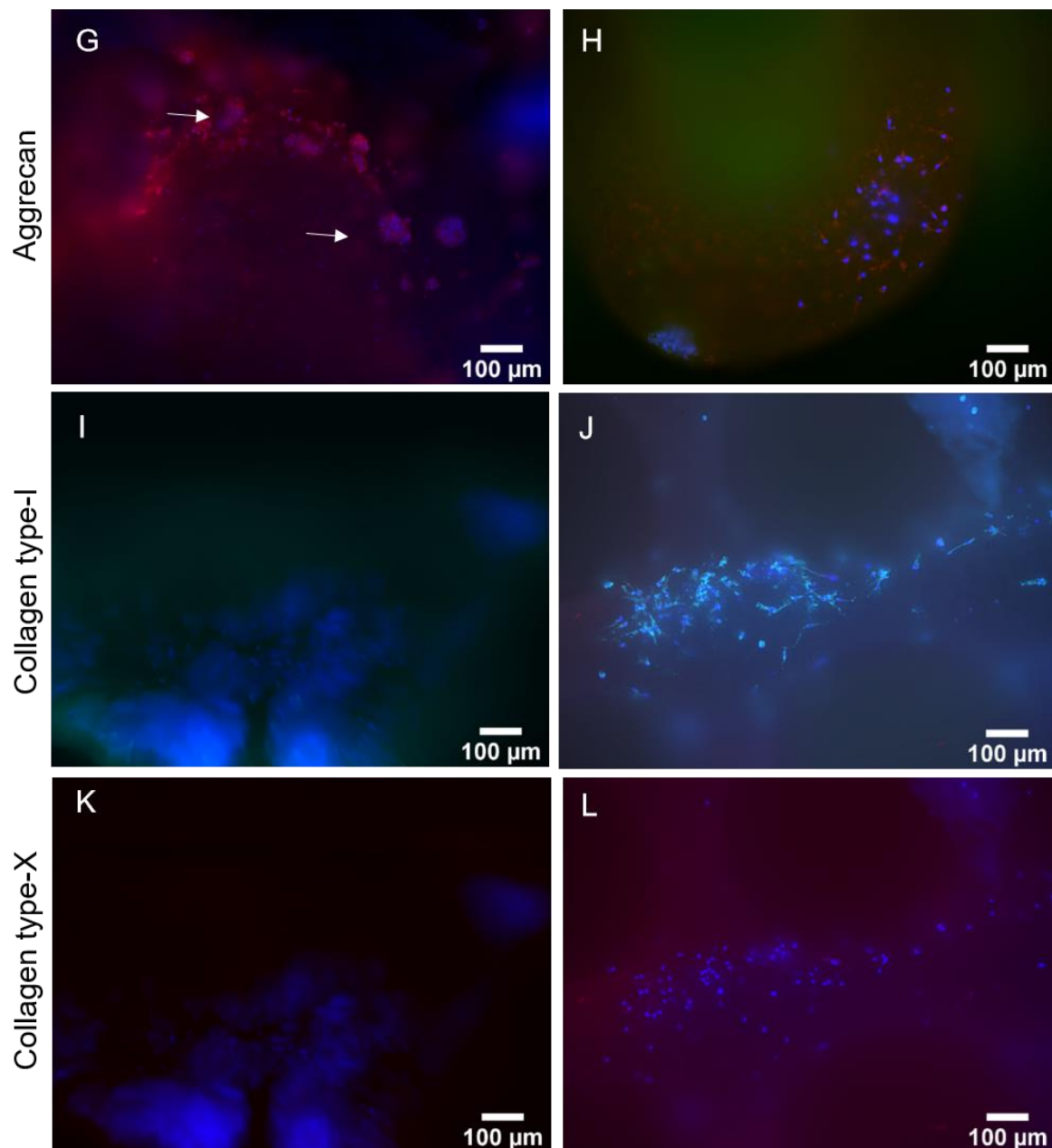
Collagen type-II

Figure 5.7. F-actin (red) and nuclei (blue) labelling of HCHs (A) in Alpha 1 (arrows point at the cell clusters) (B) and in the HA section. SOX-9 (green) and nuclei (blue) labelling of HCHs (C) in Alpha 1 and (D) in the HA section. Collagen type-II (green) and nuclei (blue) labelling of HCHs (E) in Alpha 1 (arrow depicts production in cell clusters) and (F) the HA section. Aggrecan (red) and nuclei (blue) labelling of HCHs (G) in Alpha 1 and (H) in the HA section. Collagen type-I (cyan) and nuclei (blue) labelling of HCHs (I) in Alpha 1 and (J) in the HA section. Collagen type-X (red) and nuclei (blue) labelling of HCHs in (K) the Alpha 1 section and (L) the HA section. Samples were imaged after 7 days of culture. (Negative controls are shown in Appendix A5.2, Figure A5.2.)

5.4.2.3 mRNA expression assessment through comparative qPCR of Model-1

Comparative qPCR of all chondrogenic, osteogenic and hypertrophic chondrogenic genes was performed on Model-1 and compared to the control Model-1 and 3D pellets. Figure 5.8 shows the expression profile of the Alpha 1 section in Model-1 after 7 days of culture. Data previously reported in Chapter 3 comparing Alpha 1 alone culture (control Model-1) to the 3D pellet is not described here, only compared against new data.

Figure 5.8A shows the expression of chondrogenic genes. This first graph depicts the expression of collagen type-II, aggrecan and SOX-9, comparing the new results to those reported in Chapter 3. Non-significant upregulation of collagen type-II expression was observed between the 3D pellet and the Alpha 1 section in Model-1. This suggested a higher degree of chondrogenic extracellular matrix production. Aggrecan mRNA expression showed no significant downregulation when compared to control Model-1 and no significant upregulation with respect to the 3D pellet control. This suggested that the Alpha 1 section was still promoting the expression of aggrecan mRNA. However, incorporating the ceramic scaffold diminished the chondrogenic potential of the Alpha 1, producing less chondrogenic extracellular matrix.

SOX-9 expression was significantly (* - $p < 0.05$) upregulated in Model-1 with respect to the 3D pellet control, suggesting that the incorporation of Alpha 1, regardless of the adjacent HA incorporation, promoted and maintained chondrogenesis better than the 3D pellet after 7 days of culture.

Figure 5.8B shows the expression levels of osteogenic markers, collagen type-I, RUNX2 and ALP. Significant downregulation (** - $p < 0.01$) of collagen type-I was observed between the control Model-1 and Model-1. This suggested that the chondrogenic profile of Model-1 was healthier than the control, avoiding fibrotic cartilage production [329]. RUNX2 and ALP expressions showed no significant differences across samples. The expression levels in both markers followed a similar pattern, being upregulated in Model-1, suggesting the ceramic sections' introduction drove the upregulation of these osteoblastic genes. However, these differences were not significant.

Figure 5.8C shows the expression of the hypertrophic marker, collagen type-X. This marker, characteristic of hypertrophic chondrocytes, which appear closer to the interface of the osteochondral unit, was expected to be upregulated in Model-1. However, the opposite expression was observed. There was a significant downregulation (** - $p < 0.01$) between the 3D pellet control and Model-1, as well as between the control Model-1 and Model-1 (* - $p < 0.05$), showing that the introduction of a ceramic section did not promote hypertrophy.
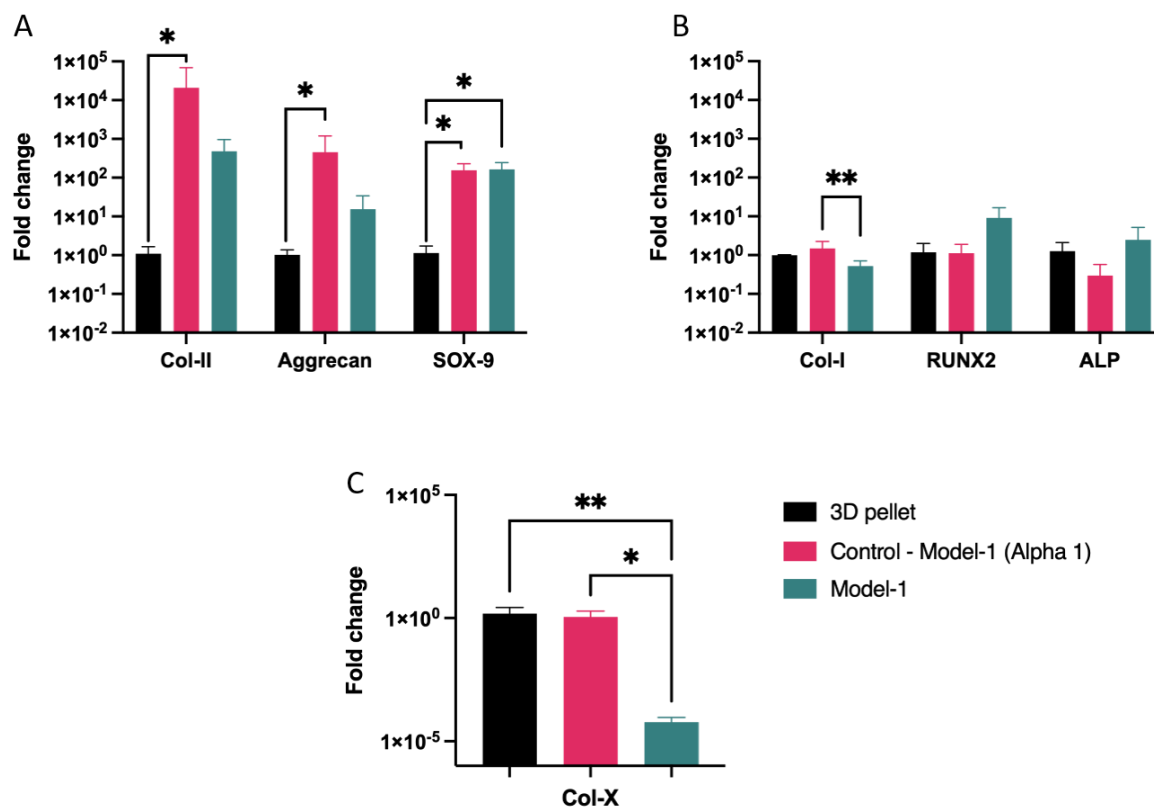
Figure 5.8. Comparative qPCR showing fold change in chondrogenic (A), osteogenic (B), and hypertrophic (C) genes in the Alpha 1 section of Model-1 on day 7 compared to 3D pellet control and control Model-1. N = 3 for the 3D pellet control; N = 6 for Alpha 1 (control Model-1), Model-1; One-way ANOVA performed with Kruskal-Wallis for each gene. * - $p < 0.05$; ** - $p < 0.01$.

5.4.3 Characterisation of Model-2 to assess the effect of Saos-2 seeded on HA on Alpha 1 embedded HCHs

5.4.3.1 Histological assessment of Model-2 and control Model-2

5.4.3.1.1 H&E staining for cell morphology, extracellular matrix deposition and Alpha 1 penetration in Model-2

Model-2 presented a similar Alpha 1 penetration into the HA scaffold pores as the Model-1. However, due to the limited Alpha 1 volume left and the high degree of ceramic particle infiltration, it became extremely difficult to differentiate cell types. Figures 5.9A and B depict the Alpha 1 section's remains and some parts of the Saos-2+HA section. Unlike Model-1, the HA section in Model-2 dissolved less than in Model-1, and the HA studs were still visible. This was potentially due to the Saos-2 cells generating their matrix, which, post-processing, stayed attached to the microscope slide. Additionally, it was difficult to discern cell morphology or distribution from the sample sections due to Alpha 1 degradation and HA particle interference, hence other imaging techniques were required.

Model-2 was compared to a control Model-2, made of Alpha 1 co-cultured with Saos-2 in a 2D cell layer. Control Model-2 presented features similar to the ones seen on day 7 of Alpha 1 (control Model-1). Cells in the centre of Alpha 1 retained the expected circular shape, and cell clusters started to be visible on the surface, Figure 5.9C and D. This suggested that when Alpha 1 was cultured in co-culture with bone-like cells (Saos-2 cells), its chondrogenic behaviour was not compromised. The nature of the HA particles and this staining made it hard to differentiate them from cells. Therefore, additional imaging analyses were performed to visualise cell morphology and configuration.
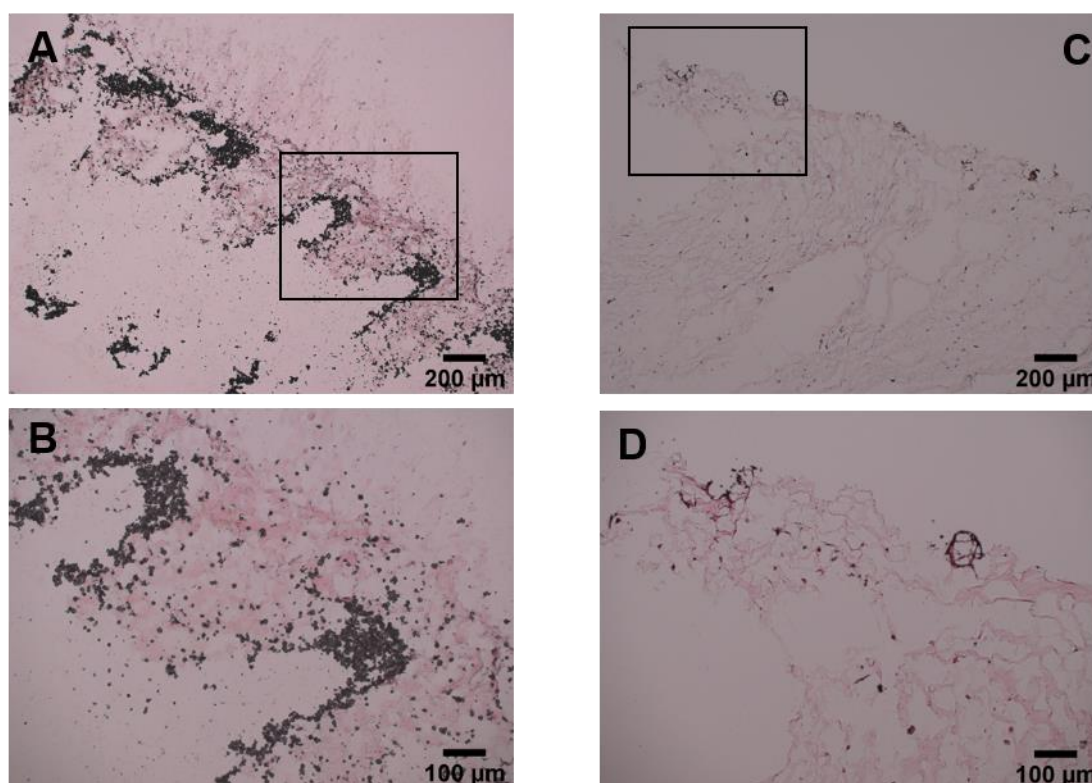
Figure 5.9. H&E staining images of (A) and (B) Model-2, and (C) and (D) control Model-2 over 21 days of culture in total. A and C show images at a lower magnification. B and D show images at a higher magnification, corresponding to the highlighted squares in A and C, respectively.

5.4.3.1.2 Histological assessment through immunofluorescence labelling of Model-2

5.4.3.1.2.1 F-actin and collagen type-II labelling for cell morphological assessment and extracellular matrix protein production in Model-2

Immunofluorescence labelling of actin filaments and collagen type-II was performed to assess cell morphology and cartilage-specific extracellular protein production. Figure 5.10 shows fluorescent images of labelled collagen type-II in green and the actin filaments labelled with phalloidin in red. The control samples, control Model-2, further confirmed what was observed in the H&E staining. Cell clusters were present, similar to those observed in the Alpha 1 (control Model-1), Figure 5.7. These presented elevated levels of collagen type-II expressed inside, and the F-actin labelling depicted

the cell morphology change from the circular-shaped cells in the centre of Alpha 1 to a more spread-out morphology in the cell clusters.

Model-2 samples were cryosectioned to assess the interactions happening at the interface between Alpha 1 and the ceramic construct. Figure 5.10 shows a transition from circular-shaped cells on the Alpha 1 section to more spindle-shaped cells when in contact with the HA scaffold. These observations coincided with the ones seen in Model-1. The intersection photos showed distinct levels of collagen type II expression, with lower levels inside the cells close to the interface but higher intensities on the HA section. Negative control images (Appendix A5.2, Figure A5.2) confirmed that this was collagen type-II deposition, not autofluorescence from the HA particles. Therefore, there was an extracellular deposition of collagen type-II which attached to the HA section.
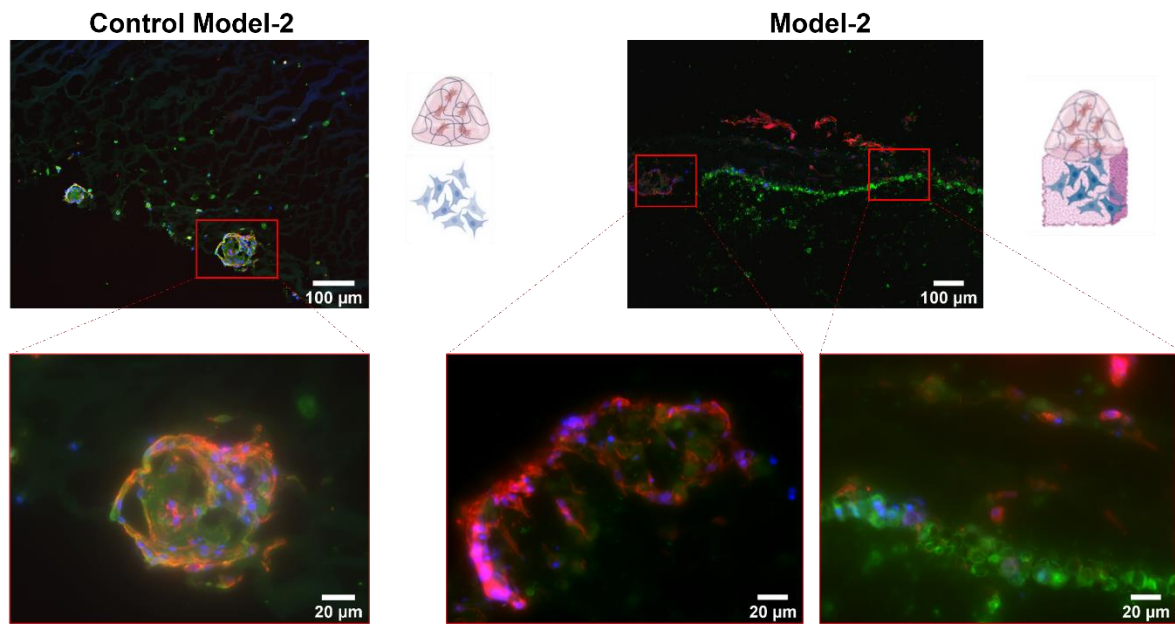
Figure 5.10. Collagen type-II (green) and F-actin (red) labelling and nuclei (blue) of HCHs in Alpha 1 co-culture with 2D Saos-2 cells control (control Model-2) and Model-2. The top row shows a lower magnification with highlighted sections in red, which are shown in the bottom row at a higher magnification. Samples were imaged on day 21. Negative control labelling is shown in Appendix A5.2, Figure A5.2. Diagrams of models are added for clarity, made with BioRender.

5.4.3.1.2.2 SOX-9 labelling to assess changes in chondrogenic potential of Alpha 1 in Model-2

SOX-9 expression was assessed to determine the chondrogenic potential and behaviour of the Alpha 1 embedded HCHs in Model-2. SOX-9 expression was observed in the cell clusters of control Model-2, Figure 5.11. In Model-2 constructs, SOX-9 expression was seen in the cells which formed the interface on the Alpha 1 side but not on those attached to the HA section. It was difficult to visualise the expression of this marker further away from the interface due to the limitations of the labelling protocol. Some of the Alpha 1 sections tended to wash away, making assessing that section of the construct complicated. Once again, further analysis techniques, such as qPCR, were required to quantify the expression levels of this transcription factor.

5.4.3.1.2.3 Aggrecan labelling to assess chondrogenic protein extracellular matrix production in Model-2

Aggrecan labelling was performed to assess cartilage-specific extracellular matrix protein production. Aggrecan labelling on the control Model-2 showed an expression on day 7 similar to that observed in Alpha 1 (control Model-1). There were higher expression levels on the surface cell clusters, but lower levels are seen in the cells embedded in the middle of Alpha 1, Figure 5.11. Model-2 constructs presented prominent levels of aggrecan in the cells on the surface of Alpha 1 and those HCHs closer to the interface. Saos-2 cells, still attached to the HA section, appeared to express this marker, a phenomenon previously reported in the literature [324].

Control Model-2

Model-2

100 µm

100 µm

20 µm

20 µm

20 µm

20 µm
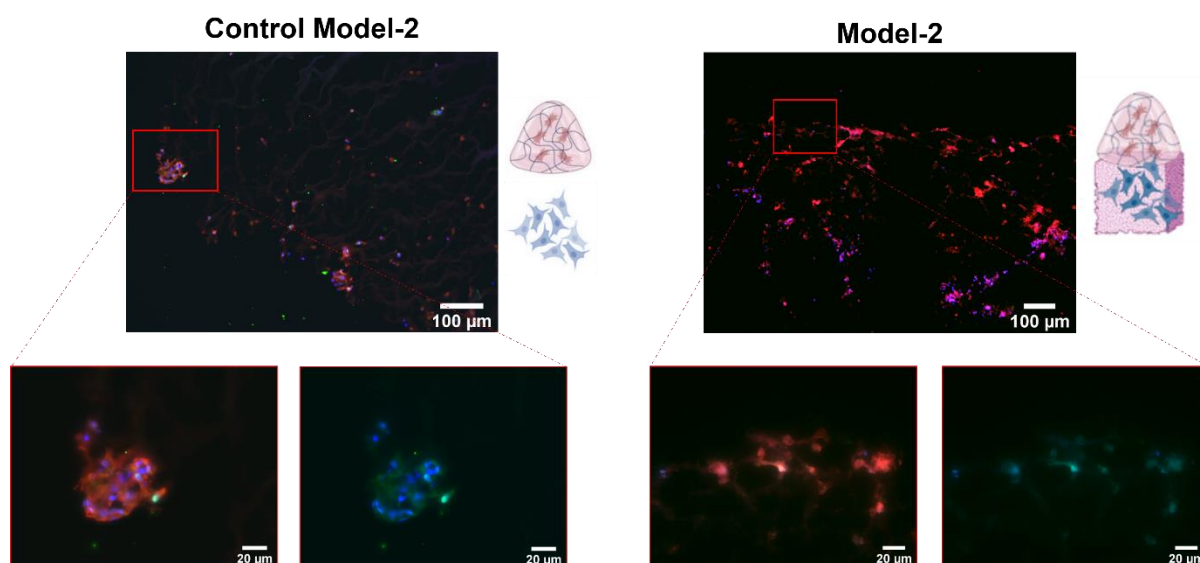
Figure 5.11. Aggrecan (red) labelling and SOX-9 (green) and nuclei (blue) of HCHs in Alpha 1 co-culture with 2D Saos-2 cells control (control Model-2) and Model-2. The top row shows a lower magnification with highlighted sections in red, which are shown in the bottom row at a higher magnification. The bottom row shows the images divided by channels for easier differentiation of the green (SOX-9) channel. Samples were imaged on day 21. Negative control labelling is shown in Appendix A5.2, Figure A5.2. Diagrams of models are added for clarity, made with BioRender.

5.4.3.1.2.4 Collagen type-I and collagen type-X labelling to assess changes in HCH behaviour towards an osteogenic or hypertrophic phenotype in Model-2

Collagen type-I and collagen type-X expression were assessed on control Model-2. Collagen type-I was expressed in the cell clusters which appeared on the surface of Alpha 1 but less intensely on the cells within Alpha 1, which were not in clusters, Figure 5.12. This suggested a transitioning towards a more fibrotic chondrogenic extracellular matrix expression on the cell clusters [329]. Additionally, no expression of collagen type-X could be observed in either the cell clusters or the cells embedded within Alpha 1. This depicted no chondrogenic hypertrophy in these cells.

Model-2 sections showed similar behaviour, where collagen type-I was highly expressed on the cells near the interface and on the cells that remained attached to the HA structure, Figure 5.12. However, only minimal collagen type-X was observed

in the interface of the construct but not in direct contact with the HA section, suggesting HCHs did not hypertrophy when in contact with Saos-2+HA constructs. Although these images gave an initial understanding of these proteins' expression levels, it was not possible to discern different cell types or quantify the expression levels. Additional analysis techniques, such as qPCR, were required to further quantify these expression levels on each section of the osteochondral constructs.

Figure 5.12. Collagen type-I (cyan) and collagen type-X (red) labelling and nuclei (blue) of HCHs in Alpha 1 co-culture with 2D Saos-2 cells control (control Model-2) and Model-2. The top row shows a lower magnification with highlighted sections in red, which are shown in the bottom row at a higher magnification. Samples were imaged on day 21. Negative control labelling is shown in Appendix A5.2, Figure A5.2. Diagrams of models are added for clarity, made with BioRender.

5.4.3.2 mRNA expression assessment through comparative qPCR of Model-2 and control Model-2

Comparative qPCR of all chondrogenic, osteogenic and hypertrophic chondrogenic genes was performed on both the cartilage and bone-like sections of Model-2 and compared to the corresponding controls, 3D pellets for the cartilage section and the 2D Saos-2 cell culture for the bone-like section. Figure 5.13 shows the expression

profile of the Alpha 1 section, and Figure 5.14 shows the HA section of Model-2. It must be noted that the Alpha 1 section is referred to as being cultured for 7 days. Although the total culture period for the biphasic construct was 21 days, Alpha 1 was added on day 14 and cultured for just 7 days. Data previously reported in Chapter 3 and Chapter 4 is not described here, only compared against new data.

Figure 5.13A shows the expression of chondrogenic genes in the Alpha 1 section of Model-1, Model-2, and control Model-2. This first graph depicted the expression of collagen type-II, aggrecan and SOX-9, comparing the new results to those reported in Chapter 3. Non-significant upregulation of collagen type-II expression was observed between the 3D pellet and the Alpha 1 section of Model-2. This suggested a higher degree of chondrogenic extracellular matrix production. However, the fold change of Model-2 was lower than Model-1, suggesting that the introduction of Saos-2 cells downregulated the expression of this protein. Additionally, a significant downregulation from Alpha 1 (control Model-1) to the Alpha 1 section from control Model-2 further confirmed that the introduction of this bone-like cell generated a change in the genetic expression of the embedded cells within Alpha 1.

Aggrecan mRNA expression showed no significant differences in Model-2 and control Model-2 when compared to the 3D pellet control. The expression of aggrecan in all these samples was downregulated with respect to the Alpha 1 (control Model-1), and not significantly upregulated with respect to the 3D pellet control. This suggested that the Alpha 1 section was still promoting the expression of aggrecan mRNA. However, incorporating Saos-2 cells and the ceramic scaffold diminished the chondrogenic potential of Alpha 1, producing less chondrogenic extracellular matrix.

SOX-9 expression was upregulated in all samples with respect to the 3D pellet control, suggesting that the incorporation of the Alpha 1, regardless of additional conditions, promoted and maintained chondrogenesis better than the 3D pellet after 7 days of culture. There were no significant differences in the expression of SOX-9 between Model-1 and Model-2. This suggested that the HA scaffold's cellularisation did not compromise this key marker's expression on the Alpha 1 section. However, there was a significant downregulation (* - $p < 0.05$) between control Model-2 and Alpha 1

(control Model-1) and Model-1. This downregulation suggested that any observed changes came from the introduction of Saos-2 cells and not from the HA scaffold.
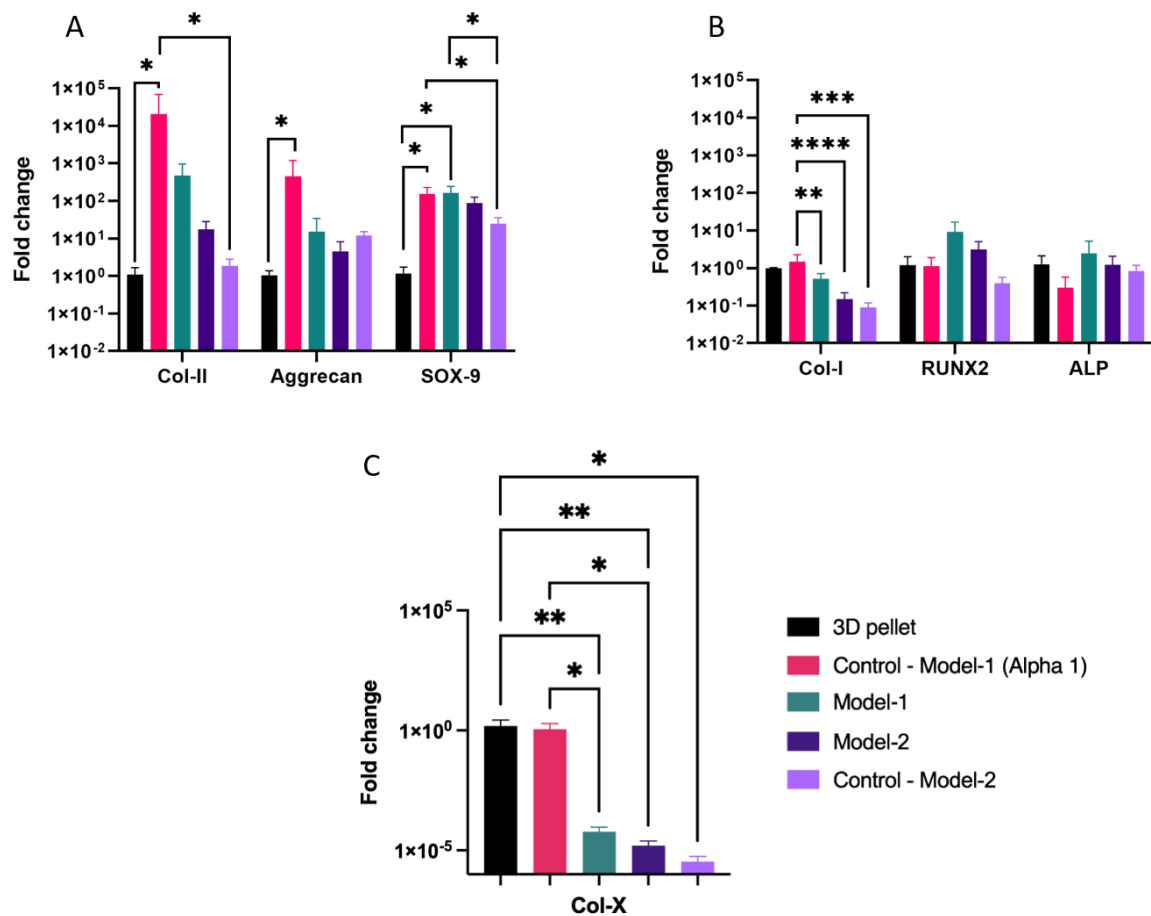
Figure 5.13. Comparative qPCR showing fold change in chondrogenic (A), osteogenic (B) and hypertrophic (C) genes in the Alpha 1 section of Model-1 and Model-2 on day 7 compared to 3D pellet control and respective controls. N = 3 for the 3D pellet control; N = 6 for Alpha 1 (control Model-1), Model-1; Model-2, control Model-2. One-way ANOVA was performed with Kruskal-Wallis for each gene. * - $p < 0.05$; ** - $p < 0.01$; * - $p < 0.001$; **** - $p < 0.0001$. Note that Alpha 1 day 7 in the biphasic constructs, is equivalent to day 21 of the biphasic construct.**

Figure 5.13B shows the expression levels of osteogenic markers, collagen type-I, RUNX2 and ALP. The expression of these markers was expected to be lower or similar to those seen in the 3D pellet control. Higher upregulations were expected to be seen on the Alpha 1 section of Model-2 compared to Model-1.

Significant downregulation (**** - p < 0.0001) of collagen type-I was observed between the Alpha 1 (control Model-1) and Model-2, as well as (*** - p < 0.001) compared to control Model-2. This suggested that the chondrogenic profile of Model-2 and the control were healthier than Alpha 1 (control Model-1), avoiding fibrotic cartilage production [329]. The expression of collagen type-I was lower in Model-2 and its control than in Model-1, suggesting that introducing Saos-2 cells was the main driving force for the downregulation. RUNX2 and ALP expressions showed no significant differences across samples. The expression levels in both markers were downregulated in Model-2 and its control with respect to Model-1. This suggested once again that Saos-2 cells were responsible for this change. However, these differences were not significant.

Figure 5.13C shows the expression of the hypertrophic marker, collagen type-X. This marker was expected to be upregulated in Model-2. However, the opposite expression was observed. There was a significant downregulation between Model-2 and the 3D pellet control (** - p < 0.01) as well as against Alpha 1 (control Model-1).   This showed that introducing ceramic sections and Saos-2 cells did not promote hypertrophy. The effect of Saos-2 cells was greater than the ceramic effect, as the downregulation of control Model-2 was the largest fold change value.

The HA section of Model-2 was also assessed. Figure 5.14A shows the expression of chondrogenic markers in the HA section and compares it to the previously reported expressions of Saos-2 cells on day 14 in 2D cultures and on HA scaffolds (Chapter 4). These samples were compared to the expression of the HA section in Model-2 and the control Model-2 (2D Saso-2 cells co-cultured with Alpha 1). The main difference across these samples relied on the change of chondrogenic media that took place from day 14 to day 21. Due to the lack of sample data on day 21 of the bone-like samples, which were cultured with osteogenic pro-calcifying media, the data from day 14 was used. It was assumed that by making this media change, the osteogenic potential of the 2D culture and HA scaffolds would be halted, and any changes observed were due to the changes in the medium.

No significant differences in collagen type-II and SOX-9 expression were observed across Saos-2 cell samples. This was expected, as they are a bone-like carcinogenic

214

cell line, which is not characterised by the expression of cartilage-like markers. Only aggrecan expression, previously reported [324] to increase in Saos-2 cells when cultured in chondrogenic media, had significant changes. A significant upregulation appeared between Saos-2+HA scaffolds cultured up to day 14 and Model-2 on day 21, after 7 days of chondrogenic medium. This upregulation showed that the medium change impacted the phenotypic expression of Saos-2 cells. It was highly increased when the Alpha 1 compartment was introduced in direct contact with Saos-2 cells.

Figure 5.14B shows expression levels of the osteogenic markers, collagen type-I, RUNX2 and ALP. The main differences were seen in co-culture samples, which experienced the chondrogenic medium change. Collagen type-I was significantly downregulated (**** - $p < 0.0001$) between the 2D culture Saos-2 control on day 14 and the control Model-2. Additionally, a further significant downregulation (**** - $p < 0.0001$) appeared between the control Model-2 and Model-2 on day 21, suggesting that the inclusion of the cartilage-like section further decreased the bone-like behaviour of Saos-2 cells and the production of a bone-like matrix, rich in collagen type-I.

RUNX2, a marker that directs immature bone growth formation [330], presented no significant differences between the 2D control on day 14 and Model-2. However, significant downregulations (*** - $p < 0.001$) were observed between the HA scaffolds on day 14 and Model-2 on day 21. No significant differences were seen across the 2D control samples on day 14 and control Model-2, suggesting that the change in culture medium had no significant effect on the expression of this marker, but the inclusion of a cartilage compartment in direct contact with the HA scaffold did.

A significant ALP downregulation (**** - $p < 0.0001$) between the HA scaffold on day 14 and Model-2 on day 21 was observed, suggesting that the medium change highly interfered with the ALP activity of Saos-2 cells. This lower ALP activity suggested a lower degree of bone matrix mineralisation and maturation. No changes were seen between the 2D control cultures on day 14 and control Model-2. Additionally, no changes were seen between control Model-2 and Model-2.

Figure 5.14C shows the changes in collagen type-X expression. No significant changes were observed, but upregulations were observed in both samples in chondrogenic medium for 7 days, potentially suggesting that this change promoted the expression of this hypertrophic gene in Saos-2, which is not characteristic of this bone cell line.
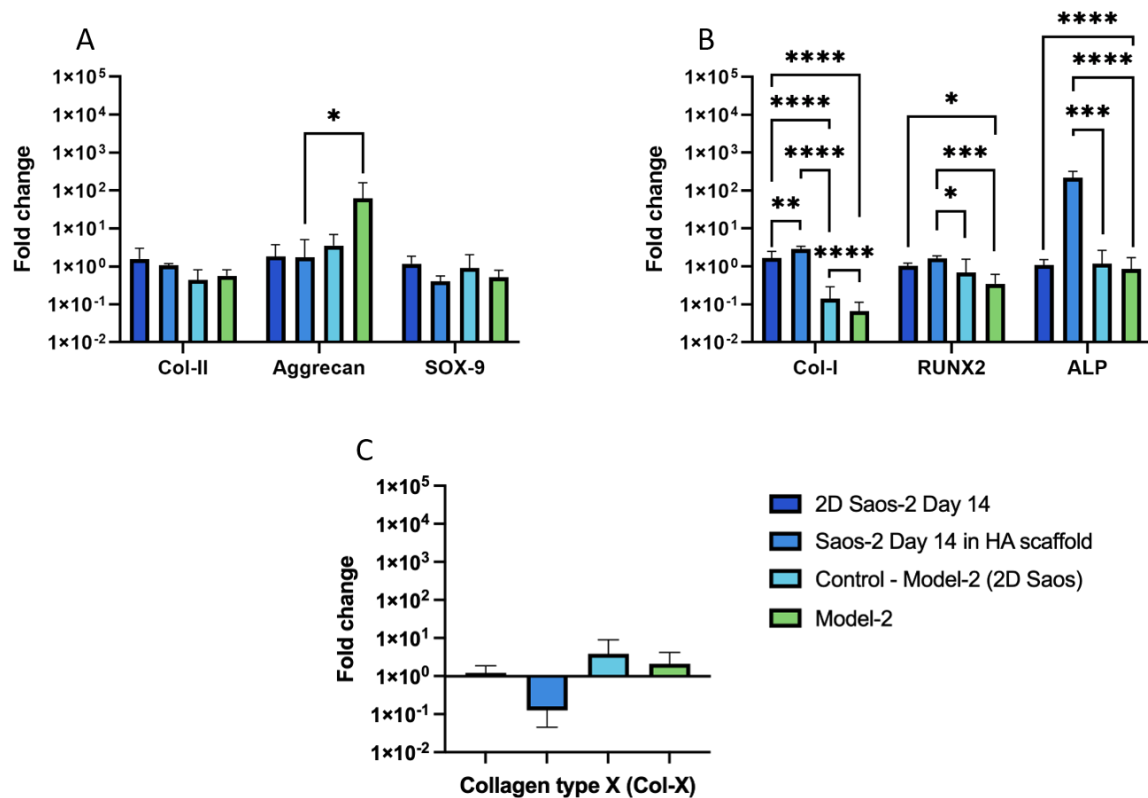
Figure 5.14. Comparative qPCR showing fold change in chondrogenic (A), osteogenic (B), and hypertrophic (C) genes of Model-2 on day 21 compared to control-Model-2 Saos-2 cells and day 14 data from Chapter 4 (2D and HA). N = 6 for the 2D Saos-2 Day 14, Saos-2 Day 14 in HA scaffold, Model-2 and control Model-3. One-way ANOVA was performed with Kruskal-Wallis for each gene. * - $p < 0.05$; ** - $p < 0.01$; *** - $p < 0.001$; **** - $p < 0.0001$.

5.4.4 Characterisation of Model-3 to assess the effect of HOBs seeded on HA on Alpha 1 embedded HCHs

5.4.4.1 Histological assessment through immunofluorescence labelling of Model-3 and control Model-3

Due to the low availability, high cost, and slow proliferation of HOBs, experiments regarding the incorporation of these cells in the biphasic tissue model have lower experimental repeats, and the analysis performed focused on understanding the tissue-specific characteristic that happened during the culture process rather than focusing on more extensive analysis.

5.4.4.1.1 F-actin and collagen type-II labelling for cell morphological assessment and extracellular matrix protein production in Model-3

F-actin filaments were immunofluorescently labelled to assess cell morphology. The samples labelled with phalloidin were also labelled with collagen type-II to assess cartilage matrix production. Figure 5.15 shows control Model-3. The characteristic cell clusters on the surface of the Alpha 1 were observed, and low levels of collagen type-II were expressed inside these clusters. Additionally, lower expression levels were observed in individual cells embedded in the centre of the Alpha 1. This suggested that the co-culture with 2D HOBs affected the chondrogenic potential of Alpha 1.

Model-3 was assessed through the immunofluorescence labelling in cryosections, Figure 5.15. The F-actin labelling depicted the existence of cell clusters in the Alpha 1 section as well as the existing interaction between HCHs and ceramic particles at the interface. Elevated levels of collagen type-II expression were seen, especially along the interface, corresponding to the ceramic particles. These images suggested that the extracellular matrix protein expression adhered to the ceramic particles; however, further tests should be performed to confirm this hypothesis.

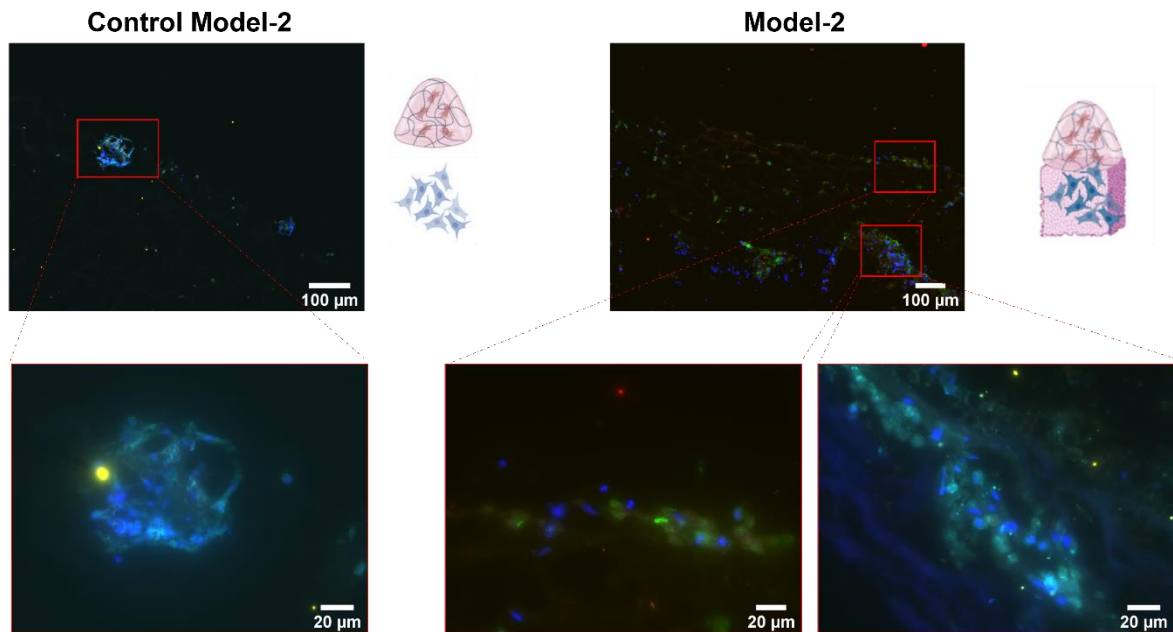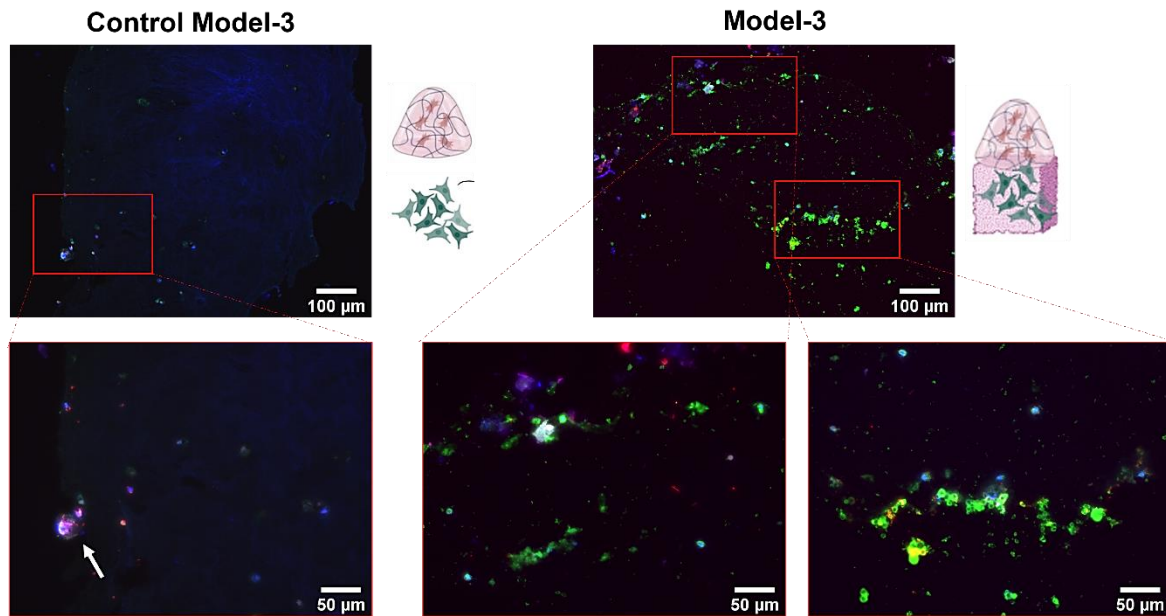**Figure 5.15. Collagen type-II (green) and F-actin (red) labelling and nuclei (blue) of HCHs in Alpha 1 co-culture with 2D HOBs cells control (control Model-3) and Model-3.The top row shows a lower magnification with highlighted sections in red, which are shown in the bottom row at a higher magnification. The white arrow points the cell cluster in Alpha 1. Samples were imaged on day 21. Negative control labelling is shown in Appendix A5.2, Figure A5.2. Diagrams of models are added for clarity, made with BioRender.**

5.4.4.1.2 SOX-9 and aggrecan labelling to assess changes in chondrogenic potential and expression of cartilage matrix proteins in Model-3

Aggrecan expression was observed in the control Model-3. The expression of this marker did not differ from the intensities observed in Alpha 1 (control Model-1), suggesting the incorporation of 2D HOBs did not affect the expression of this marker. The Model-3 sections showed that this marker was highly expressed on the interface but less in those cells further away from the interface, Figure 5.16. SOX-9 expression was visible in control Model-3. The intensities were lower than those observed in Alpha 1 (control Model-1), potentially due to the lower numbers of cell clusters in Alpha 1. Cryosections of Model-3 presented low levels of SOX-9, making it difficult to discern the expression from cell nuclei, Figure 5.17.
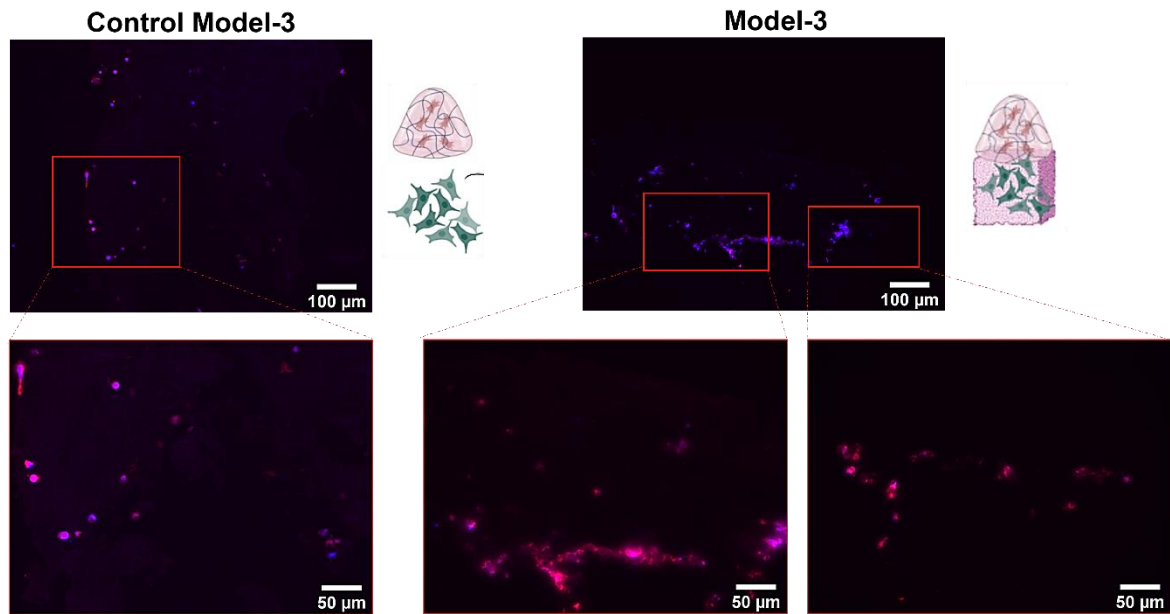
Figure 5.16. Aggrecan (red) labelling and nuclei (blue) of HCHs in Alpha 1 co-culture with 2D HOBs cells control (control Model-3) and Model-3.The top row shows a lower magnification with highlighted sections in red, which are shown in the bottom row at a higher magnification. Samples were imaged on day 21. Negative control labelling is shown in Appendix A5.2, Figure A5.2. Diagrams of models are added for clarity, made with BioRender.
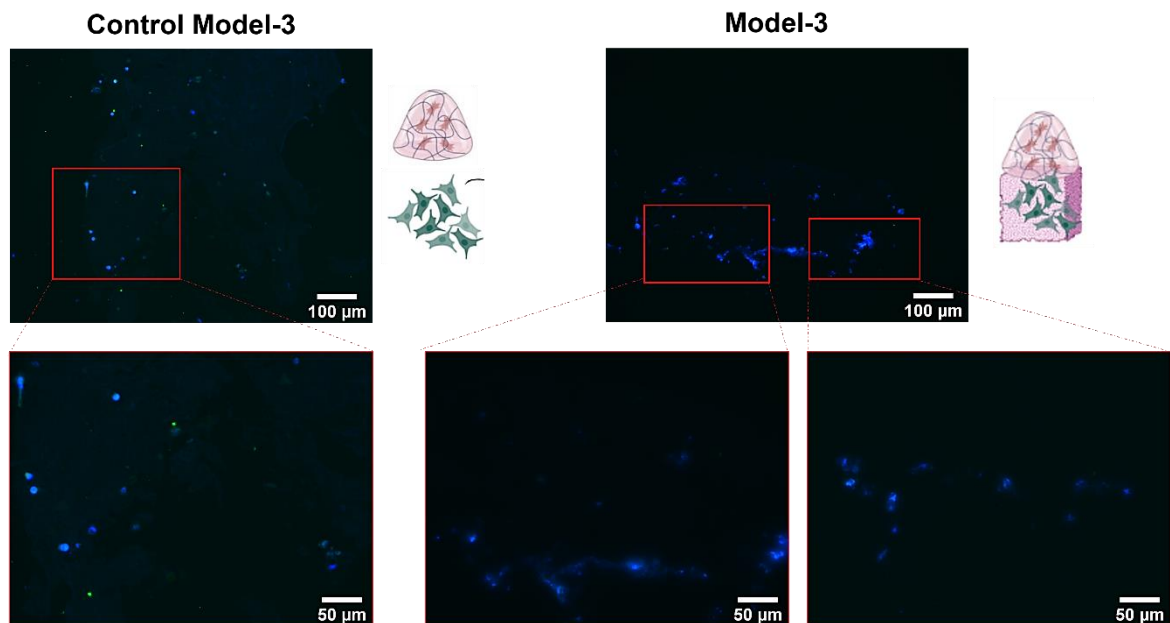
Figure 5.17. SOX-9 (green) labelling and nuclei (blue) of HCHs in Alpha 1 co-culture with 2D HOBs cells control (control Model-3) and Model-3. The top row shows a lower magnification with highlighted sections in red, which are shown in the bottom row at a higher magnification. Samples were imaged on day 21. Negative control labelling is shown in Appendix A5.2, Figure A5.2. Diagrams of models are added for clarity, made with BioRender.

5.4.4.1.3 Collagen type-I and collagen type-X labelling to assess changes in HCH behaviour towards an osteogenic or hypertrophic phenotype in Model-3

Collagen type-I labelling was performed on the control Model-3 (Figure 5.18), and a similar expression pattern was observed in the control Model-2. Collagen type-I expression appeared inside the cell clusters which formed on the surface, and it was lower in the cells embedded within the gel. The expression of collagen type-I was also observed in Model-3, both in the cell clusters that appeared on the top surface of the construct and the interface. No interaction of this protein with the ceramic particles was observed here, as opposed to in the collagen type-II images. Figure 5.19 shows the fluorescent labelling of collagen type-X. Both in control Model-3 and Model-3, the expression of this protein was minimal. This suggested that the expression of this protein was not promoted either on Alpha 1 alone or in combination with the cellularised HA scaffold, neither at the surface nor the interface.
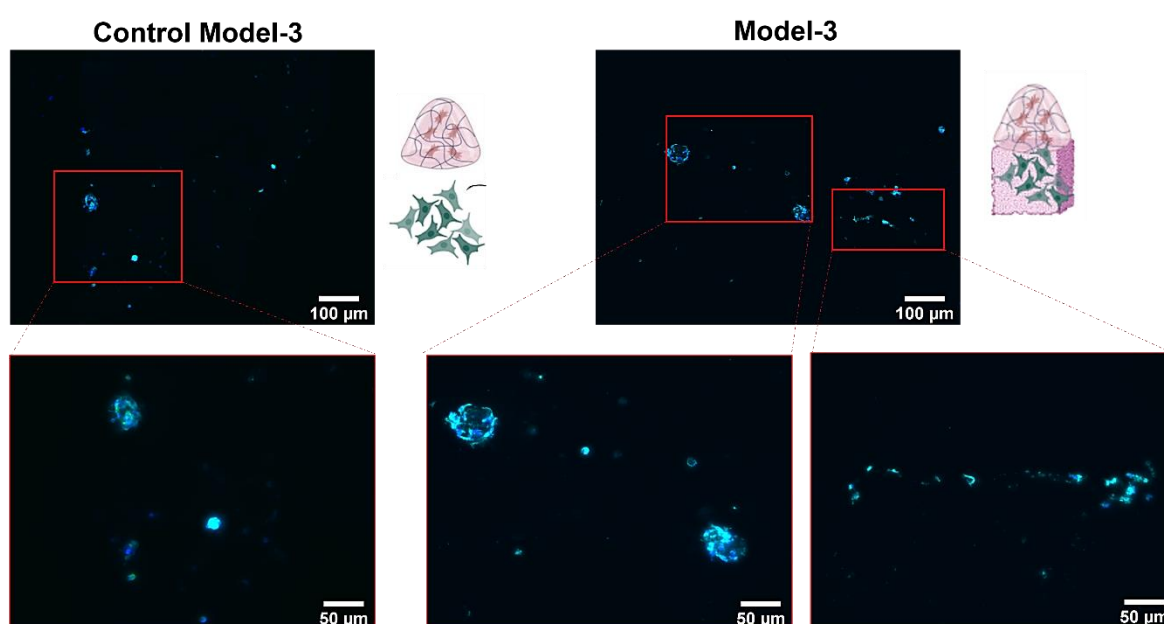
Figure 5.18. Collagen type-I (cyan) labelling and nuclei (blue) of HCHs in Alpha 1 co-culture with 2D HOBs cells control (control Model-3) and Model-3. The top row shows a lower magnification with highlighted sections in red, which are shown in the bottom row at a higher magnification. Samples were imaged on day 21. Negative control labelling is shown in Appendix A5.2, Figure A5.2. Diagrams of models are added for clarity, made with BioRender.
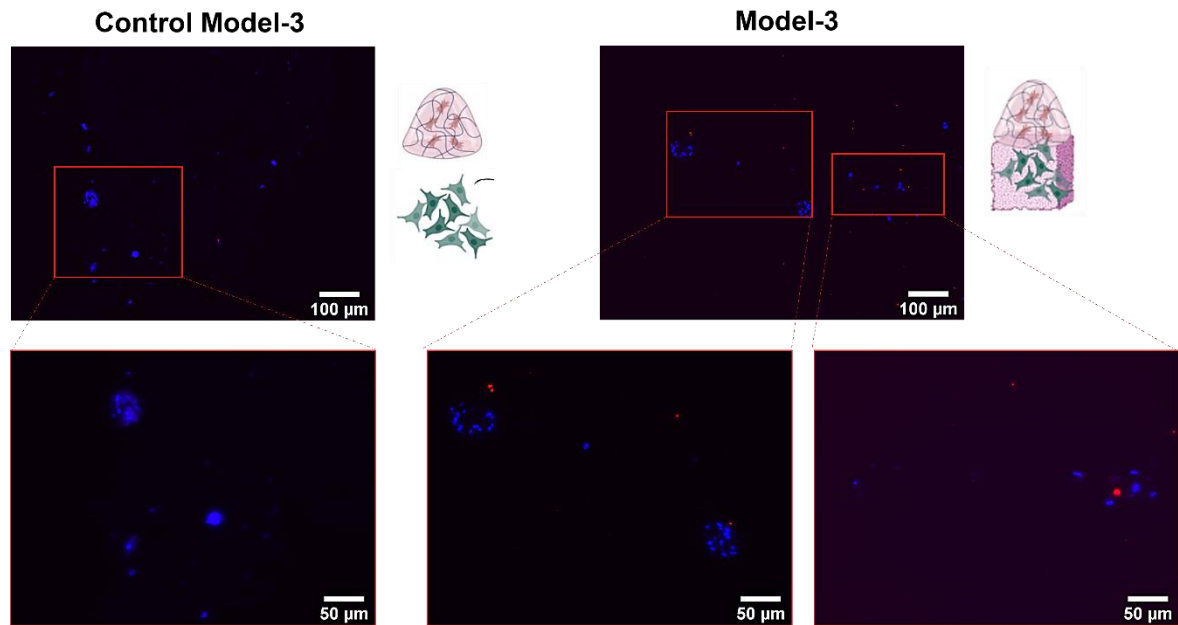
Figure 5.19. Collagen type-X (red) labelling and nuclei (blue) of HCHs in Alpha 1 co-culture with 2D HOBs cells control (control Model-3) and Model-3. The top row shows a lower magnification with highlighted sections in red, which are shown in the bottom row at a higher magnification. Samples were imaged on day 21. Negative control labelling is shown in Appendix A5.2, Figure A5.2. Diagrams of models are added for clarity, made with BioRender.

5.4.4.2 mRNA expression assessment through comparative qPCR of Model-3

Chondrogenic and osteogenic markers were assessed in Model-3 and its control against the 3D pellet control and the 2D HOB culture controls. These values are shown alongside previously obtained values to compare Model-1 and Model-2 with Model-3. Figure 5.20 shows the qPCR performed on the Alpha 1 section, and Figure 5.21 on the HA section of Model-3.

Chondrogenic marker expression is shown in Figure 5.20A. Collagen type-II expression showed that the expression observed in control Model-3 was similar to that of control Model-2. This depicted a similar level of chondrogenic extracellular matrix production. The expression of the control Model-3 was also significantly downregulated in comparison to Alpha 1 (control Model-1) (** - $p < 0.01$). However, the expression of collagen type-II in Model-3 showed similar expression levels as the

ones observed in Model-1. These levels were higher than those observed in Model-2, suggesting that HOBs promoted chondrogenesis better than Saos-2 cells in biphasic constructs. However, these differences were not significant.

A similar trend was observed both in aggrecan and SOX-9 expressions. Aggrecan expression in control Model-3 presented lower values than those observed in Model-3. Model-3 presented values similar to those of Model-1 and control Model-2. This suggested once more similar levels of chondrogenic extracellular matrix production. SOX-9 expression was significantly downregulated with respect to Alpha 1 (control Model-1) when cultured in control Model-3 (** - p < 0.01). However, the expression levels observed in Model-3 aligned with those observed in Alpha 1 (control Model-1), Model-1 and Model-2. Overall, including HOBs alongside the HA construct had an upregulating effect in the three analysed chondrogenic markers.

Osteogenic markers were also assessed in the Alpha 1 section, Figure 5.20B. Collagen type-I expression was significantly downregulated (* - p < 0.05) in Model-3, with respect to Alpha 1 (control Model-1). The expression levels were similar to those seen in the Model-2 in both the Model-3 and its control. This suggested that the phenotype of the embedded HCHs was maintained healthy and did not transition towards fibrotic cartilage [329].

RUNX2 expression was significantly downregulated in control Model-3 with respect to Model-1 (** - p < 0.01). Additionally, the expression levels observed in Model-3 were upregulated similarly to those in Model-1 and Model-2. This suggested that these chondrocytes would be subsequently transitioning towards a hypertrophic phenotype and that the expression of this bone proliferation marker was highly dependent on the incorporation of the HA substrate. The expression of this marker in HCHs could imply a dedifferentiation of these HCHs into a bone-like lineage when in contact with HA [331].

ALP activity expression levels remained low in control Model-3, similar to control Model-2. There was a significant increase in the ALP expression in Model-3 with respect to the Alpha 1 (control Model-1) (** - p < 0.01). These levels were higher than those seen in Model-1 and Model-2, suggesting that the increase in these expression levels was due to the inclusion of HOB cells in direct contact with the Alpha 1 section.

Additionally, this depicted once more the potential transition of HCHs towards a hypertrophic state. However, it is also possible that some HOB cells had migrated into Alpha 1 and that the expression that can be seen here came from these cells rather than from the HCHs themselves.

Finally, collagen type-X expression was assessed, Figure 5.20C. Following a similar trend, both the control Model-3 and Model-3 were downregulated in collagen type-X expression with respect to the 3D cell pellet. Model-3 showed a downregulation similar to Model-1. The control Model-3 showed a higher expression than Model-3, showing that when in contact with 2D HOB cells, the Alpha 1 embedded HCHs became more hypertrophic than when in contact with HA scaffolds.
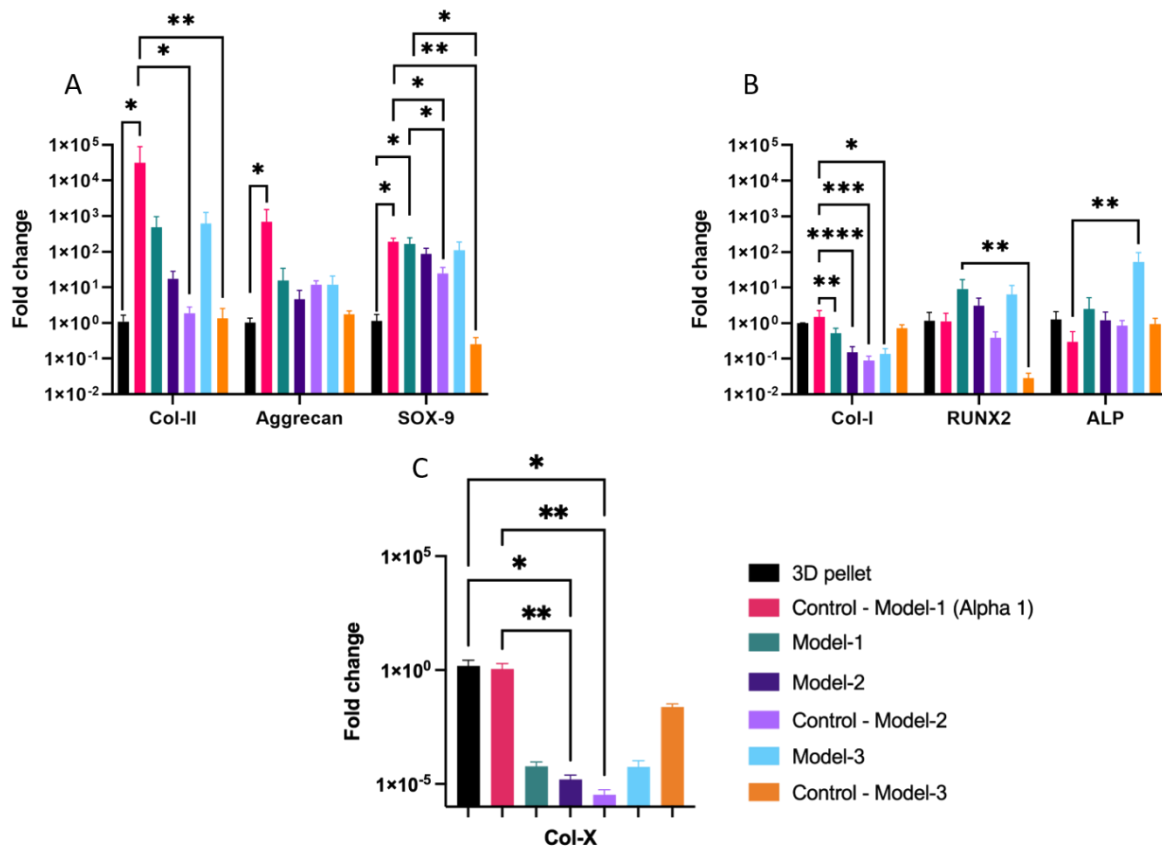
Figure 5.20. Comparative qPCR showing fold change of chondrogenic (A), osteogenic (B), and hypertrophic (C) markers in the Alpha 1 section of all tested models with respect to the 3D pellet control on day 7. N = 3 for the 3D pellet control; N = 6 for Alpha 1, Model-1; Model-2, control Model-2. N = 3 for Model-3, control Model-3. One-way ANOVA was performed with Kruskal-Wallis for each gene. * - $p < 0.05$; ** - $p < 0.01$; * - $p < 0.001$; **** - $p < 0.0001$.**

Comparative qPCR measurements were also performed on the HA section of Model-3 and on the 2D HOBs of control Model-3. The main aim was to assess the medium change's effect on the bone-like expression and behaviour of the HOBs. As expected, chondrogenic markers, collagen type-II, aggrecan and SOX-9 presented no significant differences between the samples on day 14 and day 21, Figure 5.21A. However, aggrecan downregulated when these cells were seeded on HA scaffolds compared to the 2D culture equivalents.

Osteogenic marker expression showed slight differences, Figure 5.21B. Collagen type-I expression was significantly upregulated in Model-3 after the 21 days of culture with respect to the HA day 14 sample (* - $p < 0.05$). This was surprising, as the results from Model-2 showed that the medium change highly affected collagen type-I production. With HOBs, this upregulation depicted that bone-like matrix production, rich in collagen type-I, was maintained regardless of the medium change.

RUNX2 expression appeared to be significantly downregulated in control Model-3 on day 21 with respect to the 2D control on day 14 (* - $p < 0.05$). This could be due to the medium change. However, there were no significant changes between the HA samples on day 14 and Model-3 on day 21. Although the RUNX2 levels were downregulated with respect to the 2D day 14 control, these differences were not significant, suggesting that the bone growth was not highly affected by this culture medium change.

ALP levels also presented no significant changes. However, there was a visible upregulation of this marker in Model-3 day 21, compared to both 2D and HA samples on day 14, suggesting that the medium change did not affect the ALP activity of the HOBs for the final 7 days of culture. This ALP activity upregulation showed that HOBs were still mineralising and maturing the bone-like extracellular matrix.

Finally, collagen type-X presented no significant differences across samples, Figure 5.21C. However, there was a visible downregulation on day 21 control Model-3 with respect to the 2D control on day 14 of the HOB culture. Surprisingly, there was a slight

upregulation on day 21 Model-3 compared to day 14 of the HA construct alone. This could suggest that the medium change slightly affects the osteogenic behaviour of HOBs.
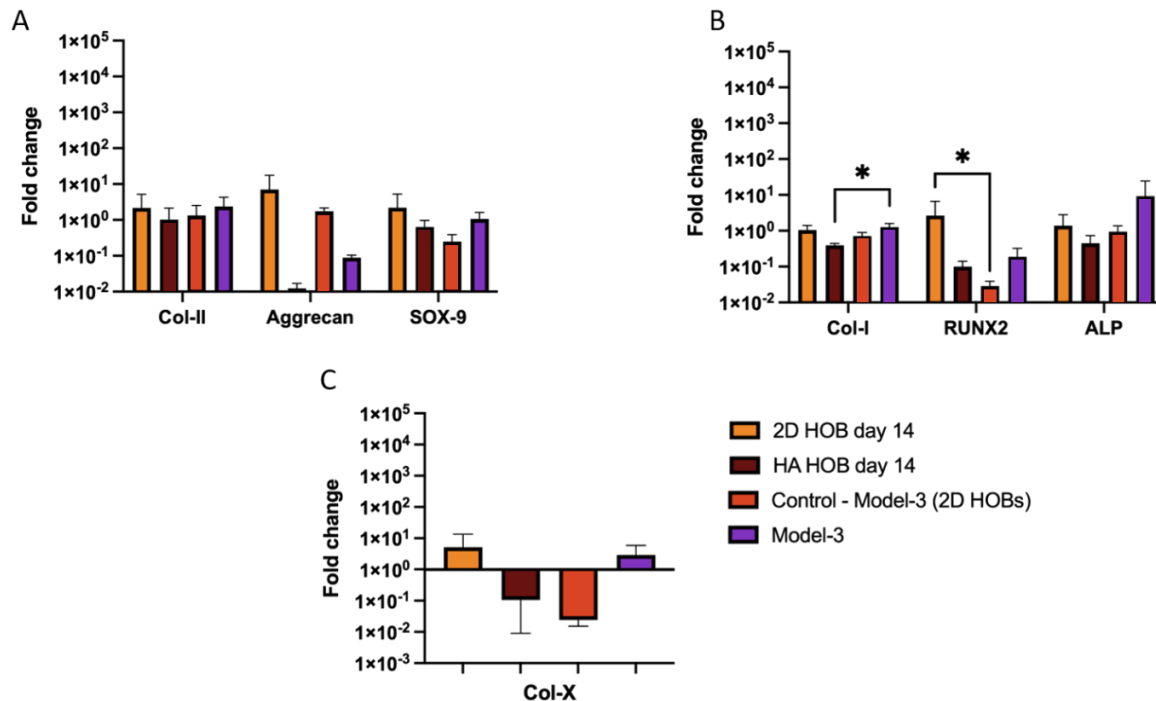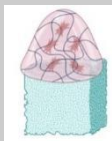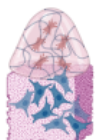
Figure 5.21. Comparative qPCR showing fold change in chondrogenic (A), osteogenic (B), and hypertrophic (C) markers in the HA section of Model-3 with respect to 2D HOB control and HOB+HA scaffolds on day 14. N = 3 for all sample types. One-way ANOVA was performed with Kruskal-Wallis for each gene. * - p < 0.05.

A summary of the results found for the various models is shown below in Table 5.2

Table 5.7. Summary of results from all tested models. Main immunofluorescence labelling and mRNA expression measured with qPCR are summarised and briefly compared across models. Diagrams were made with BioRender.

	Diagram	Protein expression	qPCR Alpha 1 section	qPCR HA section
Model-1		Expected collagen type-II and aggrecan expression in Alpha 1. HCHs on the HA section showed high levels of collagen type-I. Cell shape changed from circular to spindle when in contact with HA.	Lower levels of collagen type-II and aggrecan. SOX-9 expression was maintained. Decreased collagen type-I expression. Increased in ALP and RUNX2 expression. HA section decreased the chondrogenic potential of Alpha 1.	N/A
Model-2		Interface expression of collagen type-II, aggrecan and collagen type-I. Decreased SOX-9 and collagen type-X expression across the model.	Decreased collagen type-II and aggrecan expression. SOX-9 expression was maintained. Decreased expression of osteogenic markers and collagen type-X. Saos-2 on HA further decreased the chondrogenic potential of Alpha 1.	Increased expression of aggrecan. Decreased expression of all osteogenic markers. Chondrogenic medium for 7 days decreased the osteogenic phenotype of Saos-2 cells.
Model-3		Interface expression of collagen type-II, aggrecan and collagen type-I. Decreased SOX-9 and collagen type-X expression across the model.	Maintained expression levels in chondrogenic proteins as Model-1. Higher chondrogenic expression than Model-2. Increased expression of osteogenic markers. HOBs increased the chondrogenic potential of Alpha 1 more than Saos-2.	Chondrogenic medium for 7 days did not affect the chondrogenic HOB phenotype. Decreased RUNX2 expression, suggesting a decrease of HOB proliferation.

5.5 Discussion

Current osteochondral tissue models have focused on developing bone and cartilage compartments that gradually mix together to mimic the *in vivo* setting as closely as possible [125,327,332]. These studies have mainly focused on addressing issues such as the delamination and lack of continuity across the interface of both tissues [125,327,332], and achieving similar to *in vivo* cell behaviour in the distinct osteochondral sections [60,333–335]. Although these approaches have shown significant advancements towards reproducing these osteochondral tissues, they are complex and require various manufacturing processes. These include manufacturing an osteochondral construct with decreasing porosities [125] or 3D printing multiple materials, which require extra manufacturing steps such as PCL hydrolysing [332]. Additionally, most of them rely on the use of animal-derived materials [2], which questions the sustainability and ethical implications of their manufacturing process.

To simplify these osteochondral models whilst addressing issues such as tissue interface delamination and sustainability, this chapter investigates three biphasic models that use non-animal-derived materials. This chapter combines previously optimised cartilage tissue model manufacturing using self-assembling peptide Alpha 1 (Chapter 3) with a previously characterised bone-like tissue model made with HA (Chapter 4). Three different models have been investigated: one using the 3D bioprinted Alpha 1 with HCHs in combination with an acellular HA scaffold (Model-1); a biphasic construct with HCHs embedded in 3D bioprinted Alpha 1 with Saos-2 cells seeded on the HA scaffold (Model-2); and another biphasic construct with HCHs embedded in 3D bioprinted Alpha 1 with HOBs seeded on the HA scaffold (Model-3). Model-1 aimed to understand the effect of the HA scaffold on the Alpha 1 section, as reported in previous investigations [60,336]. Following previous investigations [64,122,327,332], Model-2 and Model-3 aimed to understand the interaction between the HCHs embedded in Alpha 1 and the bone-like cells seeded onto the HA scaffold.

Initial optimisation of the culture conditions of these 3D-printed biphasic models was performed to address and mitigate the effect of tissue interface delamination between the Alpha 1 and HA sections. Preliminary tests (Appendix A5.1, Figure A5.1) showed

that 3D bioprinting of HCH embedded Alpha 1 on top of the acellular HA scaffold (Model-1) led to Alpha 1 detaching from the scaffold within the first 3 hours of culture. This led to fast Alpha 1 degradation and loss of interaction between the two tissues. An inverted approach was tested where the Alpha 1 section was in contact with the bottom of the culture well plate, and the HA section was placed over Alpha 1 in the culture well, Figure 5.2. This approach, not previously reported in the literature, enabled the penetration of Alpha 1 inside the HA scaffold pores, prevented Alpha 1 from floating in the culture medium, and decreased the degradation rate. Based on the advantages of the inverted approach, it was adopted as the culture condition arrangement. Previous investigations focused on developing gradient porous structures between the cartilage and bone sections to avoid delamination [122,337,338]. Although this approach was successful, it required complex patterns to be designed and manufactured. Here, a simpler design is presented, ensuring a connection between the sections.

In the development of these biphasic tissue models, two variables were assessed: the effect of the HA scaffold and the effect of co-culturing different cell types. Additional variables such as culture time and culture medium type were not optimised but based upon previous findings. Firstly, the HA scaffolds' manufacturing optimisation and cell culture investigation had previously been characterised (Chapter 4). Based on those findings, it was found that 14 days of culture had a significant increase in osteogenic behaviour in HA-seeded Saos-2 cells and full cell coverage of the HA scaffolds. It was concluded that 14 days of pre-culture of Saos-2+HA scaffolds was enough to get Saos-2 cell coverage and osteogenic behaviour on the HA scaffolds.

Regarding the cartilage section, the manufacturing optimisation and culture time assessment were performed in Chapter 3. These findings reported that chondrogenesis was achieved faster in the Alpha 1 culture than in the corresponding "gold standard" 3D pellet control [244]. Comparative qPCR on day 7 showed significant differences in chondrogenic genes, suggesting that 7 days of culture of HCHs on Alpha 1 was enough to achieve chondrogenic behaviour. Based on these timelines, it was decided that a pre-conditioning of the bone compartment would be done for 14 days in pro-calcifying medium. Subsequently, an additional 7 days of culture with the

cartilage section incorporated was performed in chondrogenic medium to ensure the cartilage section developed as expected. A longer culture period demonstrated the loss of Alpha 1 due to degradation. Therefore, 21 days of culture for these biphasic constructs was chosen, and longer culture periods were not pursued.

Multiple control types were set to investigate the effect of specific variables, including different cell types in co-culture and the effect of the HA scaffold. To assess the chondrogenic behaviour changes observed in the Alpha 1 section in the three experimental set-ups, this section was compared to the "gold standard" 3D pellet, the Alpha 1 cultured alone (control Model-1), and the corresponding model controls. The effect of including a new cell type in co-culture was observed in the co-culture control of Alpha 1 with 2D cultured bone-like cells. However, in these samples, Alpha 1 detachment from the 2D bottom well plate surface made the direct interaction with the 2D culture of bone-like cells difficult. The effect of the HA scaffold was observed through the changes in Model-1. The combination of HA and bone-like cells was seen through Model-2 and Model-3 constructs. To assess changes experienced in the bone-like cells (Saos-2 or HOBs) when subjected to the change in culture medium, control samples were taken from day 14 time point data presented in Chapter 4. At this time point, both 2D controls and HA-seeded scaffolds had only been subjected to pro-calcifying media. Additional data from Chapter 4, showing the behaviour of cell-seeded HA scaffolds for 21 days under pro-calcifying medium, was unavailable. Therefore, day 14 time points were used.

The first investigation focused on understanding the HA construct's effect on the cartilage compartment. Cell proliferation, cell distribution, matrix production and genetic expression in Model-1 were assessed. Cell proliferation showed no significant differences between the Alpha 1 control and Model-1 after 7 days. This confirmed that the HA scaffolds did not affect HCH viability in the Alpha 1 section. Kilian *et al.* [60] showed similar HCH viability when alginate-based hydrogels with HCHs were 3D printed onto an HA-based scaffold. HCH numbers were maintained over 21 days of culture [60], suggesting that longer cell culture periods of Model-1 would not compromise cell viability.

Further histological investigations in Model-1 encountered issues in processing, such as the dissolution of the HA section when cryosectioned. Figure 5.6, which shows the H&E staining of these samples, presents the interference between the washed HA particles and the cell nuclei. Although HCHs in the Alpha 1 area are still visible, differentiation between HA particles and cells was not clear. Model-1 constructs were immunofluorescently labelled to circumvent this issue as a whole scaffold (without cryosection) to visualise further the extracellular matrix protein expression on the Alpha 1 and the HA section without HA particle interference.

Immunofluorescently labelled images of the Alpha 1 section of Model-1 showed similar levels of expression of chondrogenic proteins, collagen type-II and aggrecan to those seen in control Model-1. However, interferences due to light scattering in Model-1 impeded the visualisation of SOX-9 expression. Cells in this section maintained the expected circular shape and low levels of collagen type-I expression. HCHs, which migrated to the HA scaffold, changed to a spread-out morphology and expressed collagen type-I. As reported previously, collagen type-X was expected to be expressed, as the ceramic scaffold was expected to induce hypertrophy in the HCHs [339,340]. However, no expression was observed. These initial images suggested that the chondrogenic behaviour of Alpha 1 was maintained regardless of the HA scaffold addition and that only the cells directly in contact with HA changed phenotype.

qPCR analysis of Model-1 was performed to quantify and confirm the behaviour seen through immunofluorescence. This data confirmed that the Model-1 Alpha 1 section had a similar SOX-9 expression compared to the control Model-1. Lower levels of collagen type-II and aggrecan than the control were also observed. Osteogenic gene expression assessment showed lower levels of collagen type I, with higher RUNX2 and ALP expression. These results depicted that adding the HA scaffold compromised the chondrogenic potential of Alpha 1 and induced minimal phenotypical changes towards osteogenic behaviour in the embedded HCHs. However, further understanding of the spatial location of these expression levels would clarify if the changes observed were happening across all Alpha 1 or near the interface. Kilian *et al.* [60] showed qPCR results comparing a similar biphasic set-up as Model-1, made with alginate, to alginate alone. The qPCR results of one HCH donor showed similar

fold change differences in collagen type-II, aggrecan, collagen type-I, and collagen type-X as Model-1 compared to its control. However, a different donor showed the opposite observations. Therefore, multiple donors should be used to manufacture Model-1 and have a better representation. Overall, Model-1 assessment showed that the HA section did not affect cell viability and slightly affected the expression profile of HCHs, lowering their chondrogenic expression and increasing their osteogenic behaviour close to the surface.

The second investigation focused on incorporating the previously characterised Saos-2 cell line in the biphasic system. This investigation aimed to understand the effect this cell line could have on the Alpha 1 section and if the changes in culture medium in the last 7 days affected Saos-2 behaviour. Model-2 constructs were histologically assessed and compared to co-culture controls of Alpha 1 with 2D Saos-2 cells (control Model-2). H&E sections showed a lower degree of HA particle dissolving, potentially due to the matrix deposition of the Saos-2 cells, which facilitated the attachment of the cryosections to the microscope slides, Figure 5.9. Overall, Alpha 1 penetration was observed in the HA pores, and the control samples showed the expected formation of HCH clusters in the Alpha 1 surface. Further immunofluorescence labelling focused on understanding the interface of Model-2 constructs.

Control Model-2 showed the expected HCH cluster formation with high levels of collagen type-II, aggrecan, and SOX-9, as previously seen in control Model-1. Collagen type-I was also observed in these clusters but at a lower intensity than collagen type-II. This suggested that the inclusion of Saos-2 cells in a 2D surface did not change the expression profile of the Alpha 1 embedded HCHs. However, due to the Alpha 1 tendency to float in the culture medium, there was no direct contact between the 2D Saos-2 cells and Alpha 1 in this Control Model-2. The lack of this direct contact most likely affected the behaviour of the Alpha 1 embedded HCHs.

Model-2 constructs immunofluorescence labelling showed cell shape differences in the interface. Cells at the interface presented an elongated cell shape, and high levels of collagen type-II deposition and aggrecan were seen across the interface (Figure 5.10). SOX-9 expression appeared faint at the interface, showing this location's decrease in chondrogenic potential. Collagen type-I was also highly expressed at the

231

interface. Overall, there was a change in the cell morphology close to the interface, and a higher degree of osteogenic protein expression was observed near this area. However, it was surprising to see no collagen type-X expression, characteristic of hypertrophic HCHs which reside close to the mineral interface. Collagen type-X expression was expected to appear at the interface as the HA section was expected to induce hypertrophy in the HCHs as reported previously [339,340]

The qPCR analysis conducted on the Alpha 1 section of Model-2 revealed reduced collagen type-II and aggrecan levels compared to the Alpha 1 control group in Model-1. Importantly, SOX-9 expression remained consistent, indicating that the chondrogenic potential of Alpha 1 was not compromised by the introduction of Saos-2 cells on the HA scaffold. Furthermore, diminished levels of collagen type-I, RUNX2, and ALP suggested that including this cell line did not induce osteogenic behaviour in the HCHs, contributing to the formation of less fibrotic cartilage [329].

A prior study by Lutter *et al.* [341] demonstrated that HCHs when co-cultured with Saos-2 cells, led to an augmentation in hyaline cartilage production. This finding is corroborated in Model-2 by the reduced expression of collagen type-I, RUNX2, and ALP in HCHs. Nevertheless, a longer culture duration is required to ascertain whether the expression of chondrogenic proteins, which are characteristic of hyaline cartilage, experiences an upregulation.

The qPCR analysis performed on the HA section of Model-2 showed significantly increased levels of aggrecan than day 14 expression in Saos-2 cells seeded on HA. This phenomenon was previously reported [324], showing significantly higher aggrecan and collagen type-II expression after culturing Saos-2 cells for 21 days in chondrogenic medium. Reduced levels of osteogenic proteins, collagen type-I, RUNX2, and ALP showed that the change in the chondrogenic medium over the last 7 days of culture decreased the osteogenic potential of this cell line.

Model-2 showed lower levels of chondrogenic expression in the Alpha 1 section than Model-1. This suggested that the effect of this cell line compromised the ability of Alpha 1 to induce chondrogenesis in the embedded HCHs. Additionally, the change of culture medium from pro-calcifying to chondrogenic affected the osteogenic potential

232

of the HA section. Further investigations regarding cell culture medium composition should be performed to ensure both compartments of Model-2 perform closer to cartilage and bone behaviour.

Model-2, manufactured with Saos-2 cells, was demonstrated to be a starting point for developing simplified osteochondral *in vitro* tissue models. However, Saos-2 cells are still cancerous and an immortalised cell line which does not fully represent the behaviour of HOBs. Nonetheless, HOBs' behaviour highly depends on the donor [342], making them an inconsistent cell type. Chapter 4 data presented a proof-of-concept bone-like model that depicted minimal differences between the 2D control cultured HOBs and those cultured in HA scaffolds. However, these results confirmed that the HA scaffolds supported HOBs and encouraged their proliferation and the expression of osteogenic proteins. The third model focused on assessing the effect that the chondrogenic culture medium had on HOB+HA and the effect that HOBs had on the Alpha 1 embedded HCHs. Immunofluorescence labelling and comparative qPCR analysis were performed, and co-culture controls were assessed.

Immunofluorescence labelling of control Model-3 revealed the characteristic cell cluster formations with increased collagen type-I, aggrecan, and SOX-9 expression. Reduced levels of collagen type-II were seen in control Model-3, whilst no collagen type-X expression was observed. Cell shape changes in Model-3 were difficult to visualise due to HA particle interference. However, immunofluorescence labelling displayed increased expression of collagen type-II, collagen type-I, and aggrecan along the interface. Decreased expression of SOX-9 was observed across the interface and in the Alpha 1 section of Mode-3, with no expression of collagen type-X visible. This was expected following the previously characterised expression of this protein in the Saos-2-based osteochondral and control models.

The qPCR analysis of the Alpha 1 section in Model-3 showed similar collagen type-II, aggrecan and SOX-9 expression levels as Model-1, slightly higher than Model-2. Control Model-3 displayed similar collagen type-II expression to the control Model-2 and lower aggrecan and SOX-9 expression, suggesting that HOBs in 2D culture affected the chondrogenic properties of Alpha 1. These results differ from previous literature [343], where co-culture of osteoblasts and chondrocytes led to higher levels of

expression of chondrogenic proteins after 14 days of culture. However, due to the differences in culture time, it would be necessary to expand the presented experimental culture time to compare the obtained results fully.

Osteogenic marker expression of the Alpha 1 section of Model-3 was also investigated. Collagen type-I was significantly downregulated in Model-3 to similar levels as those of Model-2, suggesting once more a less fibrotic tissue formation [329]. No other differences were observed in RUNX2 and ALP expression. In terms of chondrogenic potential, Model-3 performed better than Model-2, as the observed behaviour was closer to that of Alpha 1 alone.

The qPCR analysis of chondrogenic markers in the HA section of Model-3 did not show significant differences. The change to chondrogenic medium for the extra 7 days of culture did not show significant differences in the 2D HOBs (control Model-3). Model-3 sections showed an upregulation of collagen type-II, aggrecan and SOX-9 on day 21. However, the differences were non-significant. A larger sample size is required to confirm the observed results further.

qPCR analysis of osteogenic genes showed differences in collagen type-I and RUNX2 expression. A significant upregulation of collagen type-I expression in Model-3 with respect to day 14 HA control was observed. Additionally, RUNX2 expression was significantly downregulated on the 2D HOB control Model-3 on day 21 with respect to day 14, showing the effect of media change on the proliferation rate of HOBs. No other significant differences were observed for ALP or collagen type-X expression; however, a larger sample population should be analysed to confirm these observations further.

These results confirmed that an osteochondral biphasic model made with human primary cells can be manufactured and maintained in culture for up to 21 days. The chondrogenic potential of Alpha 1 when in contact with HOB+HA compartments was not compromised. Additionally, the differences observed in the osteogenic markers on the HOB+HA section after the culture medium change did not show significant changes, confirming that the bone compartment osteogenic behaviour was maintained. Although the sample size was reduced due to the low availability of HOBs

and their reduced proliferation rate, these results were a starting point and they confirmed that this model is viable.

The three presented models focused on understanding the interaction between the cartilage section Alpha 1 and the HA section and the cellular interaction between the HCHs embedded in Alpha 1 and the bone-like cells seeded onto HA. Although histological evaluations and protein expression analysis through immunofluorescence labelling and qPCR were performed, additional variables should be assessed to improve this characterisation. These include using different cell seeding densities in both sections, cell culture medium composition, and external cues such as compressive loading or fluid flow. In a prior study, Xue *et al.* [344], developed an osteochondral construct *in vitro* with a cell seeding density 5 times higher than the one used in these investigations. Additionally, they used a bioreactor chamber to separate the cell culture medium given to the cartilage and bone sections whilst applying fluid flow [344]. Although chondrogenic and osteogenic markers were not assessed, the culture set-up showed a promising strategy to ensure tissue-specific cell culture.

Other set-ups, such as the one reported by Yu *et al.* [345], showed a different approach to separating the chondrogenic and osteogenic media to feed an osteochondral construct *in vitro*. Using a PCL membrane, they reported media separation, which increased the expression of chondrogenic and osteogenic markers in the cartilage and bone section after 28 days [345]. Additionally, their cell seeding density was 5 times higher than the one used here [345]. Therefore, the effect of cell seeding and compartmentalisation of the culture media should be further assessed in the models presented in this chapter to understand better and characterise the manufactured osteochondral model.

5.6 Limitations and Future Work

The presented chapter focuses on developing an osteochondral tissue model *in vitro* following the data presented in Chapters 2, 3, and 4. Throughout the performed investigations, multiple limitations were encountered.

Firstly, the experimental design, cell culture conditions and time frame to which these biphasic constructs were subjected could be further refined. Although the timeline follows previously reported findings, longer culture times, especially in the bone-like section, could have been implemented to ensure further bone maturation. However, to simplify the manufacturing of these osteochondral biphasic constructs and minimise the culture time, the minimal time points at which significant changes had previously been observed were implemented. Additionally, the change in culture medium type on day 14 was a variable that was not further investigated, but that should be further optimised. A full change from pro-calcifying medium to chondrogenic medium was performed, assuming that the 14-day culture time was enough for bone-like cells (Saos-2 or HOBs) to proliferate and start mineralisation. The cartilage section development was prioritised due to the short culture time, and therefore, this full media change was performed instead of using various culture medium mix ratios [129,346,347] or media separation [344,345]. However, further optimisation of this second stage of the osteochondral biphasic construct culture should be performed to ensure cartilage development without compromising bone maturation.

Secondly, the culture conditions require further investigation to understand the observed interactions. On the one hand, the inverted manufacturing set-up facilitated the adhesion of the Alpha 1 and HA sections. However, the HA section's compression on Alpha 1 must be characterised. Further experimental set-ups should be tested where an upright orientation of these biphasic constructs is maintained, avoiding Alpha 1 delamination and degradation. A comparison of both upright and inverted set-ups could be performed to understand the effect of the compression on the Alpha 1 section.

On the other hand, the controls used in the second and third investigations relied on the co-culture of Alpha 1 with 2D cell cultures of Saos-2 cells or HOBs. Due to the tendency of Alpha 1 to float, direct contact with the 2D cultured cells was not always

achieved. Therefore, the crosstalk between the 2D cells and the Alpha 1 section was limited to interactions through the cell culture medium. A control set-up with direct contact between Alpha 1 and the 2D cultured cells should be investigated for a better comparison.

Thirdly, characterisation of the HA section using qPCR was performed by comparing day 14 data from Chapter 4 to day 21 from these investigations. This was due to insufficient data on HA scaffolds cultured in pro-calcifying medium for 21 days. Further data should be obtained of the HA scaffolds on day 21 after being cultured in only pro-calcifying medium. The current comparison only depicts the differences from day 14 to day 21 when changing the cell culture medium. An extra comparison would enable us to see differences between scaffolds if the HA section had been kept in pro-calcifying medium for an extra 7 days. Additionally, there were low sample numbers of the biphasic constructs with HOBs, which were not representative. A larger sample size and HOBs from different donors are required so a better characterisation is performed.

Finally, although the immunofluorescence labelling enabled the visualisation of the Alpha 1 section, the interface, and the HA section, the qPCR did not allow for spatial analysis. Further spatial-dependent characterisation of the mRNA expression across the biphasic constructs should be investigated. This would more accurate data acquisition as different parts of the Alpha 1 section, the interface, and the HA scaffold could be investigated separately. Additionally, other characterisation techniques, such as compression testing, calcium quantification, and protein quantification, would enable the characterisation of the mechanical properties of the different models, assessment of cell mineralisation in the bone and interface section, and quantification of extracellular matrix protein deposition, respectively.

5.7 Summary

3D bioprinted Alpha 1-based cartilage sections were combined with acellular and cellularised HA scaffolds to develop biphasic tissue models *in vitro.* The manufacturing process was optimised, and an inverted approach was adopted to avoid cartilage-bone delamination and decrease Alpha 1 degradation. Initial cell viability and protein expression were assessed in Model-1. Two different cell types were used to manufacture Model-2 and Model-3, Saos-2 cells and HOBs, respectively.

Introducing a HA scaffold (Model-1) did not affect cell proliferation or chondrogenic behaviour of the Alpha 1 section, which showed chondrogenic mRNA expression levels not significantly different than those previously reported for Alpha 1 alone. The introduction of Saos-2 cells on the HA section (Model-2) showed downregulation of chondrogenic mRNA expression compared to the Model-1 samples. However, these levels were still higher than the cartilage gold standard. The Saos-2+HA section showed significant downregulation of osteogenic marker expression, depicting that further optimisation of the culture medium composition should be assessed to encourage bone formation.

Finally, HOB+HA scaffolds were used to develop Model-3. Although a reduced sample size was used to assess the effect of these primary cells, immunofluorescence labelling and comparative qPCR showed comparable levels of expression in both the cartilage and bone sections as the samples manufactured with Saos-2 cells (Model-2). These results confirmed that a fully human primary cell-based osteochondral model could be developed. However, a larger sample size is required for detailed characterisation and repeatability of the behaviour of these composite tissues.

Chapter 6:   Conclusion

The work presented in this thesis focuses on developing a human osteochondral tissue *in vitro* model using a non-animal-derived commercial self-assembling peptide (Peptigel®) and an in-house optimised hydroxyapatite (HA) bioink. Current osteochondral tissue models are developed using tissue engineering-based techniques which lack control over the geometry of the sample and have limitations such as heterogeneous cell distribution. The presented work, 3D bioprinting is used as the main technique to circumvent these issues and manufacture the tissue models with a scalable technology. Within the existing 3D bioprinted osteochondral tissue models, issues such as delamination between the cartilage and bone sections and limitations coming from using animal-derived materials are prevalent. Therefore, this work focused on developing a simplified 3D bioprinted osteochondral tissue model which did not rely on animal-derived materials and ensured adhesion between the cartilage and bone sections.

Firstly, three Peptigels® were hypothesised to be successfully screened as potential bioinks according to viscosity, diffusion and pH properties. This hypothesis was proved as these three parameters enabled the selection of two Peptigels® (Alpha 1 and Alpha 4) as bioinks (PeptiInks®), based on their shear-thinning and lower viscosity profile, neutral pH (6.5-7.5), and fast diffusion properties. The 3D bioprinting optimisation of Alpha 1 and Alpha 4 was assessed through deposited filament width according to extrusion pressure and printing speed. As expected, higher printing speeds led to thinner filaments. Higher printing pressures led to wider filaments and more material deposition. The filament width was compared to the theoretical value (diameter of the printing nozzle 25G). A printing pressure window of 8-10 kPa was optimal for both Peptigels®. Although high printing speeds (10 mm/s) led to a better printing resolution, a slower printing speed (5 mm/s) was chosen to enable the printer user to change printing pressure values without compromising filament continuity. Additionally, *in silico* modelling was hypothesised to be useful for understanding the shear stresses and pressure forces arising in the extrusion process. A CFD (computational fluid dynamics) model was successfully developed, and clear contour maps enabled the

visualisation of these forces, confirming that high shear stresses detrimental to cell viability (> 120 Pa) would only be reached at the tip of the printing nozzle.

Secondly, using the two selected Peptigels®, a 3D bioprinting protocol was developed to manufacture cartilage tissue models *in vitro*. Human primary chondrocytes (HCHs) were mixed with Alpha 1 and Alpha 4 and 3D bioprinted into circular disc structures. These samples were assessed regarding their cell viability post-bioprinting, DNA quantification, histological structure, and protein expression through immunofluorescence labelling. They were compared to the current "gold standard" in cartilage *in vitro* tissue modelling, a 3D chondrocyte pellet. These results found 33% cell survival post-bioprinting for Alpha 1, which increased significantly in the 14 days of culture to ~60%. Alpha 4 showed high levels of cell survival post-bioprinting (~87%), which decreased significantly over the 14-day culture period, down to 35% in the first 7 days and 56% on day 14.

Additionally, the gold standard showed decreased cell viability due to core pellet necrosis, reaching 54% viability on day 14. DNA quantification confirmed the observed cell viability trend. The histological assessment confirmed the homogeneous cell distribution post-bioprinting as well as showing the differences in cell morphology between Alpha 1 and Alpha 4. Alpha 1 showed the initial formation of cell clusters on the surface, similar to the control. Alpha 4 showed a fibroblastic cell morphology with cells congregating along the surface, forming a cell sheet. Immunofluorescence showed that Alpha 1 presented the expected chondrogenic protein expression (SOX-9, collagen type-II, and aggrecan). Alpha 4 showed no expression for SOX-9 or collagen type-II, which led to discarding this material as a chondrogenic PeptiInk®. Further assessment of the chondrogenic profile of embedded Alpha 1 HCHs was performed through qPCR. A significant increase in chondrogenic markers with respect to the gold standard was observed in the first 7 days of culture, confirming the chondrogenic behaviour of Alpha 1.

Thirdly, the bone section of the osteochondral model was developed using a previously optimised HA ink. The mechanical characteristics of this material were assessed and compared to previous studies. Rheological assessment showed the expected shear-thinning trend with higher viscosity values in low shear stress levels

(< 0.5 s^{-1}) than previously reported. Additionally, changes in the size of the 3D-printed constructs post-sintering were found to shrink by 15%, as opposed to 50% as previously reported. Finally, the mechanical properties were assessed through compressive testing, finding a 0.28 MPa modulus, 10 times lower than previously reported but within the range of bone compressive moduli. Subsequently, Saos-2 cells were seeded onto the HA scaffolds and cell viability, metabolic activity, cell-material interaction and protein expression were assessed. High levels of cell viability and increasing metabolic activity across the 28 days of culture were observed.

Furthermore, full HA scaffold cell coverage was achieved after 28 days of culture, showing high levels of collagen type-I expression. Finally, qPCR showed that Saos-2 cells seeded onto the HA scaffolds had upregulated expression of collagen type-I, RUNX2, and ALP, compared to the 2D control. Based on these promising results, primary human osteoblasts (HOBs) were used to develop a proof-of-concept bone-like model using primary cells. These cells demonstrated proliferation over the 28 days of culture, although slower than the Saos-2 cells. Additionally, even though collagen type-I expression was observed through immunofluorescence labelling, qPCR showed downregulation of osteogenic genes in the first 14 days of culture, which then increased and matched the expression levels of the 2D control on day 28. This demonstrated that the HA scaffolds supported these cells and promoted osteogenic behaviour. However, a larger sample population is required to characterise this behaviour fully.

Finally, the cartilage and bone-like sections were combined to form the 3D bioprinted osteochondral tissue model. An inverted manufacturing approach was used to ensure adhesion between the Alpha 1 and the HA sections. Placing the HA scaffold on top of Alpha 1 ensured the interaction of both sections without delamination and reduced degradation of Alpha 1. Once this manufacturing process was optimised, the effect of the HA scaffold on HCHs embedded in Alpha 1 (Model-1) was assessed through immunofluorescence and qPCR. The addition of this section did not interfere with cell cluster formation in Alpha 1. The expression of SOX-9 was maintained as Alpha 1 alone cultured. Collagen type-II and aggrecan expression were slightly downregulated compared to Alpha 1 alone. Additionally, collagen type-I expression was seen on those

HCHs which migrated onto the HA scaffold. However, the expression of this marker was downregulated when assessed through qPCR. Finally, as expected, RUNX2 and ALP expression was slightly upregulated due to the addition of this ceramic section.

Saos-2 cells were added to this biphasic construct, and the effect of this cell addition was investigated (Model-2). qPCR was the most informative analysis technique. It showed a further decrease in collagen type-II and aggrecan expression in the cartilage section, whilst SOX-9 was maintained. Furthermore, collagen type-X was significantly decreased. However, all chondrogenic markers were upregulated with respect to the gold standard, maintaining the expected chondrogenic potential of Alpha 1. The profile of Saos-2 cells was also assessed to investigate the effect of the cell culture medium change on day 14. An upregulation of aggrecan and downregulation of collagen type-II, RUNX2 and ALP were observed as expected. This depicted the need to optimise the cell culture medium further to ensure the HA scaffold's osteogenic potential was not compromised.

A final proof-of-concept model (Model-3) was manufactured and assessed using only human primary cells (HCHs and HOBs). The chondrogenic expression levels of the cartilage section were upregulated compared to those of the Saos-2-based samples. Overall, these primary cell models behaved in the cartilage section similarly to the Model-1, confirming that HOBs had a better impact on the HCH chondrogenic profile than Saos-2 cells. The changes observed on the HOB bone-like section were minor. Upregulation of collagen type-I, RUNX2, and ALP was observed on these samples after those 7 days of chondrogenic medium immersion compared to the previous day 14 time point. This showed that the HOBs were more resilient to this medium change and continued expressing the expected osteogenic proteins.

Overall, this investigation showed the potential of Peptigel® Alpha 1 as a PeptiInk® to develop a cartilage tissue model and its subsequent combination with an HA-based bone-like section. Although using Saos-2 cells was useful to characterise these models initially, HOBs were observed to be better at ensuring the chondrogenic behaviour of the Alpha 1 section and maintaining an osteogenic profile despite the chondrogenic medium change after 14 days of culture. These models have demonstrated the expected expression profile using human primary cells and non-

animal-derived materials. Further comparison of these models with osteochondral tissue samples should be performed to investigate how close they are to native tissue. Additionally, the inducement of diseases such as osteoarthritis (OA) on these samples should be investigated to explore their potential use as OA human disease models *in vitro.*

Bibliography

1. Gadjanski I, Vunjak-Novakovic G. 2015 Nov 2; Challenges in engineering osteochondral tissue grafts with hierarchical structures. 15(11):1583–99. 2015 Nov 2. Expert Opin Biol Ther [Internet]. Available from: http://www.tandfonline.com/doi/full/10.1517/14712598.2015.1070825

2. Santos-Beato P, Midha S, Pitsillides AA, Miller A, Torii R, Kalaskar DM. 2022 Jan 6; Biofabrication of the osteochondral unit and its applications: Current and future directions for 3D bioprinting. 13:204173142211334. 2022 Jan 6. J Tissue Eng [Internet]. Available from: http://journals.sagepub.com/doi/10.1177/20417314221133480

3. Mosher TJ. 2009. Arthritis in Color [Internet]. First Edit. 23–32 p. 2009. Bruno MA, Mosher TJ, Gold GE, editors. Arthritis in Color. Elsevier; Available from: http://dx.doi.org/10.1016/B978-1-4160-4722-3.00002-1

4. Alford JW, Cole BJ. 2005 Feb; Cartilage Restoration, Part 1. 33(2):295–306. 2005 Feb. Am J Sports Med [Internet]. Available from: http://journals.sagepub.com/doi/10.1177/0363546504273510

5. Maroudas A, Venn M. 1977 Oct 1; Chemical composition and swelling of normal and osteoarthrotic femoral head cartilage. II. Swelling. 36(5):399–406. 1977 Oct 1. Ann Rheum Dis [Internet]. Available from: https://ard.bmj.com/lookup/doi/10.1136/ard.36.5.399

6. Jay GD, Torres JR, Warman ML, Laderer MC, Breuer KS. 2007 Apr 10; The role of lubricin in the mechanical behavior of synovial fluid. 104(15):6194–9. 2007 Apr 10. Proc Natl Acad Sci [Internet]. Available from: https://pnas.org/doi/full/10.1073/pnas.0608558104

7. Schmidt TA, Gastelum NS, Nguyen QT, Schumacher BL, Sah RL. 2007 Mar; Boundary lubrication of articular cartilage: Role of synovial fluid constituents. 56(3):882–91. 2007 Mar. Arthritis Rheum [Internet]. Available from: https://onlinelibrary.wiley.com/doi/10.1002/art.22446

8. Xia Y, Moody JB, Burton-Wurster N, Lust G. 2001 Jul; Quantitative in situ correlation between microscopic MRI and polarized light microscopy studies of articular cartilage. 9(5):393–406. 2001 Jul. Osteoarthr Cartil [Internet]. Available from: https://linkinghub.elsevier.com/retrieve/pii/S1063458400904059

9. Clark JM. 1985; The organization of collagen in cryofractured rabbit articular cartilage: A scanning electron microscopic study. 3(1):17–29. 1985. J Orthop Res [Internet]. Available from: https://onlinelibrary.wiley.com/doi/10.1002/jor.1100030102

10. Bayliss MT, Venn M, Maroudas A, Ali SY. 1983 Feb 1; Structure of

proteoglycans from different layers of human articular cartilage. 209(2):387–400. 1983 Feb 1. Biochem J [Internet]. Available from: https://portlandpress.com/biochemj/article/209/2/387/14514/Structure-of-proteoglycans-from-different-layers

11. Clark JM. 1991 Mar; Variation of collagen fiber alignment in a joint surface: A scanning electron microscope study of the tibial plateau in dog, rabbit, and man. 9(2):246–57. 1991 Mar. J Orthop Res [Internet]. Available from: https://onlinelibrary.wiley.com/doi/10.1002/jor.1100090213

12. Bader DL, Kempson GE. 1994; The short-term compressive properties of adult human articular cartilage. 4(3):245–56. 1994. Biomed Mater Eng [Internet]. Available from: http://www.ncbi.nlm.nih.gov/pubmed/7950872

13. Koszyca B, Fazzalari NL, Vernon-Roberts B. 1996; Calcified cartilage, subchondral and cancellous bone morphometry within the knee of normal subjects. 3(1):15–22. 1996. Knee [Internet]. Available from: https://www.sciencedirect.com/science/article/pii/0968016096002062

14. Zhang Y, Wang F, Tan H, Chen G, Guo L, Yang L. 2012; Analysis of the Mineral Composition of the Human Calcified Cartilage Zone. 9(5):353–60. 2012. Int J Med Sci [Internet]. Available from: http://www.medsci.org/v09p0353.htm

15. Hu Y, Chen X, Wang S, Jing Y, Su J. 2021; Subchondral bone microenvironment in osteoarthritis and pain. 9(1):1–13. 2021. Bone Res [Internet]. Available from: http://dx.doi.org/10.1038/s41413-021-00147-z

16. Mente PL, Lewis JL. 1994 Sep; Elastic modulus of calcified cartilage is an order of magnitude less than that of subchondral bone. 12(5):637–47. 1994 Sep. J Orthop Res [Internet]. Available from: https://onlinelibrary.wiley.com/doi/10.1002/jor.1100120506

17. Wei W, Dai H. 2021; Articular cartilage and osteochondral tissue engineering techniques: Recent advances and challenges. 6(12):4830–55. 2021. Bioact Mater [Internet]. Available from: https://www.sciencedirect.com/science/article/pii/S2452199X21002310

18. Hallett SA, Ono W, Ono N. 2021 Oct; The hypertrophic chondrocyte: To be or not to be. 36(10):1021–36. 2021 Oct. Histol Histopathol [Internet]. Available from: http://www.ncbi.nlm.nih.gov/pubmed/34137454

19. Bonucci E. 1992. Calcification in Biological Systems [Internet]. 1992. CRC Press; Available from: https://books.google.co.uk/books?id=wfXDzQEACAAJ

20. Yang G, Zhu L, Hou N, Lan Y, Wu XM, Zhou B, et al. 2014; Osteogenic fate of hypertrophic chondrocytes. 24(10):1266–9. 2014. Cell Res [Internet]. Available from: https://doi.org/10.1038/cr.2014.111

21. Yang L, Tsang KY, Tang HC, Chan D, Cheah KSE. 2014 Aug 19; Hypertrophic chondrocytes can become osteoblasts and osteocytes in endochondral bone formation. 111(33):12097–102. 2014 Aug 19. Proc Natl Acad Sci [Internet]. Available from: https://pnas.org/doi/full/10.1073/pnas.1302703111

22. Zhou X, von der Mark K, Henry S, Norton W, Adams H, de Crombrugghe B. 2014 Dec 4; Chondrocytes Transdifferentiate into Osteoblasts in Endochondral Bone during Development, Postnatal Growth and Fracture Healing in Mice. 10(12):e1004820. 2014 Dec 4. Warman ML, editor. PLoS Genet [Internet]. Available from: https://dx.plos.org/10.1371/journal.pgen.1004820

23. Park J, Gebhardt M, Golovchenko S, Perez-Branguli F, Hattori T, Hartmann C, et al. 2015 May 15; Dual pathways to endochondral osteoblasts: a novel chondrocyte-derived osteoprogenitor cell identified in hypertrophic cartilage. 4(5):608–21. 2015 May 15. Biol Open [Internet]. Available from: https://journals.biologists.com/bio/article/4/5/608/1398/Dual-pathways-to-endochondral-osteoblasts-a-novel

24. Hu DP, Ferro F, Yang F, Taylor AJ, Chang W, Miclau T, et al. 2017 Jan 15; Cartilage to bone transformation during fracture healing is coordinated by the invading vasculature and induction of the core pluripotency genes. 144(2):221–34. 2017 Jan 15. Development [Internet]. Available from: https://journals.biologists.com/dev/article/144/2/221/48097/Cartilage-to-bone-transformation-during-fracture

25. Long JT, Leinroth A, Liao Y, Ren Y, Mirando AJ, Nguyen T, et al. 2022; Hypertrophic chondrocytes serve as a reservoir for marrow-associated skeletal stem and progenitor cells, osteoblasts, and adipocytes during skeletal development. 11:e76932. 2022. Wan M, Zaidi M, Wan M, Ono N, editors. Elife [Internet]. Available from: https://doi.org/10.7554/eLife.76932

26. JP H, B B. 2023. Histology, Osteoblasts [Internet]. 2023. StatPearls Publishing; Available from: https://www.ncbi.nlm.nih.gov/books/NBK557792/

27. Franz-Odendaal TA, Hall BK, Witten PE. 2006 Jan; Buried alive: How osteoblasts become osteocytes. 235(1):176–90. 2006 Jan. Dev Dyn [Internet]. Available from: https://onlinelibrary.wiley.com/doi/10.1002/dvdy.20603

28. Nahian A, AlEssa A. 2023. Histology, Osteocytes. 2023. StatPearls Publishing;

29. Boyce B, Yao Z, Xing L. 2009; Osteoclasts Have Multiple Roles in Bone in Addition to Bone Resorption. 19(3):171–80. 2009. Crit Rev Eukaryot Gene Expr [Internet]. Available from: http://www.dl.begellhouse.com/journals/6dbf508d3b17c437,12b6e91c2627fc7a,03210611080ec17a.html

30. Lee HJ, Kim YB, Ahn SH, Lee JS, Jang CH, Yoon H, et al. 2015 Jun; A New Approach for Fabricating Collagen/ECM-Based Bioinks Using Preosteoblasts and Human Adipose Stem Cells. 4(9):1359–68. 2015 Jun. Adv Healthc Mater

[Internet]. Available from: https://onlinelibrary.wiley.com/doi/10.1002/adhm.201500193

31. Bendtsen ST, Quinnell SP, Wei M. 2017 May 25; Development of a novel alginate-polyvinyl alcohol-hydroxyapatite hydrogel for 3D bioprinting bone tissue engineered scaffolds. 105(5):1457–68. 2017 May 25. J Biomed Mater Res Part A [Internet]. Available from: http://doi.wiley.com/10.1002/jbm.a.36036

32. Beck EC, Barragan M, Tadros MH, Gehrke SH, Detamore MS. 2016 Jul 1; Approaching the compressive modulus of articular cartilage with a decellularized cartilage-based hydrogel. 38(10):94–105. 2016 Jul 1. Acta Biomater [Internet]. Available from: https://linkinghub.elsevier.com/retrieve/pii/S0031938416312148

33. Goldstein SA. 1987 Jan; The mechanical properties of trabecular bone: Dependence on anatomic location and function. 20(11–12):1055–61. 1987 Jan. J Biomech [Internet]. Available from: https://linkinghub.elsevier.com/retrieve/pii/0021929087900236

34. Seedhom BB, Berry E, Ostell AE, Cuppone M. 2004 Mar 1; The Longitudinal Young's Modulus of Cortical Bone in the Midshaft of Human Femur and its Correlation with CT Scanning Data. 74(3):302–9. 2004 Mar 1. Calcif Tissue Int [Internet]. Available from: http://link.springer.com/10.1007/s00223-002-2123-1

35. Daly AC, Cunniffe GM, Sathy BN, Jeon O, Alsberg E, Kelly DJ. 2016 Sep; 3D Bioprinting of Developmentally Inspired Templates for Whole Bone Organ Engineering. 5(18):2353–62. 2016 Sep. Adv Healthc Mater [Internet]. Available from: http://doi.wiley.com/10.1002/adhm.201600182

36. Dhawan A, Kennedy PM, Rizk EB, Ozbolat IT. 2019 Mar; Three-dimensional Bioprinting for Bone and Cartilage Restoration in Orthopaedic Surgery. 27(5):e215–26. 2019 Mar. J Am Acad Orthop Surg [Internet]. Available from: http://journals.lww.com/00124635-201903010-00006

37. Fedorovich NE, Kuipers E, Gawlitta D, Dhert WJA, Alblas J. 2011 Oct 20; Scaffold Porosity and Oxygenation of Printed Hydrogel Constructs Affect Functionality of Embedded Osteogenic Progenitors. 17(19–20):2473–86. 2011 Oct 20. Tissue Eng Part A [Internet]. Available from: https://doi.org/10.1089/ten.tea.2011.0001

38. Mahmoodian R, Leasure J, Philip P, Pleshko N, Capaldi F, Siegler S. 2011 Oct; Changes in mechanics and composition of human talar cartilage anlagen during fetal development. 19(10):1199–209. 2011 Oct. Osteoarthr Cartil [Internet]. Available from: http://dx.doi.org/10.1016/j.joca.2011.07.013

39. Bielajew BJ, Donahue RP, Lamkin EK, Hu JC, Hascall VC, Athanasiou KA. 2022 Dec 22; Proteomic, mechanical, and biochemical development of tissue-engineered neocartilage. 26(1):34. 2022 Dec 22. Biomater Res [Internet]. Available from: https://doi.org/10.1186/s40824-022-00284-4

40. Suzuki T, Matsuura Y, Yamazaki T, Akasaka T, Ozone E, Matsuyama Y, et al. 2020 Mar; Biomechanics of callus in the bone healing process, determined by specimen-specific finite element analysis. 132(July 2019):115212. 2020 Mar. Bone [Internet]. Available from: https://doi.org/10.1016/j.bone.2019.115212

41. Salinas EY, Donahue RP, Herrera JM, Hu JC, Athanasiou KA. 2022 Apr 28; The functionality and translatability of neocartilage constructs are improved with the combination of fluid-induced shear stress and bioactive factors. 36(4):1–17. 2022 Apr 28. FASEB J [Internet]. Available from: https://onlinelibrary.wiley.com/doi/10.1096/fj.202101699R

42. Wittkowske C, Reilly GC, Lacroix D, Perrault CM. 2016 Nov 15; In Vitro Bone Cell Models: Impact of Fluid Shear Stress on Bone Formation. 4(NOV). 2016 Nov 15. Front Bioeng Biotechnol [Internet]. Available from: http://journal.frontiersin.org/article/10.3389/fbioe.2016.00087/full

43. Sharifi N, Gharravi AM. 2019 Dec 8; Shear bioreactors stimulating chondrocyte regeneration, a systematic review. 39(1):16. 2019 Dec 8. Inflamm Regen [Internet]. Available from: https://inflammregen.biomedcentral.com/articles/10.1186/s41232-019-0105-1

44. McCutchen C, June R. 2017 Apr; A Comparison of Shear- and Compression-induced Mechanotransduction in Chondrocytes. 25(2017):S278–9. 2017 Apr. Osteoarthr Cartil [Internet]. Available from: http://dx.doi.org/10.1016/j.joca.2017.02.471

45. Shea CA, Rolfe RA, Murphy P. 2015 Jul; The importance of foetal movement for co-ordinated cartilage and bone development in utero. 4(7):105–16. 2015 Jul. Bone Joint Res [Internet]. Available from: https://online.boneandjoint.org.uk/doi/10.1302/2046-3758.47.2000387

46. Zhou H. 2021 May 26; Embryonic movement stimulates joint formation and development: Implications in arthrogryposis multiplex congenita. 43(5):2000319. 2021 May 26. BioEssays [Internet]. Available from: https://onlinelibrary.wiley.com/doi/10.1002/bies.202000319

47. Occhetta P, Mainardi A, Votta E, Vallmajo-Martin Q, Ehrbar M, Martin I, et al. 2019 Jul 3; Hyperphysiological compression of articular cartilage induces an osteoarthritic phenotype in a cartilage-on-a-chip model. 3(7):545–57. 2019 Jul 3. Nat Biomed Eng [Internet]. Available from: http://dx.doi.org/10.1038/s41551-019-0406-3

48. Waldman SD, Spiteri CG, Grynpas MD, Pilliar RM, Kandel RA. 2003 Jul; Long-term intermittent shear deformation improves the quality of cartilaginous tissue formed in vitro. 21(4):590–6. 2003 Jul. J Orthop Res [Internet]. Available from: http://doi.wiley.com/10.1016/S0736-0266%2803%2900009-3

49. Yu W, Qu H, Hu G, Zhang Q, Song K, Guan H, et al. 2014 Feb 27; A Microfluidic-Based Multi-Shear Device for Investigating the Effects of Low Fluid-Induced

Stresses on Osteoblasts. 9(2):e89966. 2014 Feb 27. Engler AJ, editor. PLoS One [Internet]. Available from: https://dx.plos.org/10.1371/journal.pone.0089966

50. Aisha MD, Nor-Ashikin MNK, Sharaniza ABR, Nawawi H, Froemming GRA. 2015; Orbital fluid shear stress promotes osteoblast metabolism, proliferation and alkaline phosphates activity in vitro. 337(1):87–93. 2015. Exp Cell Res [Internet]. Available from: https://www.sciencedirect.com/science/article/pii/S0014482715300331

51. Xing J, Li Y, Lin M, Wang J, Wu J, Ma Y, et al. 2014; Surface chemistry modulates osteoblasts sensitivity to low fluid shear stress. 102(11):4151–60. 2014. J Biomed Mater Res Part A [Internet]. Available from: https://onlinelibrary.wiley.com/doi/abs/10.1002/jbm.a.35087

52. Mai Z, Peng Z, Wu S, Zhang J, Chen L, Liang H, et al. 2013 Apr 11; Single Bout Short Duration Fluid Shear Stress Induces Osteogenic Differentiation of MC3T3-E1 Cells via Integrin β1 and BMP2 Signaling Cross-Talk. 8(4):e61600. 2013 Apr 11. Shi XM, editor. PLoS One [Internet]. Available from: https://dx.plos.org/10.1371/journal.pone.0061600

53. Stone W, Leavitt L, Varacallo M. 2023. Physiology, Growth Factor [Internet]. 2023. StatPearls Publishing; Available from: https://www.ncbi.nlm.nih.gov/books/NBK442024/

54. Ansari S, Khorshidi S, Karkhaneh A. 2019; Engineering of gradient osteochondral tissue: From nature to lab. 87:41–54. 2019. Acta Biomater [Internet]. Available from: https://www.sciencedirect.com/science/article/pii/S1742706119301023

55. Reddi AH. 1998 Mar; Role of morphogenetic proteins in skeletal tissue engineering and regeneration. 16(3):247–52. 1998 Mar. Nat Biotechnol [Internet]. Available from: https://www.nature.com/articles/nbt0398-247

56. Di Luca A, Van Blitterswijk C, Moroni L. 2015 Mar; The osteochondral interface as a gradient tissue: From development to the fabrication of gradient scaffolds for regenerative medicine. 105(1):34–52. 2015 Mar. Birth Defects Res Part C Embryo Today Rev [Internet]. Available from: https://onlinelibrary.wiley.com/doi/10.1002/bdrc.21092

57. Tozzi G, De Mori A, Oliveira A, Roldo M. 2016 Apr 2; Composite Hydrogels for Bone Regeneration. 9(4):267. 2016 Apr 2. Materials (Basel) [Internet]. Available from: http://www.mdpi.com/1996-1944/9/4/267

58. Responte DJ, Natoli RM, Athanasiou KA. 2007; Collagens of Articular Cartilage: Structure, Function, and Importance in Tissue Engineering. 35(5):363–411. 2007. Crit Rev Biomed Eng [Internet]. Available from: http://www.dl.begellhouse.com/journals/4b27cbfc562e21b8,4d8cbde20903daf 0,1fff0bc6456f7bb7.html

59. Spiller KL, Maher SA, Lowman AM. 2011 Aug; Hydrogels for the Repair of Articular Cartilage Defects. 17(4):281–99. 2011 Aug. Tissue Eng Part B Rev [Internet]. Available from: https://www.liebertpub.com/doi/10.1089/ten.teb.2011.0077

60. Kilian D, Ahlfeld T, Akkineni AR, Bernhardt A, Gelinsky M, Lode A. 2020 Dec 19; 3D Bioprinting of osteochondral tissue substitutes – in vitro-chondrogenesis in multi-layered mineralized constructs. 10(1):8277. 2020 Dec 19. Sci Rep [Internet]. Available from: http://www.nature.com/articles/s41598-020-65050-9

61. Meinert C, Schrobback K, Hutmacher DW, Klein TJ. 2017; A novel bioreactor system for biaxial mechanical loading enhances the properties of tissue-engineered human cartilage. 7(1):1–14. 2017. Sci Rep [Internet]. Available from: http://dx.doi.org/10.1038/s41598-017-16523-x

62. Cui X, Breitenkamp K, Finn MG, Lotz M, D'Lima DD. 2012 Jun; Direct Human Cartilage Repair Using Three-Dimensional Bioprinting Technology. 18(11–12):1304–12. 2012 Jun. Tissue Eng Part A [Internet]. Available from: http://www.ncbi.nlm.nih.gov/pubmed/22394017

63. Nguyen D, Hägg DA, Forsman A, Ekholm J, Nimkingratana P, Brantsing C, et al. 2017 Dec 6; Cartilage Tissue Engineering by the 3D Bioprinting of iPS Cells in a Nanocellulose/Alginate Bioink. 7(1):658. 2017 Dec 6. Sci Rep [Internet]. Available from: http://www.nature.com/articles/s41598-017-00690-y

64. Daly AC, Kelly DJ. 2019 Mar; Biofabrication of spatially organised tissues by directing the growth of cellular spheroids within 3D printed polymeric microchambers. 197(September 2018):194–206. 2019 Mar. Biomaterials [Internet]. Available from: https://doi.org/10.1016/j.biomaterials.2018.12.028

65. Gao G, Yonezawa T, Hubbell K, Dai G, Cui X. 2015 Oct 1; Inkjet-bioprinted acrylated peptides and PEG hydrogel with human mesenchymal stem cells promote robust bone and cartilage formation with minimal printhead clogging. 10(10):1568–77. 2015 Oct 1. Biotechnol J [Internet]. Available from: https://doi.org/10.1002/biot.201400635

66. Martin-Iglesias S, Milian L, Sancho-Tello M, Salvador-Clavell R, Martín de Llano JJ, Carda C, et al. 2022; BMP-2 Enhances Osteogenic Differentiation of Human Adipose-Derived and Dental Pulp Stem Cells in 2D and 3D *In Vitro* Models. 2022:4910399. 2022. Chimenti I, editor. Stem Cells Int [Internet]. Available from: https://doi.org/10.1155/2022/4910399

67. Yang Z, Wang B, Liu W, Li X, Liang K, Fan Z, et al. 2023; In situ self-assembled organoid for osteochondral tissue regeneration with dual functional units. 27:200–15. 2023. Bioact Mater [Internet]. Available from: https://www.sciencedirect.com/science/article/pii/S2452199X23001202

68. Peck M, Dusserre N, McAllister TN, L'Heureux N. 2011; Tissue engineering by self-assembly. 14(5):218–24. 2011. Mater Today [Internet]. Available from:

https://www.sciencedirect.com/science/article/pii/S1369702111701171

69. Ofek G, Revell CM, Hu JC, Allison DD, Grande-Allen KJ, Athanasiou KA. 2008 Jul 30; Matrix Development in Self-Assembly of Articular Cartilage. 3(7):e2795. 2008 Jul 30. PLoS One [Internet]. Available from: https://doi.org/10.1371/journal.pone.0002795

70. Lee JK, Link JM, Hu JCY, Athanasiou KA. 2017 Nov; The Self-Assembling Process and Applications in Tissue Engineering. 7(11):a025668. 2017 Nov. Cold Spring Harb Perspect Med [Internet]. Available from: http://perspectivesinmedicine.cshlp.org/lookup/doi/10.1101/cshperspect.a025668

71. Zhang Z, McCaffery JM, Spencer RGS, Francomano CA. 2004 Sep; Hyaline cartilage engineered by chondrocytes in pellet culture: histological, immunohistochemical and ultrastructural analysis in comparison with cartilage explants. 205(3):229–37. 2004 Sep. J Anat [Internet]. Available from: https://onlinelibrary.wiley.com/doi/10.1111/j.0021-8782.2004.00327.x

72. Yang IH, Kim SH, Kim YH, Sun HJ, Kim SJ, Lee JW. 2004. Comparison of Phenotypic Characterization between "Alginate Bead" and "Pellet" Culture Systems as Chondrogenic Differentiation Models for Human Mesenchymal Stem Cells [Internet]. p. 891–900. 2004. Vol. 45, Yonsei Medical Journal. Available from: http://www.ncbi.nlm.nih.gov/pubmed/15515201

73. Gurkan UA, Kishore V, Condon KW, Bellido TM, Akkus O. 2011 May 12; A Scaffold-Free Multicellular Three-Dimensional In Vitro Model of Osteogenesis. 88(5):388–401. 2011 May 12. Calcif Tissue Int [Internet]. Available from: http://link.springer.com/10.1007/s00223-011-9467-3

74. Costantini M, Barbetta A. 2018. 6 - Gas foaming technologies for 3D scaffold engineering. p. 127–49. 2018. In: Deng Y, Kuiper JBTF 3D TES, editors. Woodhead Publishing; Available from: https://www.sciencedirect.com/science/article/pii/B9780081009796000069

75. Deng C, Chang J, Wu C. 2019 Apr; Bioactive scaffolds for osteochondral regeneration. 17:15–25. 2019 Apr. J Orthop Transl [Internet]. Available from: https://linkinghub.elsevier.com/retrieve/pii/S2214031X18301700

76. Chen Y, Xu W, Shafiq M, Tang J, Hao J, Xie X, et al. 2021; Three-dimensional porous gas-foamed electrospun nanofiber scaffold for cartilage regeneration. 603:94–109. 2021. J Colloid Interface Sci [Internet]. Available from: https://www.sciencedirect.com/science/article/pii/S0021979721009413

77. Giannitelli SM, Basoli F, Mozetic P, Piva P, Bartuli FN, Luciani F, et al. 2015 Jun; Graded porous polyurethane foam: A potential scaffold for oro-maxillary bone regeneration. 51:329–35. 2015 Jun. Mater Sci Eng C [Internet]. Available from: https://linkinghub.elsevier.com/retrieve/pii/S0928493115001848

78. Abdelaziz AG, Nageh H, Abdo SM, Abdalla MS, Amer AA, Abdal-hay A, et al. 2023 Feb 3; A Review of 3D Polymeric Scaffolds for Bone Tissue Engineering: Principles, Fabrication Techniques, Immunomodulatory Roles, and Challenges. 10(2):204. 2023 Feb 3. Bioengineering [Internet]. Available from: https://www.mdpi.com/2306-5354/10/2/204

79. Chemistry RS of. 2023 [cited 2023 Jul 10]. Thermally induced phase separation definition [Internet]. 2023. Available from: https://www.rsc.org/publishing/journals/prospect/ontology.asp?id=CMO:00022 16

80. Conoscenti G, Schneider T, Stoelzel K, Carfì Pavia F, Brucato V, Goegele C, et al. 2017; PLLA scaffolds produced by thermally induced phase separation (TIPS) allow human chondrocyte growth and extracellular matrix formation dependent on pore size. 80:449–59. 2017. Mater Sci Eng C [Internet]. Available from: https://www.sciencedirect.com/science/article/pii/S0928493116316514

81. Kumawat VS, Ghosh SB, Bandyopadhyay-Ghosh S. 2019; Microporous biocomposite scaffolds with tunable degradation and interconnected microarchitecture-A synergistic integration of bioactive chain silicate glass-ceramic and poly(ε-caprolactone). 165:20–6. 2019. Polym Degrad Stab [Internet]. Available from: https://www.sciencedirect.com/science/article/pii/S0141391019301351

82. Szustakiewicz K, Gazińska M, Kryszak B, Grzymajło M, Pigłowski J, Wiglusz RJ, et al. 2019; The influence of hydroxyapatite content on properties of poly(L-lactide)/hydroxyapatite porous scaffolds obtained using thermal induced phase separation technique. 113:313–20. 2019. Eur Polym J [Internet]. Available from: https://www.sciencedirect.com/science/article/pii/S001430571831824X

83. Degli Esposti M, Chiellini F, Bondioli F, Morselli D, Fabbri P. 2019 Jul; Highly porous PHB-based bioactive scaffolds for bone tissue engineering by in situ synthesis of hydroxyapatite. 100:286–96. 2019 Jul. Mater Sci Eng C [Internet]. Available from: https://linkinghub.elsevier.com/retrieve/pii/S0928493118327875

84. Gandolfi MG, Gardin C, Zamparini F, Ferroni L, Esposti MD, Parchi G, et al. 2020 Feb 29; Mineral-Doped Poly(L-lactide) Acid Scaffolds Enriched with Exosomes Improve Osteogenic Commitment of Human Adipose-Derived Mesenchymal Stem Cells. 10(3):432. 2020 Feb 29. Nanomaterials [Internet]. Available from: https://www.mdpi.com/2079-4991/10/3/432

85. Dai Y, Shen T, Ma L, Wang D, Gao C. 2018 Mar 27; Regeneration of osteochondral defects in vivo by a cell-free cylindrical poly(lactide-co-glycolide) scaffold with a radially oriented microstructure. 12(3):e1647–61. 2018 Mar 27. J Tissue Eng Regen Med [Internet]. Available from: https://onlinelibrary.wiley.com/doi/10.1002/term.2592

86. Feng X, Xu P, Shen T, Zhang Y, Ye J, Gao C. 2020; Influence of pore architectures of silk fibroin/collagen composite scaffolds on the regeneration of

osteochondral defects in vivo. 8(3):391–405. 2020. J Mater Chem B [Internet]. Available from: http://xlink.rsc.org/?DOI=C9TB01558B

87.   Erickson AE, Sun J, Lan Levengood SK, Swanson S, Chang FC, Tsao CT, et al. 2019 Jun 25; Chitosan-based composite bilayer scaffold as an in vitro osteochondral defect regeneration model. 21(2):34. 2019 Jun 25. Biomed Microdevices [Internet]. Available from: http://link.springer.com/10.1007/s10544-019-0373-1

88.   Zeinali R, del Valle LJ, Torras J, Puiggalí J. 2021 Mar 28; Recent Progress on Biodegradable Tissue Engineering Scaffolds Prepared by Thermally-Induced Phase Separation (TIPS). 22(7):3504. 2021 Mar 28. Int J Mol Sci [Internet]. Available from: https://www.mdpi.com/1422-0067/22/7/3504

89.   Lombardo ME, Carfì Pavia F, Vitrano I, Ghersi G, Brucato V, Rosei F, et al. 2019; PLLA scaffolds with controlled architecture as potential microenvironment for in vitro tumor model. 58:33–41. 2019. Tissue & cell [Internet]. Available from: http://europepmc.org/abstract/MED/31133244

90.   Siddiqui N, Asawa S, Birru B, Baadhe R, Rao S. 2018 Jul 14; PCL-Based Composite Scaffold Matrices for Tissue Engineering Applications. 60(7):506–32. 2018 Jul 14. Mol Biotechnol [Internet]. Available from: http://link.springer.com/10.1007/s12033-018-0084-5

91.   Fereshteh Z. 2018. 7 - Freeze-drying technologies for 3D scaffold engineering. p. 151–74. 2018. In: Deng Y, Kuiper JBTF 3D TES, editors. Woodhead Publishing; Available from: https://www.sciencedirect.com/science/article/pii/B9780081009796000070

92.   Chen L, Wu Z, Zhou Y, Li L, Wang Y, Wang Z, et al. 2017 Oct 5; Biomimetic porous collagen/hydroxyapatite scaffold for bone tissue engineering. 134(37):45271. 2017 Oct 5. J Appl Polym Sci [Internet]. Available from: https://doi.org/10.1002/app.45271

93.   Zhai C, Fei H, Hu J, Wang Z, Xu S, Zuo Q, et al. 2018 Nov; Repair of Articular Osteochondral Defects Using an Integrated and Biomimetic Trilayered Scaffold. 24(21–22):1680–92. 2018 Nov. Tissue Eng Part A [Internet]. Available from: https://www.liebertpub.com/doi/10.1089/ten.tea.2018.0086

94.   Haugh MG, Murphy CM, O'Brien FJ. 2010 Oct; Novel Freeze-Drying Methods to Produce a Range of Collagen–Glycosaminoglycan Scaffolds with Tailored Mean Pore Sizes. 16(5):887–94. 2010 Oct. Tissue Eng Part C Methods [Internet]. Available from: https://www.liebertpub.com/doi/10.1089/ten.tec.2009.0422

95.   Capuana E, Lopresti F, Carfì Pavia F, Brucato V, La Carrubba V. 2021 Jun 22; Solution-Based Processing for Scaffold Fabrication in Tissue Engineering Applications: A Brief Review. 13(13):2041. 2021 Jun 22. Polymers (Basel) [Internet]. Available from: https://www.mdpi.com/2073-4360/13/13/2041

96. Gonçalves AM, Moreira A, Weber A, Williams GR, Costa PF. 2021 Jun 29; Osteochondral Tissue Engineering: The Potential of Electrospinning and Additive Manufacturing. 13(7):983. 2021 Jun 29. Pharmaceutics [Internet]. Available from: https://www.mdpi.com/1999-4923/13/7/983

97. Naderi P, Zarei M, Karbasi S, Salehi H. 2020; Evaluation of the effects of keratin on physical, mechanical and biological properties of poly (3-hydroxybutyrate) electrospun scaffold: Potential application in bone tissue engineering. 124:109502. 2020. Eur Polym J [Internet]. Available from: https://www.sciencedirect.com/science/article/pii/S0014305719325145

98. Garrigues NW, Little D, Sanchez-Adams J, Ruch DS, Guilak F. 2014 Nov; Electrospun cartilage-derived matrix scaffolds for cartilage tissue engineering. 102(11):3998–4008. 2014 Nov. J Biomed Mater Res Part A [Internet]. Available from: https://onlinelibrary.wiley.com/doi/10.1002/jbm.a.35068

99. Zheng X, Wang W, Liu S, Wu J, Li F, Cao L, et al. 2016 Jan; Enhancement of chondrogenic differentiation of rabbit mesenchymal stem cells by oriented nanofiber yarn-collagen type I/hyaluronate hybrid. 58:1071–6. 2016 Jan. Mater Sci Eng C [Internet]. Available from: https://linkinghub.elsevier.com/retrieve/pii/S0928493115302526

100. Chen W, Xu Y, Liu Y, Wang Z, Li Y, Jiang G, et al. 2019; Three-dimensional printed electrospun fiber-based scaffold for cartilage regeneration. 179:107886. 2019. Mater Des [Internet]. Available from: https://www.sciencedirect.com/science/article/pii/S0264127519303247

101. Ng WL, Lee JM, Zhou M, Chen YW, Lee KXA, Yeong WY, et al. 2020 Feb 7; Vat polymerization-based bioprinting—process, materials, applications and regulatory challenges. 12(2):022001. 2020 Feb 7. Biofabrication [Internet]. Available from: https://iopscience.iop.org/article/10.1088/1758-5090/ab6034

102. Pati F, Jang J, Lee JW, Cho DW. 2015. Chapter 7 - Extrusion Bioprinting. p. 123–52. 2015. In: Atala A, Yoo JJBTE of 3D B and T, editors. Boston: Academic Press; Available from: https://www.sciencedirect.com/science/article/pii/B9780128009727000074

103. Zhou D, Chen J, Liu B, Zhang X, Li X, Xu T. 2019; Bioinks for jet-based bioprinting. 16:e00060. 2019. Bioprinting [Internet]. Available from: https://www.sciencedirect.com/science/article/pii/S2405886619300260

104. Keriquel V, Oliveira H, Rémy M, Ziane S, Delmond S, Rousseau B, et al. 2017 May 11; In situ printing of mesenchymal stromal cells, by laser-assisted bioprinting, for in vivo bone regeneration applications. 7(1):1778. 2017 May 11. Sci Rep [Internet]. Available from: https://www.nature.com/articles/s41598-017-01914-x

105. Liu F, Wang X. 2020 Aug 7; Synthetic Polymers for Organ 3D Printing. 12(8):1765. 2020 Aug 7. Polymers (Basel) [Internet]. Available from:

https://www.mdpi.com/2073-4360/12/8/1765

106. Vijayavenkataraman S, Fuh J, Lu W. 2017 Jul 13; 3D Printing and 3D Bioprinting in Pediatrics. 4(3):63. 2017 Jul 13. Bioengineering [Internet]. Available from: https://www.mdpi.com/2306-5354/4/3/63

107. Morouço P, Azimi B, Milazzo M, Mokhtari F, Fernandes C, Reis D, et al. 2020 Dec 21; Four-Dimensional (Bio-)printing: A Review on Stimuli-Responsive Mechanisms and Their Biomedical Suitability. 10(24):9143. 2020 Dec 21. Appl Sci [Internet]. Available from: https://www.mdpi.com/2076-3417/10/24/9143

108. Dababneh AB, Ozbolat IT. 2014 Dec 1; Bioprinting Technology: A Current State-of-the-Art Review. 136(6):1–11. 2014 Dec 1. J Manuf Sci Eng [Internet]. Available from: https://asmedigitalcollection.asme.org/manufacturingscience/article/doi/10.1115/1.4028512/377608/Bioprinting-Technology-A-Current-StateoftheArt

109. Fedorovich NE, De Wijn JR, Verbout AJ, Alblas J, Dhert WJA. 2008 Jan 1; Three-Dimensional Fiber Deposition of Cell-Laden, Viable, Patterned Constructs for Bone Tissue Printing. 14(1):127–33. 2008 Jan 1. Tissue Eng Part A [Internet]. Available from: https://doi.org/10.1089/ten.a.2007.0158

110. Griffith LG, Swartz MA. 2006 Mar; Capturing complex 3D tissue physiology in vitro. 7(3):211–24. 2006 Mar. Nat Rev Mol Cell Biol [Internet]. Available from: http://www.nature.com/articles/nrm1858

111. Caron MMJ, Emans PJ, Coolsen MME, Voss L, Surtel DAM, Cremers A, et al. 2012 Oct; Redifferentiation of dedifferentiated human articular chondrocytes: comparison of 2D and 3D cultures. 20(10):1170–8. 2012 Oct. Osteoarthr Cartil [Internet]. Available from: http://dx.doi.org/10.1016/j.joca.2012.06.016

112. Costantini M, Idaszek J, Szöke K, Jaroszewicz J, Dentini M, Barbetta A, et al. 2016 Jul 19; 3D bioprinting of BM-MSCs-loaded ECM biomimetic hydrogels for in vitro neocartilage formation. 8(3):035002. 2016 Jul 19. Biofabrication [Internet]. Available from: https://iopscience.iop.org/article/10.1088/1758-5090/8/3/035002

113. Filardo G, Petretta M, Cavallo C, Roseti L, Durante S, Albisinni U, et al. 2019 Feb; Patient-specific meniscus prototype based on 3D bioprinting of human cell-laden scaffold. 8(2):101–6. 2019 Feb. Bone Joint Res [Internet]. Available from: https://online.boneandjoint.org.uk/doi/10.1302/2046-3758.82.BJR-2018-0134.R1

114. Möller T, Amoroso M, Hägg D, Brantsing C, Rotter N, Apelgren P, et al. 2017 Feb; In Vivo Chondrogenesis in 3D Bioprinted Human Cell-laden Hydrogel Constructs. 5(2):e1227. 2017 Feb. Plast Reconstr Surg - Glob Open [Internet]. Available from: http://journals.lww.com/01720096-201702000-00013

115. Park JY, Choi JC, Shim JH, Lee JS, Park H, Kim SW, et al. 2014 Apr 24; A

comparative study on collagen type I and hyaluronic acid dependent cell behavior for osteochondral tissue bioprinting. 6(3):035004. 2014 Apr 24. Biofabrication [Internet]. Available from: https://iopscience.iop.org/article/10.1088/1758-5082/6/3/035004

116. Shim JH, Lee JS, Kim JY, Cho DW. 2012 Aug 1; Bioprinting of a mechanically enhanced three-dimensional dual cell-laden construct for osteochondral tissue engineering using a multi-head tissue/organ building system. 22(8):085014. 2012 Aug 1. J Micromechanics Microengineering [Internet]. Available from: https://iopscience.iop.org/article/10.1088/0960-1317/22/8/085014

117. Joshi A, Kaur T, Singh N. 2022 Jun 20; 3D Bioprinted Alginate-Silk-Based Smart Cell-Instructive Scaffolds for Dual Differentiation of Human Mesenchymal Stem Cells. 5(6):2870–9. 2022 Jun 20. ACS Appl Bio Mater [Internet]. Available from: https://pubs.acs.org/doi/10.1021/acsabm.2c00251

118. Liu Y, Peng L, Li L, Huang C, Shi K, Meng X, et al. 2021 Dec; 3D-bioprinted BMSC-laden biomimetic multiphasic scaffolds for efficient repair of osteochondral defects in an osteoarthritic rat model. 279:121216. 2021 Dec. Biomaterials [Internet]. Available from: https://linkinghub.elsevier.com/retrieve/pii/S0142961221005731

119. Breathwaite EK, Weaver JR, Murchison AC, Treadwell ML, Odanga JJ, Lee JB. 2019 Oct 3; Scaffold-free bioprinted osteogenic and chondrogenic systems to model osteochondral physiology. 14(6):065010. 2019 Oct 3. Biomed Mater [Internet]. Available from: https://iopscience.iop.org/article/10.1088/1748-605X/ab4243

120. Askari M, Afzali Naniz M, Kouhi M, Saberi A, Zolfagharian A, Bodaghi M. 2021; Recent progress in extrusion 3D bioprinting of hydrogel biomaterials for tissue regeneration: a comprehensive review with focus on advanced fabrication techniques. 9(3):535–73. 2021. Biomater Sci [Internet]. Available from: http://xlink.rsc.org/?DOI=D0BM00973C

121. Potyondy T, Uquillas JA, Tebon PJ, Byambaa B, Hasan A, Tavafoghi M, et al. 2021 Apr 1; Recent advances in 3D bioprinting of musculoskeletal tissues. 13(2):022001. 2021 Apr 1. Biofabrication [Internet]. Available from: https://iopscience.iop.org/article/10.1088/1758-5090/abc8de

122. Idaszek J, Costantini M, Karlsen TA, Jaroszewicz J, Colosi C, Testa S, et al. 2019 Jul 1; 3D bioprinting of hydrogel constructs with cell and material gradients for the regeneration of full-thickness chondral defect using a microfluidic printing head. 11(4):044101. 2019 Jul 1. Biofabrication [Internet]. Available from: https://iopscience.iop.org/article/10.1088/1758-5090/ab2622

123. Sun Y, You Y, Jiang W, Wang B, Wu Q, Dai K. 2020; 3D bioprinting dual-factor releasing and gradient-structured constructs ready to implant for anisotropic cartilage regeneration. 6(37):eaay1422. 2020. Sci Adv [Internet]. Available from: https://www.science.org/doi/abs/10.1126/sciadv.aay1422

124. Critchley S, Sheehy EJ, Cunniffe G, Diaz-Payno P, Carroll SF, Jeon O, et al. 2020 Sep; 3D printing of fibre-reinforced cartilaginous templates for the regeneration of osteochondral defects. 113:130–43. 2020 Sep. Acta Biomater [Internet]. Available from: https://doi.org/10.1016/j.actbio.2020.05.040

125. Mancini IAD, Vindas Bolaños RA, Brommer H, Castilho M, Ribeiro A, van Loon JPAM, et al. 2017 Nov; Fixation of Hydrogel Constructs for Cartilage Repair in the Equine Model: A Challenging Issue. 23(11):804–14. 2017 Nov. Tissue Eng Part C Methods [Internet]. Available from: https://www.liebertpub.com/doi/10.1089/ten.tec.2017.0200

126. Al-Modawi RN, Brinchmann JE, Karlsen TA. 2019 Sep; Multi-pathway Protective Effects of MicroRNAs on Human Chondrocytes in an In Vitro Model of Osteoarthritis. 17(776):776–90. 2019 Sep. Mol Ther - Nucleic Acids [Internet]. Available from: https://doi.org/10.1016/j.omtn.2019.07.011

127. Samavedi S, Diaz-Rodriguez P, Erndt-Marino JD, Hahn MS. 2017 Feb; A Three-Dimensional Chondrocyte-Macrophage Coculture System to Probe Inflammation in Experimental Osteoarthritis. 23(3–4):101–14. 2017 Feb. Tissue Eng Part A [Internet]. Available from: https://www.liebertpub.com/doi/10.1089/ten.tea.2016.0007

128. Zhang RK, Li GW, Zeng C, Lin CX, Huang LS, Huang GX, et al. 2018 Nov; Mechanical stress contributes to osteoarthritis development through the activation of transforming growth factor beta 1 (TGF-β1). 7(11):587–94. 2018 Nov. Bone Joint Res [Internet]. Available from: https://online.boneandjoint.org.uk/doi/10.1302/2046-3758.711.BJR-2018-0057.R1

129. Singh YP, Moses JC, Bandyopadhyay A, Mandal BB. 2022 Dec 19; 3D Bioprinted Silk-Based In Vitro Osteochondral Model for Osteoarthritis Therapeutics. 11(24):1–15. 2022 Dec 19. Adv Healthc Mater [Internet]. Available from: https://onlinelibrary.wiley.com/doi/10.1002/adhm.202200209

130. Swain S, Sarmanova A, Mallen C, Kuo CF, Coupland C, Doherty M, et al. 2020 Jun; Trends in incidence and prevalence of osteoarthritis in the United Kingdom: findings from the Clinical Practice Research Datalink (CPRD). 28(6):792–801. 2020 Jun. Osteoarthr Cartil [Internet]. Available from: https://www.sciencedirect.com/science/article/pii/S1063458420309183

131. Barbour KE, Helmick CG, Boring M, Brady TJ. 2017 Mar 10; Vital Signs: Prevalence of Doctor-Diagnosed Arthritis and Arthritis-Attributable Activity Limitation — United States, 2013–2015. 66(9):246–53. 2017 Mar 10. MMWR Morb Mortal Wkly Rep [Internet]. Available from: http://www.cdc.gov/mmwr/volumes/66/wr/mm6609e1.htm

132. Arthritis Research UK. 2013 [cited 2022 Sep 12]. VERSUS Arthritis [Internet]. 2013. Osteoarthritis in general practice. Available from: https://www.versusarthritis.org

133. Lawrence RC, Felson DT, Helmick CG, Arnold LM, Choi H, Deyo RA, et al. 2008 Jan; Estimates of the prevalence of arthritis and other rheumatic conditions in the United States: Part II. 58(1):26–35. 2008 Jan. Arthritis Rheum [Internet]. Available from: https://onlinelibrary.wiley.com/doi/10.1002/art.23176

134. Buckwalter JA., Saltzman C, Brown T. 2004 Oct; The Impact of Osteoarthritis. 427(427 SUPPL.):S6–15. 2004 Oct. Clin Orthop Relat Res [Internet]. Available from: http://journals.lww.com/00003086-200410001-00004

135. Woolf A. 2018 [cited 2020 Apr 7]. Tackling the Elephant in the Room [Internet]. 2018 Jul. NHS Blog. Available from: https://www.england.nhs.uk/blog/tackling-the-elephant-in-the-room/

136. Lories RJ, Luyten FP. 2011 Jan 7; The bone–cartilage unit in osteoarthritis. 7(1):43–9. 2011 Jan 7. Nat Rev Rheumatol [Internet]. Available from: http://www.nature.com/articles/nrrheum.2010.197

137. Felson DT. 1990 Dec; The epidemiology of knee osteoarthritis: Results from the framingham osteoarthritis study. 20(3):42–50. 1990 Dec. Semin Arthritis Rheum [Internet]. Available from: https://linkinghub.elsevier.com/retrieve/pii/004901729090046I

138. Nguyen L, Sharma A, Chakraborty C, Saibaba B, Ahn M eob, Lee S soo. 2017 Mar 12; Review of Prospects of Biological Fluid Biomarkers in Osteoarthritis. 18(3):601. 2017 Mar 12. Int J Mol Sci [Internet]. Available from: http://www.mdpi.com/1422-0067/18/3/601

139. Brandt KD. 2006 Mar 28; Yet more evidence that osteoarthritis is not a cartilage disease. 65(10):1261–4. 2006 Mar 28. Ann Rheum Dis [Internet]. Available from: https://ard.bmj.com/lookup/doi/10.1136/ard.2006.058347

140. Thambyah A, Broom N. 2009 Apr; On new bone formation in the pre-osteoarthritic joint. 17(4):456–63. 2009 Apr. Osteoarthr Cartil [Internet]. Available from: http://dx.doi.org/10.1016/j.joca.2008.09.005

141. Neogi T, Felson D, Niu J, Lynch J, Nevitt M, Guermazi A, et al. 2009 Nov 15; Cartilage loss occurs in the same subregions as subchondral bone attrition: A within-knee subregion-matched approach from the multicenter osteoarthritis study. 61(11):1539–44. 2009 Nov 15. Arthritis Rheum [Internet]. Available from: https://onlinelibrary.wiley.com/doi/abs/10.1002/art.24824

142. Roemer FW, Neogi T, Nevitt MC, Felson DT, Zhu Y, Zhang Y, et al. 2010 Jan; Subchondral bone marrow lesions are highly associated with, and predict subchondral bone attrition longitudinally: the MOST study. 18(1):47–53. 2010 Jan. Osteoarthr Cartil [Internet]. Available from: https://www.sciencedirect.com/science/article/pii/S1063458409002192

143. Suri S, Walsh DA. 2012 Aug; Osteochondral alterations in osteoarthritis. 51(2):204–11. 2012 Aug. Bone [Internet]. Available from:

http://dx.doi.org/10.1016/j.bone.2011.10.010

144. Chiesa I, De Maria C, Lapomarda A, Fortunato GM, Montemurro F, Di Gesù R, et al. 2020 Apr 1; Endothelial cells support osteogenesis in an in vitro vascularized bone model developed by 3D bioprinting. 12(2):025013. 2020 Apr 1. Biofabrication [Internet]. Available from: https://iopscience.iop.org/article/10.1088/1758-5090/ab6a1d

145. Schulz RM, Bader A. 2007 Apr 10; Cartilage tissue engineering and bioreactor systems for the cultivation and stimulation of chondrocytes. 36(4–5):539–68. 2007 Apr 10. Eur Biophys J [Internet]. Available from: http://link.springer.com/10.1007/s00249-007-0139-1

146. Yeatts AB, Fisher JP. 2011 Feb 1; Bone tissue engineering bioreactors: Dynamic culture and the influence of shear stress. 48(2):171–81. 2011 Feb 1. Bone [Internet]. Available from: http://dx.doi.org/10.1016/j.bone.2010.09.138

147. Young IC, Chuang ST, Gefen A, Kuo WT, Yang CT, Hsu CH, et al. 2017 May 22; A novel compressive stress-based osteoarthritis-like chondrocyte system. 242(10):1062–71. 2017 May 22. Exp Biol Med [Internet]. Available from: http://journals.sagepub.com/doi/10.1177/1535370217699534

148. Houtman E, van Hoolwerff M, Lakenberg N, Suchiman EHD, van der Linden-van der Zwaag E, Nelissen RGHH, et al. 2021 Mar 20; Human Osteochondral Explants: Reliable Biomimetic Models to Investigate Disease Mechanisms and Develop Personalized Treatments for Osteoarthritis. 8(1):499–515. 2021 Mar 20. Rheumatol Ther [Internet]. Available from: https://doi.org/10.1007/s40744-021-00287-y

149. Kleuskens MWA, Donkelaar CC, Kock LM, Janssen RPA, Ito K. 2021 Apr 10; An ex vivo human osteochondral culture model. 39(4):871–9. 2021 Apr 10. J Orthop Res [Internet]. Available from: https://onlinelibrary.wiley.com/doi/10.1002/jor.24789

150. Bertassoni LE, Cecconi M, Manoharan V, Nikkhah M, Hjortnaes J, Cristino AL, et al. 2014 Jul 7; Hydrogel bioprinted microchannel networks for vascularization of tissue engineering constructs. 14(13):2202–11. 2014 Jul 7. Lab Chip [Internet]. Available from: http://xlink.rsc.org/?DOI=C4LC00030G

151. Kolesky DB, Homan KA, Skylar-Scott MA, Lewis JA. 2016 Mar 22; Three-dimensional bioprinting of thick vascularized tissues. 113(12):3179–84. 2016 Mar 22. Proc Natl Acad Sci [Internet]. Available from: https://pnas.org/doi/full/10.1073/pnas.1521342113

152. Stellavato A, Vassallo V, La Gatta A, Pirozzi AVA, De Rosa M, Balato G, et al. 2019 Apr 23; Novel Hybrid Gels Made of High and Low Molecular Weight Hyaluronic Acid Induce Proliferation and Reduce Inflammation in an Osteoarthritis In Vitro Model Based on Human Synoviocytes and Chondrocytes. 2019:1–13. 2019 Apr 23. Biomed Res Int [Internet]. Available from:

https://www.hindawi.com/journals/bmri/2019/4328219/

153. Wang W, Narain R, Zeng H. 2020. Chapter 10 - Hydrogels. p. 203–44. 2020. In: Narain R, editor. Polymer Science and Nanotechnology [Internet]. Elsevier; Available from: https://www.sciencedirect.com/science/article/pii/B9780128168066000108

154. Waseeq Ur Rehman, Asim M, Hussain S, Khan SA, Khan SB. 2020 Dec 24; Hydrogel: A Promising Material in Pharmaceutics. 26(45):5892–908. 2020 Dec 24. Curr Pharm Des [Internet]. Available from: https://www.eurekaselect.com/188134/article

155. Hafezi M, Nouri Khorasani S, Zare M, Esmaeely Neisiany R, Davoodi P. 2021 Nov 30; Advanced Hydrogels for Cartilage Tissue Engineering: Recent Progress and Future Directions. 13(23):4199. 2021 Nov 30. Polymers (Basel) [Internet]. Available from: https://www.mdpi.com/2073-4360/13/23/4199

156. Murphy S V, Atala A. 2014; 3D bioprinting of tissues and organs. 32(8):773–85. 2014. Nat Biotechnol [Internet]. Available from: https://doi.org/10.1038/nbt.2958

157. Moroni L, Boland T, Burdick JA, De Maria C, Derby B, Forgacs G, et al. 2018 Apr; Biofabrication: A Guide to Technology and Terminology. 36(4):384–402. 2018 Apr. Trends Biotechnol [Internet]. Available from: https://linkinghub.elsevier.com/retrieve/pii/S0167779917302792

158. Starly B, Shirwaiker R. 2015. Chapter 3 - 3D Bioprinting Techniques. p. 71–91. 2015. In: Zhang LG, Fisher JP, Leong KWBT 3D B and N in TE and RM (Second E, editors. Academic Press; Available from: https://www.sciencedirect.com/science/article/pii/B9780128245521000207

159. Goel A, Meher MK, Gulati K, Poluri KM. 2019. Chapter 3 - Fabrication of Biopolymer-Based Organs and Tissues Using 3D Bioprinting. p. 43–62. 2019. In: Ahmad N, Gopinath P, Dutta RBT 3D PT in N, editors. Elsevier; Available from: https://www.sciencedirect.com/science/article/pii/B9780128158906000037

160. Unagolla JM, Jayasuriya AC. 2020 Mar; Hydrogel-based 3D bioprinting: A comprehensive review on cell-laden hydrogels, bioink formulations, and future perspectives. 18:100479. 2020 Mar. Appl Mater Today [Internet]. Available from: https://linkinghub.elsevier.com/retrieve/pii/S2352940719305980

161. Wu Y, Kennedy P, Bonazza N, Yu Y, Dhawan A, Ozbolat I. 2021 Jan 29; Three-Dimensional Bioprinting of Articular Cartilage: A Systematic Review. 12(1):76–92. 2021 Jan 29. Cartilage [Internet]. Available from: http://journals.sagepub.com/doi/10.1177/1947603518809410

162. Antich C, de Vicente J, Jiménez G, Chocarro C, Carrillo E, Montañez E, et al. 2020 Apr 1; Bio-inspired hydrogel composed of hyaluronic acid and alginate as a potential bioink for 3D bioprinting of articular cartilage engineering constructs.

106:114–23. 2020 Apr 1. Acta Biomater [Internet]. Available from: https://doi.org/10.1016/j.actbio.2020.01.046

163. Abbadessa A, Mouser VHM, Blokzijl MM, Gawlitta D, Dhert WJA, Hennink WE, et al. 2016 Jun 13; A Synthetic Thermosensitive Hydrogel for Cartilage Bioprinting and Its Biofunctionalization with Polysaccharides. 17(6):2137–47. 2016 Jun 13. Biomacromolecules [Internet]. Available from: https://pubs.acs.org/doi/10.1021/acs.biomac.6b00366

164. Caliari SR, Burdick JA. 2016 May 28; A practical guide to hydrogels for cell culture. 13(5):405–14. 2016 May 28. Nat Methods [Internet]. Available from: https://www.nature.com/articles/nmeth.3839

165. Haug IJ, Draget KI. 2009. Gelatin. p. 142–63. 2009. In: Phillips GO, Williams PABTH of H (Second E, editors. Handbook of Hydrocolloids [Internet]. Elsevier; Available from: https://www.sciencedirect.com/science/article/pii/B9781845694142500060

166. Siegford JM, Powers W, Grimes-Casey HG. 2008; Environmental Aspects of Ethical Animal Production1. 87(2):380–6. 2008. Poult Sci [Internet]. Available from: https://www.sciencedirect.com/science/article/pii/S0032579119391321

167. Ahmad Z, Salman S, Khan SA, Amin A, Rahman ZU, Al-Ghamdi YO, et al. 2022 Mar 7; Versatility of Hydrogels: From Synthetic Strategies, Classification, and Properties to Biomedical Applications. 8(3):167. 2022 Mar 7. Gels [Internet]. Available from: https://www.mdpi.com/2310-2861/8/3/167

168. Khoeini R, Nosrati H, Akbarzadeh A, Eftekhari A, Kavetskyy T, Khalilov R, et al. 2021 Aug 1; Natural and Synthetic Bioinks for 3D Bioprinting. 1(8):2000097. 2021 Aug 1. Adv NanoBiomed Res [Internet]. Available from: https://doi.org/10.1002/anbr.202000097

169. Matson JB, Stupp SI. 2012; Self-assembling peptide scaffolds for regenerative medicine. 48(1):26–33. 2012. Chem Commun [Internet]. Available from: http://xlink.rsc.org/?DOI=C1CC15551B

170. Gao J, Tang C, Elsawy MA, Smith AM, Miller AF, Saiani A. 2017 Mar 13; Controlling Self-Assembling Peptide Hydrogel Properties through Network Topology. 18(3):826–34. 2017 Mar 13. Biomacromolecules [Internet]. Available from: https://pubs.acs.org/doi/10.1021/acs.biomac.6b01693

171. Elsawy MA, Smith AM, Hodson N, Squires A, Miller AF, Saiani A. 2016 May 17; Modification of β-Sheet Forming Peptide Hydrophobic Face: Effect on Self-Assembly and Gelation. 32(19):4917–23. 2016 May 17. Langmuir [Internet]. Available from: https://pubs.acs.org/doi/10.1021/acs.langmuir.5b03841

172. Mancha Sánchez E, Gómez-Blanco JC, López Nieto E, Casado JG, Macías-García A, Díaz Díez MA, et al. 2020 Aug 6; Hydrogels for Bioprinting: A Systematic Review of Hydrogels Synthesis, Bioprinting Parameters, and

Bioprinted Structures Behavior. 8(August). 2020 Aug 6. Front Bioeng Biotechnol [Internet]. Available from: https://www.frontiersin.org/article/10.3389/fbioe.2020.00776/full

173. Xin S, Chimene D, Garza JE, Gaharwar AK, Alge DL. 2019; Clickable PEG hydrogel microspheres as building blocks for 3D bioprinting. 7(3):1179–87. 2019. Biomater Sci [Internet]. Available from: http://xlink.rsc.org/?DOI=C8BM01286E

174. Irvine SA, Agrawal A, Lee BH, Chua HY, Low KY, Lau BC, et al. 2015 Feb 1; Printing cell-laden gelatin constructs by free-form fabrication and enzymatic protein crosslinking. 17(1):16. 2015 Feb 1. Biomed Microdevices [Internet]. Available from: http://link.springer.com/10.1007/s10544-014-9915-8

175. Schmieg B, Schimek A, Franzreb M. 2018 Sep 3; Development and performance of a 3D-printable poly(ethylene glycol) diacrylate hydrogel suitable for enzyme entrapment and long-term biocatalytic applications. 18(9):659–67. 2018 Sep 3. Eng Life Sci [Internet]. Available from: https://onlinelibrary.wiley.com/doi/10.1002/elsc.201800030

176. Yu F, Han X, Zhang K, Dai B, Shen S, Gao X, et al. 2018 Nov 17; Evaluation of a polyvinyl alcohol-alginate based hydrogel for precise 3D bioprinting. 106(11):2944–54. 2018 Nov 17. J Biomed Mater Res Part A [Internet]. Available from: https://onlinelibrary.wiley.com/doi/10.1002/jbm.a.36483

177. Aied A, Song W, Wang W, Baki A, Sigen A. 2018 Mar; 3D Bioprinting of stimuli-responsive polymers synthesised from DE-ATRP into soft tissue replicas. 9:37–43. 2018 Mar. Bioprinting [Internet]. Available from: https://linkinghub.elsevier.com/retrieve/pii/S2405886617300210

178. Lin HH, Hsieh FY, Tseng CS, Hsu S hui. 2016; Preparation and characterization of a biodegradable polyurethane hydrogel and the hybrid gel with soy protein for 3D cell-laden bioprinting. 4(41):6694–705. 2016. J Mater Chem B [Internet]. Available from: http://xlink.rsc.org/?DOI=C6TB01501H

179. Hsiao SH, Hsu S hui. 2018 Sep 5; Synthesis and Characterization of Dual Stimuli-Sensitive Biodegradable Polyurethane Soft Hydrogels for 3D Cell-Laden Bioprinting. 10(35):29273–87. 2018 Sep 5. ACS Appl Mater Interfaces [Internet]. Available from: https://pubs.acs.org/doi/10.1021/acsami.8b08362

180. Chen Y, Wang Y, Yang Q, Liao Y, Zhu B, Zhao G, et al. 2018; A novel thixotropic magnesium phosphate-based bioink with excellent printability for application in 3D printing. 6(27):4502–13. 2018. J Mater Chem B [Internet]. Available from: http://xlink.rsc.org/?DOI=C8TB01196F

181. Yan C, Pochan DJ. 2010; Rheological properties of peptide-based hydrogels for biomedical and other applications. 39(9):3528. 2010. Chem Soc Rev [Internet]. Available from: http://xlink.rsc.org/?DOI=b919449p

182. Yan C, Altunbas A, Yucel T, Nagarkar RP, Schneider JP, Pochan DJ. 2010; Injectable solid hydrogel: mechanism of shear-thinning and immediate recovery of injectable β-hairpin peptide hydrogels. 6(20):5143. 2010. Soft Matter [Internet]. Available from: http://xlink.rsc.org/?DOI=c0sm00642d

183. Biogel M. 2022 [cited 2022 Oct 28]. Peptigels(R) [Internet]. 2022. Available from: https://manchesterbiogel.com/products/peptigels/

184. Ligorio C, Zhou M, Wychowaniec JK, Zhu X, Bartlam C, Miller AF, et al. 2019; Graphene oxide containing self-assembling peptide hybrid hydrogels as a potential 3D injectable cell delivery platform for intervertebral disc repair applications. 92:92–103. 2019. Acta Biomater [Internet]. Available from: https://doi.org/10.1016/j.actbio.2019.05.004

185. Wan S, Borland S, Richardson SM, Merry CLR, Saiani A, Gough JE. 2016; Self-assembling peptide hydrogel for intervertebral disc tissue engineering. 46:29–40. 2016. Acta Biomater [Internet]. Available from: https://www.sciencedirect.com/science/article/pii/S1742706116305062

186. Mujeeb A, Miller AF, Saiani A, Gough JE. 2013; Self-assembled octapeptide scaffolds for in vitro chondrocyte culture. 9(1):4609–17. 2013. Acta Biomater [Internet]. Available from: http://dx.doi.org/10.1016/j.actbio.2012.08.044

187. Faroni A, Workman VL, Saiani A, Reid AJ. 2019 Sep 26; Self-Assembling Peptide Hydrogel Matrices Improve the Neurotrophic Potential of Human Adipose-Derived Stem Cells. 8(17). 2019 Sep 26. Adv Healthc Mater [Internet]. Available from: https://onlinelibrary.wiley.com/doi/10.1002/adhm.201900410

188. Treacy NJ, Clerkin S, Davis JL, Kennedy C, Miller AF, Saiani A, et al. 2023; Growth and differentiation of human induced pluripotent stem cell (hiPSC)-derived kidney organoids using fully synthetic peptide hydrogels. 21:142–56. 2023. Bioact Mater [Internet]. Available from: https://www.sciencedirect.com/science/article/pii/S2452199X22003334

189. King K, Njegic A, Facchi C, Prehar S, Oceandy D, Saiani A, et al. 2022; Development of a pro-angiogenic injectable self-assembling biomaterial for the delivery of induced pluripotent stem cell derived cardiomyocytes to the heart. 173:S181. 2022. J Mol Cell Cardiol [Internet]. Available from: https://www.sciencedirect.com/science/article/pii/S0022282822004977

190. Raphael B, Khalil T, Workman VL, Smith A, Brown CP, Streuli C, et al. 2017; 3D cell bioprinting of self-assembling peptide-based hydrogels. 190:103–6. 2017. Mater Lett [Internet]. Available from: https://www.sciencedirect.com/science/article/pii/S0167577X16320122

191. Paxton N, Smolan W, Böck T, Melchels F, Groll J, Jungst T. 2017 Nov 14; Proposal to assess printability of bioinks for extrusion-based bioprinting and evaluation of rheological properties governing bioprintability. 9(4):044107. 2017

Nov 14. Biofabrication [Internet]. Available from: https://iopscience.iop.org/article/10.1088/1758-5090/aa8dd8

192. Nelson AZ, Schweizer KS, Rauzan BM, Nuzzo RG, Vermant J, Ewoldt RH. 2019 Oct; Designing and transforming yield-stress fluids. 23(5):100758. 2019 Oct. Curr Opin Solid State Mater Sci [Internet]. Available from: https://www.sciencedirect.com/science/article/pii/S1359028619300762

193. Cooke ME, Rosenzweig DH. 2021 Mar 1; The rheology of direct and suspended extrusion bioprinting. 5(1). 2021 Mar 1. APL Bioeng [Internet]. Available from: https://pubs.aip.org/apb/article/5/1/011502/1021206/The-rheology-of-direct-and-suspended-extrusion

194. O'Connell C, Ren J, Pope L, Li Y, Mohandas A, Blanchard R, et al. 2020. Characterizing Bioinks for Extrusion Bioprinting: Printability and Rheology. p. 111–33. 2020. In: Crook J, editor. 3D bioprinting Methods in Moleculr Biology, vol 2140 [Internet]. Humana, New York, NY; Available from: http://link.springer.com/10.1007/978-1-0716-0520-2_7

195. Bercea M. 2023 Mar 19; Rheology as a Tool for Fine-Tuning the Properties of Printable Bioinspired Gels. 28(6):2766. 2023 Mar 19. Molecules [Internet]. Available from: https://www.mdpi.com/1420-3049/28/6/2766

196. Highley CB, Rodell CB, Burdick JA. 2015 Sep 1; Direct 3D Printing of Shear-Thinning Hydrogels into Self-Healing Hydrogels. 27(34):5075–9. 2015 Sep 1. Adv Mater [Internet]. Available from: https://doi.org/10.1002/adma.201501234

197. Townsend JM, Beck EC, Gehrke SH, Berkland CJ, Detamore MS. 2019; Flow behavior prior to crosslinking: The need for precursor rheology for placement of hydrogels in medical applications and for 3D bioprinting. 91:126–40. 2019. Prog Polym Sci [Internet]. Available from: https://www.sciencedirect.com/science/article/pii/S0079670017302253

198. Bertsch P, Diba M, Mooney DJ, Leeuwenburgh SCG. 2023 Jan 25; Self-Healing Injectable Hydrogels for Tissue Regeneration. 123(2):834–73. 2023 Jan 25. Chem Rev [Internet]. Available from: https://doi.org/10.1021/acs.chemrev.2c00179

199. He Y, Yang F, Zhao H, Gao Q, Xia B, Fu J. 2016 Jul 20; Research on the printability of hydrogels in 3D bioprinting. 6(1):29977. 2016 Jul 20. Sci Rep [Internet]. Available from: https://www.nature.com/articles/srep29977

200. Lemarié L, Anandan A, Petiot E, Marquette C, Courtial EJ. 2021 Mar; Rheology, simulation and data analysis toward bioprinting cell viability awareness. 21(December 2020):e00119. 2021 Mar. Bioprinting [Internet]. Available from: https://linkinghub.elsevier.com/retrieve/pii/S2405886620300464

201. Yallapu MM, Jaggi M, Chauhan SC. 2012 Jan; Curcumin nanoformulations: a future nanomedicine for cancer. 17(1–2):71–80. 2012 Jan. Drug Discov Today

[Internet]. Available from: http://www.ncbi.nlm.nih.gov/pubmed/21959306

202. Ribeiro A, Blokzijl MM, Levato R, Visser CW, Castilho M, Hennink WE, et al. 2017 Nov 30; Assessing bioink shape fidelity to aid material development in 3D bioprinting. 10(1):014102. 2017 Nov 30. Biofabrication [Internet]. Available from: https://iopscience.iop.org/article/10.1088/1758-5090/aa90e2

203. Sodupe-Ortega E, Sanz-Garcia A, Pernia-Espinoza A, Escobedo-Lucea C. 2018 Aug 10; Accurate Calibration in Multi-Material 3D Bioprinting for Tissue Engineering. 11(8):1402. 2018 Aug 10. Materials (Basel) [Internet]. Available from: http://www.mdpi.com/1996-1944/11/8/1402

204. BioPrinter B. 2020 [cited 2020 May 4]. Syringe Specs [Internet]. 2020. Available from: https://sites.google.com/site/bioprinterwiki/so-you-want-to-build-your-own-bioprinter/diy-bioprinter/diy-syringe-pump/syringe-specs

205. CELLINK. 2020 [cited 2020 Sep 1]. Needles and nozzles [Internet]. 2020. Available from: https://www.cellink.com/product/sterile-high-precision-blunt-needles-27g-50-pcs/

206. Docampo-Sanchez J, Haimes R. 2019. Towards fully regular quad mesh generation. p. 1–14. 2019 Jan 7. In: AIAA Scitech 2019 Forum [Internet]. Reston, Virginia: American Institute of Aeronautics and Astronautics; Available from: https://arc.aiaa.org/doi/10.2514/6.2019-1988

207. ANSYS. 2013 [cited 2020 May 21]. 7.3.15 Symmetry Boundary Conditions - ANSYS Fluent Theory Guide [Internet]. 2013. ANSYS FLuent Theory Guide. Available from: https://www.afs.enea.it/project/neptunius/docs/fluent/html/ug/node251.htm

208. ANSYS. 2013 [cited 2020 May 21]. ANSYS FLuent THeory Guide [Internet]. 2013. Available from: https://www.afs.enea.it/project/neptunius/docs/fluent/html/th/node421.htm

209. ANSYS. 2013 [cited 2020 May 21]. 25.3.1 Choosing the Pressure-Velocity Coupling Method [Internet]. 2013. Available from: https://www.afs.enea.it/project/neptunius/docs/fluent/html/ug/node785.htm#sec-uns-solve-pvel

210. ANSYS. 2013 [cited 2020 May 21]. 18.4.3 Pressure-Velocity Coupling [Internet]. 2013. Available from: https://www.afs.enea.it/project/neptunius/docs/fluent/html/th/node373.htm

211. Fakhruddin K, Hamzah MSA, Razak SIA. 2018 Oct 31; Effects of extrusion pressure and printing speed of 3D bioprinted construct on the fibroblast cells viability. 440:012042. 2018 Oct 31. IOP Conf Ser Mater Sci Eng [Internet]. Available from: https://iopscience.iop.org/article/10.1088/1757-899X/440/1/012042

212. Zoro BJH, Owen S, Drake RAL, Hoare M. 2008 Feb 1; The impact of process stress on suspended anchorage-dependent mammalian cells as an indicator of likely challenges for regenerative medicines. 99(2):468–74. 2008 Feb 1. Biotechnol Bioeng [Internet]. Available from: http://www.ncbi.nlm.nih.gov/pubmed/8982823

213. Chiesa I, Ligorio C, Bonatti AF, De Acutis A, Smith AM, Saiani A, et al. 2020 Oct 15; Modeling the Three-Dimensional Bioprinting Process of β-Sheet Self-Assembling Peptide Hydrogel Scaffolds. 2(October):1–16. 2020 Oct 15. Front Med Technol [Internet]. Available from: https://www.frontiersin.org/article/10.3389/fmedt.2020.571626/full

214. Echalier C, Levato R, Mateos-Timoneda MA, Castaño O, Déjean S, Garric X, et al. 2017; Modular bioink for 3D printing of biocompatible hydrogels: sol–gel polymerization of hybrid peptides and polymers. 7(20):12231–5. 2017. RSC Adv [Internet]. Available from: http://dx.doi.org/10.1039/C6RA28540F

215. Jian H, Wang M, Dong Q, Li J, Wang A, Li X, et al. 2019 Dec 18; Dipeptide Self-Assembled Hydrogels with Tunable Mechanical Properties and Degradability for 3D Bioprinting. 11(50):46419–26. 2019 Dec 18. ACS Appl Mater Interfaces [Internet]. Available from: https://doi.org/10.1021/acsami.9b13905

216. Farsheed AC, Thomas AJ, Pogostin BH, Hartgerink JD. 2023 Mar 1; 3D Printing of Self-Assembling Nanofibrous Multidomain Peptide Hydrogels. 35(11):2210378. 2023 Mar 1. Adv Mater [Internet]. Available from: https://doi.org/10.1002/adma.202210378

217. Lachowski D, Matellan C, Cortes E, Saiani A, Miller AF, del Río Hernández AE. 2021 Jun 30; Self-Assembling Polypeptide Hydrogels as a Platform to Recapitulate the Tumor Microenvironment. 13(13):3286. 2021 Jun 30. Cancers (Basel) [Internet]. Available from: https://www.mdpi.com/2072-6694/13/13/3286

218. Minocha SC. 1987. PH of the Medium and the Growth and Metabolism of Cells in Culture. p. 125–41. 1987. In: Bonga JM, Durzan DJ, editors. Cell and Tissue Culture in Forestry: General Principles and Biotechnology [Internet]. Dordrecht: Springer Netherlands; Available from: https://doi.org/10.1007/978-94-017-0994-1_8

219. Figueiredo L, Le Visage C, Weiss P, Yang J. 2020 May 30; Quantifying Oxygen Levels in 3D Bioprinted Cell-Laden Thick Constructs with Perfusable Microchannel Networks. 12(6):1260. 2020 May 30. Polymers (Basel) [Internet]. Available from: https://www.mdpi.com/2073-4360/12/6/1260

220. Panwar A, Tan L. 2016 May 25; Current Status of Bioinks for Micro-Extrusion-Based 3D Bioprinting. 21(6):685. 2016 May 25. Molecules [Internet]. Available from: http://www.mdpi.com/1420-3049/21/6/685

221. Nair K, Gandhi M, Khalil S, Yan KC, Marcolongo M, Barbee K, et al. 2009 Aug 14; Characterization of cell viability during bioprinting processes. 4(8):1168–77.

2009 Aug 14. Biotechnol J [Internet]. Available from: https://onlinelibrary.wiley.com/doi/10.1002/biot.200900004

222. Webb B, Doyle BJ. 2017; Parameter optimization for 3D bioprinting of hydrogels. 8:8–12. 2017. Bioprinting [Internet]. Available from: https://www.sciencedirect.com/science/article/pii/S2405886617300143

223. Li M, Tian X, Zhu N, Schreyer DJ, Chen X. 2010 Jun; Modeling Process-Induced Cell Damage in the Biodispensing Process. 16(3):533–42. 2010 Jun. Tissue Eng Part C Methods [Internet]. Available from: https://www.liebertpub.com/doi/10.1089/ten.tec.2009.0178

224. Buckwalter JA, Mow VC, Ratcliffe A. 1994 Jul; Restoration of Injured or Degenerated Articular Cartilage. 2(4):192–201. 1994 Jul. J Am Acad Orthop Surg [Internet]. Available from: http://journals.lww.com/00124635-199407000-00002

225. O'Hara BP, Urban JP, Maroudas A. 1990 Jul 1; Influence of cyclic loading on the nutrition of articular cartilage. 49(7):536–9. 1990 Jul 1. Ann Rheum Dis [Internet]. Available from: https://ard.bmj.com/lookup/doi/10.1136/ard.49.7.536

226. Chang AA, Reuther MS, Briggs KK, Schumacher BL, Williams GM, Corr M, et al. 2012 Jan; In vivo implantation of tissue-engineered human nasal septal neocartilage constructs: a pilot study. 146(1):46–52. 2012 Jan. Otolaryngol Head Neck Surg [Internet]. 2011/10/26. Available from: https://pubmed.ncbi.nlm.nih.gov/22031592

227. Jin CZ, Cho JH, Choi BH, Wang LM, Kim MS, Park SR, et al. 2011 Dec; The maturity of tissue-engineered cartilage in vitro affects the repairability for osteochondral defect. 17(23–24):3057–65. 2011 Dec. Tissue Eng Part A [Internet]. 2011/10/17. Available from: https://pubmed.ncbi.nlm.nih.gov/21736425

228. Neybecker P, Henrionnet C, Pape E, Mainard D, Galois L, Loeuille D, et al. 2018; In vitro and in vivo potentialities for cartilage repair from human advanced knee osteoarthritis synovial fluid-derived mesenchymal stem cells. 9(1):329. 2018. Stem Cell Res Ther [Internet]. Available from: https://doi.org/10.1186/s13287-018-1071-2

229. Sanjurjo-Rodríguez C, Castro-Viñuelas R, Hermida-Gómez T, Fuentes-Boquete IM, de Toro FJ, Blanco FJ, et al. 2017 Sep 28; Human Cartilage Engineering in an In Vitro Repair Model Using Collagen Scaffolds and Mesenchymal Stromal Cells. 14(12):1257–62. 2017 Sep 28. Int J Med Sci [Internet]. Available from: https://pubmed.ncbi.nlm.nih.gov/29104482

230. Christensen BB, Foldager CB, Hansen OM, Kristiansen AA, Le DQS, Nielsen AD, et al. 2012 Jun 5; A novel nano-structured porous polycaprolactone scaffold improves hyaline cartilage repair in a rabbit model compared to a collagen type I/III scaffold: in vitro and in vivo studies. 20(6):1192–204. 2012 Jun 5. Knee

Surgery, Sport Traumatol Arthrosc [Internet]. Available from: http://link.springer.com/10.1007/s00167-011-1692-9

231. Tsai MC, Hung KC, Hung SC, Hsu S hui. 2015 Jan 1; Evaluation of biodegradable elastic scaffolds made of anionic polyurethane for cartilage tissue engineering. 125:34–44. 2015 Jan 1. Colloids Surfaces B Biointerfaces [Internet]. Available from: https://linkinghub.elsevier.com/retrieve/pii/S0927776514006171

232. Jung Y, Kim SH, You HJ, Kim SH, Ha Kim Y, Min BG. 2008 Jan 2; Application of an elastic biodegradable poly(L-lactide-co-ε-caprolactone) scaffold for cartilage tissue regeneration. 19(8):1073–85. 2008 Jan 2. J Biomater Sci Polym Ed [Internet]. Available from: https://www.tandfonline.com/doi/full/10.1163/156856208784909336

233. Chen CH, Shyu VBH, Chen JP, Lee MY. 2014 Jan 15; Selective laser sintered poly-ε-caprolactone scaffold hybridized with collagen hydrogel for cartilage tissue engineering. 6(1):015004. 2014 Jan 15. Biofabrication [Internet]. Available from: https://iopscience.iop.org/article/10.1088/1758-5082/6/1/015004

234. Wasyłeczko M, Sikorska W, Chwojnowski A. 2020 Nov 17; Review of Synthetic and Hybrid Scaffolds in Cartilage Tissue Engineering. 10(11):348. 2020 Nov 17. Membranes (Basel) [Internet]. Available from: https://pubmed.ncbi.nlm.nih.gov/33212901

235. Daly AC, Critchley SE, Rencsok EM, Kelly DJ. 2016 Oct 7; A comparison of different bioinks for 3D bioprinting of fibrocartilage and hyaline cartilage. 8(4):045002. 2016 Oct 7. Biofabrication [Internet]. Available from: https://iopscience.iop.org/article/10.1088/1758-5090/8/4/045002

236. Duchi S, Onofrillo C, O'Connell CD, Blanchard R, Augustine C, Quigley AF, et al. 2017 Jul 19; Handheld Co-Axial Bioprinting: Application to in situ surgical cartilage repair. 7(1):5837. 2017 Jul 19. Sci Rep [Internet]. Available from: https://www.nature.com/articles/s41598-017-05699-x

237. Gao G, Schilling AF, Hubbell K, Yonezawa T, Truong D, Hong Y, et al. 2015 Nov 22; Improved properties of bone and cartilage tissue from 3D inkjet-bioprinted human mesenchymal stem cells by simultaneous deposition and photocrosslinking in PEG-GelMA. 37(11):2349–55. 2015 Nov 22. Biotechnol Lett [Internet]. Available from: http://link.springer.com/10.1007/s10529-015-1921-2

238. Levato R, Visser J, Planell JA, Engel E, Malda J, Mateos-Timoneda MA. 2014 Jul 22; Biofabrication of tissue constructs by 3D bioprinting of cell-laden microcarriers. 6(3):035020. 2014 Jul 22. Biofabrication [Internet]. Available from: https://iopscience.iop.org/article/10.1088/1758-5082/6/3/035020

239. Levato R, Webb WR, Otto IA, Mensinga A, Zhang Y, van Rijen M, et al. 2017

Oct; The bio in the ink: cartilage regeneration with bioprintable hydrogels and articular cartilage-derived progenitor cells. 61:41–53. 2017 Oct. Acta Biomater [Internet]. Available from: https://linkinghub.elsevier.com/retrieve/pii/S1742706117304956

240. Mouser VHM, Melchels FPW, Visser J, Dhert WJA, Gawlitta D, Malda J. 2016 Jul 19; Yield stress determines bioprintability of hydrogels based on gelatin-methacryloyl and gellan gum for cartilage bioprinting. 8(3):035003. 2016 Jul 19. Biofabrication [Internet]. Available from: https://iopscience.iop.org/article/10.1088/1758-5090/8/3/035003

241. O'Connell CD, Di Bella C, Thompson F, Augustine C, Beirne S, Cornock R, et al. 2016 Mar 23; Development of the Biopen: a handheld device for surgical printing of adipose stem cells at a chondral wound site. 8(1):015019. 2016 Mar 23. Biofabrication [Internet]. Available from: https://iopscience.iop.org/article/10.1088/1758-5090/8/1/015019

242. Zhu W, Cui H, Boualam B, Masood F, Flynn E, Rao RD, et al. 2018 May 4; 3D bioprinting mesenchymal stem cell-laden construct with core–shell nanospheres for cartilage tissue engineering. 29(18):185101. 2018 May 4. Nanotechnology [Internet]. Available from: https://iopscience.iop.org/article/10.1088/1361-6528/aaafa1

243. Gatenholm B, Lindahl C, Brittberg M, Simonsson S. 2020 Feb 18; Collagen 2A Type B Induction after 3D Bioprinting Chondrocytes In Situ into Osteoarthritic Chondral Tibial Lesion. :1–15. 2020 Feb 18. Cartilage [Internet]. Available from: http://journals.sagepub.com/doi/10.1177/1947603520903788

244. Santos-Beato P, A. Pitsillides A, Saiani A, Miller A, Torii R, M. Kalaskar D. 2023 Sep 6; Evaluation of a synthetic peptide-based bioink (PeptiInk Alpha 1) for in vitro 3D bioprinting of cartilage tissue models. 0(0):0899. 2023 Sep 6. Int J Bioprinting [Internet]. Available from: https://accscience.com/journal/IJB/0/0/10.36922/ijb.0899

245. Yeung P, Cheng KH, Yan CH, Chan BP. 2019; Collagen microsphere based 3D culture system for human osteoarthritis chondrocytes (hOACs). 9(1):1–14. 2019. Sci Rep [Internet]. Available from: http://dx.doi.org/10.1038/s41598-019-47946-3

246. Al-Maslamani NA, Oldershaw R, Tew S, Curran J, D'Hooghe P, Yamamoto K, et al. 2022 Dec 12; Chondrocyte De-Differentiation: Biophysical Cues to Nuclear Alterations. 11(24):4011. 2022 Dec 12. Cells [Internet]. Available from: https://www.mdpi.com/2073-4409/11/24/4011

247. Lemare F, Steimberg N, Le Griel C, Demignot S, Adolphe M. 1998 Aug; Dedifferentiated chondrocytes cultured in alginate beads: Restoration of the differentiated phenotype and of the metabolic responses to Interleukin-1β. 176(2):303–13. 1998 Aug. J Cell Physiol [Internet]. Available from: https://onlinelibrary.wiley.com/doi/10.1002/(SICI)1097-

4652(199808)176:2%3C303::AID-JCP8%3E3.0.CO;2-S

248. Schulze-Tanzil G. 2009 Jan 1 [cited 2019 Nov 28]; Activation and dedifferentiation of chondrocytes: Implications in cartilage injury and repair. 191(4):325–38. 2009 Jan 1. Ann Anat - Anat Anzeiger [Internet]. Available from: https://www.sciencedirect.com/science/article/abs/pii/S0940960209000703?via %3Dihub

249. Lefebvre V, Dvir-Ginzberg M. 2017 Jan 2; SOX9 and the many facets of its regulation in the chondrocyte lineage. 58(1):2–14. 2017 Jan 2. Connect Tissue Res [Internet]. Available from: https://www.tandfonline.com/doi/full/10.1080/03008207.2016.1183667

250. Haseeb A, Kc R, Angelozzi M, de Charleroy C, Rux D, Tower RJ, et al. 2021; SOX9 keeps growth plates and articular cartilage healthy by inhibiting chondrocyte dedifferentiation/osteoblastic redifferentiation. 118(8):e2019152118. 2021. Proc Natl Acad Sci [Internet]. Available from: https://www.pnas.org/doi/abs/10.1073/pnas.2019152118

251. Bosnakovski D, Mizuno M, Kim G, Ishiguro T, Okumura M, Iwanaga T, et al. 2004 May; Chondrogenic differentiation of bovine bone marrow mesenchymal stem cells in pellet cultural system. 32(5):502–9. 2004 May. Exp Hematol [Internet]. Available from: https://linkinghub.elsevier.com/retrieve/pii/S0301472X04000669

252. Schon BS, Schrobback K, van der Ven M, Stroebel S, Hooper GJ, Woodfield TBF. 2012 Mar 1; Validation of a high-throughput microtissue fabrication process for 3D assembly of tissue engineered cartilage constructs. 347(3):629–42. 2012 Mar 1. Cell Tissue Res [Internet]. Available from: http://link.springer.com/10.1007/s00441-011-1311-6

253. Gao Y, Liu S, Huang J, Guo W, Chen J, Zhang L, et al. 2014; The ECM-Cell Interaction of Cartilage Extracellular Matrix on Chondrocytes. 2014:1–8. 2014. Biomed Res Int [Internet]. Available from: http://www.hindawi.com/journals/bmri/2014/648459/

254. Castillo Diaz LA, Elsawy M, Saiani A, Gough JE, Miller AF. 2016 Jan 1; Osteogenic differentiation of human mesenchymal stem cells promotes mineralization within a biodegradable peptide hydrogel. 7:204173141664978. 2016 Jan 1. J Tissue Eng [Internet]. Available from: http://www.ncbi.nlm.nih.gov/pubmed/27493714

255. Andrews SHJ, Kunze M, Mulet-Sierra A, Williams L, Ansari K, Osswald M, et al. 2017 Jul 26; Strategies to Mitigate Variability in Engineering Human Nasal Cartilage. 7(1):6490. 2017 Jul 26. Sci Rep [Internet]. Available from: https://doi.org/10.1038/s41598-017-06666-2

256. Garcia J, Mennan C, McCarthy HS, Roberts S, Richardson JB, Wright KT. 2016; Chondrogenic Potency Analyses of Donor-Matched Chondrocytes and

Mesenchymal Stem Cells Derived from Bone Marrow, Infrapatellar Fat Pad, and Subcutaneous Fat. 2016:1–11. 2016. Sivak WN, editor. Stem Cells Int [Internet]. Available from: https://doi.org/10.1155/2016/6969726

257. Tallheden T, Van Der Lee J, Brantsing C, Månsson JE, Sjögren-Jansson E, Lindahl A. 2005 Aug 22; Human Serum for Culture of Articular Chondrocytes. 14(7):469–79. 2005 Aug 22. Cell Transplant [Internet]. Available from: http://journals.sagepub.com/doi/10.3727/000000005783982909

258. Feng X. 2009 May 1; Chemical and Biochemical Basis of Cell-Bone Matrix Interaction in Health and Disease. 3(2):189–96. 2009 May 1. Curr Chem Biol [Internet]. Available from: http://openurl.ingenta.com/content/xref?genre=article&issn=1872-3136&volume=3&issue=2&spage=189

259. Boskey AL. 2007 Dec 1; Mineralization of Bones and Teeth. 3(6):385–91. 2007 Dec 1. Elements [Internet]. Available from: https://doi.org/10.2113/GSELEMENTS.3.6.385

260. Young MF. 2003; Bone matrix proteins: their function, regulation, and relationship to osteoporosis. 14(3):35–42. 2003. Osteoporos Int [Internet]. Available from: https://doi.org/10.1007/s00198-002-1342-7

261. Boskey AL, Coleman R. 2010 Oct 5; Aging and Bone. 89(12):1333–48. 2010 Oct 5. J Dent Res [Internet]. Available from: https://doi.org/10.1177/0022034510377791

262. Gregson CL, Paggiosi MA, Crabtree N, Steel SA, McCloskey E, Duncan EL, et al. 2013 Feb 1; Analysis of Body Composition in Individuals With High Bone Mass Reveals a Marked Increase in Fat Mass in Women But Not Men. 98(2):818–28. 2013 Feb 1. J Clin Endocrinol Metab [Internet]. Available from: https://doi.org/10.1210/jc.2012-3342

263. Donnelly E, Meredith DS, Nguyen JT, Boskey AL. 2012 May 1; Bone tissue composition varies across anatomic sites in the proximal femur and the iliac crest. 30(5):700–6. 2012 May 1. J Orthop Res [Internet]. Available from: https://doi.org/10.1002/jor.21574

264. National Institute of Arthritis and Musculoskeletal and Skin Diseases. 2022 [cited 2023 Sep 18]. Osteoporosis [Internet]. 2022. Available from: https://www.niams.nih.gov/health-topics/osteoporosis

265. Wright NC, Looker AC, Saag KG, Curtis JR, Delzell ES, Randall S, et al. 2014 Nov; The Recent Prevalence of Osteoporosis and Low Bone Mass in the United States Based on Bone Mineral Density at the Femoral Neck or Lumbar Spine. 29(11):2520–6. 2014 Nov. J Bone Miner Res [Internet]. Available from: https://onlinelibrary.wiley.com/doi/10.1002/jbmr.2269

266. National Institute of Arthritis and Musculoskeletal and Skin Diseases. 2022 [cited

2023 Sep 18]. Osteoporosis treatment [Internet]. 2022. Available from: https://www.nhs.uk/conditions/osteoporosis/treatment/

267. NHS. 2021 [cited 2023 Sep 18]. Rickets and osteomalacia, treatment [Internet]. 2021. Available from: https://www.nhs.uk/conditions/rickets-and-osteomalacia/treatment/

268. NHS. 2021 [cited 2023 Sep 18]. Rickets and osteomalacia, symptoms [Internet]. 2021. Available from: https://www.nhs.uk/conditions/rickets-and-osteomalacia/symptoms/).

269. NHS. 2021 [cited 2023 Sep 18]. Bone cancer [Internet]. 2021. Available from: https://www.nhs.uk/conditions/bone-cancer/

270. National Cancer Intelligence Network. 2012; Bone Sarcoma Incidence and Survival. :2–3. 2012. Available from: http://www.wmciu.nhs.uk/documents/ReportR1205_BoneSarcomaIncidenceAndSurvival.pdf

271. Chindamo G, Sapino S, Peira E, Chirio D, Gonzalez MC, Gallarate M. 2020 May 1; Bone Diseases: Current Approach and Future Perspectives in Drug Delivery Systems for Bone Targeted Therapeutics. 10(5):875. 2020 May 1. Nanomaterials [Internet]. Available from: https://www.mdpi.com/2079-4991/10/5/875

272. Yazdanpanah Z, Johnston JD, Cooper DML, Chen X. 2022 Apr 11; 3D Bioprinted Scaffolds for Bone Tissue Engineering: State-Of-The-Art and Emerging Technologies. 10(April). 2022 Apr 11. Front Bioeng Biotechnol [Internet]. Available from: https://www.frontiersin.org/articles/10.3389/fbioe.2022.824156/full

273. Zhang R, Ma PX. 1999 Mar 15; Poly(α-hydroxyl acids)/hydroxyapatite porous composites for bone-tissue engineering. I. Preparation and morphology. 44(4):446–55. 1999 Mar 15. J Biomed Mater Res [Internet]. Available from: https://doi.org/10.1002/(SICI)1097-4636(19990315)44:4%3C446::AID-JBM11%3E3.0.CO

274. Niu X, Feng Q, Wang M, Guo X, Zheng Q. 2009 Mar; Porous nano-HA/collagen/PLLA scaffold containing chitosan microspheres for controlled delivery of synthetic peptide derived from BMP-2. 134(2):111–7. 2009 Mar. J Control Release [Internet]. Available from: https://linkinghub.elsevier.com/retrieve/pii/S0168365908007463

275. Aboudzadeh N, Imani M, Shokrgozar MA, Khavandi A, Javadpour J, Shafieyan Y, et al. 2010 Jul; Fabrication and characterization of poly(D,L-lactide-co-glycolide)/hydroxyapatite nanocomposite scaffolds for bone tissue regeneration. 94A(1):137–45. 2010 Jul. J Biomed Mater Res Part A [Internet]. Available from: https://onlinelibrary.wiley.com/doi/10.1002/jbm.a.32673

276. Zhu N, Li MG, Cooper D, Chen XB. 2011 Sep 1; Development of novel hybrid poly(l-lactide)/chitosan scaffolds using the rapid freeze prototyping technique. 3(3):034105. 2011 Sep 1. Biofabrication [Internet]. Available from: https://iopscience.iop.org/article/10.1088/1758-5082/3/3/034105

277. Cholas R, Kunjalukkal Padmanabhan S, Gervaso F, Udayan G, Monaco G, Sannino A, et al. 2016 Jun; Scaffolds for bone regeneration made of hydroxyapatite microspheres in a collagen matrix. 63:499–505. 2016 Jun. Mater Sci Eng C [Internet]. Available from: https://linkinghub.elsevier.com/retrieve/pii/S0928493116301941

278. Kim SH, Lim BK, Sun F, Koh K, Ryu SC, Kim HS, et al. 2009 Jan 20; Preparation of High Flexible Composite Film of Hydroxyapatite and Chitosan. 62(1):111–8. 2009 Jan 20. Polym Bull [Internet]. Available from: http://link.springer.com/10.1007/s00289-008-1008-5

279. Guarino V, Causa F, Netti PA, Ciapetti G, Pagani S, Martini D, et al. 2008 Aug; The role of hydroxyapatite as solid signal on performance of PCL porous scaffolds for bone tissue regeneration. 86B(2):548–57. 2008 Aug. J Biomed Mater Res Part B Appl Biomater [Internet]. Available from: https://onlinelibrary.wiley.com/doi/10.1002/jbm.b.31055

280. Verma N, Zafar S, Talha M. 2019 Jun 12; Influence of nano-hydroxyapatite on mechanical behavior of microwave processed polycaprolactone composite foams. 6(8):085336. 2019 Jun 12. Mater Res Express [Internet]. Available from: https://iopscience.iop.org/article/10.1088/2053-1591/ab260d

281. Bendtsen ST, Wei M. 2017 Dec 13; In vitro evaluation of 3D bioprinted tri-polymer network scaffolds for bone tissue regeneration. 105(12):3262–72. 2017 Dec 13. J Biomed Mater Res Part A [Internet]. Available from: https://onlinelibrary.wiley.com/doi/10.1002/jbm.a.36184

282. Demirtaş TT, Irmak G, Gümüşderelioğlu M. 2017 Jul 13; A bioprintable form of chitosan hydrogel for bone tissue engineering. 9(3):035003. 2017 Jul 13. Biofabrication [Internet]. Available from: http://www.ncbi.nlm.nih.gov/pubmed/28639943

283. Raja N, Yun H suk. 2016; A simultaneous 3D printing process for the fabrication of bioceramic and cell-laden hydrogel core/shell scaffolds with potential application in bone tissue regeneration. 4(27):4707–16. 2016. J Mater Chem B [Internet]. Available from: http://xlink.rsc.org/?DOI=C6TB00849F

284. Kim YB, Lee H, Yang GH, Choi CH, Lee D, Hwang H, et al. 2016 Jan; Mechanically reinforced cell-laden scaffolds formed using alginate-based bioink printed onto the surface of a PCL/alginate mesh structure for regeneration of hard tissue. 461:359–68. 2016 Jan. J Colloid Interface Sci [Internet]. Available from: https://linkinghub.elsevier.com/retrieve/pii/S0021979715302150

285. Park JY, Shim JH, Choi SA, Jang J, Kim M, Lee SH, et al. 2015; 3D printing

technology to control BMP-2 and VEGF delivery spatially and temporally to promote large-volume bone regeneration. 3(27):5415–25. 2015. J Mater Chem B [Internet]. Available from: http://xlink.rsc.org/?DOI=C5TB00637F

286. Ahn S, Lee H, Kim G. 2013 Oct; Functional cell-laden alginate scaffolds consisting of core/shell struts for tissue regeneration. 98(1):936–42. 2013 Oct. Carbohydr Polym [Internet]. Available from: https://linkinghub.elsevier.com/retrieve/pii/S0144861713006917

287. Chen YW, Shen YF, Ho CC, Yu J, Wu YHA, Wang K, et al. 2018 Oct; Osteogenic and angiogenic potentials of the cell-laden hydrogel/mussel-inspired calcium silicate complex hierarchical porous scaffold fabricated by 3D bioprinting. 91:679–87. 2018 Oct. Mater Sci Eng C [Internet]. Available from: https://linkinghub.elsevier.com/retrieve/pii/S0928493117345332

288. Neufurth M, Wang X, Schröder HC, Feng Q, Diehl-Seifert B, Ziebart T, et al. 2014; Engineering a morphogenetically active hydrogel for bioprinting of bioartificial tissue derived from human osteoblast-like SaOS-2 cells. 35(31):8810–9. 2014. Biomaterials [Internet]. Available from: https://www.sciencedirect.com/science/article/pii/S0142961214007844

289. Akkineni AR, Ahlfeld T, Lode A, Gelinsky M. 2016 Oct 7; A versatile method for combining different biopolymers in a core/shell fashion by 3D plotting to achieve mechanically robust constructs. 8(4):045001. 2016 Oct 7. Biofabrication [Internet]. Available from: https://iopscience.iop.org/article/10.1088/1758-5090/8/4/045001

290. Huang J, Fu H, Wang Z, Meng Q, Liu S, Wang H, et al. 2016; BMSCs-laden gelatin/sodium alginate/carboxymethyl chitosan hydrogel for 3D bioprinting. 6(110):108423–30. 2016. RSC Adv [Internet]. Available from: http://xlink.rsc.org/?DOI=C6RA24231F

291. Das S, Pati F, Choi YJ, Rijal G, Shim JH, Kim SW, et al. 2015 Jan; Bioprintable, cell-laden silk fibroin–gelatin hydrogel supporting multilineage differentiation of stem cells for fabrication of three-dimensional tissue constructs. 11:233–46. 2015 Jan. Acta Biomater [Internet]. Available from: https://linkinghub.elsevier.com/retrieve/pii/S1742706114004061

292. Luo Y, Lode A, Akkineni AR, Gelinsky M. 2015; Concentrated gelatin/alginate composites for fabrication of predesigned scaffolds with a favorable cell response by 3D plotting. 5(54):43480–8. 2015. RSC Adv [Internet]. Available from: http://xlink.rsc.org/?DOI=C5RA04308E

293. Luo Y, Li Y, Qin X, Wa Q. 2018 May; 3D printing of concentrated alginate/gelatin scaffolds with homogeneous nano apatite coating for bone tissue engineering. 146:12–9. 2018 May. Mater Des [Internet]. Available from: https://linkinghub.elsevier.com/retrieve/pii/S0264127518301680

294. Muzzarelli RAA, Greco F, Busilacchi A, Sollazzo V, Gigante A. 2012 Jul;

Chitosan, hyaluronan and chondroitin sulfate in tissue engineering for cartilage regeneration: A review. 89(3):723–39. 2012 Jul. Carbohydr Polym [Internet]. Available from: https://linkinghub.elsevier.com/retrieve/pii/S0144861712004092

295. Chimene D, Lennox KK, Kaunas RR, Gaharwar AK. 2016 Jun 16; Advanced Bioinks for 3D Printing: A Materials Science Perspective. 44(6):2090–102. 2016 Jun 16. Ann Biomed Eng [Internet]. Available from: http://link.springer.com/10.1007/s10439-016-1638-y

296. Narayanan LK, Huebner P, Fisher MB, Spang JT, Starly B, Shirwaiker RA. 2016 Oct 10; 3D-Bioprinting of Polylactic Acid (PLA) Nanofiber–Alginate Hydrogel Bioink Containing Human Adipose-Derived Stem Cells. 2(10):1732–42. 2016 Oct 10. ACS Biomater Sci Eng [Internet]. Available from: https://pubs.acs.org/doi/10.1021/acsbiomaterials.6b00196

297. You F, Wu X, Zhu N, Lei M, Eames BF, Chen X. 2016 Jul 11; 3D Printing of Porous Cell-Laden Hydrogel Constructs for Potential Applications in Cartilage Tissue Engineering. 2(7):1200–10. 2016 Jul 11. ACS Biomater Sci Eng [Internet]. Available from: https://pubs.acs.org/doi/10.1021/acsbiomaterials.6b00258

298. Luo Y, Luo G, Gelinsky M, Huang P, Ruan C. 2017 Feb; 3D bioprinting scaffold using alginate/polyvinyl alcohol bioinks. 189:295–8. 2017 Feb. Mater Lett [Internet]. Available from: https://linkinghub.elsevier.com/retrieve/pii/S0167577X16318882

299. Park J, Lee SJ, Chung S, Lee JH, Kim WD, Lee JY, et al. 2017 Feb; Cell-laden 3D bioprinting hydrogel matrix depending on different compositions for soft tissue engineering: Characterization and evaluation. 71:678–84. 2017 Feb. Mater Sci Eng C [Internet]. Available from: https://linkinghub.elsevier.com/retrieve/pii/S0928493116318070

300. Aldaadaa A, Owji N, Knowles J. 2018 Jan 1; Three-dimensional Printing in Maxillofacial Surgery: Hype versus Reality. 9:204173141877090. 2018 Jan 1. J Tissue Eng [Internet]. Available from: http://journals.sagepub.com/doi/10.1177/2041731418770909

301. Giuseppe M Di, Law N, Webb B, A. Macrae R, Liew LJ, Sercombe TB, et al. 2018 Mar; Mechanical behaviour of alginate-gelatin hydrogels for 3D bioprinting. 79:150–7. 2018 Mar. J Mech Behav Biomed Mater [Internet]. Available from: https://linkinghub.elsevier.com/retrieve/pii/S1751616117305623

302. Milazzo M, Contessi Negrini N, Scialla S, Marelli B, Farè S, Danti S, et al. 2019 Aug 4; Additive Manufacturing Approaches for Hydroxyapatite-Reinforced Composites. 29(35):1903055. 2019 Aug 4. Adv Funct Mater [Internet]. Available from: https://onlinelibrary.wiley.com/doi/10.1002/adfm.201903055

303. Roopavath UK, Malferrari S, Van Haver A, Verstreken F, Rath SN, Kalaskar DM. 2019 Jan; Optimization of extrusion based ceramic 3D printing process for

complex bony designs. 162:263–70. 2019 Jan. Mater Des [Internet]. Available from: https://linkinghub.elsevier.com/retrieve/pii/S0264127518308608

304. Witek L, Shi Y, Smay J. 2017 Jun 16; Controlling calcium and phosphate ion release of 3D printed bioactive ceramic scaffolds: An in vitro study. 6(2):157–64. 2017 Jun 16. J Adv Ceram [Internet]. Available from: http://link.springer.com/10.1007/s40145-017-0228-2

305. Warnke PH, Seitz H, Warnke F, Becker ST, Sivananthan S, Sherry E, et al. 2010 Apr 1; Ceramic scaffolds produced by computer-assisted 3D printing and sintering: Characterization and biocompatibility investigations. 93B(1):212–7. 2010 Apr 1. J Biomed Mater Res Part B Appl Biomater [Internet]. Available from: https://doi.org/10.1002/jbm.b.31577

306. Simon JL, Michna S, Lewis JA, Rekow ED, Thompson VP, Smay JE, et al. 2007 Dec 1; In vivo bone response to 3D periodic hydroxyapatite scaffolds assembled by direct ink writing. 83A(3):747–58. 2007 Dec 1. J Biomed Mater Res Part A [Internet]. Available from: https://doi.org/10.1002/jbm.a.31329

307. Miranda P, Pajares A, Saiz E, Tomsia AP, Guiberteau F. 2008 Apr 9; Mechanical properties of calcium phosphate scaffolds fabricated by robocasting. 85A(1):218–27. 2008 Apr 9. J Biomed Mater Res Part A [Internet]. Available from: https://onlinelibrary.wiley.com/doi/10.1002/jbm.a.31587

308. Cesarano J, Dellinger JG, Saavedra MP, Gill DD, Jamison RD, Grosser BA, et al. 2005 May 2; Customization of Load-Bearing Hydroxyapatite Lattice Scaffolds. 2(3):212–20. 2005 May 2. Int J Appl Ceram Technol [Internet]. Available from: https://ceramics.onlinelibrary.wiley.com/doi/10.1111/j.1744-7402.2005.02026.x

309. Liang H, Wang Y, Chen S, Liu Y, Liu Z, Bai J. 2022 Jan 1; Nano-Hydroxyapatite Bone Scaffolds with Different Porous Structures Processed by Digital Light Processing 3D Printing. 8(1):502. 2022 Jan 1. Int J Bioprinting [Internet]. Available from: https://accscience.com/journal/IJB/8/1/10.18063/ijb.v8i1.502

310. Yao Y, Qin W, Xing B, Sha N, Jiao T, Zhao Z. 2021 Feb 18; High performance hydroxyapatite ceramics and a triply periodic minimum surface structure fabricated by digital light processing 3D printing. 10(1):39–48. 2021 Feb 18. J Adv Ceram [Internet]. Available from: http://link.springer.com/10.1007/s40145-020-0415-4

311. Le Guéhennec L, Van hede D, Plougonven E, Nolens G, Verlée B, De Pauw MC, et al. 2020 Mar 21; In vitro and in vivo biocompatibility of calcium-phosphate scaffolds three-dimensional printed by stereolithography for bone regeneration. 108(3):412–25. 2020 Mar 21. J Biomed Mater Res Part A [Internet]. Available from: https://onlinelibrary.wiley.com/doi/10.1002/jbm.a.36823

312. Malferrari S. 2021. Direct Ink Writing 3D printing technology for bone tissue

engineering. 2021.

313. Pautke C, Schieker M, Tischer T, Kolk A, Neth P, Mutschler W, et al. 2004; Characterization of osteosarcoma cell lines MG-63, Saos-2 and U-2 OS in comparison to human osteoblasts. 24(6):3743–8. 2004. Anticancer Res [Internet]. Available from: http://www.ncbi.nlm.nih.gov/pubmed/15736406

314. Neufurth M, Wang X, Schröder HC, Feng Q, Diehl-Seifert B, Ziebart T, et al. 2014 Oct; Engineering a morphogenetically active hydrogel for bioprinting of bioartificial tissue derived from human osteoblast-like SaOS-2 cells. 35(31):8810–9. 2014 Oct. Biomaterials [Internet]. Available from: https://linkinghub.elsevier.com/retrieve/pii/S0142961214007844

315. Tattersall L, Davison Z, Gartland A. 2020. Osteosarcoma. p. 362–78. 2020. In: Encyclopedia of Bone Biology [Internet]. Elsevier; Available from: https://linkinghub.elsevier.com/retrieve/pii/B9780128012383622596

316. Ayobian-Markazi N, Fourootan T, Kharazifar M. 2012 Jan; Comparison of cell viability and morphology of a human osteoblast-like cell line (SaOS-2) seeded on various bone substitute materials: An in vitro study. 9(1):86. 2012 Jan. Dent Res J (Isfahan) [Internet]. Available from: http://www.drj.ir/text.asp?2012/9/1/86/92959

317. Roys R. 2022. Design and Characterisation of 3D Printed Customised Ceramic Bone Implants Master of Biomedical Science. 2022.

318. Castilho M, Moseke C, Ewald A, Gbureck U, Groll J, Pires I, et al. 2014 Jan 15; Direct 3D powder printing of biphasic calcium phosphate scaffolds for substitution of complex bone defects. 6(1):015006. 2014 Jan 15. Biofabrication [Internet]. Available from: https://iopscience.iop.org/article/10.1088/1758-5082/6/1/015006

319. Misch CE, Qu Z, Bidez MW. 1999 Jun; Mechanical properties of trabecular bone in the human mandible: Implications for dental implant treatment planning and surgical placement. 57(6):700–6. 1999 Jun. J Oral Maxillofac Surg [Internet]. Available from: https://linkinghub.elsevier.com/retrieve/pii/S0278239199904378

320. Rico-Llanos GA, Borrego-González S, Moncayo-Donoso M, Becerra J, Visser R. 2021 Feb 17; Collagen Type I Biomaterials as Scaffolds for Bone Tissue Engineering. 13(4):599. 2021 Feb 17. Polymers (Basel) [Internet]. Available from: https://www.mdpi.com/2073-4360/13/4/599

321. Leukers B, Gülkan H, Irsen SH, Milz S, Tille C, Schieker M, et al. 2005 Dec; Hydroxyapatite scaffolds for bone tissue engineering made by 3D printing. 16(12):1121–4. 2005 Dec. J Mater Sci Mater Med [Internet]. Available from: http://link.springer.com/10.1007/s10856-005-4716-5

322. Will J, Melcher R, Treul C, Travitzky N, Kneser U, Polykandriotis E, et al. 2008 Aug 29; Porous ceramic bone scaffolds for vascularized bone tissue

regeneration. 19(8):2781–90. 2008 Aug 29. J Mater Sci Mater Med [Internet]. Available from: http://link.springer.com/10.1007/s10856-007-3346-5

323. Zhao N, Wang Y, Qin L, Guo Z, Li D. 2017; Effect of composition and macropore percentage on mechanical and in vitro cell proliferation and differentiation properties of 3D printed HA/β-TCP scaffolds. 7(68):43186–96. 2017. RSC Adv [Internet]. Available from: http://xlink.rsc.org/?DOI=C7RA07204J

324. Smith HL, Gray JC, Beers SA, Kanczler JM. 2023 Feb 11; Tri-Lineage Differentiation Potential of Osteosarcoma Cell Lines and Human Bone Marrow Stromal Cells from Different Anatomical Locations. 24(4):3667. 2023 Feb 11. Int J Mol Sci [Internet]. Available from: https://www.mdpi.com/1422-0067/24/4/3667

325. Horobin RW. 2010. Chapter 18: How Do Dyes Impart Color to Different Components of the Tissues? p. 159–66. 2010. In: Educational Guide: Special Stains and H & E.

326. Shim JH, Jang KM, Hahn SK, Park JY, Jung H, Oh K, et al. 2016 Feb 4; Three-dimensional bioprinting of multilayered constructs containing human mesenchymal stromal cells for osteochondral tissue regeneration in the rabbit knee joint. 8(1):014102. 2016 Feb 4. Biofabrication [Internet]. Available from: http://www.ncbi.nlm.nih.gov/pubmed/26844597

327. Mancini IAD, Schmidt S, Brommer H, Pouran B, Schäfer S, Tessmar J, et al. 2020 Jul 1; A composite hydrogel-3D printed thermoplast osteochondral anchor as example for a zonal approach to cartilage repair: in vivo performance in a long-term equine model. 12(3):035028. 2020 Jul 1. Biofabrication [Internet]. Available from: https://iopscience.iop.org/article/10.1088/1758-5090/ab94ce

328. Duan M, Xia S, Liu Y, Pu X, Chen Y, Zhou Y, et al. 2023 Jun; Stiffened fibre-like microenvironment based on patterned equidistant micropillars directs chondrocyte hypertrophy. 20:100682. 2023 Jun. Mater Today Bio [Internet]. Available from: https://linkinghub.elsevier.com/retrieve/pii/S2590006423001424

329. Wu L, Petrigliano FA, Ba K, Lee S, Bogdanov J, McAllister DR, et al. 2015 Feb; Lysophosphatidic acid mediates fibrosis in injured joints by regulating collagen type I biosynthesis. 23(2):308–18. 2015 Feb. Osteoarthr Cartil [Internet]. Available from: https://linkinghub.elsevier.com/retrieve/pii/S106345841401334X

330. Zhang M, Grote C, Wang J. 2019. Epigenetic mechanisms underlying the pathogenesis of osteoarthritis and their clinical relevance. p. 245–68. 2019. In: Sharma SBTPE, editor. Prognostic Epigenetics [Internet]. Elsevier; Available from: https://www.sciencedirect.com/science/article/pii/B9780128142592000108

331. Rashid H, Chen H, Javed A. 2021 Dec; Runx2 is required for hypertrophic chondrocyte mediated degradation of cartilage matrix during endochondral ossification. 12:100088. 2021 Dec. Matrix Biol Plus [Internet]. Available from:

https://linkinghub.elsevier.com/retrieve/pii/S2590028521000326

332. Diloksumpan P, Abinzano F, de Ruijter M, Mensinga A, Plomp S, Khan I, et al. 2021 Mar 23; The Complexity of Joint Regeneration: How an Advanced Implant could Fail by Its In Vivo Proven Bone Component. 2(1). 2021 Mar 23. J Trial Error [Internet]. Available from: https://archive.jtrialerror.com/pub/jointregeneration

333. Kilian D, Cometta S, Bernhardt A, Taymour R, Golde J, Ahlfeld T, et al. 2022 Jan 1; Core–shell bioprinting as a strategy to apply differentiation factors in a spatially defined manner inside osteochondral tissue substitutes. 14(1):014108. 2022 Jan 1. Biofabrication [Internet]. Available from: https://iopscience.iop.org/article/10.1088/1758-5090/ac457b

334. Deng C, Yang J, He H, Ma Z, Wang W, Zhang Y, et al. 2021; 3D bio-printed biphasic scaffolds with dual modification of silk fibroin for the integrated repair of osteochondral defects. 9(14):4891–903. 2021. Biomater Sci [Internet]. Available from: http://xlink.rsc.org/?DOI=D1BM00535A

335. Liu J, Li L, Suo H, Yan M, Yin J, Fu J. 2019; 3D printing of biomimetic multi-layered GelMA/nHA scaffold for osteochondral defect repair. 171:107708. 2019. Mater Des [Internet]. Available from: https://doi.org/10.1016/j.matdes.2019.107708

336. Kilian D, Sembdner P, Bretschneider H, Ahlfeld T, Mika L, Lützner J, et al. 2021 Dec 21; 3D printing of patient-specific implants for osteochondral defects: workflow for an MRI-guided zonal design. 4(4):818–32. 2021 Dec 21. Bio-Design Manuf [Internet]. Available from: https://link.springer.com/10.1007/s42242-021-00153-4

337. Zhang H, Huang H, Hao G, Zhang Y, Ding H, Fan Z, et al. 2021 Jan 24; 3D Printing Hydrogel Scaffolds with Nanohydroxyapatite Gradient to Effectively Repair Osteochondral Defects in Rats. 31(1):1–13. 2021 Jan 24. Adv Funct Mater [Internet]. Available from: https://onlinelibrary.wiley.com/doi/10.1002/adfm.202006697

338. Hu Q, Jiang B, Zhang H. 2019 Jan 1; Method for Novel 3d Bioprinting of Gradient Scaffold For Osteochondral Regeneration Using a Coaxial Multi-nozzle and Software. 9(1):24–31. 2019 Jan 1. J Biomater Tissue Eng [Internet]. Available from: https://www.ingentaconnect.com/content/10.1166/jbt.2019.1954

339. Yu X, Zhao T, Qi Y, Luo J, Fang J, Yang X, et al. 2018 Dec 17; In vitro Chondrocyte Responses in Mg-doped Wollastonite/Hydrogel Composite Scaffolds for Osteochondral Interface Regeneration. 8(1):17911. 2018 Dec 17. Sci Rep [Internet]. Available from: https://doi.org/10.1038/s41598-018-36200-x

340. Khanarian NT, Jiang J, Wan LQ, Mow VC, Lu HH. 2012 Mar; A Hydrogel-Mineral Composite Scaffold for Osteochondral Interface Tissue Engineering. 18(5–6):533–45. 2012 Mar. Tissue Eng Part A [Internet]. Available from:

https://www.liebertpub.com/doi/10.1089/ten.tea.2011.0279

341. Lutter AH, Liedtke V, Scholka J, Muschter A, Becker R, Anderer U. 2019 Jan 16; Co-culture of human chondrogenic microtissues with osteoblast-like Saos-2 cells or HFF-1 fibroblasts influence the differentiation potential of spheroids. 4(1–2):31–42. 2019 Jan 16. J Cell Biotechnol [Internet]. Available from: https://www.medra.org/servlet/aliasResolver?alias=iospress&doi=10.3233/JCB -189005

342. Becerikli M, Jaurich H, Schira J, Schulte M, Döbele C, Wallner C, et al. 2017 Nov; Age-dependent alterations in osteoblast and osteoclast activity in human cancellous bone. 21(11):2773–81. 2017 Nov. J Cell Mol Med [Internet]. Available from: https://onlinelibrary.wiley.com/doi/10.1111/jcmm.13192

343. Nakaoka R, Hsiong SX, Mooney DJ. 2006 Sep; Regulation of Chondrocyte Differentiation Level via Co-culture with Osteoblasts. 12(9):2425–33. 2006 Sep. Tissue Eng [Internet]. Available from: https://www.liebertpub.com/doi/10.1089/ten.2006.12.2425

344. Xue R, Chung B, Tamaddon M, Carr J, Liu C, Cartmell SH. 2019 Nov; Osteochondral tissue coculture: An in vitro and in silico approach. 116(11):3112–23. 2019 Nov. Biotechnol Bioeng [Internet]. Available from: https://onlinelibrary.wiley.com/doi/10.1002/bit.27127

345. Yu J, Lee S, Choi S, Kim KK, Ryu B, Kim CY, et al. 2020 Sep 25; Fabrication of a Polycaprolactone/Alginate Bipartite Hybrid Scaffold for Osteochondral Tissue Using a Three-Dimensional Bioprinting System. 12(10):2203. 2020 Sep 25. Polymers (Basel) [Internet]. Available from: https://www.mdpi.com/2073-4360/12/10/2203

346. Moses JC, Saha T, Mandal BB. 2020 Mar; Chondroprotective and osteogenic effects of silk-based bioinks in developing 3D bioprinted osteochondral interface. 17:e00067. 2020 Mar. Bioprinting [Internet]. Available from: https://linkinghub.elsevier.com/retrieve/pii/S2405886619300363

347. Ayan B, Wu Y, Karuppagounder V, Kamal F, Ozbolat IT. 2020 Dec 4; Aspiration-assisted bioprinting of the osteochondral interface. 10(1):13148. 2020 Dec 4. Sci Rep [Internet]. Available from: https://www.nature.com/articles/s41598-020-69960-6

348. Sun D, Gao W, Hu H, Zhou S. 2022 Jul; Why 90% of clinical drug development fails and how to improve it? 12(7):3049–62. 2022 Jul. Acta Pharm Sin B [Internet]. Available from: https://www.sciencedirect.com/science/article/pii/S2211383522000521

349. Loewa A, Feng JJ, Hedtrich S. 2023 May 11; Human disease models in drug development. 1(8):545–59. 2023 May 11. Nat Rev Bioeng [Internet]. Available from: https://www.nature.com/articles/s44222-023-00063-3

350. Löfvall H, Katri A, Dąbrowska A, Karsdal MA, Luo Y, He Y, et al. 2019 Feb 28; GPDPLQ1237—A Type II Collagen Neo-Epitope Biomarker of Osteoclast- and Inflammation-Derived Cartilage Degradation in vitro. 9(1):3050. 2019 Feb 28. Sci Rep [Internet]. Available from: https://www.nature.com/articles/s41598-019-39803-0

351. Löfvall H, Newbould H, Karsdal MA, Dziegiel MH, Richter J, Henriksen K, et al. 2018 Dec 10; Osteoclasts degrade bone and cartilage knee joint compartments through different resorption processes. 20(1):67. 2018 Dec 10. Arthritis Res Ther [Internet]. Available from: https://arthritis-research.biomedcentral.com/articles/10.1186/s13075-018-1564-5

352. Charni-Ben Tabassi N, Desmarais S, Bay-Jensen AC, Delaissé JM, Percival MD, Garnero P. 2008 Oct; The type II collagen fragments Helix-II and CTX-II reveal different enzymatic pathways of human cartilage collagen degradation. 16(10):1183–91. 2008 Oct. Osteoarthr Cartil [Internet]. Available from: https://linkinghub.elsevier.com/retrieve/pii/S1063458408000496

353. DiMicco MA, Patwari P, Siparsky PN, Kumar S, Pratta MA, Lark MW, et al. 2004 Mar; Mechanisms and kinetics of glycosaminoglycan release following in vitro cartilage injury. 50(3):840–8. 2004 Mar. Arthritis Rheum [Internet]. Available from: https://onlinelibrary.wiley.com/doi/10.1002/art.20101

Appendices

Appendix 1: ENGD Requirement Chapter

A1.1 Industrial and commercial learning outcomes – Impact of developing 3D bioprinted cartilage tissue models

This doctoral in engineering thesis focused on developing an osteochondral tissue model *in vitro* for subsequent use as an osteoarthritis (OA) disease model. The osteochondral tissue models were developed using a combination of commercial synthetic self-assembling peptides, or Peptigels®, for the cartilage section and an in-house optimised hydroxyapatite (HA) ink for the bone compartment. The development of these tissue models had an impact industrially and commercially. The industrial impact relies on the new field of application and novel investigations regarding the Peptigels®. A novel screening of multiple Peptigels® was performed to assess the potential use of these hydrogels as bioinks, further expanding previous investigations [190]. Following this, Alpha 1 and Alpha 4 were selected for investigation as bioinks for developing human cartilage tissue models *in vitro*. These novel investigations regarding the use of the Peptigels®, specifically Alpha 1, had multiple academic, economic, and societal impacts, further discussed below.

A1.1.1   Academic impacts

Multiple Peptigels® were screened for their potential application as bioinks (Chapter 2). This novel investigation further expanded the academic knowledge regarding the physico-chemical properties of the different Peptigels®, Alpha 1, Alpha 2, and Alpha 4, especially their printability. Rheological assessments demonstrated a decrease in viscosity when mixed with cell culture medium of Alpha 1 and Alpha 4. The viscosity of Alpha 2 was found not to change significantly, regardless of the cell culture medium added. Additionally, pH and diffusion rate analyses found that Alpha 1 and Alpha 4 maintained physiological pH in culture and had a fast diffusion rate. Alpha 2, on the other hand, demonstrated an acidic pH nature and slow diffusion rates, discarding it as a potential bioink. Printability investigations of Alpha 1 and Alpha 4 showed that

when using a 25G nozzle, both bioinks could be 3D bioprinted with optimised bioprinting settings using 5 mm/s printing speed and a printing window of 8-10 kPa.

Furthermore, Alpha 1 and Alpha 4 were also investigated as potential bioinks for developing human cartilage tissue models *in vitro* (Chapter 3). The chondrogenic behaviour of Alpha 1 has already been reported with different non-human cell types, such as bovine nucleus pulposus cells [184,185]. However, no investigations on using Alpha 1 or Alpha 4 with human primary chondrocytes (HCHs) had been previously reported. These investigations contributed academically to further understanding the potential applications of Alpha 1 and Alpha 4 to develop these human cartilage tissue models. A novel strategy for 3D bioprinting human cartilage tissue models without animal-derived materials was developed. This further expanded the academic knowledge regarding materials and bioinks used to develop these tissue models more sustainably and ethically than current animal-derived models, which use animal industry by-products such as gelatine [2].

Moreover, these models were combined with bone constructs to develop osteochondral tissue models, expanding the field of osteochondral tissue engineering. This thesis has elucidated the complex interaction of cells and materials to fabricate a complex composite tissue, such as the osteochondral tissue. The various models developed and presented in this thesis using different cells and materials (Chapter 5) have added understanding and further progressed the osteochondral tissue engineering field. Alpha 1 demonstrated the ability to maintain and promote chondrogenesis in the embedded HCHs better than the current gold standards, regardless of the addition of the HA scaffold with or without bone-like cells. Furthermore, adding the bone section to the osteochondral constructs showed a reduction of fibrotic cartilage markers, such as collagen type-I, expressed in the Alpha 1 section. The combination of both sections promoted a better development of healthy cartilage. However, issues regarding the structural stability of Alpha 1 after 14 days of culture have conditioned the possible culture time of these constructs. Therefore, further work regarding the long-term effect between these two osteochondral sections has not been able to be investigated in this thesis.

Finally, although these models were not directly tested as disease models, their potential use to develop disease models and drug testing platforms would greatly impact academically in the future. These platforms represent a simple model that could accelerate disease modelling and drug discovery research.

A1.1.2   Economic impacts

The Peptigels® used in this thesis are commercial products from Manchester Biogel Ltd (MBG). MBG developed their peptide sequences, manufactured the hydrogels, and performed quality checks. The investigations reported in this thesis did not focus on improving any of these manufacturing steps but expanded the potential applications of these Peptigels®.

Economically, the main impact of these investigations focused on improving the sales of these materials by testing and characterising their potential use further. Alpha 4 was assessed regarding its potential use to develop cartilage models. The results showed that this specific Peptigel® was not optimal for developing these models. Alpha 1, on the other hand, was further investigated as a potential bioink and material for developing human cartilage models. These investigations commercially have an impact because MBG can confidently advise customers to choose Alpha 1 as the best candidate to develop cartilage tissue models over Alpha 4. This new information communicated through peer-reviewed research articles [244], presents solid knowledge that new customers who wish to develop cartilage models using non-animal-derived materials for future applications can read.

Additionally, slight batch-to-batch variations were found throughout the investigations performed. This information was fed back to MBG, and better manufacturing and quality control procedures were implemented. The quality of the manufactured Peptigels® was subsequently improved. Furthermore, already existing characterisation protocols were optimised further. The newly developed strategies were communicated to MBG, which used them in-house and shared with other clients. These included histological processing, immunofluorescence labelling, and bioprinting process protocols.

Overall, these new investigations gave MBG new knowledge to be used as case studies to further commercialise its products and guide and advise customers more efficiently.

A1.1.3   Societal impacts

These osteochondral tissues were investigated to develop an OA disease model. OA is a disease that affects one in ten adults in the UK [130] and 54.4 million adults in the US [131] and whose prevalence increases with age (further information in Chapter 1). The current knowledge about the disease progression and the potential therapies is limited. No drugs reverse the symptoms; the prescribed treatment focuses on symptomatic relief. Developing these osteochondral tissue models opens a door for personalised medicine, where osteochondral tissue models of patients' cells could be developed. Personalised disease models could be made, and different drug types could be tested to assess which one could be the best one for that specific patient.

Furthermore, these models could be made from healthy cells, and the disease could be induced in different ways, mimicking *in vitro* diverse OA stages. These OA models could be used to develop and test new drugs to help reverse or halt specific symptoms. Overall, the main societal impact of this project is based on the potential application that osteochondral tissue models would have on further understanding osteoarthritis and developing treatments against it. Drug trials, which tend to fail in the last clinical stages [348], could be shortened and made more efficient by having a validated human disease model *in vitro* [349]. However, quantifying the financial and societal effects that these disease models could have is extremely complex.

A1.2 Practical application of 3D bioprinting of osteochondral tissues

The development of these osteochondral biphasic constructs had a practical application for MBG in such a way that this new use of the Peptigels® expanded the current knowledge. Alpha 1, as a bioink to develop a human cartilage tissue model, has a practical application for MBG as further information regarding Alpha 1 properties such as degradation, chondrogenic potential, and printability has been characterised.

Full printability characterisation and optimisation were performed for Alpha 4 and Alpha 1, giving useful commercial information such as rheological properties and optimal printing parameters to achieve the best printing resolution. Additionally, the chondrogenic characterisation of Alpha 1 was achieved by optimising multiple processing protocols regarding cryosectioning, immunofluorescently labelling, mRNA extraction, and comparative qPCR. Although some of these processing protocols were previously supplied by MBG, further optimisation and troubleshooting were performed throughout the EngD course to achieve consistent results. These refined protocols were fed back to MBG and adopted for future use by their growing customer base.

Appendix 2: Additional data from Chapter 2

A2.1 Convergence study of CFD model

The CFD model developed for simulating the fluid flow in the extrusion process of the Peptigels® was tested for mesh convergence. The variable chosen to assess mesh convergence was maximum strain. Figure A2.1 shows the maximum strain versus the number of mesh nodes. The design with fewer nodes was chosen when the mesh presented less than 5% variation in the maximum strain between the last two sets of nodes tested. The final number of nodes for the full-dimension designs was 11371 for the nozzle.
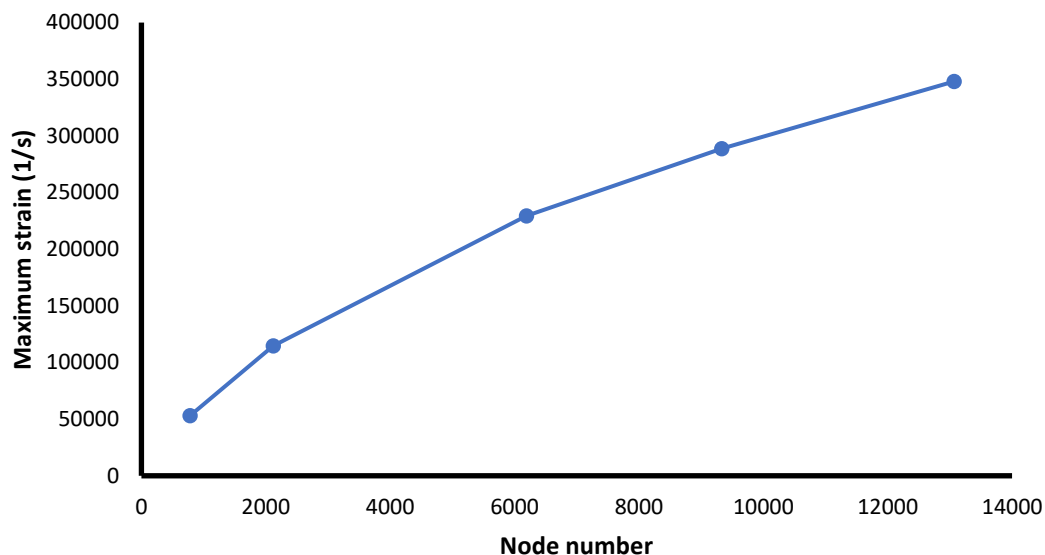
Figure A2.1. Mesh convergence test in the nozzle section of the CFD model. Maximum strain vs. number of nodes is presented.

A2.2 Amplitude sweep characterisation data of Peptigels®

Amplitude sweep rheological measurements were performed in the three tested Peptigels® in their pure form and mixed with cell culture medium in the two ratios of interest (1:10 and 1:5). These amplitude sweeps enabled the visualisation of the storage modulus (G') and loss modulus (G''). These two moduli were measured in a strain interval between 0.5 and 100 %. All Figures, Figure A2.2, A2.3, A2.4, show the expected cross over between the G' and G'' moduli within the strain range of 10-100%. This crossover was expected, showing that at higher strain levels the Peptigels® behaved like a fluid and behaved like a solid in lower strain levels, confirming once again the shear-thinning behaviour of the Peptigels®. These data sets were excluded from the main body of the thesis due to differences in material batches and erratic data obtained in high strain levels.

Firstly, the batches tested here were provided by MBG at a pH of 4, which was then not used in the 3D bioprinting and cell culture processes shown in Chapter 3. Although previous research has shown minimal rheological differences in Peptigels® at different pH levels, this data is shown in the Appendix to ensure coherence and continuity in material use across the thesis. Further measurements with Peptigels® at a pH of 7 should be tested to compare potential rheological differences across batches.

Secondly, erratic data was obtained in strain levels higher than 100% for some materials such as Alpha 4 (Figure A2.4), Alpha 2 (1:5) (Figure A2.3C), and Alpha 1 (Figure A2.2A). This data behaviour is potentially due errors in the rheometer software or insufficient amount of material added for testing. Therefore, these Figures are indicative and further measurements should be performed to confirm the observed data.
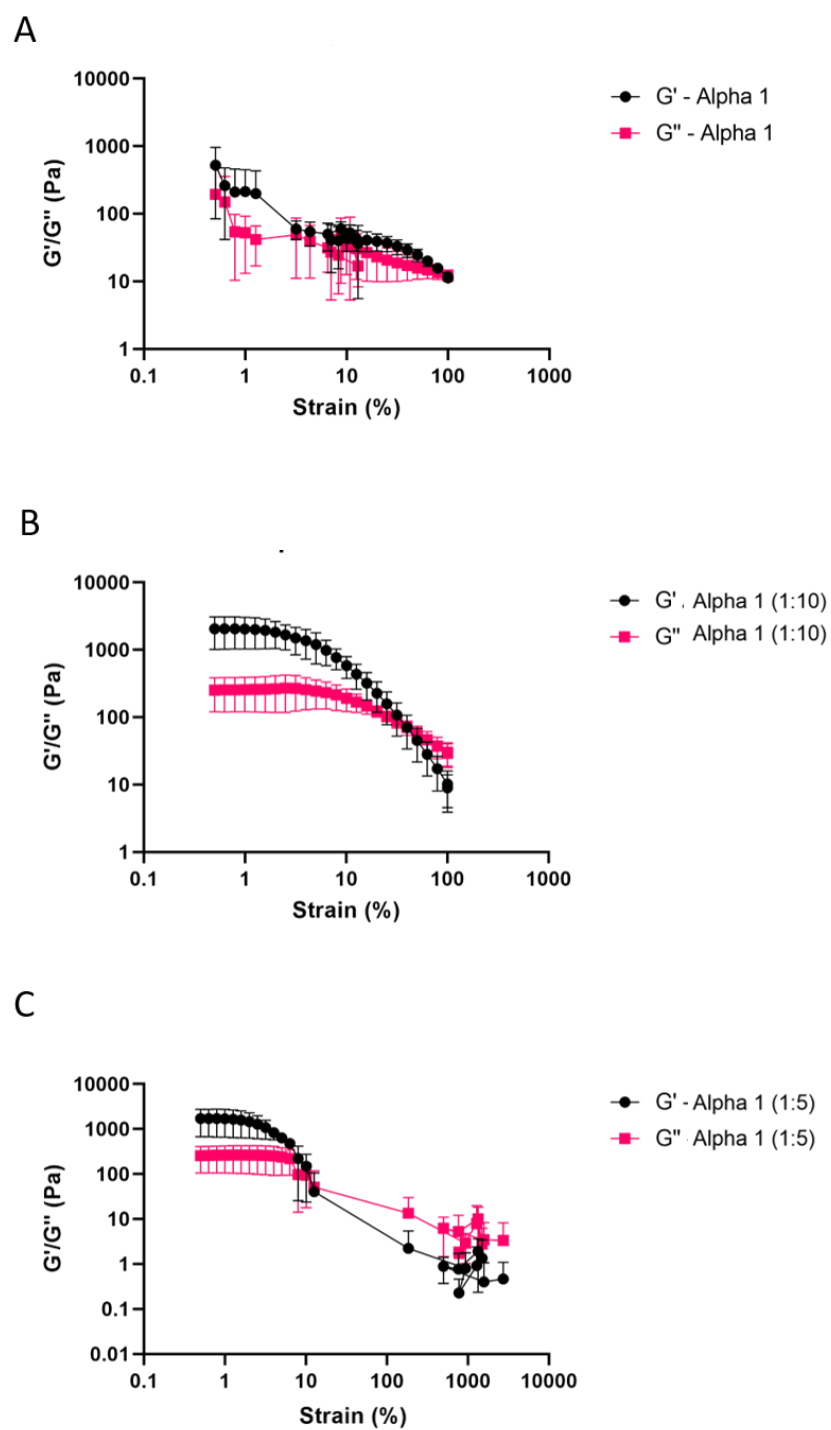
A

B

C

Figure A2.2. Amplitude sweep data (A) Alpha 1, (B) Alpha 1 in a 1:10 ratio mixed with cell culture medium, (C) Alpha 1 in a 1:5 ratio mixed with cell culture medium.
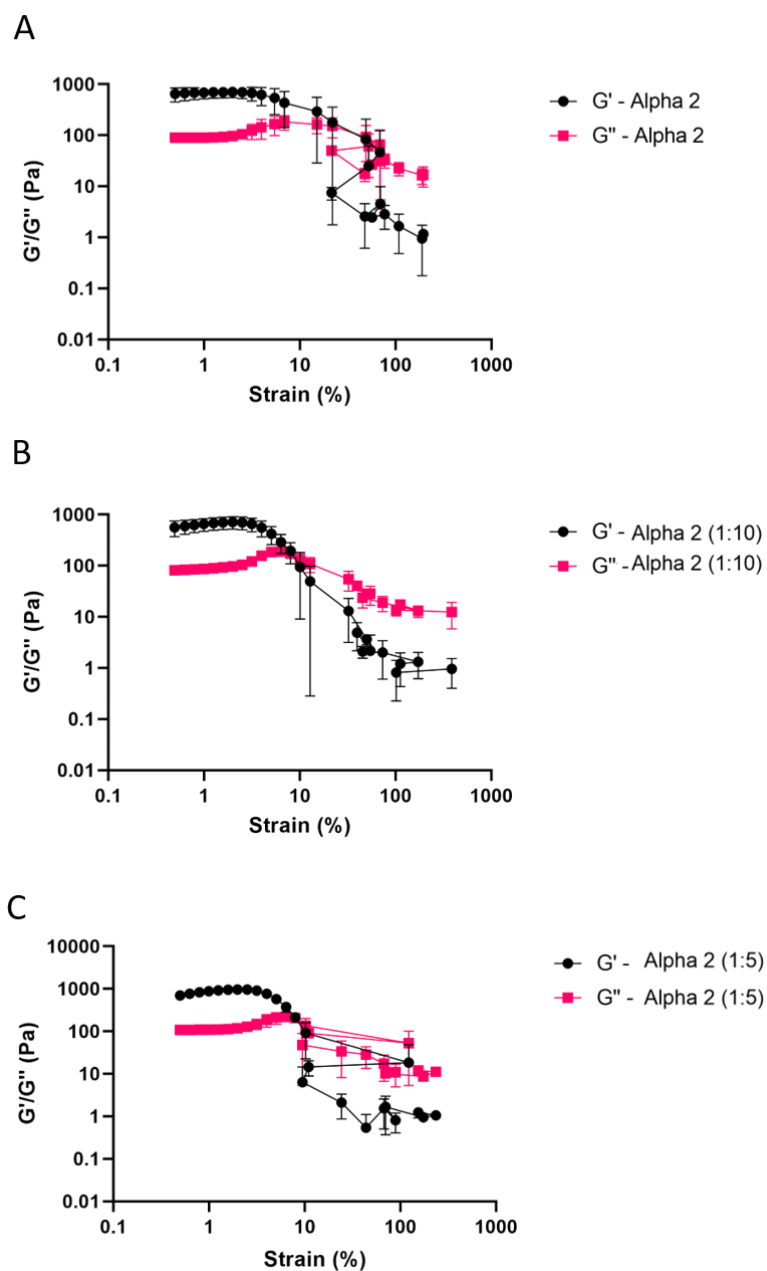
289

Figure A2.3. Amplitude sweep data (A) Alpha 2, (B) Alpha 2 in a 1:10 ratio mixed with cell culture medium, (C) Alpha 2 in a 1:5 ratio mixed with cell culture medium.
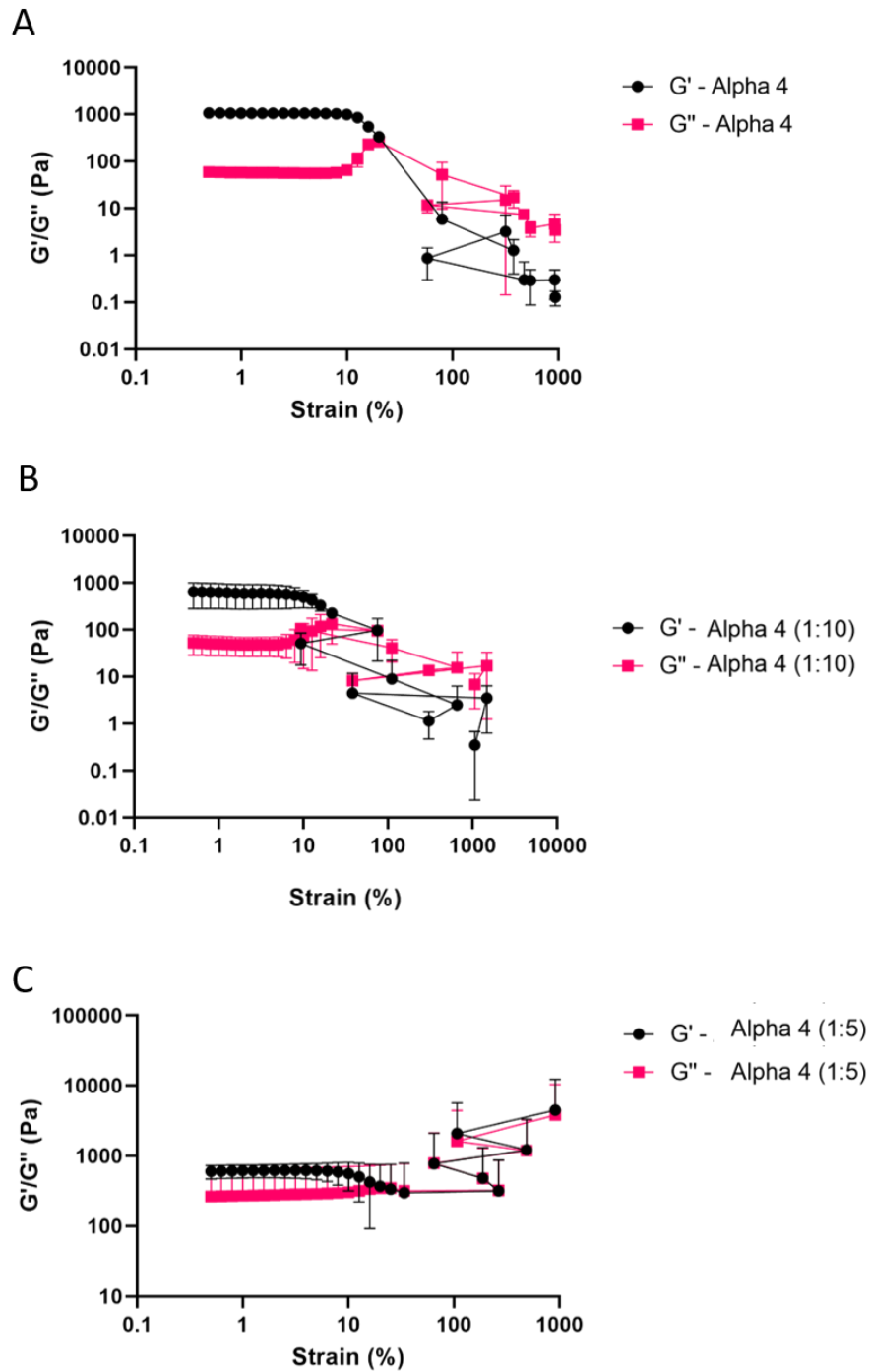
290

Figure A2.4. Amplitude sweep data (A) Alpha 4, (B) Alpha 4 in a 1:10 ratio mixed with cell culture medium, (C) Alpha 4 in a 1:5 ratio mixed with cell culture medium.

Appendix 3: Additional data from Chapter 3

A3.1 Assessment of cell viability in non-printed Peptigels®

Initial live/dead assessment of cell viability in non-printed Peptigels® focused on addressing the cytocompatibility of these materials for HCHs. As shown in Figure A3.1, cells thrived in both materials, presenting some cell death on day 3, which then decreased on day 7, showing a higher cell viability. These were compared to the 2D HCHs culture, which depicted no cell death across that cell culture time, suggesting that the cell culture medium chosen and the culture conditions were optimal for cell survival.
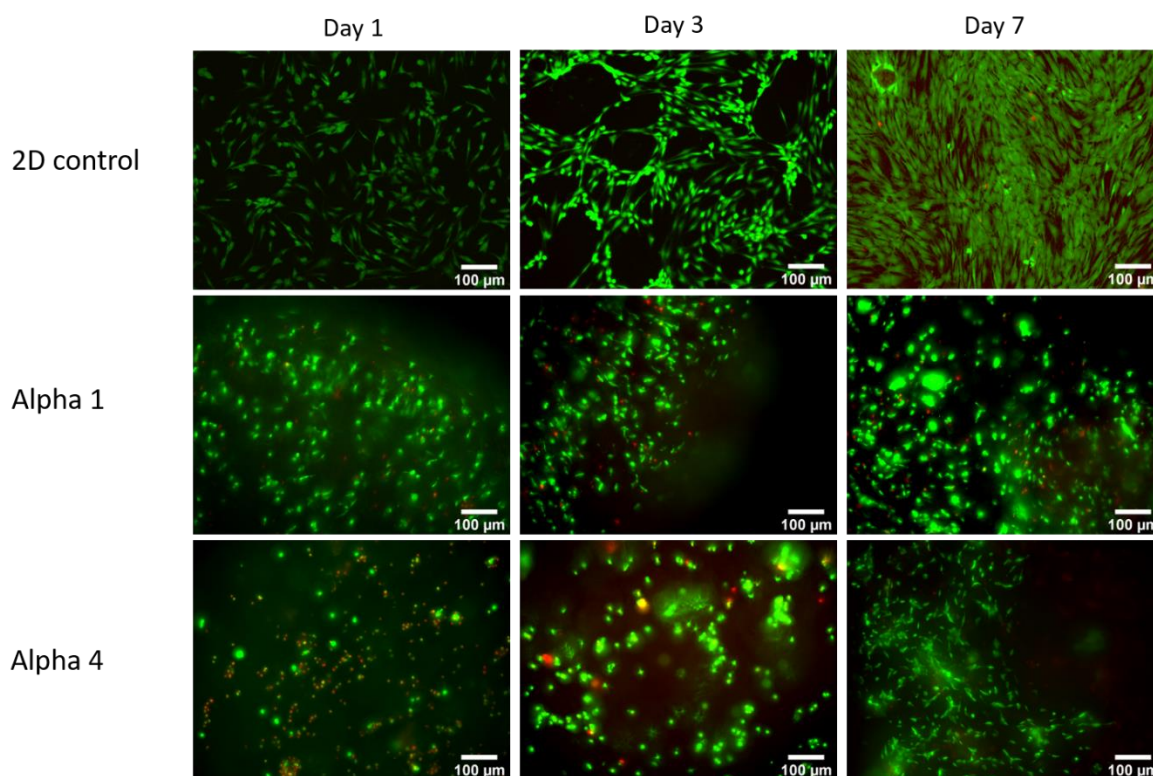

Figure A3.1. Live/dead staining of human primary chondrocytes (HCHs) across 7 days of culture. 2D control cells show close to 100% viability. Alpha 1 and Alpha 4 were pipetted, not printed, Peptigels®; they show initial cell death at day 1, maintained across to day 7. Green shows alive cells and red shows dead cells.

A3.2 Complete staining of gels and 3D pellets with Alcian blue for GAG quantification

To assess GAG production, 3D chondrocyte pellets, Alpha 1 and Alpha 4 Peptigels®, were stained whole with Alcian blue. A staining time of 15 minutes was performed, and then samples were washed in PBS for 1.5 hours. Figure A3.2 shows the full staining of both acellular and cellularised Alpha 1 and Alpha 4. Acellular Peptigel® Alcian blue staining confirmed that there was background staining from the Peptigel® and that GAG production could not be accurately determined with this staining protocol.
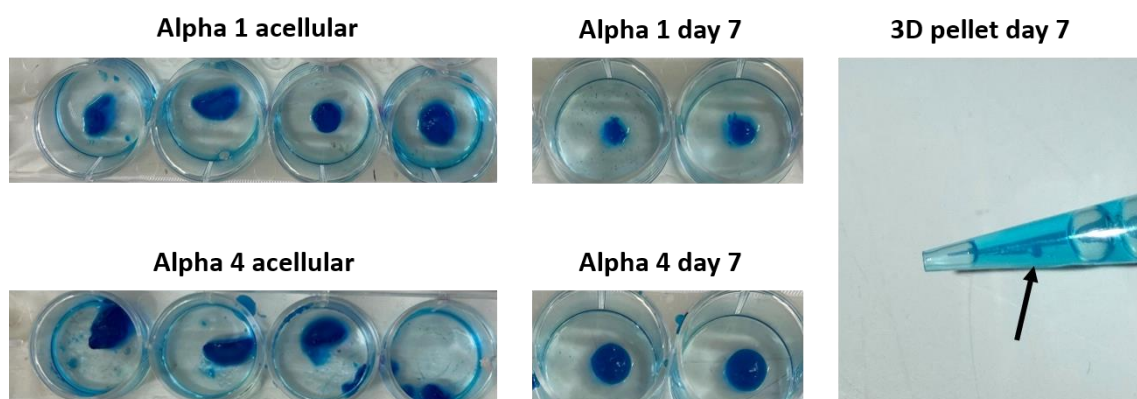

Figure A3.2. Photographs of Alcian blue stained acellular Alpha 1 and Alpha 4; HCH embedded Alpha 1 and Alpha 4 after 7 days of culture; 3D pellet control after 7 days of culture.

A3.3 Optimisation of the RNA extraction process

Comparative qPCR required mRNA material to be isolated from all systems. The peptide hydrogel manufacturer, MBG, suggested a specific protocol and the QIAGEN RNAeasy kit. The suggested protocol involved digesting the Peptigel® with pronase and mixing it with the lysis buffer provided in the QIAGEN kit for 3 minutes under 3,000 rpm centrifugation. This protocol was compared to an alternative standardised RNA extraction method. This standard alternative consisted of digesting the samples with protease solution and continuing with a standard TRIzol and chloroform RNA

separation. Subsequently, the same steps from the QIAGEN RNAeasy kit were followed. As seen in Figure A3.3, the protocol from MBG gave higher levels of RNA extraction; therefore, this method was used for all RNA extraction.
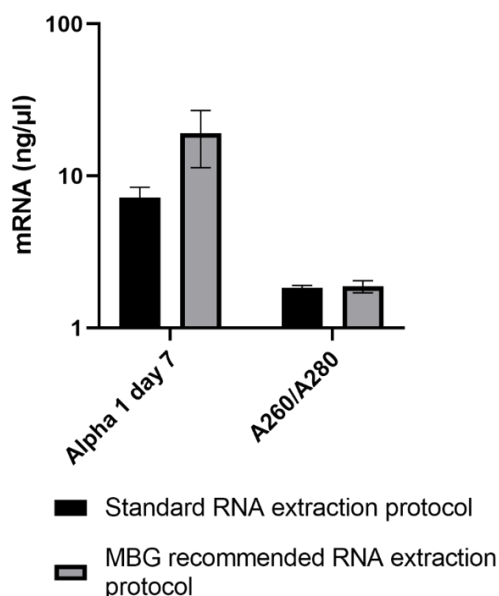

Figure A3.3. RNA levels were obtained through two different RNA extraction protocols. The standard RNA extraction protocol followed TRIzol and chloroform-based extraction. The MBG recommended extraction protocol used protease solution to digest the Peptigel® and the QIAGEN RNAeasy Kit.

A3.4 Alpha 1 stability acellularly for 32 days.

Acellular Alpha 1 degradation was assessed for 32 days *in vitro*. This Peptigel® was found to degrade when mixed with HCHs promptly. To further assess whether this degradation was material-dependent or cell-mediated, a long-term study of acellular Alpha 1 degradation was performed. Images of Alpha 1 were taken at different time points, Figure A3.4. Some samples degraded between days 13 and 26, but others were stable for up to 32 days. This further confirmed that the degradation was cell-mediated and not material-dependent.
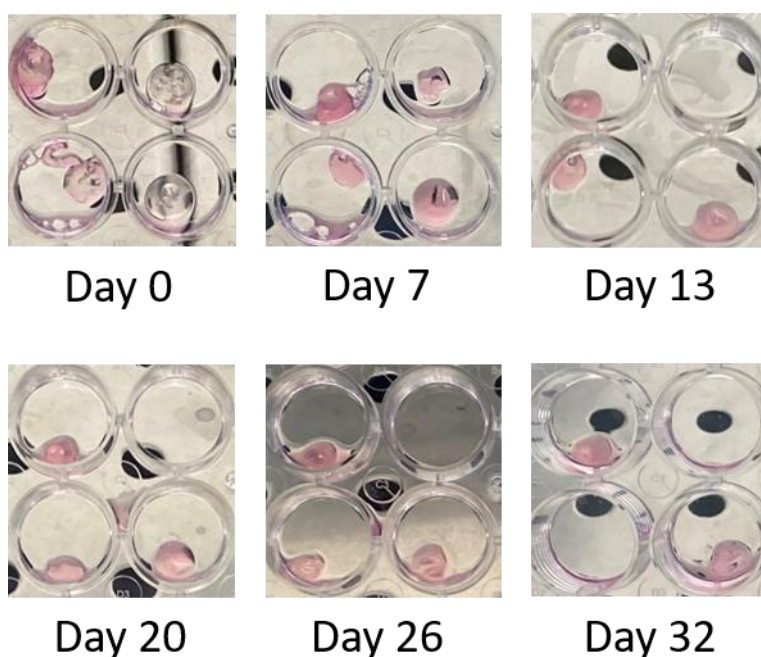
Figure A3.4. Photographs of acellular Alpha 1 across 32 days of culture to assess acellular Alpha 1 degradation rate.

A3.5 Ilomastat experiment

A preliminary experiment was set up with Alpha 1 in culture with ilomastat, a general MMP inhibitor, to address whether suppressing MMPs would decrease Alpha 1 degradation and affect its chondrogenic behaviour. Ilomastat was added into the chondrogenic medium in a 10 µM concentration, chosen based on previous literature [350–353]. The effect of this inhibitor on cell viability was assessed through live/dead assay and DNA quantification, Figure A3.5. This Figure depicts low levels of cell death and comparable levels of DNA between Alpha 1 and Alpha 1 with ilomastat.

A

3D pellet cultured in ilomastat   **Alpha 1 with ilomastat**
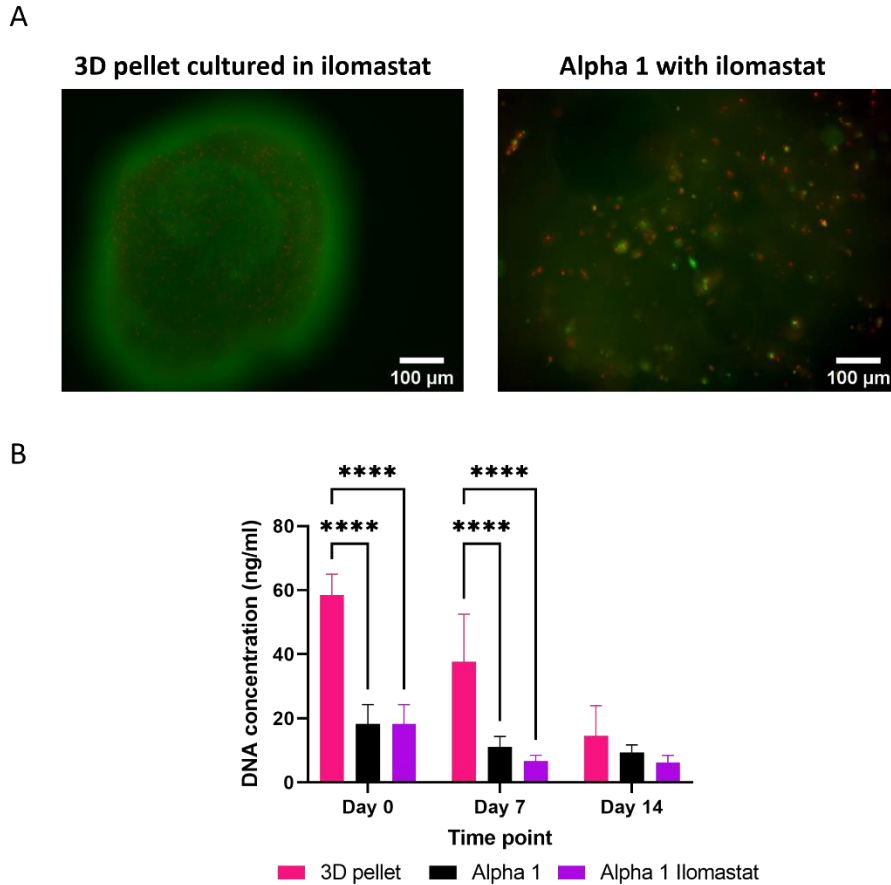
B

Figure A3.5. A) Live/dead staining of human primary chondrocyte cells at day 7 on the 3D pellet control and Alpha 1 3D bioprinted hydrogel. These systems were cultured in the commercial chondrocyte medium with 10 µM of ilomastat. Green shows alive cells and red shows dead cells. B) DNA concentration measurements obtained through PicoGreen assay across 14 days of culture of human primary chondrocytes in the 3D pellet control and 3D bioprinted Alpha 1 cultured in chondrocyte culture medium. Alpha 1 ilomastat is Alpha 1 cultured with chondrocyte culture medium and 10 µM ilomastat. Error bars show standard deviation. Two-way ANOVA was performed; ** - p < 0.0001. N = 6 for 3D pellet; N = 9 for Alpha 1; N = 3 for Alpha 1 ilomastat.**

H&E staining was performed in the Alpha 1 sections and compared to those Alpha 1 cultured in normal conditions to assess whether adding this inhibitor decreased the rate of Alpha 1 degradation. Figure A3.6 shows that Alpha 1 cultured with ilomastat had bigger sections on day 14, suggesting less degradation. However, day 7 samples appeared smaller when cultured in ilomastat than in normal conditions. These discrepancies between culture days concluded that these results were not conclusive.

Further tests and a larger sample population with ilomastat culture conditions should be tested to confirm the effect on Alpha 1 degradation. A main difference was observed between the two culture set-ups: ilomastat conditions did not promote the formation of Alpha 1 surface cell clusters. This suggested that the chondrogenic behaviour observed in these cell clusters was missing from the ilomastat culture conditions.
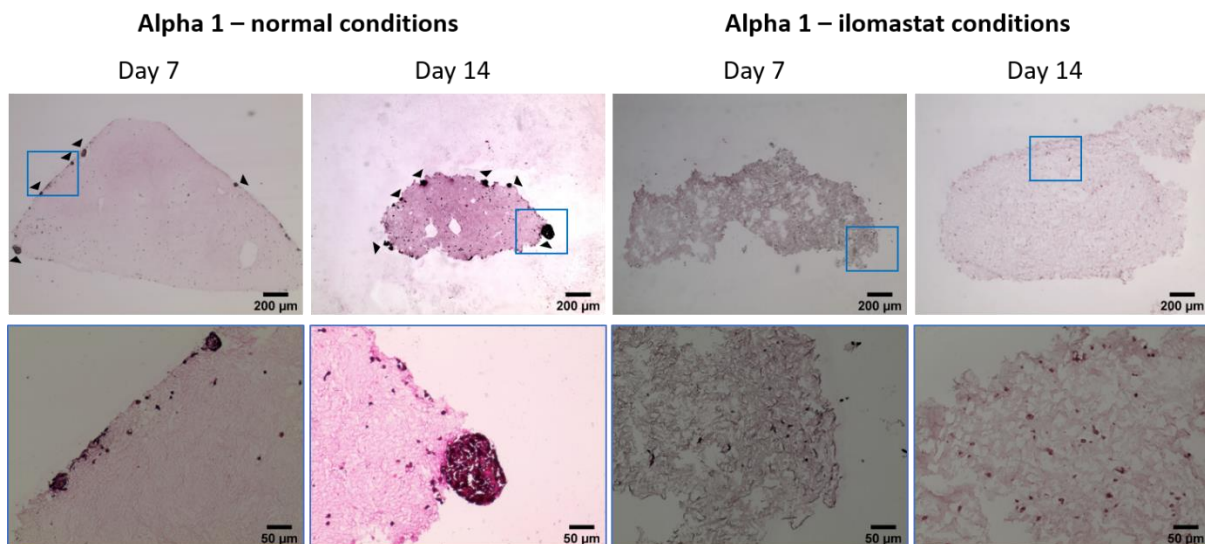

Figure A3.6. H&E staining images of Alpha 1 cultured in normal conditions and Alpha 1 cultured with ilomastat over the 14 days of culture. The top row in each sample shows images at a lower magnification, and the bottom row has higher magnification images corresponding to the highlighted squares in the images above.

Further tests regarding this inhibitor's effect on the chondrogenic behaviour of Alpha 1 were performed through immunofluorescence labelling of chondrogenic markers. F-actin and collagen type-II expression were assessed, Figure A3.7. F-actin labelling confirmed the lack of cell cluster formations in the Alpha 1 samples cultured with ilomastat and the maintenance of circular cell shape of chondrocytes when embedded in samples treated with ilomastat. Additionally, collagen type-II showed lower intensity values observed in the ilomastat cultures, suggesting that the lack of cell cluster formation compromised the chondrogenic behaviour of the Alpha 1 embedded chondrocytes. Aggrecan and SOX-9 were also immunofluorescently labelled, Figure A3.8. Both aggrecan and SOX-9 showed a lower expression than the one observed in

Alpha 1 cultured in normal conditions. This further confirmed that by inhibiting MMPs, Alpha 1 embedded cells could not self-assemble in cell clusters and lost chondrogenic potential. Based on these observations, further analysis was not performed, and this strategy for decreasing Alpha 1 degradation was not pursued as it compromised the chondrogenic ability of Alpha 1.
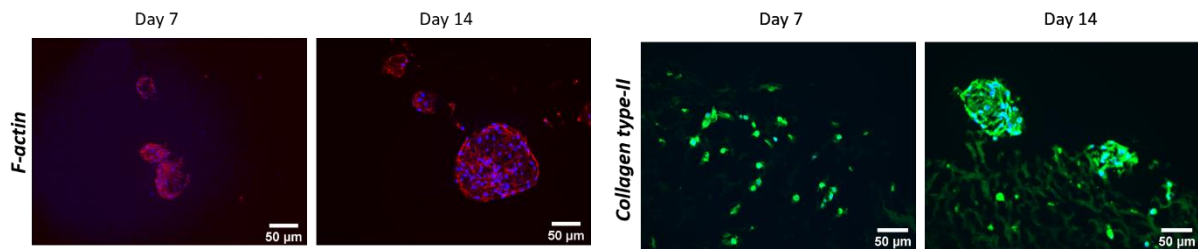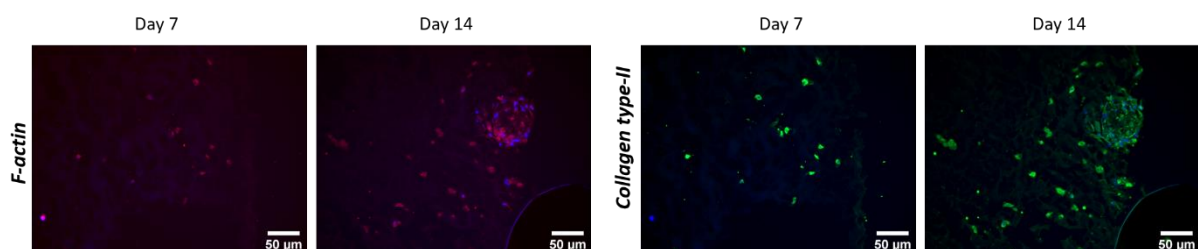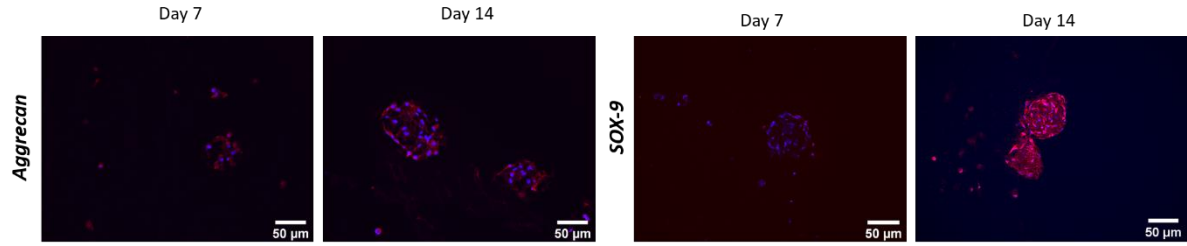

Figure A3.7. Left: F-actin labelling (red) and nuclei (blue) of human primary chondrocytes in Alpha 1 3D bioprinted structures across 14 days of culture in normal conditions and cultured with 10 μM ilomastat supplementation. Right: Collagen type-II labelling (green) and nuclei (blue) of human primary chondrocytes in Alpha 1 3D bioprinted structures across 14 days of culture in normal conditions and cultured with 10 μM ilomastat supplementation.
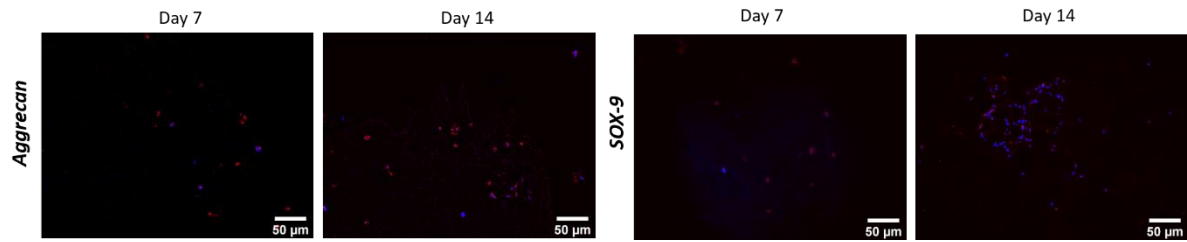
Figure A3.8. Left: Aggrecan labelling (red) and nuclei (blue) of human primary chondrocytes in Alpha 1 3D bioprinted structures across 14 days of culture in normal conditions and cultured with 10 µM ilomastat supplementation. Right: SOX-9 labelling (red) and nuclei (blue) of human primary chondrocytes in Alpha 1 3D bioprinted structures across 14 days of culture in normal conditions and cultured with 10 µM ilomastat supplementation.

Appendix 4: Additional data from Chapter 4

A4.1 Additional literature review on 3D printed HA-based scaffolds for bone tissue modelling

Table A4.1. Summarising table of 3D printing HA-based scaffolds investigations.

3D printing technique	Cell type used *in vitro*	Cell culture time	Findings	Reference
Photopolymerisation-based	Rat BMSCs	7 days	HA-based scaffolds were manufactured with 70% porosity. Different pore shapes were compared, and the cubic pore-shaped scaffolds showed the highest compressive strength (22.5 MPa) and modulus (400 MPa). They also showed the highest metabolic activity of the rat BMSCs after 7 days of culture. However, no long-term (> 28 days) culture investigations or testing for osteogenic differentiation of the rat BMSCs was performed.	[309]
Photopolymerisation-based	Rat BMSCs	7 days	HA-based scaffolds were 3D-printed, and different sintering atmospheres were tested. They found that a wet CO_2 atmosphere improved the densification process and led to better mechanical properties for HA (flexural modulus of 3.24 GPa). Additionally, this wet CO_2 atmosphere enhanced the biological activity of the seeded cells. However, no long-term (> 28 days) culture investigations or testing for osteogenic differentiation of the rat BMSCs was performed. Additionally, no information on the compressive strength was reported.	[310]
Photopolymerisation-based	MG-63	3 days	Pure HA scaffolds and pellets were manufactured and compared against HA and TCP biphasic samples. MG-63 cells were used to test *in vitro* the biocompatibility of the pellets. These samples were also tested *in vivo* in a cranial rat model. Cells were cultured for	[311]

			only 3 days, and no long-term *in vitro* culture was performed. The 3-day experiment showed that cells that adhered to the HA scaffolds were viable and metabolically active. However, no compressive strength assessment was performed.	
Extrusion-based	No cells	N/A	A clinically approved HA ink was optimised, and different printing parameters, such as printing speed, extrusion pressure, accuracy, and infill density, were tested. They found the existing relationship between the different infill densities and the shrinkage level post-sintering of the scaffolds. Additionally, they showed the accuracy of the prints by 3D printing a patient-specific bone defect from CT scans. However, no *in vitro* cell-based experiments were performed to investigate the effect of these scaffolds on bone-like cell behaviour, short or long-term.	[303]
Extrusion-based	No cells	N/A	The characterisation of calcium and phosphate release of 3D-printed HA scaffolds was performed. They compared pure HA to beta-TCP and different HA/beta-TCP ratios. Pure HA showed the lowest release of Ca ions in the culture medium, showing the low dissolution behaviour of HA and its long-term (14 days) stability compared to the different ratios. No cytocompatibility or compressive strength assessments were performed.	[304]
Extrusion-based	HOBs	7 days	HA 3D-printed scaffolds are compared to TCP 3D printed scaffolds. HOBs were cultured for 7 days on the samples, and proliferation and cytotoxicity were measured. No assessment of the mechanical characteristics of the 3D scaffolds was performed. However, HOBs were shown to be more proliferative in the HA scaffolds during the 7 days. Further long-term cultures and assessment of bone-specific markers should be performed.	[305]
Extrusion-based	No cells – *in vivo*	8-16 weeks	Two HA 3D-printed scaffolds with different spacing between rods were tested *in vivo* in New Zealand White rabbits. Tissue response was evaluated at 8 and 16 weeks through micro-computed tomography, histology and SEM. Although no *in vitro* assessment or	[306]

			mechanical characterisation is reported, *in vivo* implantation showed bone healing, suggesting that this material promoted bone regeneration. However, further tests *in vitro* should be performed.	
Extrusion-based	No cells	N/A	Two 3D-printed scaffolds made of HA or beta-TCP were compared regarding their compressive strength, elastic modulus and stability in simulated body fluid for 3 weeks. HA demonstrated higher compressive strength, which increased from 50 MPa to 110 MPa after being immersed in simulated body fluid. This demonstrated the ability of HA as a better load-bearing material than beta-TCP. However, no cell-based experiments were performed. Therefore, cell cytocompatibility should be further investigated.	[307]
Extrusion-based	No cells	N/A	Pure HA lattices were 3D printed as load-bearing scaffolds for bone repair were manufactured. They shaped the scaffolds into computed tomography-based maxillary implants. The scaffolds demonstrated different compressive strength values depending on the sintering temperature and the microporosity. 1300°C and no microporosity showed to generate the higher compressive strength ~750 MPa. No cytocompatibility studies *in vitro* with bone-like cells were performed prior to implantation.	[308]

A4.2 2D optimisation of the 3D printing of HA scaffold

2D filament deposition of the HA ink was tested with a range of pressures (120-200 kPa) at two printing speeds (5 and 8 mm/s). The filament width of the deposited filaments was calculated and plotted. These values were compared to the theoretical value of 410 μm, corresponding to the diameter of the 22G needle used. Figure A4.1 shows the filament with HA deposited with the selected parameters. Due to the large standard deviations shown, the range was kept, and the printer user adjusted the printing parameters according to the behaviour of HA.
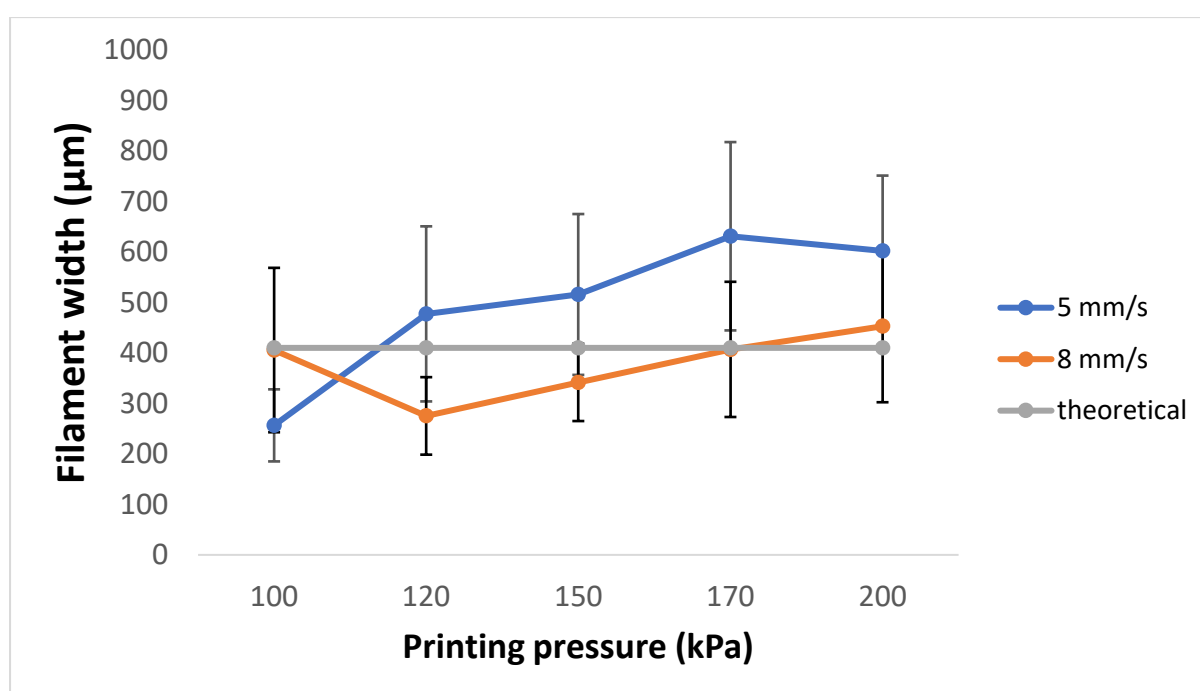

Figure A4.1. Filament width deposition of HA at two different printing speeds (5 and 8 mm/s). Error bars show standard deviations. The theoretical value corresponds to the diameter of the 22G needle used to 3D print the filaments.

A4.3 Staining of Alizarin Red

Alizarin red is a common staining to visualise calcium deposition, a bone mineralisation characteristic. However, when this staining is performed in the HA scaffolds, there is interference from the scaffold, which is largely made of calcium. Staining with alizarin red and subsequent retrieval of this dye was performed to

investigate whether this labelling process could be used to investigate mineralisation. Acellular HA and Saos-2 cell-seeded scaffolds cultured for 28 days in a pro-calcifying medium were stained. Alizarin red immersion was performed for 30 minutes, and alizarin red retrieval using 10% acetic acid and 10% NH$_4$OH neutralisation was performed. The solutions' optical density was measured at 405 nm, but acellular scaffolds gave higher intensity levels than the cellularised samples. The staining of Saos-2 cell-seeded HA scaffolds and the acellular scaffold were inconsistent. Additionally, there were no clear differences between acellular and cellularised scaffolds before and after retrieval measurements. Therefore, this technique was not used to determine the mineralisation on HA scaffolds.
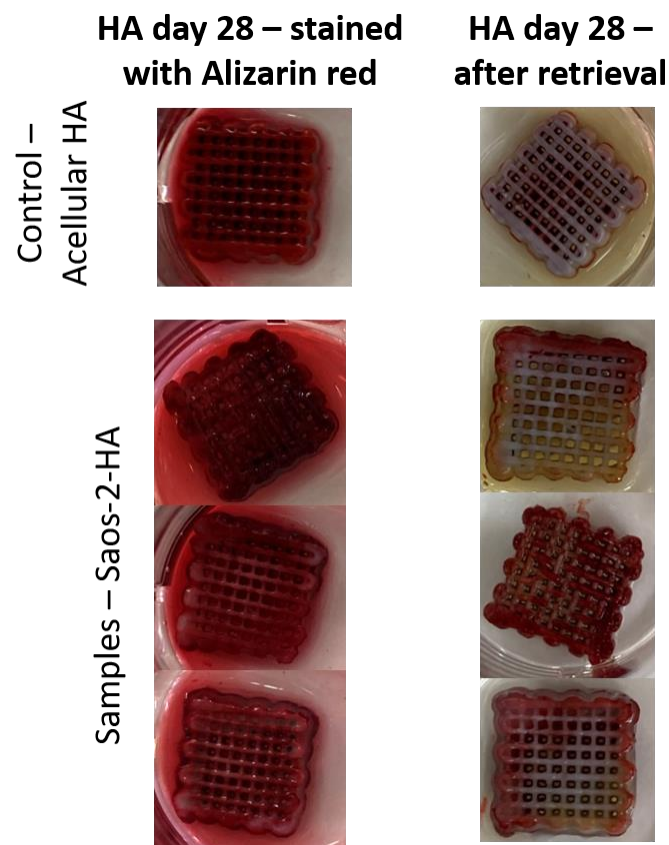

Figure A4.2. Left: Alizarin red stained acellular and Saos-2 cell-seeded scaffolds after 28 days of culture. Right: Samples after retrieving Alizarin red staining.

A4.4 Negative immunofluorescence labelling of samples

Negative immunofluorescence labelling of 2D control cultures and HA scaffolds was performed to assess the autofluorescence of the seeded cells and the HA particles. Figure A4.2 shows images of 2D cultures and cell-seeded HA scaffolds where the secondary antibody for collagen type-I labelling (green) was added alongside phalloidin. Minimal green autofluorescence was detected, confirming that the green intensities in Figures 4.6 and 4.9 are collagen type-I depositions.
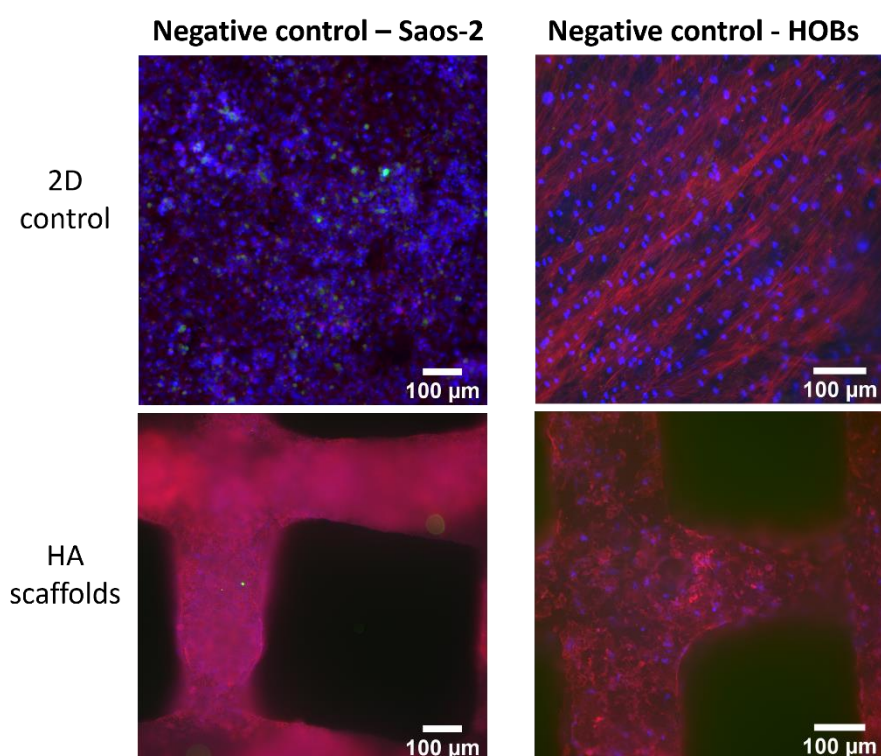

Figure A4.3. Negative Immunofluorescence labelling of collagen type-I (green) and F-actin (red) of Saos-2 cells seeded on a 2D well plate or an HA scaffold and HOB seeded on a 2D well plate or an HA scaffold. The cell nuclei are depicted in blue.

Appendix 5: Additional data from Chapter 5

A5.1 Delamination issues with upright manufacturing

Upright manufacturing of the biphasic osteochondral construct demonstrated multiple disadvantages, such as the detachment of the Alpha 1 section from the HA scaffold and the fast degradation experienced by Alpha 1. Figure A5.1 showed this phenomenon, depicting multiple samples delaminated and degraded after 7 days of culture.
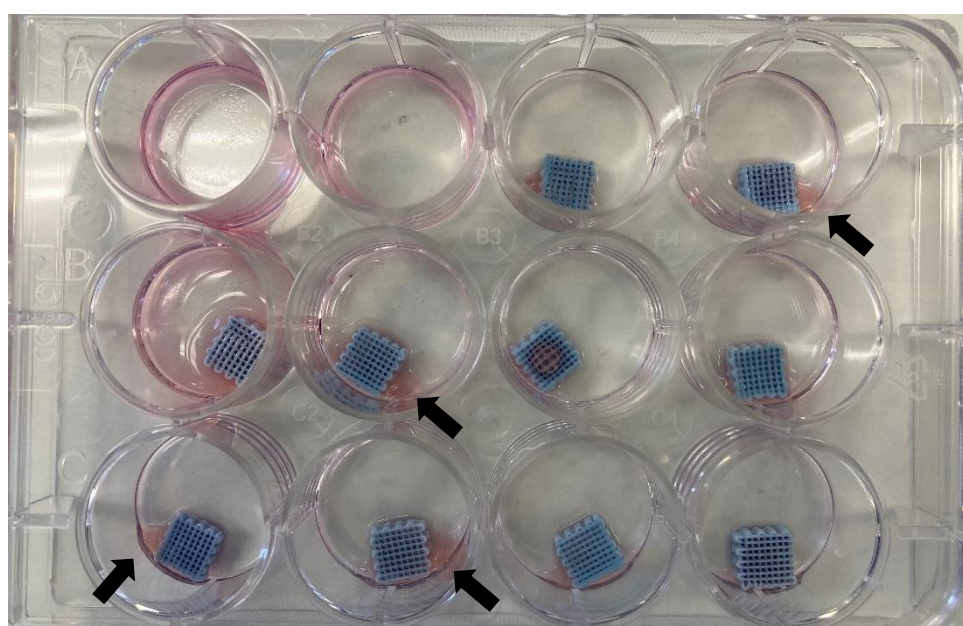

Figure A5.1. Photograph of osteochondral biphasic constructs manufactured upright after 7 days of culture. Arrows point to the Alpha 1 sections, which have delaminated from the HA constructs and have heavily degraded.

A5.2 Negative staining control of samples

Negative immunofluorescence labelling of osteochondral biphasic constructs was performed to assess the autofluorescence of the seeded cells and the HA particles. Figure A5.2 shows images of both osteochondral biphasic constructs manufactured with Saos-2 cells and HOB cell-seeded HA with the secondary antibody AlexaFluor 488, AlexaFluor 555, and AlexaFluor 594. These secondary antibodies were used for

immunofluorescently labelling proteins of interest, as explained in section 5.3.3.2. Minimal green autofluorescence was detected, Figure A5.2, confirming that the intensities seen across the immunofluorescently labelled cryosections represented the proteins labelled.

Negative control – AlexaFluor 488 and phalloidin

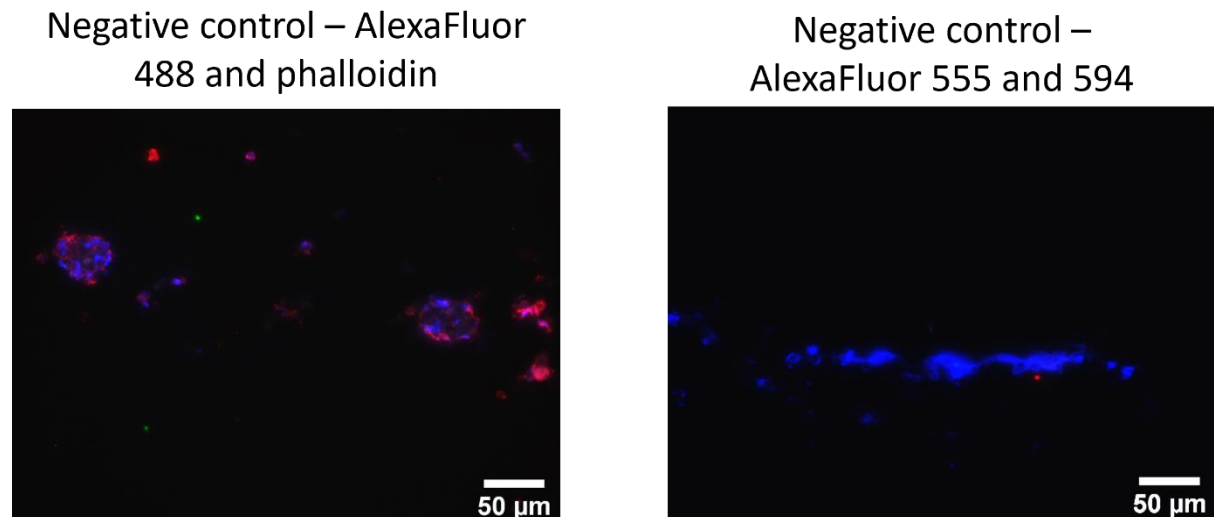Negative control – AlexaFluor 555 and 594

Figure A5.2. Left: negative Immunofluorescence labelling of AlexaFluor 488 (green) and F-actin (red) of HOB-HA osteochondral biphasic construct. Right: negative Immunofluorescence labelling of AlexaFluor 455 (green) and AlexaFluor 594 (red) of HOB-HA osteochondral biphasic construct. The cell nuclei are depicted in blue.